



**HAL**  
open science

# Beta-Cyclodextrin-based artificial nanochannel scaffolds inserted in polymeric membrane

Haiqin Du

► **To cite this version:**

Haiqin Du. Beta-Cyclodextrin-based artificial nanochannel scaffolds inserted in polymeric membrane. Polymers. Sorbonne Université, 2021. English. NNT : 2021SORUS262 . tel-03558201

**HAL Id: tel-03558201**

**<https://theses.hal.science/tel-03558201v1>**

Submitted on 4 Feb 2022

**HAL** is a multi-disciplinary open access archive for the deposit and dissemination of scientific research documents, whether they are published or not. The documents may come from teaching and research institutions in France or abroad, or from public or private research centers.

L'archive ouverte pluridisciplinaire **HAL**, est destinée au dépôt et à la diffusion de documents scientifiques de niveau recherche, publiés ou non, émanant des établissements d'enseignement et de recherche français ou étrangers, des laboratoires publics ou privés.

# Sorbonne Université

ED 397 Physique et Chimie des Matériaux

*IPCM / Equipe de Chimie des Polymères (ECP)*

## ***beta*-Cyclodextrin-based Artificial Nanochannel Scaffolds Inserted in Polymeric Membrane**

By Haiqin DU

Thesis in Polymer Chemistry

Supervised by Philippe GUÉGAN and Cécile HUIN

Defended in Paris on 6<sup>th</sup> December 2021

### JURY MEMBERS

M. Olivier COLOMBANI, Maître de conférences, HDR, Rapporteur

M. Patrice WOISEL, Professeur, Rapporteur

M. Patrick PERRIN, Professeur, Président

M. Philippe GUÉGAN, Professeur, Directeur de thèse

Mme. Cécile HUIN, Maître de conférences, Co-Encadrante de thèse





*Les Ans 2017–2021*

*à Paris*

## Acknowledgments

The 4-years experience in ECP, in Paris, is invaluable to me because I've learned a lot from the process of scientific investigations and from the life itself. At the same time, I'm very sure that, it is the great and kind people I've met and I'm meeting that help me to learn, and to grow up. Thank you very much!

First of all, I would like to express my sincere thanks to my supervisors, Pr. Philippe GUÉGAN and Dr. Cécile HUIN, who helped me a lot with thesis writing, to solve scientific problems and other problems I encountered especially in the "adaptive period" at the beginning. I am so lucky to have such great tutors!

I would also like to thank my thesis committee: Dr. Olivier Colombani, Pr. Patrice Woisel, and Pr. Patrick Perrin, for agreeing to evaluate my work.

I would like to thank all the members in ECP for their kind help with a diversity of things. Thank Dr. Gaëlle Pembouong for her patient assistance with SEC and ITC operations, Dr. Claire Troufflard for her assistance for NMR characterization, Dr. David Kreher for his nice presence in my Comité de Suivi de Thèse (CST) meetings and his help with fluorescence spectrometer, Dr. Fabrice Mathevet for his help with fluorescence spectrometer also, Dr. Nicolas Illy for his great help in organic chemistry and suggestions on polymer science, Dr. Veronique Bennevault for her nice help with DOSY NMR characterizations, Madame Sylvie Paller Jammes for her kind help with the dialysis membrane orders and ASDB applications, and so on.

I would like to specially thank my colleagues, Gwendoline Delecourt, Pauline Le Bellec, Valentin Puchelle, Özgül Tezgel, Laetitia Plet, Simon Le Luyer, Thibaut Kalem, and Sandra Kalem, for their kind help and big smiles.

Besides the members in ECP, I would like to thank Pr. Fernando Carlos Giacomelli of Universidade Federal do ABC (São Paulo, Brazil) for his huge help during my experiments in the polymersome field, Dr. Guillaume Tresset of LPS Orsay for his kind assistance for SAXS and TEM, as well as Dr. Cédric Vancaeyzeele (CY Cergy Paris Université) and Pr. Olivier Durupthy (Sorbonne Université) for their kind presence in my CST meetings as well as for their great suggestions on my work.

Additionally, I would like to thank China Scholarship Council (CSC) and Sorbonne University, for the financial supports. Without the funds, I could not have such an impressive journey in ECP, in Paris, or to meet such great people.

At last, I would like to thank my parents for their supports, Pr. Yanmei Wang for her encouragement, as well as my close friend Cen Wang who inspires me more than I've realized.

**Thank you very much, dear everyone.**

## General Table of Contents

Acknowledgments

Résumé.....	1
Abbreviations.....	7
General Introduction.....	9
Chapter 1. State of the Art: Literature review.....	15
Chapter 2. Linear Amphiphilic Copolymers: Syntheses, structural characterizations, and self-assemblies.....	77
Chapter 3. $\beta$ CD-cored Star Amphiphilic Copolymers: Syntheses, structural characterizations, and self-assemblies.....	125
Chapter 4. Polymersome Membrane Permeability to $H^+$ .....	181
Chapter 5. Polymeric Membrane Permeability to $K^+$ and $Cl^-$ : Black lipid membrane-type electric measurements.....	215
General Conclusion and Perspectives.....	235



## **Résumé**

## **Chapitre 1 : contexte du projet de thèse et état de l'art**

Ce projet de thèse s'inscrit dans une approche biomimétique et vise à construire un organite synthétique.

L'une des caractéristiques communes aux organites est d'effectuer des réactions biochimiques de manière contrôlée, grâce à la propriété de compartimentation. Des systèmes qui réalisent des réactions enzymatiques confinées à l'échelle nanométrique sont appelés nanoréacteurs. En termes de structure, le nanoréacteur est un nanocompartiment catalytique incorporant des enzymes et d'autres types de catalyseurs et il peut être constitué de liposomes, de polymersomes, de capsules polymères, etc. Les polymersomes possèdent des propriétés intéressantes pour la construction de compartiments, puisqu'ils présentent une stabilité, une robustesse et une diversité chimique, meilleures que celles des liposomes, et ceci grâce à un auto-assemblage de copolymères amphiphiles, procédé avantageux par rapport aux procédés fastidieux utilisés pour préparer des capsules polymères.

Outre cet aspect de confinement, le compartiment doit être perméable aux substrats et produits. Cependant, peu de polymersomes présentent cette perméabilité nécessaire au développement des applications de ces objets. Diverses stratégies de perméabilisation ont été proposées, dont l'utilisation de protéines membranaires, mais beaucoup de discordances existent entre ces objets et les membranes polymères, à la fois sur le plan physique et chimique. Une autre option est d'envisager des nanocanaux synthétiques utilisés dans le contexte des bicouches lipidiques planes et 3D. Les nanocanaux synthétiques sont attrayants par de nombreux aspects, notamment les paramètres structurels sur mesure, une meilleure stabilité et une bonne robustesse, ainsi qu'un coût moindre pour les applications à grande échelle par rapport aux protéines naturelles. Peu d'études concernent leur incorporation dans des membranes polymères.

Un système entièrement synthétique construit en insérant des nanocanaux synthétiques dans une membrane polymère devrait avoir un large éventail d'applications en nanotechnologie. Ainsi, ce projet de thèse consiste à développer une plateforme entièrement synthétique, constituée de polymersomes et de nanocanaux artificiels.

Les surfaces à base de polyglycidol (PGL) ont une bonne biocompatibilité avec une faible immunogénicité et une faible cytotoxicité, ce qui est crucial pour les applications biomédicales. En combinaison avec le segment poly(oxyde de butylène) (PBO) hydrophobe, qui est également biocompatible, les copolymères amphiphiles linéaires dibloc poly(oxyde de butylène)-*b*-polyglycidol (PBO-PGL) et tribloc polyglycidol-*b*-poly(oxyde de butylène)-*b*-polyglycidol (PGL-PBO-PGL) sont envisagés pour s'auto-assembler en polymersomes, en fonction du rapport hydrophobe/hydrophile utilisé.

Les nanocanaux artificiels à base de  $\beta$ CD sont connus comme des nanocanaux polyvalents dans les bicouches lipidiques, formant des héli-canaux, avec ou sans réactivité aux stimuli, des canaux unimoléculaires formés par des polymères en étoile à cœur  $\beta$ CD ou des nanotubes de cyclodextrine. Ce projet accorde une attention particulière aux polymères en étoile à cœur  $\beta$ CD, où l'oligosaccharide cyclique est décoré symétriquement de 14 bras amphiphiles PBO-PGL. L'objectif est de minimiser l'inadéquation chimique et dimensionnelle entre les membranes polymères et les nanocanaux artificiels. Gardant ces points à l'esprit, ce projet est mené en commençant par la préparation et la caractérisation de chaque constituant et la combinaison ultérieure de ces deux unités.

Le premier chapitre a consisté en la revue de la littérature des sujets pertinents pour l'étude, dont l'auto-assemblage de copolymères amphiphiles, les applications des polymersomes dans le domaine des nanoréacteurs et les copolymères en étoile à base de  $\beta$ CD, afin de positionner ce projet de doctorat, ainsi que de fournir un arrière-plan théorique à ce projet.

## **Chapitre 2 : Copolymères amphiphiles linéaires : synthèse, caractérisation structurale et auto-assemblage**

Le chapitre 2 traite de la question de comment former le compartiment.

Des copolymères séquencés amphiphiles linéaires diblocs PBO-PGL et triblocs PGL-PBO-PGL ont été synthétisés via des procédures optimisées et reproductibles. Une copolymérisation anionique séquentielle par ouverture de cycles (oxyde de butylène, ethoxyethyl glycidyl éther, glycidol protégé), catalysée par une base phosphazène tBuP4, suivie d'une déprotection en milieu acide. Ces polymères ont ensuite été caractérisés par RMN  $^1\text{H}$  et SEC.

Les comportements d'auto-assemblage de ces copolymères ont ensuite été étudiés par diffusion dynamique de la lumière (DLS), diffusion statique de la lumière (SLS), diffusion des rayons X aux petits angles (SAXS) et microscopie électronique à transmission (MET) (Figure 1). Les auto-assemblages obtenus à partir des PGL-PBO-PGL dépendent grandement du rapport massique en blocs PGL ( $w_{\text{PGL}}$ ) : quand  $w_{\text{PGL}} \leq 0,21$ , des agrégats ont été obtenus ; quand  $0,22 \leq w_{\text{PGL}} \leq 0,40$ , les assemblages sont de type polymersomes ; des micelles sphériques ont été formées quand  $w_{\text{PGL}} \geq 0,46$ . Ces résultats sont en accord avec la littérature. En outre, l'épaisseur de la couche hydrophobe ( $t_h$ ) augmente avec le DP du bloc hydrophobe PBO ( $DP_{\text{PBO}}$ ) selon la relation  $t_h \sim DP_{\text{PBO}}^{0.64}$ , montrant que les chaînes PBO sont étirées dans la membrane.

Enfin, la capacité « antifouling » des auto-assemblages a également été évaluée par

DLS, calorimétrie de titration isotherme (ITC), spectroscopie de fluorescence et dichroïsme circulaire. Cette étude a montré que les assemblages stabilisés par le PGL avait une capacité antifouling à partir de  $DP_{PGL} \sim 20$ , valeur beaucoup plus faible que dans le cas du PEG ( $DP_{PEG} \sim 100$ ).

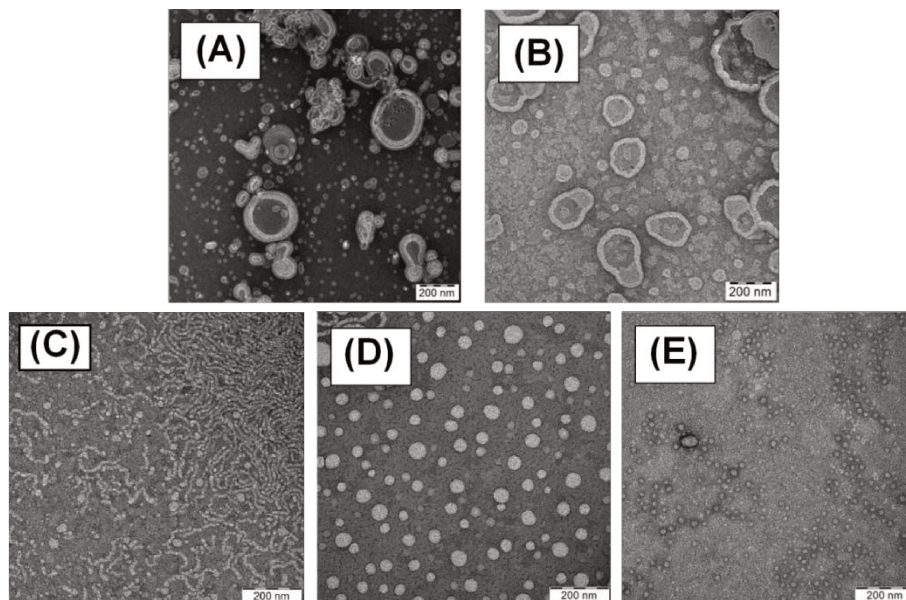


**Figure 1.** Images TEM des assemblages obtenus à partir de copolymères triblocs: (A) polymersomes  $PGL_{12}$ - $PBO_{84}$ - $PGL_{12}$ , (B) polymersomes  $PGL_{21}$ - $PBO_{84}$ - $PGL_{21}$ , (C) micelles sphériques et cylindriques  $PGL_{16}$ - $PBO_{41}$ - $PGL_{16}$ , (D) micelles sphériques  $PGL_{10}$ - $PBO_{21}$ - $PGL_{10}$  et (E) micelles sphériques  $PGL_{22}$ - $PBO_{13}$ - $PGL_{22}$ .

### **Chapitre 3 : Copolymères amphiphiles en étoile : synthèse, caractérisation structurale et auto-assemblage**

Dans le chapitre 3, une librairie de copolymères amphiphiles à cœur  $\beta$ CD et bras PBO-PGL a été synthétisée par une approche « core-first », à partir d'un amorceur modifié de manière symétrique, la per(2-O-méthyl-3,6-di-O-(3-hydroxypropyl))- $\beta$ CD ( $\beta$ CD-(OH)<sub>14</sub>). Ces copolymères ont été synthétisés par une copolymérisation anionique séquentielle par ouverture de cycles, catalysée par la base phosphazène tBuP4, suivie d'une étape de déprotection en milieu acide. Cependant, avec le protocole initial, nous avons observé une limitation du DP des chaînes PBO avec une valeur maximale atteinte d'environ 16. Afin d'augmenter ce DP en PBO, une stratégie de changement de solvant a été utilisée lors de la synthèse, nous permettant d'atteindre des valeurs de 30.

Les copolymères en étoile synthétisés ont été étudiés pour leurs comportements d'auto-assemblage, par DLS, SLS et SAXS (Figure 2). Afin de comparer les résultats

avec ceux des analogues linéaires, la relation entre la morphologie obtenue et le rapport hydrophobe/hydrophile, ainsi que la relation entre l'épaisseur de la membrane et le DP du PBO, ont été discutées, une fois les polymersomes construits. Quand  $w_{\text{PGL}} \leq 0,19$ , des agrégats et des précipités ont été obtenus; quand  $0,23 \leq w_{\text{PGL}} \leq 0,35$ , les assemblages obtenus sont de type polymersomes; quand  $w_{\text{PGL}} \geq 0,57$ , des micelles sphériques ont été formées. Ces morphologies sont en accord avec celles obtenues pour les analogues linéaires. En outre, la courbe maîtresse obtenue en traçant l'épaisseur de la couche hydrophobe ( $t_i$ ) en fonction du DP du bloc hydrophobe PBO ( $\text{DP}_{\text{PBO}}$ ) a donné une pente environ égale à 0,72, valeur un peu plus grande que celle des copolymères linéaires assemblés, ce qui peut être expliquée par la contribution du cœur  $\beta\text{CD}$ .

En parallèle de ces caractérisations, la question du chapitre 3 était aussi la construction de nanopores artificiels.

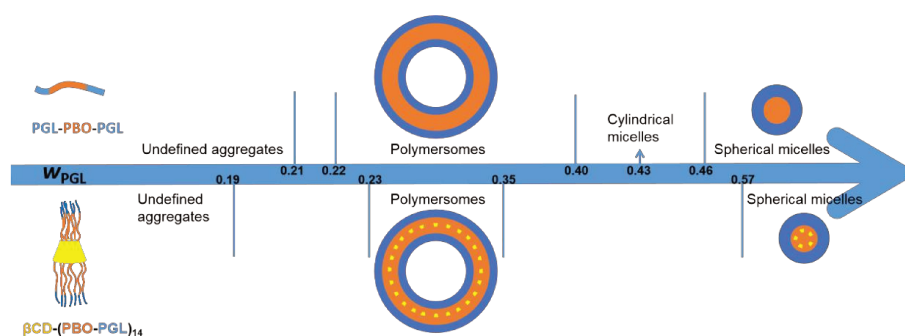


**Figure 2.** Evolution de la morphologie en fonction de la fraction massique en blocs PGL ( $w_{\text{PGL}}$ ) des copolymères linéaires triblocs (PGL-PBO-PGL, haut) et des copolymères en étoile ( $\beta\text{CD}-(\text{PBO-PGL})_{14}$ , bas)

Les chapitres 4 et 5 s'intéressent à la création du nanoréacteur, formé d'un polymersome équipé d'un nanopore artificiel, selon deux méthodes.

#### **Chapitre 4 : Etude de la perméabilité des membranes aux ions $\text{H}^+$**

Nous nous sommes concentrés sur la perméabilité des membranes polymères seules, constituées soit de copolymères à blocs linéaires, soit de copolymères en étoile à cœur  $\beta\text{CD}$ , sous la forme 3D de polymersomes.

La perméabilité de la membrane polymère aux ions  $\text{H}^+$  a été étudiée par spectroscopie de fluorescence, à l'aide d'une sonde pH, le 8-hydroxypyrrène-1,3,6-trisulfonate (HPTS). Les sondes HPTS ont été encapsulées dans les polymersomes par hydratation des films polymères avec une solution de HPTS. L'efficacité d'encapsulation est

relativement basse, sans doute limitée par le mode de préparation utilisée et des dialyses à répétition pour éliminer l'HPTS libre. En outre, dans les conditions utilisées, les valeurs d'efficacité d'encapsulation semblent liées à l'épaisseur des membranes polymères et à la fraction massique des blocs PGL, ceci à la fois pour les copolymères linéaires mais aussi en étoile. Les valeurs les plus hautes ont été obtenues pour les polymersomes purs et définis avec des membranes épaisses.

Lors de ces études de perméabilité aux ions  $H^+$ , il a été trouvé que :

- toutes les membranes étaient rapidement perméables aux ions  $H^+$  dans les conditions utilisées,
- que le temps de diffusion des ions  $H^+$  à travers la membrane dépend de l'épaisseur de la membrane pour les polymersomes composés des copolymères linéaires triblocs,
- et que la cavité hydrophobe de la  $\beta$ CD présente dans la membrane empêchait dans une certaine mesure le passage des ions  $H^+$  dans les polymersomes.

### **Chapitre 5 : Etude de la perméabilité des membranes aux ions $K^+$ et $Cl^-$**

Nous nous sommes enfin intéressés à la perméabilité des membranes polymères seules, constituées par les deux familles de copolymères (linéaires et en étoile) en bicouches planes. La perméabilité aux ions  $K^+$  et  $Cl^-$  a alors été estimée en adaptant la technique électrique BLM (membrane lipidique noire).

Il a été possible de former des membranes polymères planes isolantes aux  $K^+$  et  $Cl^-$ , à partir des copolymères linéaires amphiphiles, quelles que soient la longueur de la partie hydrophobe et la morphologie en solution, ce qui ne semble pas le cas pour les copolymères en étoile (porosité à vérifier).

La possibilité d'insérer un copolymère en étoile à cœur  $\beta$ CD dans la membrane polymère plane n'a pas été totalement prouvée, même si une perméabilisation/porosité a été détectée.

L'insertion d'un nanopore biologique (mellitine) semble possible dans les membranes polymères formées à partir du tribloc PGL<sub>9</sub>-PBO<sub>33</sub>-PGL<sub>9</sub>.

## Abbreviations

9-BBN	9-borabicyclo[3.3.1]nonane
AROP	anionic ring-opening polymerization
BA	benzyl alcohol
BDM	1,4-benzenedimethanol
BLM	black lipid membrane
BO	butylene oxide
BSA	bovine serum albumin
COSY	( <sup>1</sup> H- <sup>1</sup> H) correlation spectroscopy
<i>D</i>	polydispersity index of polymer
DCM	dichloromethane
DLS	dynamic light scattering
DMAP	4-(dimethylamino)pyridine
DP	degree of polymerization
EE	encapsulation efficiency
EEGE	ethoxyethyl glycidyl ether
ELS	electrophoresis light scattering
<i>eq.</i>	equivalent
HPTS	8-hydroxypyrene-1,3,6- trisulfonate
IgG	immunoglobulin G
ITC	isothermal titration calorimetry
Lz	lysozyme
MeOH	methanol
MWCO	molecular weight cut-off
<i>N</i> <sub>agg</sub>	number of aggregation
PBO	poly(butylene oxide)
PDI	polydispersity index of particle
PEG	poly(ethylene glycol)
PGL	polyglycidol
PMMA	poly(methyl methacrylate)
pos	polymersome(s)
PSD	particle size distribution
PTFE	polytetrafluoroethylene
r.t.	room temperature
<i>R</i> <sub>H</sub>	hydrodynamic radius
RI	refractive index
ROP	ring-opening polymerization
SAXS	small angle X-ray scattering
SEC	size exclusion chromatography
SLS	static light scattering

TBAF	tetrabutylammonium fluoride
TBDMS	<i>tert</i> -butyldimethylsilyl
TEM	transmission electron microscopy
<i>w</i>	weight fraction
βCD	<i>beta</i> -cyclodextrin
βCD-(OH) <sub>14</sub>	per(2-O-methyl-3,6-di-O-(3-hydroxypropyl))-βCD
δ	chemical shift
ζ	zeta potential
λ <sub>em</sub>	emission wavelength

## **General Introduction**

The motivation of this research project is to add a brick to the wall of biomimeticism of eukaryotic cell. Following the bottom-up approach and taking into account the architectural point of view, the biomimetic cell can be constructed by combining various subunits, *i.e.*, synthetic or artificial organelles (AOs) [1,2].

One of the common characteristics of organelles is to perform biochemical reactions in a controlled manner, thanks to compartmentalization [3]. Synthetic systems performing confined enzymatic reactions at nanometric scale are called nanoreactors. Nanoreactors have a huge range of potential applications, such as to facilitate the study of biochemical reactions at molecular level under controlled and tunable conditions, or to further be functionalized as AOs [4]. In terms of structure, a nanoreactor is a catalytic nanocompartment incorporating enzymes. The compartment can be built up with liposomes, polymersomes, polymer capsules, and so forth. Among these structures, polymersomes are attractive for the construction of compartments presenting enhanced stability, robustness and chemical diversity, compared to the liposomes. Polymersomes are built via facile self-assembly of amphiphilic copolymers, advantage over the polymer capsules prepared via tedious processes [5].

Besides the confinement purpose, the compartment is required to be permeable to the substrates and products [6]. However, the thicker membrane of polymersome, mainly resulting from the larger molar mass of the hydrophobic segment of the amphiphilic copolymers, produces more barrier to molecular translocation compared to its counterpart, *i.e.*, the liposome.

To date, few cases of polymersomes with sufficient permeability to serve as versatile platforms for enzymatic reactions have been reported. At the same time, a variety of permeabilization strategies has been proposed, such as permeabilization by stimuli-triggering or by inserting membrane proteins (MPs) [7].

Different kinds of MPs have been successfully inserted into polymersome membranes. However, it is inevitable to cope with the inherent mismatches between MPs and polymeric membranes in both physical and chemical respects [8].

Fortunately, synthetic nanochannels have gained a lot of achievements in the contexts of lipid bilayers. However, few studies exist concerning their incorporation in polymeric membranes [9]. Synthetic nanochannels are attractive for many matters, including the tailor-made structural parameters, better stability and robustness, as well as less costing for applications in large scale in contrast to the natural MPs.

The fully synthetic system constructed by inserting synthetic nanochannels into polymeric membrane is anticipated to have a broad range of applications in nanotechnology, for instance, serving as the scaffolds for nanoreactors or even AOs. Therefore, this PhD project consists in developing a fully synthetic platform, which

comprises polyglycidol (PGL)-based polymersomes and *beta*-cyclodextrin ( $\beta$ CD)-based artificial nanochannels.

PGL-based surfaces have good biocompatibility with low immunogenicity and low cytotoxicity [10], which is crucial for biomedical applications. Combining with the hydrophobic poly(butylene oxide) (PBO) segment, which is also biocompatible, the resultant linear amphiphilic copolymer can self-assemble into polymersomes, providing the hydrophobic-to-hydrophilic ratio is appropriate [11,12].

As the other important content of the targeted system,  $\beta$ CD-based artificial nanochannels are especially of interest, being known as versatile nanochannels in lipid bilayers, such as hemi-channels with or without stimuli-responsiveness [13,14], and unimolecular channels formed by  $\beta$ CD-cored star polymers or cyclodextrin nanotubes [15,16]. This project pays particular attention to the  $\beta$ CD-cored star polymers, where  $\beta$ CD is symmetrically decorated with 14 amphiphilic PBO-PGL arms, intending to minimize the chemical and dimensional mismatches between the polymersome membranes and the artificial nanochannels. Having these points in mind, this project is conducted by starting with the preparation and characterization of each constituent and subsequent combination of these two units.

In the context of this PhD thesis, the first chapter is the literature review of the relevant topics including the self-assembly of amphiphilic copolymers, the polymersome nanoreactors, and the  $\beta$ CD-based star-like copolymers, in order to position this PhD project, as well as to provide theoretic background to this project.

The chapter 2 deals with the question of how to form the compartment (*i.e.*, polymersome). The linear amphiphilic block copolymers, including PBO-PGL and PGL-PBO-PGL, are synthesized via sequential ring-opening polymerization and characterized by  $^1\text{H}$  NMR and SEC. Their self-assembly behaviors are subsequently systematically studied by dynamic light scattering (DLS), static light scattering (SLS), small angle X-ray scattering (SAXS) and transmission electron microscopy (TEM), in order to construct a relation between the self-assembled morphology and the hydrophobic-to-hydrophilic ratio of these amphiphilic copolymers. The obtained polymersomes are especially investigated in terms of the influence of the degree of polymerization (DP) of PBO block on the thickness of polymersome membrane, according to SAXS data. At last, the protein-repelling capacity of the self-assemblies, which have PGL outer corona, is also evaluated by DLS, isothermal titration calorimetry (ITC), fluorescence and circular dichroism spectroscopy.

Chapter 3 devotes to preparing  $\beta$ CD-based artificial nanochannel scaffolds (*i.e.*,  $\beta$ CD-cored star polymers). The amphiphilic star copolymers with  $\beta$ CD as the core and PBO-PGL as the arms are synthesized by core-first approach. A defined  $\beta$ CD initiator is first prepared for the sequential ring-opening polymerization. The

synthetic procedure is optimized for targeting at defined polymers with desirable arm length and satisfactory purity. The defined star copolymers are also studied in terms of their self-assembly behaviors. For the purpose of comparison with the linear analogues, the relation between self-assembled morphology and hydrophobic-to-hydrophilic ratio, as well as the relation between membrane thickness and DP of PBO, are discussed, once the polymersomes are constructed.

At last (Chapters 4 and 5), we focus on the permeability of the polymeric membranes made of linear copolymers or  $\beta$ CD-cored star copolymers. In the three-dimensional format, the membrane permeability of polymersomes to  $H^+$  is investigated by fluorescence spectroscopy, with the aid of a pH probe, 8-hydroxypyrene-1,3,6-trisulfonate (HPTS) (Chapter 4). In the planar format, the membrane permeability to  $K^+$  and  $Cl^-$  is estimated via the technique of black lipid membrane (BLM). Furthermore, the possibility of  $\beta$ CD-cored star copolymer to insert into the planar polymeric membrane made of linear copolymers and to form nanochannels is studied by BLM method.

The PhD thesis is ended with some general conclusions on the work which has been performed, together with some perspectives on this research topic.

## References

1. Roodbeen R, Van Hest J C M. Synthetic cells and organelles: compartmentalization strategies[J]. *BioEssays*, 2009, 31(12): 1299-1308.
2. LoPresti C, Lomas H, Massignani M, et al. Polymersomes: nature inspired nanometer sized compartments[J]. *Journal of Materials Chemistry*, 2009, 19(22): 3576-3590.
3. Schoonen L, Van Hest J C M. Compartmentalization approaches in soft matter science: from nanoreactor development to organelle mimics[J]. *Advanced Materials*, 2016, 28(6): 1109-1128.
4. Belluati A, Craciun I, Meyer C E, et al. Enzymatic reactions in polymeric compartments: nanotechnology meets nature[J]. *Current opinion in biotechnology*, 2019, 60: 53-62.
5. York-Durán M J, Godoy-Gallardo M, Labay C, et al. Recent advances in compartmentalized synthetic architectures as drug carriers, cell mimics and artificial organelles[J]. *Colloids and Surfaces B: Biointerfaces*, 2017, 152: 199-213.
6. Klermund L, Castiglione K. Polymersomes as nanoreactors for preparative biocatalytic applications: current challenges and future perspectives[J]. *Bioprocess and biosystems engineering*, 2018, 41(9): 1233-1246.
7. Larrañaga A, Lomora M, Sarasua J R, et al. Polymer capsules as micro-/nanoreactors for therapeutic applications: Current strategies to control membrane permeability[J]. *Progress in Materials Science*, 2017, 90: 325-357.
8. Ren T, Erbakan M, Shen Y, et al. Membrane protein insertion into and compatibility with

- biomimetic membranes[J]. *Advanced Biosystems*, 2017, 1(7): 1700053.
9. Zheng S, Huang L, Sun Z, et al. Self-assembled artificial ion-channels toward natural selection of functions[J]. *Angewandte Chemie International Edition*, 2021, 60(2): 566-597.
  10. Lila A S A, Nawata K, Shimizu T, et al. Use of polyglycerol (PG), instead of polyethylene glycol (PEG), prevents induction of the accelerated blood clearance phenomenon against long-circulating liposomes upon repeated administration[J]. *International journal of pharmaceutics*, 2013, 456(1): 235-242.
  11. Du H, de Oliveira F A, Albuquerque L J C, et al. Polyglycidol-Stabilized Nanoparticles as a Promising Alternative to Nanoparticle PEGylation: Polymer Synthesis and Protein Fouling Considerations[J]. *Langmuir*, 2020, 36(5): 1266-1278.
  12. Wehr R, Gaitzsch J, Daubian D, et al. Deepening the insight into poly (butylene oxide)-block-poly (glycidol) synthesis and self-assemblies: micelles, worms and vesicles[J]. *RSC advances*, 2020, 10(38): 22701-22711.
  13. Badi N, Auvray L, Guégan P. Synthesis of Half-Channels by the Anionic Polymerization of Ethylene Oxide Initiated by Modified Cyclodextrin[J]. *Advanced Materials*, 2009, 21(40): 4054-4057.
  14. El Ghoul Y, Renia R, Faye I, et al. Biomimetic artificial ion channels based on beta-cyclodextrin[J]. *Chemical Communications*, 2013, 49(99): 11647-11649.
  15. Eskandani Z, Le Gall T, Montier T, et al. Polynucleotide transport through lipid membrane in the presence of starburst cyclodextrin-based poly(ethylene glycol)s[J]. *The European Physical Journal E*, 2018, 41(11): 1-7.
  16. Mamad-Hemouch H, Bacri L, Huin C, et al. Versatile cyclodextrin nanotube synthesis with functional anchors for efficient ion channel formation: design, characterization and ion conductance[J]. *Nanoscale*, 2018, 10(32): 15303-15316.



**Chapter 1.**  
**State of the Art:**  
**Literature review**

## Content

<b>1. Introduction.....</b>	<b>17</b>
<b>2. Self-assembly of Non-ionic Amphiphilic Copolymers.....</b>	<b>17</b>
2.1 General principles of the self-assembly of amphiphilic copolymers.....	17
2.1.1 Influence of polymer characteristics.....	18
2.1.2 Influence of preparation conditions.....	20
2.2 Self-assembly of amphiphilic star-like copolymers.....	22
2.2.1 General synthetic strategies of star-like polymers.....	23
2.2.2 Self-assembly of star-like polymers and applications.....	25
<b>3. Polymersome Nanoreactors.....</b>	<b>30</b>
3.1 Overview of polymersome nanoreactors.....	31
3.1.1 General enzyme-loading strategies.....	31
3.1.2 Nanoreactor functions.....	33
3.2 Permeability of polymersome membrane.....	37
3.2.1 Intrinsic permeability.....	38
3.2.2 Stimuli-responsive permeability.....	41
3.2.3 Insertion of nanochannels.....	45
<b>4. <math>\beta</math>CD-based Amphiphiles and Applications.....</b>	<b>48</b>
4.1 Amphiphilic $\beta$ CD derivatives.....	49
4.2 $\beta$ CD-cored amphiphilic star-like copolymers.....	52
4.2.1 General synthetic strategies of $\beta$ CD-cored star-like polymers.....	53
4.2.2. $\beta$ CD-cored amphiphilic star-like polymers acting as artificial nanochannel scaffolds.....	55
4.2.3 Self-assemblies of $\beta$ CD-cored amphiphilic star-like copolymers.....	56
<b>5. Conclusion and Objectives.....</b>	<b>61</b>
<b>6. References.....</b>	<b>63</b>

## 1. Introduction

In this project, we aim to study the self-assembly behavior of star amphiphilic copolymers constituted of a *beta*-cyclodextrin ( $\beta$ CD) core and 14 poly(butylene oxide)-*block*-polyglycidol (PBO-PGL) arms, in comparison with the behaviors of their linear counterparts. We are also interested in the potential applications of the resultant self-assemblies as nanoreactors. Focusing on these subjects, this chapter will introduce, in the first section, the general principles of the self-assembly of amphiphilic copolymers and the advances in the self-assembly of star-like copolymers; in the second section, an overview on the applications of polymer vesicles (*i.e.*, polymersomes) as nanoreactors with an emphasis on the permeability of polymersome membranes; in the last section, a review of  $\beta$ CD-based amphiphilic derivatives and star-like copolymers will be performed in terms of structures, self-assembly behaviors and relevant applications.

## 2. Self-assembly of Non-ionic Amphiphilic Copolymers

The self-assembly process of amphiphilic copolymers in solution has been investigated over the past several decades due to the morphological diversity and potential applications. In the purpose to provide a theoretical background to this project, the general principles of the self-assembly of non-ionic amphiphilic copolymers in aqueous solution will be first overviewed. Then, we will focus on star-like amphiphilic copolymers in terms of synthetic strategies, self-assembly and the applications of self-assembled nanoobjects, especially in the nanomedical field.

### 2.1 General principles of the self-assembly of amphiphilic copolymers

For the general introduction, the self-assembly of non-ionic amphiphilic block copolymers in aqueous solution is considered. When the concentration of the amphiphilic copolymers is above the critical micelle concentration (CMC) or critical aggregation concentration (CAC), the copolymers in unimer state self-assemble into aggregated structures. This process is driven by the minimization of the free energy between different blocks and of the free energy between each block with the surrounding solvent (*i.e.*, water) [1]. In a quantitative aspect, these interactions can be expressed using the packing parameter, which was first introduced by Israelachvili to describe the micellization of low-molar-mass surfactants [2].

In the case of surfactant molecules, packing parameter ( $p$ ) is calculated by following equation.

$$p = \frac{V_0}{a_0 l_c} \quad (1)$$

in which,  $a_0$  is the area of the hydrophilic head,  $l_c$  is the length of the hydrophobic tail, and  $V_0$  is the occupied volume by the hydrophobic tail.

The dimensionless packing parameter  $p$  especially describes the relationship between the curvature of the hydrophobic–hydrophilic interface and the resulting thermodynamically preferred morphology: when  $p \leq 1/3$ , spherical micelles are formed; when  $1/3 < p \leq 1/2$ , cylindrical micelles are formed; and vesicles are formed when  $1/2 < p \leq 1$  [2].

This concept is extended to the macromolecular amphiphilic block copolymers, as shown in Figure 1. In this case, the parameters in Equation 1 are substituted by those of amphiphilic block copolymers, in specific,  $a_0$  is interfacial area between the hydrophilic and hydrophobic blocks in a polymer chain,  $l_c$  is the length of the hydrophobic block, and  $V_0$  is the volume occupied by the hydrophobic block [3].

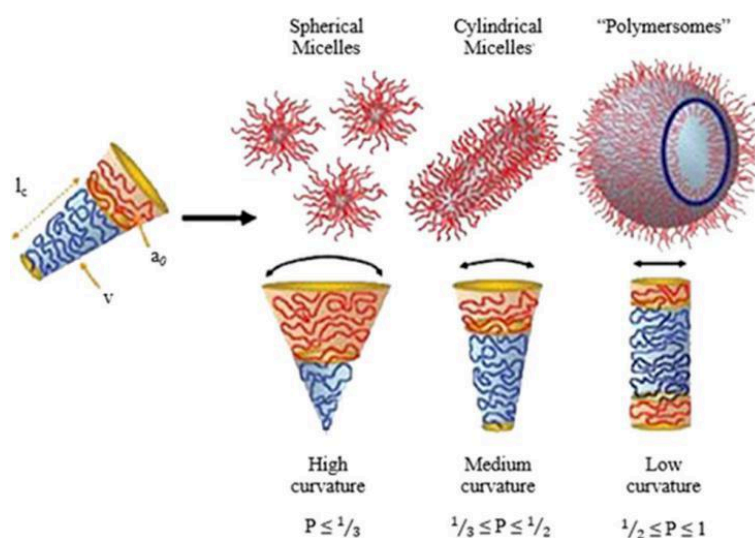


**Figure 1.** The dimensionless packing parameter ( $p$ ) especially describes the relationship between the curvature of the hydrophobic/hydrophilic interface and the resulting thermodynamically preferred morphology. [3]

Packing parameter is based on geometric considerations and paves a convenient way to predict the self-assembled morphologies of amphiphilic copolymers. However, the behaviors of polymers sometimes can be rather different from that model and more complicated than the ones of low-molar-mass surfactants, which means more factors are expected to affect the self-assembly behaviors and the resulting self-assembled morphologies of amphiphilic copolymers [4]. These factors relate to polymer characteristics and preparation conditions, as will be discussed in the next parts.

### 2.1.1 Influence of polymer characteristics

In the aspect of polymer characteristics, the main features affecting the self-assembly of amphiphilic copolymers are the hydrophilic-to-hydrophobic ratio, the chemical nature of segments/blocks and the macromolecular topology.

### (1) Hydrophilic-to-hydrophobic ratio

Volume fraction of the hydrophilic block is proposed as a synthetically accessible parameter to predict the self-assembled morphologies. Based on experimental data, Discher and Ahmed proposed an empirical relation between the volume fraction ( $f_v$ ) of hydrophilic segment and the self-assembled morphology [5]: when  $25\% < f_v < 40\%$ , amphiphilic polymers are likely to self-assemble into vesicles; when  $f_v > 50\%$ , amphiphilic polymers tend to aggregate into spherical micelles (Figure 2). This relation has been confirmed in numerous research works later then [6–10], giving the conclusion that the self-assembled morphology is greatly governed by the hydrophilic-to-hydrophobic ratio. It is noteworthy that the molar mass of each block of copolymer is not taken in account and may affect this simplistic approach.

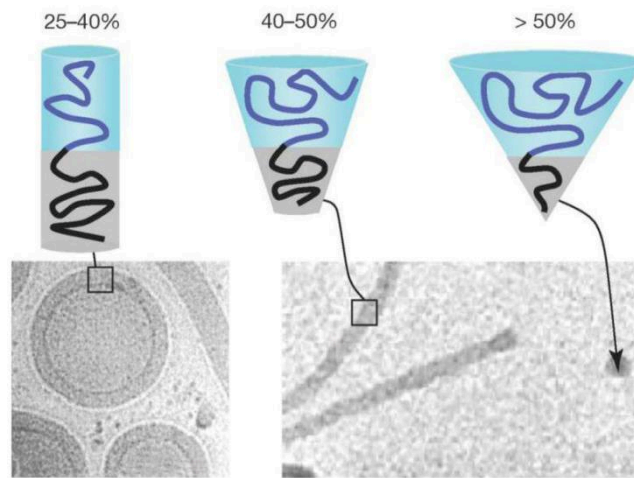


**Figure 2.** The volume fraction ( $f_v$ ) of hydrophilic block (blue) decides the self-assembled morphology [5].

### (2) Chemical nature of the segments

As mentioned, self-assembly is partially induced by the chemical incompatibility between the segments. Thus, the self-assembly process can be tuned by the chemical composition of the segments.

For example, amphiphilic rod–coil copolymers can exhibit distinct self-assembly behaviors, profiting from the introduction of rigid segments, such as liquid crystalline polymers, polypeptides, and helical polymers [11]. The great geometric difference and the unique interplay between the microphases of the rod and coil blocks lead to the formation of a variety of nanostructures including some unusual morphologies, such as ribbons, helices, and nanosheets, which are difficult to be obtained using coil–coil copolymers [12].

Similarly, fluorine-containing copolymers can be used to obtain some unusual morphologies originating from the superphobicity of the fluorine-containing segments. For instance, poly(*tert*-butyl acrylate)-*block*-poly(2-((perfluorononyl)oxy)ethyl methacrylate) (PtBA-PFNEMA) was reported to self-assemble into nanospheres with onion-like structures inside. What's more, the onion-like structures consisted of

several polygon stripes resulting from the super-strong segregation of the fluorinated segments [13].

### (3) Macromolecular topology

The arrangement of blocks, namely the polymer topology, may also affect the interactions between different blocks as well as the interactions between each block with the solvent, and thus may affect the resulting self-assemblies [14,15]. For example, cyclic poly(ethylene glycol)-*block*-poly( $\epsilon$ -caprolactone) (cPEG-PCL) diblock copolymers formed smaller micelles comparing to the ones formed from their linear counterparts: there were more unfavourable core-solvent junctions in the cyclic structure originating from its confined and looped nature [16]. In another case, the self-assemblies of the cyclic poly(ethylene glycol)-*block*-poly(butyl acrylate) (cPEG-PBA) diblock copolymers were similar to those of the linear poly(butyl acrylate)-*block*-poly(ethylene glycol)-*block*-poly(butyl acrylate) (PBA-PEG-PBA) triblock copolymers, because the linear hydrophobic-hydrophilic-hydrophobic copolymers also need to loop when they aggregate [17]. As one can see, the resultant morphologies were similar although the involved interactions were varied. Such phenomena were also observed with branched star-like copolymers. For instance, well-defined 8-armed star triblock copolymers, 8-armed poly( $\epsilon$ -caprolactone)-*block*-poly(acrylic acid)-*block*-poly( $\epsilon$ -caprolactone) (star-(PCL-PAA-PCL)<sub>8</sub>), self-assembled into spherical micelles like the linear counterparts did [18].

Defined copolymers with complicated topologies are usually difficult to achieve by synthetic chemistry, while they can be relatively easily designed by computational simulation. Then, the influence of polymer topology on their self-assembly behaviors can be investigated by many methods, such as dissipative particle dynamic simulation, and so on [19–21].

## 2.1.2 Influence of preparation conditions

It is worth noting that the exchange between polymer unimers and the self-assembled aggregates is usually very slow compared to the assembly process, meaning that the thermodynamic equilibrium is not always achieved in the timescale of preparation and kinetically “frozen” intermediate structures are usually formed [3]. Therefore, the experimental conditions play an important role in the non-covalent interactions and thus control the self-assembly process. These conditions include polymer concentration, manufacture procedure and some other conditions, such as the pH of solution and temperature, to name but a few.

### (1) Polymer concentration

Self-assembly is generally performed in a dilute polymer solution. However, when the polymer concentration increases, some complex and hierarchical morphologies can be obtained [22].

## (2) Manufacture methods

As aforementioned, the observed self-assemblies are usually in kinetically “frozen” states. Thus, manufacture method may affect the observed self-assembled structures to some extent. Commonly adopted methods are thin-film rehydration, solvent-switch, electroformation, and microfluidic methods. Among them, electroformation and microfluidic methods are dedicated to preparing vesicle-like structures, such as giant unilamellar vesicles and polymer capsules. Additionally, polymerization-induced self-assembly (PISA) has recently been studied as a mild, one-pot, and versatile strategy.

- Thin-film rehydration method

Thin-film rehydration is a frequently adopted method. Typically, the amphiphilic copolymer is first entirely dissolved in an organic solvent. The organic solvent is subsequently removed to form a polymer thin film which is rehydrated by adding aqueous solution. This method is simple, and the set-ups applied are easily accessible. But this method sometimes produces not that homogeneous assemblies, dependent on the copolymer. Then, additional treatments are often required to prepare homogeneous self-assemblies, such as repeated extrusions via polycarbonate membrane, sonication, or freeze-thaw cycles [23,24].

- Solvent-switch method

In a solvent-switch procedure, amphiphilic copolymer is first dissolved in a water-miscible solvent. Then, the solution is dropwise added into water under vigorous stirring for a period of time. At last, the organic solvent is removed by evaporation, dialysis, or freeze-drying. This method is reported to have a better control on the self-assemblies' sizes and distributions, once the experimental parameters, such as addition rate and stirring rate, are optimized [25,26]. It is important to note that the presence of organic solvent is a risk to denature the fragile protein and DNA, and thus these biological macromolecules can usually not be encapsulated in the course of assemblies forming [27].

- Electroformation method

Electroformation method is a variation of thin-film rehydration method but is dedicated to producing vesicular structures. Typically, polymer film is first casted on the surface of electrodes. Then, in an electric field, the film detaches and the lamella enclose to form vesicles. The experimental parameters, including electric potential, frequency and temperature, can be tuned to prepare defined giant unilamellar vesicles with wanted sizes [28].

- Microfluidic method

Microfluidic method is also uniquely used to prepare vesicular structures. Typically, amphiphilic copolymer is dissolved in an organic solvent, and then the organic solution is mixed with water, forming a water-in-oil-in-water (W/O/W) double emulsion template in microchannels. At last, micrometer-sized polymersomes are obtained after the removal of organic solvent [29]. Thanks to locally modulated environment, this method always provides a high degree of control over the self-assembly process and thus can produce defined polymersomes having high homogeneity in structural parameters (*e.g.*, size, membrane thickness ...) [30].

- Polymerization-induced self-assembly (PISA)

In conventional self-assembly methods, organic solvents are often required to dissolve the pre-synthesized polymers, before the suspension of the self-assemblies in aqueous solution. Additionally, the low polymer concentration (usually less than 1 wt%), as well as the multiple steps in the formulation and purification treatments, the scalability of these manufacture methods is limited. In this aspect, PISA has recently emerged as a promising strategy to overcome this limitation. In a typical aqueous PISA process, the soluble macroinitiator, for example a polymeric reversible addition-fragmentation chain transfer (RAFT)-agent, is extended with hydrophobic block. As the hydrophobic block grows, the amphiphilic block copolymers self-assemble into various morphologies in situ [31,32]. Apart from the straightforward procedure, PISA is attractive due to the potential to obtain unusual multicompartamental or even hierarchical self-assembled structures taking advantage of the high polymer concentration and the continuous process [33,34].

### (3) Other conditions

Many “smart” self-assemblies are designed to respond to a stimulus or more stimuli, thus in these cases, the preparation conditions may greatly decide the self-assembled morphologies. For example, the pH-sensitive poly(2-dimethylaminoethyl methacrylate) (PDMAEMA) is hydrophilic in acidic conditions, due to the protonated amino groups, but it turns hydrophobic, when the pH of solution increases. Because of the hydrophilic-to-hydrophobic transition, the fraction of the hydrophilic segments in the copolymer decreases and the morphology changes [35]. Similarly, the thermo-responsive poly(N-isopropylacrylamide) (PNIPAM) segment, having a lower critical solution temperature (LCST), is hydrophilic when the temperature is lower than its LCST, and becomes hydrophobic, when the temperature raises above LCST. The temperature-induced hydrophilic/phobic translation can also result in the change of morphology [36,37].

*In short*, the self-assembly process of amphiphilic copolymers is controlled by both thermodynamic and kinetic parameters. The self-assembled morphology is dependent on the hydrophilic-to-hydrophobic ratio, the chemical nature and the architecture of copolymer itself, as well as preparation conditions, such as polymer concentration, solution properties and manufacture method. In the next section, amphiphilic star-like copolymers will be in the center of our attention, on the background of these general principles.

## 2.2 Self-assembly of amphiphilic star-like copolymers

Linear amphiphilic copolymers have shown great success in the field of aqueous self-assembly. In the meantime, non-linear amphiphilic copolymers, such as star-like polymers, have attracted more and more attention, benefiting from the progress and developments in polymerization and chemical modification strategies [38–41].

Star-like polymers typically have at least three macromolecular arms, radiating from a central core. Based on the composition of arms, star-like polymers can be generally categorized into homoarm and miktoarm star polymers (Figure 3). Homoarm star polymers, or star polymers for short, have the arms with identical chemical composition and structure, while miktoarm star polymers contain two or more different arms in chemical composition or structure [42,43].

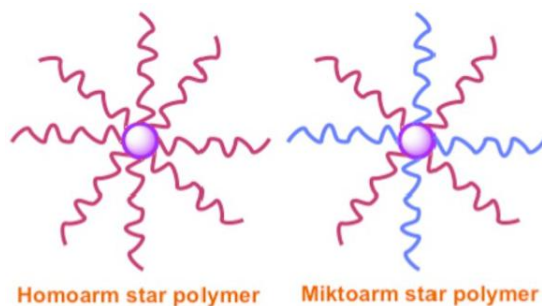


**Figure 3.** Star-like copolymers can be categorized into (homoarm) star polymer and miktoarm star polymer according to the composition of arms [42].

Besides the unique topological structure, star-like polymers usually have a plenty of functional groups that can be potentially modified, hence, they are expected to build multifunctional nanostructures for various applications [44,45].

In this part, the general synthetic strategies of star-like polymers are first introduced. Then, their self-assembly characters are overviewed with the focuses on the resulting morphology and the applications, especially the biomedicine-related applications. There are many reviews dedicated to the synthetic methodologies or/and potential applications of star-like polymers [43,46,47]. Herein, a brief introduction on the star-like copolymers is performed to provide a general background to this PhD project. It is noteworthy to mention that *beta*-cyclodextrin ( $\beta$ CD)-based star-like polymers will be specifically discussed later.

### 2.2.1 General synthetic strategies of star-like polymers

Various polymerization methodologies have been adopted to prepare star-like polymers, such as atom transfer radical polymerization (ATRP) [48,49], reversible addition-fragmentation chain transfer (RAFT) polymerization [50,51], and ring-opening polymerization (ROP) [52–54]. Regardless of the adopted polymerization strategies, from the point of view of the unique core–arm structure, star-like polymers are generally prepared by core-first, arm-first, or/and grafting-onto strategies, as illustrated in Figure 4.

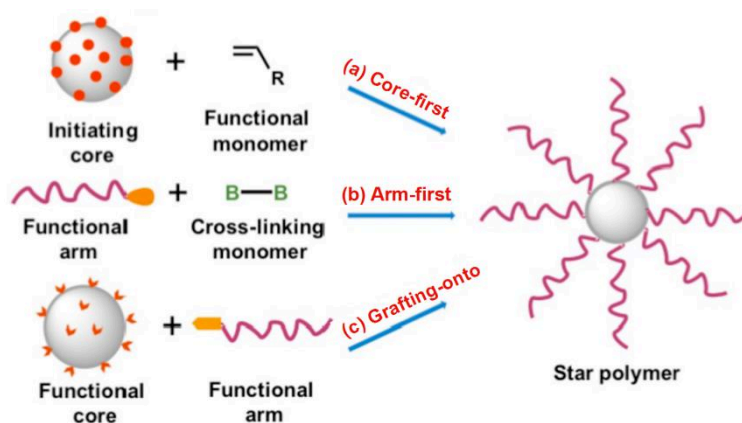


**Figure 4.** Star-like polymers can be prepared via core-first, arm-first, and grafting-onto strategies, modified based on ref [42].

### (1) Core-first strategy

Core-first strategy consists in first preparing an appropriate core, usually a multifunctional initiator, able to form multiple polymer arms radiating from the core (Figure 4a). Taking advantage of the tailor-made core, star-like polymers with a precise number of arms can be obtained. Additionally, by carefully designing the initiating moieties, it allows for the preparations of homoarm star polymers via identical polymerizations of one kind of monomer [54] or the preparation of miktoarm star polymers via orthogonal polymerizations of different monomers [55].

Obviously, in this approach, the number of arms is limited by the number of active sites on the core, usually being a small number. The length of arms is usually limited by the worsened solubility of the resulting polymers, or the increasingly crowding environment during the polymerization process, especially in radical polymerizations [56]. In this aspect, a larger-sized and rigid core, such as calixarene, is thought favorable to overcome the crowding environment [57].

Another point worthy noting is that the homogeneity of the polymer arms is critically dependent on the activity homogeneity of the active sites. Additionally, the precise properties of each arm, such as the molar mass and polydispersity, are not easy to characterize unless using some indirect methods such as end-group analysis or arm-cleavage method [58,59].

### (2) Arm-first strategy

Arm-first strategy consists in first preparing polymer arms, which are subsequently connected together to form the star-like polymer (Figure 4b). Thus, polymer arms are usually designed to bear end-functional groups, such as terminal initiating sites or polymerizable groups for polymerizations, or crosslinkable moieties for coupling reactions.

Contrary to core-first approach, the polymer arms in arm-first strategy are independently pre-synthesized and thus can be clearly characterized before star-like polymer formation. Therefore, arm-first strategy is attractive to prepare miktoarm star

polymers. Compared with core-first strategy, this method can also produce star-like polymers possessing more arms, since there is no limitation from the pre-formed core. However, the converged star-like polymers usually have broader arm number distributions [60], and low yield because of the incomplete arm-to-star conversion. The number of arms able to be incorporated into the final star polymers is decided by many factors, including the chemical composition, the structure and the length of the arm precursors, as well as the nature of crosslinker and the crosslinker-to-arm ratio when the arms are converged via crosslinking chemistry [61].

### (3) Grafting-onto strategy

Grafting-onto strategy consists in converging the pre-synthesized polymer arms with the pre-modified core (Figure 4c). Similar to the other two approaches, the core is multifunctionally modified and the polymer arms are designed to have complementary end-functions, so as to connect with each other via coupling reactions. This approach is also facile to prepare miktoarm star polymers by using different arm precursors.

In this method, both the core and the arms are pre-synthesized and clearly characterized independently prior to the formation of star polymer. Hence, the resulting star polymers are supposed to have the highest level of control over chemical composition and structure, among all the three synthetic approaches. Nevertheless, this strategy might have some limitations similar with the other two strategies. For instance, there might be limitation on arm numbers as the core-first strategy, and the broaden polydispersity on arm numbers like the arm-first strategy. Therefore, in this method, highly efficient coupling reactions, adequate reaction time and an excess of arms are often required to prepare defined star-like polymers.

In brief, all the three methodologies are well studied and can be implemented via various kinds of polymerizations and coupling reactions. Yet, each synthetic route possesses certain advantages and shortcomings as stated. When choosing the appropriate strategy to prepare star-like copolymers, many factors should be taken into consideration, for example, the reactivity of the active sites on the core, the nature of the monomers, as well as the targeted applications of the star-like polymers [62,63].

## 2.2.2 Self-assembly of star-like polymers and applications

As stated, a variety of morphologies can be obtained from a toolbox of linear amphiphilic copolymers with systematically varied compositions [9,10,64]. However, there are less investigations devoted to systematically studying the self-assembly behaviors of the non-linear amphiphilic copolymers [65], although many studies have interestingly shown that non-linear architectures could self-assemble into nanoparticulate structures having different sizes or morphologies than their linear analogues, known as architectural effect [56,66]. For one reason, it is more difficult to prepare a library of defined non-linear copolymers with various properties (*e.g.*, molar mass, hydrophilic fraction ...) in a systematic way. In this aspect, star-like polymer is one of the most accessible non-linear polymers thanks to the aforementioned well-developed controlled/living polymerization strategies.

Analogue to their linear counterparts, star-like copolymers also have found their applications in many fields in the form of self-assembled nanostructures, such as serving as drug delivery nanosystems [67,68]. The most common morphologies are spherical micelles and polymersomes. These two types of nanostructures are built of hundreds to thousands unimers. Another nanostructure, consisting of only one macromolecule, called unimolecular micelle, can also be obtained from the star-like polymers at a concentration lower than the CMC.

### (1) Unimolecular micelle

Star-like amphiphilic copolymer intrinsically has a covalently core-shell structure, enabling to form micellar structure by itself when dispersed in an aqueous solution. Such micelles are named as unimolecular micelles [69].

Unimolecular micelles can be detected by dynamic light scattering (DLS) technique. The idea is to dissolve star-like polymer in a good solvent for all the segments, at a low concentration, to ensure the macromolecules are dissolved as single units. The particle size and distribution are characterized by DLS. Then, the star-like polymer is dispersed in water at the same concentration, and the particle size and distribution are measured to compare with those obtained in the good solvent. In this way, if the values measured in two conditions are close to each other, then it can conclude that the star-like polymer formed unimolecular micelle in water. Transmission electron microscopy (TEM) permits more direct observation of the unimolecular micelles for some specific star-like polymers, for example, the ones with a defined core and highly contract arms (Figure 5) [70].

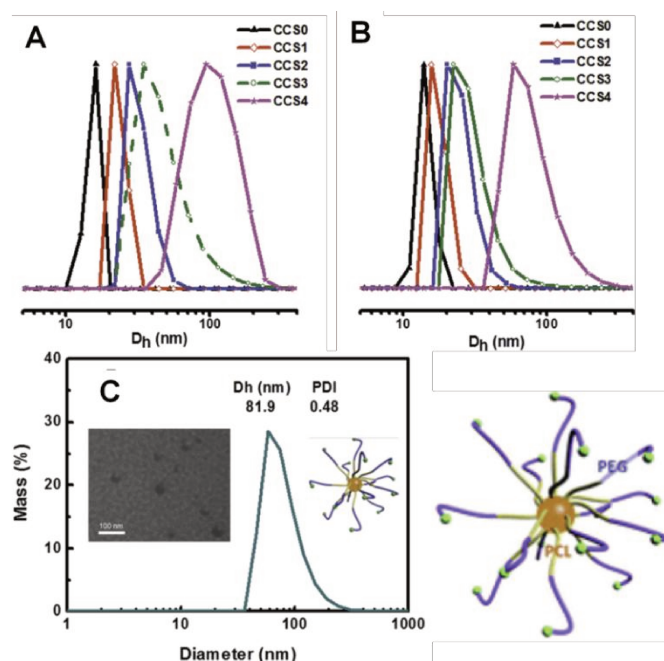


**Figure 5.** Particle size ( $D_h$ ) distribution curves of a series of star copolymers of different compositions (CCS0–CCS4) measured in (A) THF and (B) water by DLS. (C) The DLS size distribution curve and the TEM image of CCS4 in water ( $1 \text{ mg mL}^{-1}$ ) [70].

Unimolecular micelles are attractive for the potential therapeutic/biomedical applications because they are generally highly stable against dilution, in comparison to the conventional micelles formed by aggregation of hundreds of unimers.

For instance, a self-fluorescent unimolecular micelle was designed to serve as a tumor-targeting bioimaging probe [71]. The unimolecular micelle was formed from an amphiphilic star-like copolymer, which was prepared via connecting a Boltron® H40 core (H40, hyperbranched) with amphiphilic block copolymer arm precursors. The amphiphilic arms were dual-functionalized with the composition of biodegradable photo-luminescent polymer (BPLP, hydrophobic block) and cRGD peptide-conjugated PEG (PEG-cRGD, hydrophilic block). Thus, when such star-like copolymers were dissolved in water at a concentration below CMC, the resultant unimolecular micelles can exhibit both photostability and tumor-targeting capacity.

A more multifunctional therapeutic unimolecular micellar system combining tumor-targeted delivery, pH-induced release, and photodynamic therapy was reported [72]. The unimolecular micelle was formed by a biotin-functionalized amphiphilic star-like block copolymer, consisting of a polyhedral oligomeric silsesquioxane (POSS) core and eight poly( $\epsilon$ -caprolactone)-*block*-poly(2-(dimethylamino)ethyl methacrylate) (PCL-PDMAEMA) arms. The biotin-functionality allowed the unimolecular micelles tumor-targeting, and the PDMAEMA segment imparted the micelle with pH-responsiveness. These micelles were further used for photodynamic therapy (PDT) by encapsulating pheophorbide A (PPa) photosensitizers.

Although unimolecular micelles have outstanding stability, the applied concentration is rather low and the dimension is rather small to load enough drugs for effective therapeutic purpose in some circumstances. Therefore, the conventional self-assemblies or aggregations of star-like polymers are still of great interest.

## (2) Spherical micelles

Spherical micelle is the dominantly reported morphology in the context of star-like polymers so far. Due to the spherical nanostructure, these micelles have been widely investigated serving as therapeutic/imaging nanoparticulate systems.

For instance, a promising self-reporting theranostic system with a pH-induced drug releasing character was constructed by the self-assembly of star-like polymer which was prepared via grafting hydrophilic PEG arms onto a hydrophobic fluorescent hyperbranched conjugated polymer (HCP) core via pH-cleavable acylhydrazone linkers [73]. The star polymer self-assembled into fluorescent micelles in aqueous solution. When doxorubicin (DOX) was loaded into the micelles, the fluorescence emission of both DOX and HCP were quenched via the strong  $\pi$ - $\pi^*$  interactions. While in acidic conditions, the acylhydrazone linkers were cleaved, allowing the release of DOX and the recovery of fluorescence emission. In this way, the drug release profile was demonstrated.

Many efforts have been done to design multifunctional micellar systems for targeted therapeutic applications. Recently, a work devoted to studying the relation between the topology of miktoarm star copolymers and their performances as drug delivery systems was reported [74]. To elucidate the structure–property relationship, four

different miktoarm star copolymers based on hydrophilic poly(oligo(ethylene glycol)monomethyl ether methacrylate) (POEGMA) and hydrophobic PCL arms were prepared. The molar masses of hydrophilic and hydrophobic segments were fixed, but the molecular structures were varied, forming  $A_1B_2$ ,  $A_2B_2$ ,  $A_1B_3$ , and  $A_3B_1$  miktoarm star copolymers, with A and B being respectively POEGMA and PCL segments. All the four miktoarm polymers formed spherical micelles in aqueous solution. Then, the micelles were systematically assayed in the aspects of micelle stability, *in vitro* drug loading capacity, drug release properties, cellular uptake efficacy, and cytotoxicity with DOX as the model drug. The screening experiments showed that  $POEGMA_1PCL_3$  micelle was the optimal formulation for anti-cancer drug delivery, possessing the lowest CMC, the highest drug loading content and the enhanced therapeutic efficiency for DOX. This was thought to result from the highest degree of branching (DB) of PCL moiety among all the four architectures.

### (3) Polymersomes

The polymersomes made from star-like copolymers have gained increasing attention because of their numerous potential applications, analogizing to the case of the linear amphiphilic copolymers which has been extensively explored.

As stated, for the given chemical composition, it is thought that the self-assembled morphology of amphiphilic copolymers is primarily dictated by the hydrophobic-to-hydrophilic ratio [8,75]. In other words, polymersomes are anticipated to be obtained by properly adjusting the fraction of hydrophobic segment of the amphiphilic star-like copolymers.

For example, a histidine (His)-based  $AB_2$ -miktoarm copolymer (mPEG-(polyHis)<sub>2</sub>) self-assembled into varied morphologies resulting from the pH-induced hydrophilicity/phobicity change of polyHis segments: stable polymersomes were obtained above pH 7.4. However, when the pH of the solution decreased from pH 6.8 to pH 5.0, the polymersomes transitioned to cylindrical micelles, spherical micelles, and finally unimers as a result of the gradual protonation of the imidazole groups, *i.e.*, the gradual increase of the hydrophilicity [76]. The pH-induced morphology transformation is useful in drug release. However, the drug-loading efficiency was not mentioned in the cited work.

In another research, the drug-loading efficiency in polymersomes was assessed and compared with that in micelles [77]. Amphiphilic  $A(AB)_2$ -miktoarm star copolymer and linear AB diblock copolymers, composed of hydrophobic poly(trimethylene carbonate) (PTMC) (A) and hydrophilic PEG (B) segments, were synthesized as defined structures. It was interesting to find that the star-like copolymers self-assembled into vesicles with a hydrophilic content  $\sim 64$  wt%, while the linear diblock polymers formed micelles with a lower hydrophilic content  $\sim 46$  wt%. It was supposed that, in the star-like polymer, the rigid methyl cholate core along with the PTMC segments affected the interfacial curvature, and thus allowed to aggregate into vesicles with relatively high hydrophilicity. Subsequently, the nanoparticles, both polymersomes and micelles, were investigated as to their potential applications as drug delivery systems with DOX as the model drug. The results showed that polymersomes had a higher DOX loading capacity due to the larger available loading

space (both core and membrane) than the micelles. The results also showed that the DOX-loaded polymersomes exhibited greater kinetic stability than the DOX-loaded micelles.

Additionally, stimuli-responsive polymersomes have been obtained by introducing stimuli-responsive moieties into the star-like copolymers. For example, a pH- and redox- dual responsive polymersome was constructed by ABCD-miktoarm star quaterpolymers [78]. The miktoarm star copolymer was prepared via click reaction between azide/bromine-functionalized poly(ethylene glycol)-*block*-polystyrene (PEG-PS) and alkyne/disulfide-functionalized poly( $\epsilon$ -caprolactone)-*block*-poly(tert-butyl acrylate) (PCL-PtBA). The sequential selective hydrolysis of PtBA segment resulted in the targeted star-like copolymer with a pH-responsive polyacrylic acid (PAA) segment and a redox-responsive disulfide linkage in the core. The amphiphilic star-like copolymers self-assembled into vesicles, and the size could be tuned by pH and reductive stimuli.

#### (4) Other morphologies

Unusual self-assembled morphologies can be obtained via tuning chemical composition so as to adjust the interactions between different segments and the interactions between each segment with the solvent.

For example, a fluorine-containing amphiphilic ABC type miktoarm star polymer was found to self-assemble into multicompartment micelles [79]. This amphiphilic copolymer was composed of one hydrophilic arm (PEG) and two hydrophobic but immiscible arms (a polymeric hydrocarbon and a perfluorinated polyether). When the copolymer was dispersed in water, both hydrophobic blocks formed cores, and both were forced to contact PEG, originating from both hydrophobic and oleophobic nature of the fluorinated segment. Tuning the relative length of each block, namely changing the interactions in this system, the self-assemblies could transform from discrete multicompartment micelles to extended wormlike structures with segmented cores.

Recently, more complex and unusual morphologies have been obtained via self-assembly of a ABC miktoarm terpolymer, including perforated stomatocytes, raspberry-like micelles, and segmented worm-like micelles (Figure 6) [80]. The terpolymer consisted of mutually immiscible mPEG (hydrophilic), PS (hydrophobic) and poly(1H,1H,5H-octafluoropentyl methacrylate) (POFPMA, superhydrophobic) segments. A diversity of morphologies was obtained with fixed mPEG and varied PS-to-POFPMA ratio. This type of polymer was expected to serve as a reliable platform for the discovery of novel self-assembly morphologies.

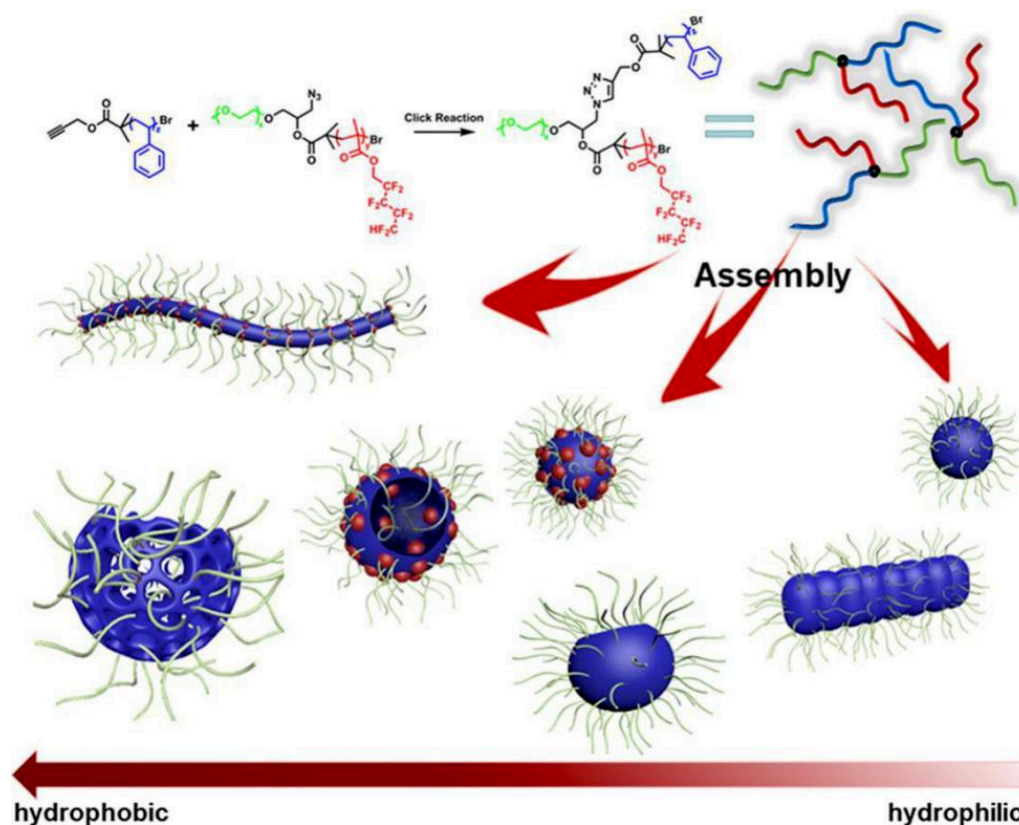


**Figure 6.** Various morphologies obtained via the self-assembly of a fluorine-containing ABC miktoarm terpolymer [80].

**Briefly**, amphiphilic star-like copolymers can be prepared via some well-established strategies, which favors the investigations on their self-assembly processes and their applications in the form of self-assembled nanoparticles. Spherical micelle is the dominantly explored morphology, when vesicle shows great potentials analogizing to their linear counterparts. In the next section, polymersomes will be focused by overviewing their application as nanoreactors, one of the most attractive applications of polymersomes. The field of nanoreactors has great advances with numerous amphiphilic linear copolymers, and such an overview is thought favorable for the full exploration of amphiphilic star-like copolymers.

### 3. Polymersome Nanoreactors

As stated in Section 2, amphiphilic copolymers can self-assemble into varieties of morphologies. Among them, vesicle (*i.e.*, polymersome) is a most intriguing one for its great potentials [68,81,82]. Polymersomes are featured by an aqueous interior enclosed by the hydrophobic membrane, which is further stabilized by the outer hydrophilic corona, and thus they can load both hydrophilic molecules (inside the aqueous interior) and hydrophobic molecules (in the membrane). This feature is very

attractive as drug delivery nanosystems [83]. Instead of drugs, enzymes have been loaded, turning polymersomes into nanoreactors [84]. Compared with free enzymes, the enzymes loaded in polymersome compartments are protected from external harmful environments. The compartmentalization by polymersomes also makes enzymatic reactions more effective profiting from the confined environment.

In this part, the concept to use polymersomes as compartments of nanoreactors is first overviewed, with the introduction of general enzyme-loading strategies, allowing to construct nanoreactors, as well as the functions of the resulting nanoreactors. Then, the permeability of polymersome membranes, a critical characteristic of polymersome nanoreactors, is focused, regarding to the intrinsic permeability and some permeabilization strategies.

### **3.1 Overview of polymersome nanoreactors**

Before the appearance of polymersome nanoreactors, liposome nanoreactors, namely enzyme-loaded liposomes, have been designed and explored for several decades, for the purpose to investigate the overwhelming undiscovered synthetic pathways occurring in cells at molecular level [85]. This topic keeps attracting great deal of attention due to the biocompatible nature of lipids and the facility to construct modular vesicle structures.

In the meantime, polymersome nanoreactors have also been attracting attention due to the great breakthroughs in living/controlled polymerization strategies and effective post-modification methods, which make possible to obtain various polymersomes possessing specific characters [84,86,87]. In comparison to liposome nanoreactors, polymersome nanoreactors can be tailor-made smarter in property and more stable and complicated in structure. For example, polymersomes can be designed with stimuli-responsive abilities due to the designable monomers. Polymersomes are more stable due to the entanglements of polymer chains producing thicker membrane and thus more resistant to dilution. All these attractive characteristics make polymersomes promising compartments for nanoreactors.

This section will introduce the general strategies to load enzymes into polymersomes allowing the construction of polymersome nanoreactors as well as the functions of the resultant nanoreactors.

#### **3.1.1 General enzyme-loading strategies**

##### **(1) Thin-film rehydration**

Thin-film rehydration is the most frequently applied method allowing enzymes to be loaded into polymersomes in the process of polymersome formation. In a typical procedure, polymer is dissolved in an organic solvent, and then the solvent is removed to form thin polymer film. Subsequently, an enzyme aqueous solution is added to hydrate the polymer film with the aid of stirring or sonication to accelerate the hydration process. The obtained assemblies suspension is usually further treated by

some post-preparation treatments, such as extrusions or sonication, to obtain homogeneous unilamellar enzyme-loaded vesicles [88,89]. In this way, enzymes are expected to be encapsulated in the aqueous interior of polymersomes [90]. Limited by the mechanism of thin-film rehydration method, the encapsulation yield is usually relatively low.

## (2) Electroporation

Alternatively, electroporation is suggested in some studies to improve the encapsulation yield. Electroporation has been widely used in cellular biology to introduce biomolecules into living cells [91]. In an external electric field, the cellular membrane can be temporarily permeabilized when the electric potential exceeds a certain threshold, triggering phospholipids to rearrange. The formed transient nanoscopic pores allow the passage of ions, molecules, and even macromolecules [92]. So far, only a few of works has been reported in the context of polymersomes because polymersomes are somewhat resistant to electroporation [93]. For instance, some macromolecules, such as bovine serum albumin (BSA), myoglobin (Mb), Lysozyme (Lz), plasmid DNA (pDNA), and small interfering RNA (siRNA)) were successfully encapsulated into the poly(2-(methacryloyloxy)ethyl phosphorylcholine)-*block*-poly(2-(diisopropylamino)ethyl methacrylate) (PMPC-PDPA) polymersomes via electroporation method, without influencing the size, intactness, or morphology of the vesicles [91]. However, the encapsulation efficiency (EE) was found dependent on the surface charge of macromolecules, with higher EEs for anionic biomacromolecules compared to cationic molecules. This effect of surface charge was confirmed by using lysozyme (Lz) as model: at pH 11, Lz is negatively charged (zeta potential -7.8 mV), and an EE of 6.36% was achieved. However, at pH 7.3, Lz is positively charged (zeta potential +3.2 mV), and the EE decreased to 0.83%.

## (3) Microfluidic method

Microfluidic technique is widely used to prepare macro-sized enzyme-loaded polymersomes. Taking advantage of the locally defined environment formed via a W/O/W double emulsion, this method usually has a higher degree of control over the size and size distribution of the produced nanoreactors [94,95]. It also permits to prepare stimuli-responsive polymersomes by simply adjusting the solution properties. For instance, the pH-responsive PMPC-PDPA polymersomes were formed via pH-induced self-assembly within the microchannels by tuning the pH of the aqueous solution [96]. At the same time, BSA was encapsulated in the polymersomes in the process of polymersome formation by adding the protein in the aqueous solution. The encapsulation efficiency was found to be comparable to the one obtained with the solution production method (performed not in a microfluidic device). In this work, the pH-induced self-assembly process avoided using organic solvent which was compatible with the use of biomacromolecules. From a more general point of view, the most attractive advantage of microfluidic system is that it enables the continuous production of polymersomes with little batch-to-batch variations. Additionally, complex multicompartmental polymersomes-based structures can be obtained by using a co-flow microfluidic device [97].

#### (4) Polymerization-induced self-assembly (PISA)

Recently, PISA strategy is also proposed to manufacture nanoreactors for many advantages: PISA allows to produce nanoreactors in one-pot via simultaneous polymerization, self-assembly and encapsulation of enzymes under mild aqueous conditions. At the same time, the high solid content is favorable to increase loading efficiency [98]. For example, horseradish peroxidase (HRP)-loaded and glucose oxidase (GOx)-loaded poly(ethylene glycol)-*block*-poly(2-hydroxypropyl methacrylate) (PEG-PPMA) polymersomes were separately prepared via an initiator-free visible light-mediated PISA (photo-PISA) in aqueous and mild conditions. It was interestingly found that the activities of both enzymes was maintained and the enzyme-loaded polymersomes could perform the GOx-HRP cascade reactions smoothly [99]. In another work, an oxygen-tolerant and high-throughput photo-PISA platform was reported [100]. With the assistance of GOx, an enzyme that can remove the dissolved oxygen in the solution rapidly and constantly, the photo-PISA process was allowed to be conducted under air environments. In the mild conditions, not only the function of GOx was retained during PISA, but also the activity of the encapsulated protein (HRP). Additionally, the encapsulation efficiency of HRP and BSA was observed as high as 50–52%, decided by the ratio of the polymersome interior volume to the solution volume, demonstrating the advantage originating from the high solid content of PISA.

### 3.1.2 Nanoreactor functions

Regardless of the preparation methods, the functions of the constructed nanoreactor and the related applications are greatly dictated by the loaded enzyme(s). Contrary to the huge number of low-molar-mass drugs encapsulated in polymersome-based drug delivery nanosystems, in the field of nanoreactors, which is in its early investigation stage, only several commercial model enzymes are under studies, such as *Candida antarctica* lipase B (CalB), HRP and GOx. Other enzymes are also involved to extend the realm of nanoreactors and applications. Some exemplary polymersome nanoreactors are listed in Table 1 in chronological order so as to have a view on the development of the nanoreactor field. The polymers used to form the polymersome compartments, the functional enzymes and the function of the nanoreactor (system) are all gathered in Table 1.

**Table 1.** Examples of Enzyme(s)-loaded Polymersome Nanoreactors.

Loaded enzyme(s) <sup>1</sup>	Polymer(s) <sup>2</sup>	Permeabilization	Remarks/Functions	Year, main author	Ref.
GOx	PEG-PPS	Intrinsic	Oxidation-induced disassembly; Potential application in drug delivery	2004, Sommerdijk	101
TvNH	PMOXA-PDMS-PMOXA	OmpF, Tsx	Model for therapeutic nanoreactor	2005, Meier	102
acid phosphatase	PMOXA-PDMS-PMOXA	OmpF	Model for channel protein-equipped nanoreactor	2006, Meier	103
GOx, HRP	PS-PIAT	Intrinsic	Model for positioning loading of enzymes in separate domains within one polymersome	2007, van Hest	90
SOD	PMOXA-PDMS-PMOXA	Intrinsic	Model for antioxidant nanoreactor	2008, Palivan	104
Tr	PS-PAA	Impermeable	Demonstration of the confinement effect on the enhancing of enzyme activity	2009, Vancso	105
GOx, CalB, HRP	PS-PIAT	Intrinsic	Model for positioning loading of enzymes in one polymersome to facile cascade enzymatic reactions	2009, van Hest	106
Hb	PMOXA-PDMS-PMOXA	OmpF	Dual functional nanoreactor with antioxidant and O <sub>2</sub> -transport capacities	2012, Palivan	107
SOD, LPO, Cat	PMOXA-PDMS-PMOXA	OmpF	Artificial peroxisome; Promising application as cell implant	2013, Palivan	108
SOD, Cat	PS-PIAT, PS-PEG	Intrinsic	Investigation on the influence of membrane permeability on the confined enzyme activity	2013, van Hest	109
PAMO, CalB, Alc, ADH	PS-PIAT, PB-PEG	Intrinsic	Model for artificial cell by pos-in-pos	2014, van Hest	110
Lac	PNVP-PDMS-PNVP	Intrinsic	Oxidizing agents for industrial or technical applications	2014, Meier	111
GOx, Mb, HRP	PEG-P(DEAEM-co-DMIBM)	pH-responsive	Model nanoreactor platform with controllable molecular diffusion	2014, Voit	112
HRP, GOx	PMOXA-PDMS-PMOXA, PS-PIAT	OmpF, Intrinsic	Mimicry of the compartmentalization of cells via pos-in-pos	2014, Liedberg	113
Cat	PGLA	Intrinsic	Model for photodynamic therapy with a selectivity to cancer	2015, Guo	114

Table 1. Continued

Loaded enzyme(s) <sup>1</sup>	Polymer(s) <sup>2</sup>	Permeabilization	Remarks/Functions	Year, main author	Ref.
HRP	PMOXA-PDMS-PMOXA	pH-responsive OmpF	Model for triggered permeabilization with channel protein	2015, Palivan	115
$\beta$ -Gal	Carbohydrate-PPG	Intrinsic	Model for enzyme prodrug cancer therapy	2017, Akiyoshi	116
AGE, NAL, CSS	PMOXA-PDMS-PMOXA	OmpF mutant	Model for incompatible reaction cascades via positional-loading enzymes and selective permeability	2017, Castiglione	117
GOx	PEG-P(CPTMA- <i>co</i> -PEMA)	pH-responsive	Model polymer prodrug nanoreactor for cancer therapy	2017, Ge	118
HRP	PMOXA-PDMS-PMOXA	OmpF	Model platform to characterize enzyme activities in milieu similar to their native crowding environments.	2017, Meier	119
GOx, HRP	PEG-PHPMA	Intrinsic	Application of aqueous photo-PISA to prepare enzyme-loaded intrinsic permeable polymersomes	2017, O'Reilly	120
HRP	PMOXA-PDMS-PMOXA	pH-responsive OmpF	Model strategy to impart polymer membrane with reversible stimuli-responsive permeability with channel protein	2017, Palivan	121
PGM	PMOXA-PDMS-PMOXA	$\alpha$ -HL mutant	Promising for enzyme replacement therapy	2017, Palivan	122
HRP	PMOXA-PDMS-PMOXA	Redox-responsive OmpF	A proof of concept to illustrate nanoreactor function as artificial organelle and cellular implant in living organisms	2018, Palivan	123
HRP	PMOXA-PDMS-PMOXA	OmpF	A micrometer-sized platform to facilitate the straightforward investigation of specific catalytic reactions in confined spaces	2018, Meier	124
UOx, HRP	PMOXA-PDMS-PMOXA	OmpF	Therapeutic nanoreactor for hyperuricemia	2018, Palivan	125
HRP	PEG-P(HPMA- <i>co</i> -GlyMA)	Inherent	Fundamental study on the relationship between membrane permeability with membrane thickness, cross-linking density	2019, O'Reilly	126
HRP	PEG-PHPMA-P(NIPAM- <i>co</i> -ALAM)	Thermo-responsive	Aqueous visible-light initiated seed RAFT-mediated PISA to prepare enzyme-loaded crosslinked polymersomes	2020, Tan	127
GOx, Mb	PEG-P(DMIHMA- <i>co</i> -DEAEMA)	pH-responsive	A spatio-temporally controllable catalytic compartment	2020, Appelhans	128

**Table 1. Continued**

Loaded enzyme(s) <sup>1</sup>	Polymer(s) <sup>2</sup>	Permeabilization	Remarks/Functions	Year, main author	Ref.
GOx/UOx	PEG-P(DMIHMA- <i>co</i> -DEAEMA), PEG-P(DMIHMA- <i>co</i> -DPAEMA)	pH-responsive	Reversible system with feedback-induced and oscillating pH regulation; Model for artificial cell	2021, Appelhans	129
GOx	PEG-P(FcMA- <i>co</i> -PEMA)	Acid-triggered	Tumor-targeting capacity, together with prodrug to enhance the chemicodynamic therapy efficiency	2021, Ge	130
β-Gal	PBO-PGL, PDMS-PMOXA	OmpF	First study to discriminate the effect of tacticity from crystallinity in aqueous self-assemblies of amphiphilic block copolymers	2021, Meier	95

**Abbreviations:**

<sup>1</sup>**Enzymes:** glucose oxidase, GOx; trypanosoma ViVax nucleoside hydrolase, TvNH; horseradish peroxidase, HRP; superoxide dismutase, SOD; trypsin, Tr; Candida antarctica lipase B, CalB; hemoglobin, Hb; lactoperoxidase, LPO; catalase, Cat; phenylacetone monooxygenase, PAMO; alcalase, Alc; alcohol dehydrogenase, ADH; laccases, Lac; myoglobin, Mb; β-galactosidase, β-Gal; N-acyl-D-glucosamine 2-epimerase, AGE; N-acetylneuraminase lyase, NAL; CMP-sialic acid synthetase, CSS; phosphoglucomutase, PGM; urate oxidase, UOx;

<sup>2</sup>**Polymer blocks:** poly(ethylene glycol), PEG; poly(propylene sulfid), PPS; poly(2-methyloxazoline), PMOXA; poly(dimethylsiloxane), PDMS; polystyrene, PS; poly(L-isocyanoalanine(2-thiophen-3-yl-ethyl)amide), PIAT; polyacrylic acid, PAA; polybutadiene, PB; poly(N-vinylpyrrolidone), PNVP; polypoly(diethylaminoethyl methacrylate)-*co*-poly(3,4-dimethyl maleicimidobutyl methacrylate), P(DEAEM-*co*-DMIBM); poly(D,L-lactic-*co*-glycolic acid), PGLA; poly(propylene glycol), PPG; poly((2-(methacryloyloxy)ethyl camptothecin oxalate)-*co*-(2-(piperidin-1-yl)ethyl methacrylate)), P(CPTMA-*co*-PEMA); poly(2-hydroxypropyl methacrylate), PHPMA; poly(2-hydroxypropyl methacrylate)-*co*-(glycidyl methacrylate), P(HPMA-*co*-GlyMA); poly(N-isopropylacrylamide-*co*-(allyl acrylamide)), P(NIPAM-*co*-ALAM); poly((6-(3,4-dimethylmaleimidio)hexyl methacrylate)-*co*-(2-(diethylamino)ethyl methacrylate)), P(DMIHMA-*co*-DEAEMA); poly((6-(3,4-dimethylmaleimidio)hexyl methacrylate)-*co*-(2-(diisopropylamino)ethyl methacrylate)), P(DMIHMA-*co*-DPAEMA); poly((2-(methacryloyloxy)ethyl ferrocene-carboxylate)-*co*-(2-(piperidin-1-yl)ethyl methacrylate)), P(FcMA-*co*-PEMA); poly(butylene oxide), PBO; polyglycidol, PGL.

In general, nanoreactors are turning into more complex systems in the aspects of structure, composition and function in the developing course. From a structural point of view, more multicompartmental systems are constructed to biomimic the complex structure of cell. At the same time, the composition has been more complicated by using channel proteins, stimuli-responsive polymers, as well as multiple functional enzymes. The developments are mostly directing to therapeutic nanoreactors for practical purpose.

### 3.2 Permeability of polymersome membrane

Polymersomes have great potential to construct nanoreactors by incorporating enzymes, as displayed in Table 1 (Section 3.1). One can see that, besides polymersome compartment and functional enzyme(s), membrane protein and stimuli-responsiveness are required in most of the nanoreactors, to facilitate the transportation of enzymatic substrates (and products). Obviously, sufficient and appropriate membrane permeability is crucial to make nanoreactor functional. Typically, enzymes are encapsulated in the aqueous cavity of polymersomes, therefore, polymersome membrane is required to be permeable to enzymatic substrates to trigger the enzymatic reaction inside. However, the high-molar-mass constituents of polymersomes generally produce robust and stable compartments, and consequently increase the barrier against substrate diffusion [5,131,132]. To this end, the permeability of polymersome membranes will be discussed together with some permeabilization methods.

Before going further, it is important to note that membrane permeability is closely related to the permeates [133]. For example, a size-selective membrane can be permeable to small molecules but impermeable to relatively large molecules. Strictly speaking, membrane permeability is relative, but for simplicity herein polymersome membranes are categorized into intrinsically permeable and impermeable membranes. In this context, intrinsically permeable membrane stands for a membrane which is permeable to the substrates of interest in a specific investigation. On the other hand, the membrane which is intrinsically impermeable to the substrates of interest needs to be permeabilized.

To date, only few polymersomes are found to be intrinsically permeable enough to serve as a versatile platform for the construction of diverse nanoreactors [134,135]. Fortunately, various permeabilization strategies have been proposed. For example, the permeability of polymersome membranes can be regulated by responding to external stimuli [81], or be modified via post-polymerization methods [136]. Additionally, inserting channel proteins is suggested as a more versatile and straightforward way to tune the permeability of polymersome membranes [95].

### 3.2.1 Intrinsic permeability

The permeability of polymersome membranes is primarily influenced by the chemical nature and the length of the hydrophobic segment of amphiphilic copolymers. It is thought that size-selective permeability is generally a result of the loosely packed membrane-forming polymer chains. For instance, it was reported that the flexible hydrophobic polybutadiene (PB) membrane was more permeable to  $\text{OH}^-$  than the more solid-like polystyrene (PS) membrane [137]. At the same time, the intrinsic permeability will decrease as a consequence of the increase of membrane thickness. Membrane thickness scales with the molar mass ( $M$ ), namely, the degree of polymerization (DP) of the hydrophobic block, in a relation of  $d \sim M^\alpha$  or  $d \sim \text{DP}^\alpha$ , with the exponent ( $\alpha$ ) indicating the stretching extent of the hydrophobic polymer chain. For instance, in the case of PBO-PEO, the exponent was found close to 0.66, which agreed with strong segregation theory. However, the exponent was simulated close to 0.83, when the membrane thickness was below 7 nm, reflecting a more stretched or ordered configuration of the chains [138].

Furthermore, the permeation of substrates through membrane generally obeys Fick's first law. Hence, permeability ( $P$ ) is dependent on the membrane thickness ( $d$ ) and the apparent diffusion coefficient ( $D^*$ ) in a relation of  $P = D^*/d$  [139].

Yet, for some permeates, especially some ions, various permeation models have been proposed to explain some extraordinary and unexpected phenomena [140]. Additionally, regarding to the qualitative determinations of permeability, such as the permeability to  $\text{H}^+$ , the reported values varied a lot, with orders-of-magnitude variability, due to the lack of standard protocols, the heterogeneous vesicles, as well as some other reasons. The values even varied from batch to batch in one lab [141]. The permeation mechanism is also incompletely resolved with several models being supposed [133,141,142], although the studies have been performed since the appearance of liposomes in 1980s [142,143]. From a practical point of view, in the cases of polymersome nanoreactors, the membrane permeability to enzymatic substrates and products is considered more in a qualitative way than in an aspect of the precise values.

In the reported nanoreactors to date, limited amphiphilic copolymers are able to construct inherently permeable polymersomes. PS-PIAT is one of them. Originating from the coil-rod nature, PS-PIAT is able to self-assemble into inherently porous polymersomes owing to the frustrated packing of the polymers in the membrane [90]. For example, the enzyme SOD1 was encapsulated in PS-PIAT or PS-PEG polymersomes, and its activity to neutralize superoxide radicals ( $\text{O}_2^{\cdot-}$ ) into  $\text{H}_2\text{O}_2$  was assayed. In comparison to the PS-PEG polymersomes, it was found that the PS-PIAT membrane was more permeable to  $\text{H}_2\text{O}_2$  [109].

Further, PS-PIAT polymersomes were successfully used to construct a three-enzymes loaded nanoreactor to facilitate the cascade reactions (Figure 7) [105]. The enzymes, including GOx, HRP and CalB, were delicately loaded at three accessible positions of a polymersome according to each enzyme's physical and chemical properties: GOx was encapsulated in the aqueous interior due to its largest size of the three enzymes. CalB was embedded in the hydrophobic membrane, considering it is more hydrophobic than HRP, which was immobilized on the outer surface of membrane. The cascade reactions were triggered by the hydrolysis of 1,2,3,4-tetra-O-acetyl- $\beta$ -glucopyranose (GAc4, added in the bulk suspension) by CalB. The generated glucose was subsequently oxidized by GOx in the polymersome cavity. The produced  $H_2O_2$  permeated the membrane and was finally used to convert 2,2'-azino-bis(3-ethylbenzothiazoline-6-sulfonate) (ABTS, added in the bulk solution) to  $ABTS^{*+}$  by HRP. The reactions were performed smoothly in sequence, showing the membrane was permeable to all the involved substrates and products.

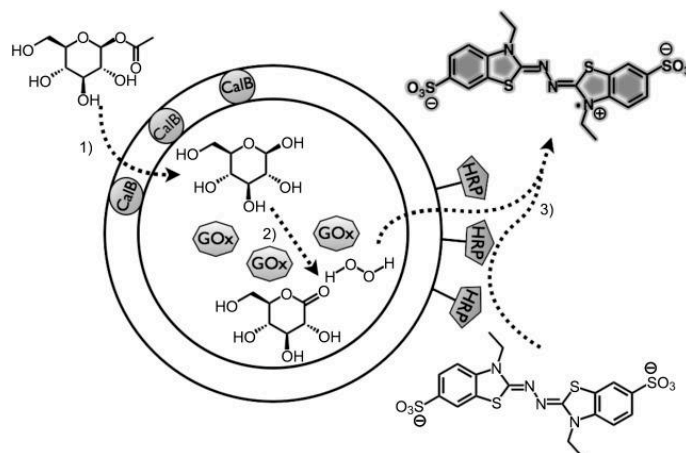


**Figure 7.** A three-enzymes loaded PS-PIAT polymersome facilitating the cascade enzymatic reactions [105].

PS-PIAT polymersomes were also used to mimic the eukaryotic cell, in a polymersomes-in-polymersome architecture (Figure 8) [110]. Different enzymes were separately loaded in PS-PIAT polymersomes to function as artificial organelles (AOs). These AOs, together with free cytosolic enzymes and cofactors, were then co-encapsulated in a micrometric PB-PEG polymersome to mimic the structure of an eukaryotic cell. The cascade enzymatic reactions inside this cell mimetic system proceeded smoothly because the substrates could diffuse from one AO to the next. Such a polymersomes-in-polymersome system provided an elegant model for cell mimicry and paved a way to study cellular processes involving multiple successive reactions.

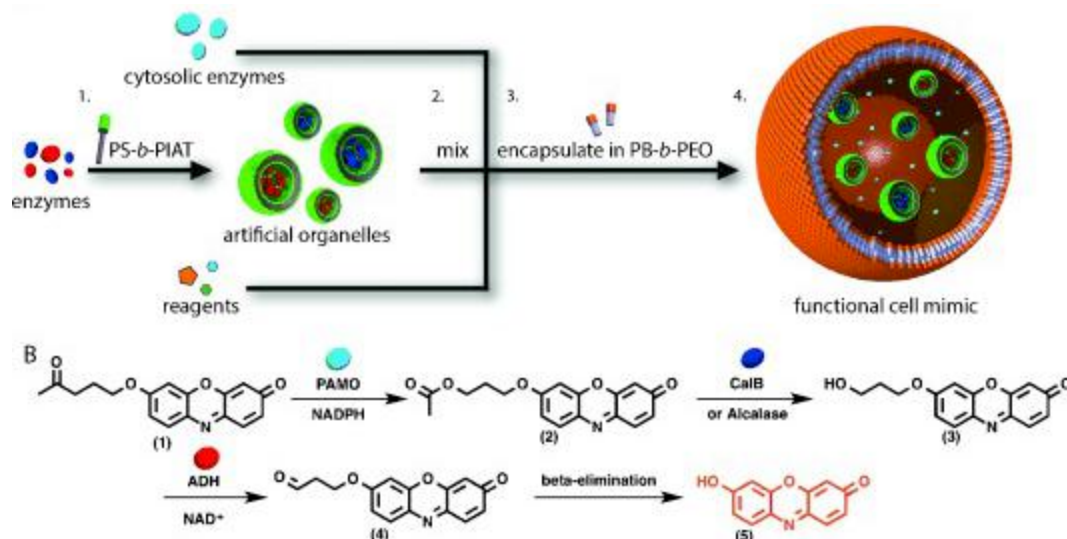


**Figure 8.** (A) Illustration of an eukaryotic cell mimetic system constructed in a polymersomes-in-polymerosome architecture, and (B) the cascade reactions studied [110].

PHPMA-based polymersomes are also reported to have intrinsic permeability attributed to the highly hydrated PHPMA segments. For instance, enzyme-loaded intrinsically permeable polymersomes made of PHPMA-PEG were obtained via photo-PISA (Figure 9) [144]. These polymersomes were intrinsically permeable to the enzymatic substrates, while prevented enzymes from leaking. It deserves to be noted that this work was also highlighted by the adopted PISA strategy. PISA has attracted increasing attention for the possibility to prepare nanostructures with high cargo-loading efficiency via a relatively simple procedure [145]. At the same time, the mild aqueous conditions in the visible light-induced RAFT-mediated PISA process allowed the loaded enzyme (HRP or GOx) to retain its activity.

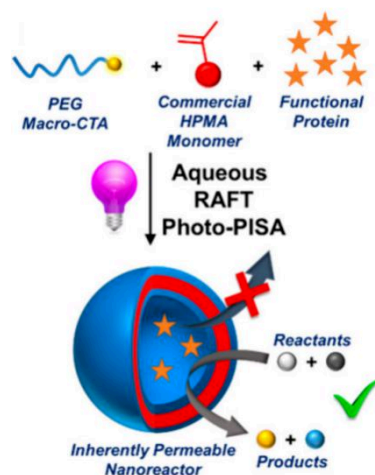


**Figure 9.** Visible light-induced RAFT-mediated PISA to prepare enzyme-loaded intrinsically permeable PHPMA-PEG polymersomes [144].

As stated, flexible hydrophobic polymers (*i.e.*, PPO, PBO ...) have more possibility to construct permeable membranes than solid-like polymers (*i.e.*, PS, PDMS ...) [95,137]. However, the formed membrane are sometimes not stable enough [95]. To this end, co-assembly of different copolymers is proposed as a facile method to tune both the permeability and the stability of the co-assembled membrane, via adjusting the composition of the polymer blend. For example, the permeability of Pluronic L121 (PEO<sub>5</sub>-PPO<sub>67</sub>-PEO<sub>5</sub>) vesicles was tuned by blending with other Pluronics (PEO-PPO-PEO, with varied degrees of polymerization of PEO and PPO) [146]. In another work, PEO-PPO-PEO was used to increase the membrane permeability of PEG-PB polymersomes without losing the membrane stability [147]. The permeability assessments showed that the hybrid membrane was permeable to molecules with molar masses below 5 kDa but retained molecules with molar masses larger than 10 kDa. In these two works, the blend polymers co-assembled into symmetric vesicles, while asymmetric polymersomes were reported elsewhere [148]. The asymmetric polymersomes were made of a mixture of PMPC-PDPA and PBO-PEG, which were more different in chemical nature. Into these asymmetric polymersomes, the enzyme L-Asparaginase (ASNS) was encapsulated and its capacity to hydrolyze L-asparagine was retained, demonstrating that the membranes were permeable to the substrate. Co-assembly strategy is simple and straightforward, but the chemical compatibility between each component should be well matched.

### 3.2.2 Stimuli-responsive permeability

Stimuli-responsive polymersomes are typically made of amphiphilic copolymers with special functional groups, which are able to respond to the changes in the local environment. When exposed to the specific stimulus, such polymersomes can undergo morphology or phase transition, resulting in a change in membrane permeability [149].

A great amount of stimuli-responsive polymersomes has been designed to respond to a wide range of stimuli for various applications [150–152]. However, the stimulus-responsive polymersome nanoreactors are less investigated, and the stimuli are generally limited to pH and light.

#### (1) pH-responsive permeability

pH-responsive polymersomes are usually prepared by the copolymer chains with the presence of pH-responsive moieties. Typically, the pH-responsive segment undergoes a hydrophobic-to-hydrophilic transition, inducing the increase of membrane permeability. One of the widely studied pH-responsive polymers is poly(2-(diethylamino)ethyl methacrylate) (PDEAEMA), which has a pKa suitable with the cellular environment. For example, a polymersome nanoreactor with pH tunable permeability was developed with PDEAEMA and PEG segments [153]. In acidic

conditions, PDEAEMA segment was protonated and became hydrophilic. In order to keep the polymersome structure intact, crosslinking agent 3,4-dimethyl maleic imidoethyl methacrylate (DMIEM) or 3,4-dimethyl maleic imidobutyl methacrylate (DMIBM) was copolymerized into the hydrophobic part (Figure 10A). After crosslinking (Figure 10B), the polymersomes showed high mechanical stability. The membrane permeability could also be finely tuned by adjusting crosslinking degree, besides the pH of the solution.

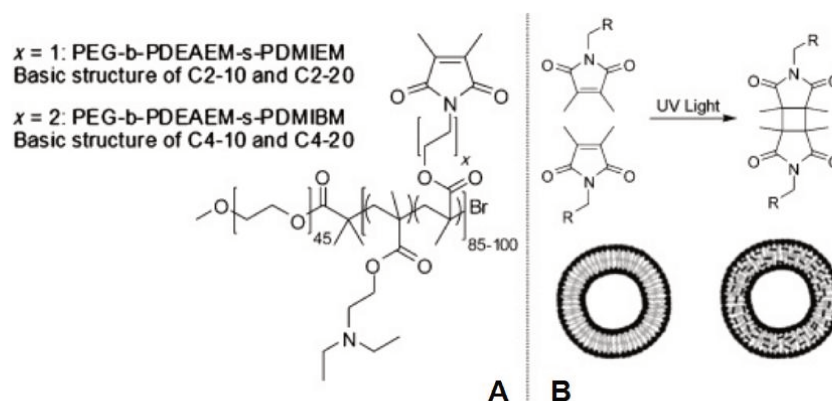


**Figure 10.** (A) Chemical structure of the amphiphilic block copolymer with the crosslinking units DMIEM and DMIBM being incorporated in the hydrophobic segment, and (B) the crosslinking reaction occurring within membrane [153].

Instead of the strategy conducted by chemical modifications with pH-responsive moieties followed with crosslinking treatments, co-assembly of pH-responsive polymer with inert polymer is reported as an easier strategy. The idea is to use the pH-responsive polymer as a sacrificial component of the membrane. Upon exposing to the stimulus, it turns hydrophilic and is dissolved, leaving the polymersome membrane porous. For instance, the pH-responsive copolymer poly(ethylene glycol)-*block*-poly(styrene boronic acid) (PEG-PSBA) was mixed with PEG-PS. The polymers then co-assembled into polymersomes. In alkaline conditions, the PSBA segment was ionized to boronate, and the complexation with glucose or fructose gave rise to the increased solubility of PSBA block in water. The subsequent removal from the polymer membrane produced permeable polymersomes, allowing for the transportation of substrates across the membranes and the achievement of enzymatic reactions inside the polymersomes. The degree of porosity of the membranes could be adjusted by varying the ratio between PEG-PS and PEG-PSBA [154].

## (2) Light-responsive permeability

Photo-responsive polymersomes are attractive since light can provide spatio-temporal control over the membrane permeability. For instance, the light-responsive polymersome nanoreactors were reported: they switched on by visible light and self-

reverted fast to their inactive state in dark. The fast and reversible permeability transition originated from the isomerization of donor-acceptor Stenhouse adducts (DASAs) (Figure 11) [155]. Specifically, the aromatic amine precursors, N-(4-methoxyphenyl)-1,3-diaminepropane (MPDP), were incorporated in the hydrophobic segment of the amphiphilic PEG-P(PEPMA-*co*-HMA) copolymer producing the DASA block copolymers. The DASA block copolymers self-assembled into light-responsive polymersomes: under visible light irradiation, DASAs were able to isomerize with a transition from a non-polar state to a more polar state, resulting in the increase of membrane permeability. Therefore, the enzymatic reactions in the polymersomes could be triggered-on by light and stopped immediately when the light irradiation was removed.

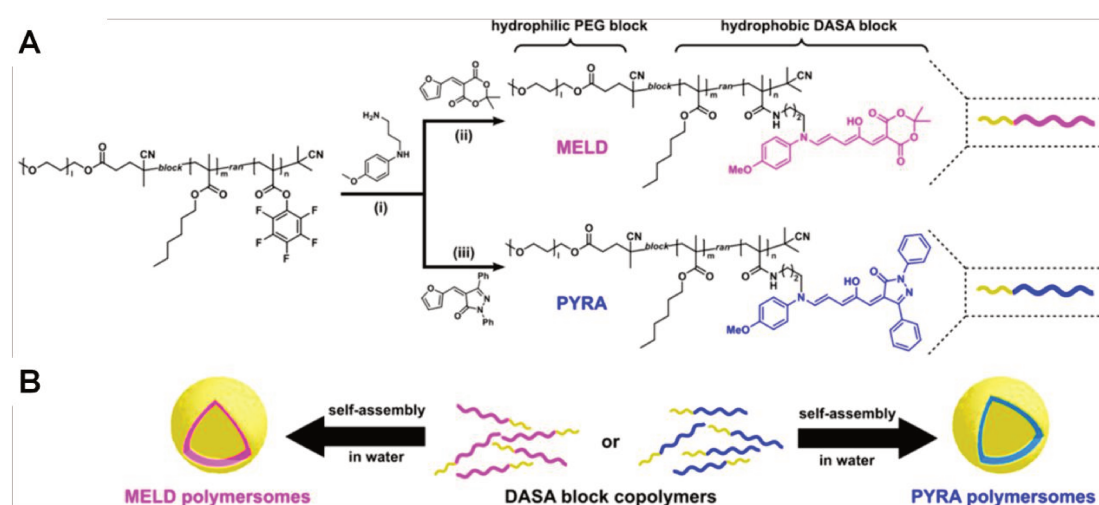


**Figure 11.** (A) Synthetic procedure for DASA-functionalized block copolymers, and (B) preparation of DASA-functionalized visible light-responsive polymersomes via self-assembly [155].

Recently, a convenient and versatile approach to tune the permeability of polymersome membranes was proposed, via UV irradiation but without using functional monomers [156]. 2-hydroxy-4-2-(hydroxyethoxy)-2-methylpropiophenone (PPOH), a water-soluble  $\alpha$ -hydroxyalkylphenone, was added into the polymersome solution. Upon UV irradiation, PPOH generated radicals which reacted with the membrane polymers, giving rise to the increase of the hydrophilicity of the membrane-forming polymers, and the increase of membrane permeability, as a consequence. The versatility of this method was confirmed by the successes obtained with  $\alpha,\omega$ -hydroxyl-end-capped PMOXA-PDMS-PMOXA,  $\alpha,\omega$ -acrylate-end-capped PMOXA-PDMS-PMOXA, and PEO-PB polymersomes, three chemically different copolymers. HRP was used as the model enzyme and was encapsulated inside polymersomes. Enzymatic activity assessment results showed that the generated nanoreactors had a “photo-triggered ON” character with retained enzymatic activity.

A system combining light-control and pH-responsiveness was recently reported [127]. In this system, the photoacid (merocyanine) was incorporated into a pH-responsive polymersome formation. The permeability of the pH-responsive polymersomes could be modulated by the light-driven proton transfer of the photoacid. In the presence of photoacid molecules, it allowed to control the protonation and deprotonation of the polymersome membrane, cyclically and temporally. Therefore, the membrane could undergo repeated light-driven swelling–contraction cycles. Encapsulating enzymes in the polymersome compartments, the resulting nanoreactor could rapidly respond to the light irradiation and switch the enzymatic reactions ON and OFF on demand.

### (3) Thermo-responsive permeability

Thermo-responsiveness has been incorporated into polymersomes. However, most of the polymersomes deconstruct under stimuli which hampers their applications as nanoreactors. To keep the polymersome compartments intact, crosslinking is always necessary. Recently, a thermo-responsive crosslinked nanoreactor was constructed by using the thermo-responsive PNIPAM segment and allyl acrylamide crosslinking agents, via a visible light-initiated seeded RAFT-mediated PISA process [128]. The permeability of polymersome membrane was switched by the phase transfer of PNIPAM segment. Additionally, the phase transfer temperature of vesicles could be easily tuned by copolymerizing NIPAM with other acrylamide-based monomers. Due to the thermo-responsive permeability, the enzymatic reaction rates of HRP-loaded vesicles were able to be regulated through changing the temperature. In contrast, the non-crosslinked vesicles transitioned into micelles at lower temperature, causing the release of the loaded cargoes.

### (4) Redox-responsive permeability

Redox-responsive segments can also be incorporated into the construction of polymersomes. But the cleavage of the redox-sensitive linkages usually induces the rupture of polymersome compartments [101,157]. Crosslinking again is necessary to keep the structure intact. Recently, an intracellular milieu-triggered in-situ oxidation-induced crosslinking strategy was reported [158]. The amphiphilic copolymer, bearing pendent arylboronate ester groups in the hydrophobic segment, self-assembled into polymersomes. The polymersome surface was further decorated with peptides to target towards mitochondrion. Such that in mitochondrial oxidative milieu, arylboronate moieties could be cleaved, followed by the cascade cleavage reactions and the generation of primary amines. The primary amines further resulted in crosslinking. Additionally, the reactions were accompanied with the hydrophobic-to-hydrophilic transition which allowed to permeabilize membrane.

Compared to crosslinking strategies, co-assembly of inert and oxidation-responsive polymers seems more facile. For instance, the polymer blend of PEG-PS and poly(ethylene glycol)-*block*-poly(acrylbenzyl borate) (PEG-PABB) first co-assembled

into polymersomes. Then, in a  $\text{H}_2\text{O}_2$  solution, PABB was oxidized into PAA, triggering the hydrophobic-to-hydrophilic transition. This transformation resulted in the perforation of the polymersome membrane due to the oxidation-induced dissolution of PABB domains in the hydrophobic membrane [159]. The pore size could be altered through a facile modulation of the blending ratio (Figure 12), due to the microphase separation of PS and PABB polymers in the hybrid membrane, in specific, PABB segments formed isolated islands in PS matrix via nucleation-and-growth mechanism as indicated by AFM images. The tunability in membrane permeability was also evidenced by TEM and Cryo-TEM images, as well as fluorescein-release assessment results.

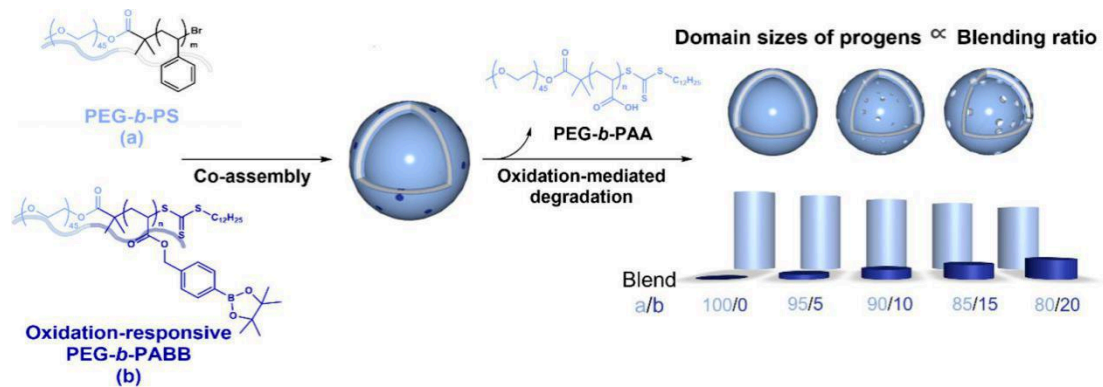


**Figure 12.** Tunable size-selective permeability of co-assembled polymersome membrane, achieved by adjusting the composition ratio of a PEG-PS/PEG-PABB blend [159].

### 3.2.3 Insertion of nanochannels

Insertion of nanochannels into polymersome membranes is a bio-inspired strategy, analogue to the natural cell membranes being decorated with diversity of membrane proteins. The nanochannels applied to permeabilize polymersome membranes can be natural or synthetic nanochannels.

#### (1) Insertion of natural nanochannels

Since the first investigations on the insertion of outer membrane protein F (OmpF) into the membrane of PMOXA-PDMS-PMOXA polymersomes [102,160], the topic of membrane protein (MP)-equipped polymersomes has advanced by using other types of MPs [161] and other polymeric membranes [95].

PMOXA-PDMS-PMOXA polymersome membranes were intrinsically permeable for  $\text{O}_2$  and  $\text{O}_2^-$  but impermeable to  $\text{H}_2\text{O}$  [104]. The membrane was endowed with size-selective permeability by the insertion of OmpF (MWCO 600 Da), allowing the OmpF-equipped PMOXA-PDMA-PMOXA polymersomes to function as versatile nanoreactor compartments [109].

OmpF can be further chemically modified with a pH-responsive [115,123] or redox-responsive [121] molecular cap serving as a sensitive gate when inserted in polymersome membranes. The diffusion of molecules through the channels was regulated by the on-off switch of OmpF gates, imparting the polymersome nanoreactors capable of responding on demand.

Integrating multiple membrane proteins (MPs) with different transport properties is helpful to specifically transport chemically diverse molecules in the complex cascade reactions. For example, the incorporation of OmpF and other functional MPs in one polymersome nanoreactor was recently reported (Figure 13) [162]. As model reaction, a two-enzymes system consisting of ketoreductase (KR) and formate dehydrogenase (FDH) was studied. For the transportation of the hydrophobic substrate and product of KR, the MPs including AlkL, OmpW, OprG and TodX were investigated, while OmpF, PhoE and FocA were studied for the transport of formate. It was found that when the MP pair of TodX and PhoE was used, the system had the highest channel-specific effects on the mass transfer. And in consequence, the space-time yield of the product was improved by 2.32-fold in comparison to the nanoreactors without MPs.

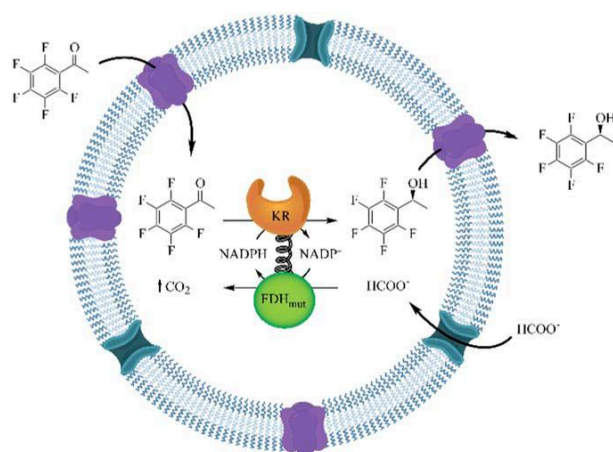


**Figure 13.** A polymersome nanoreactor, equipped with multiple membrane proteins with different transport properties for transposition of chemically diverse molecules in the cascade reactions of ketoreductase (KR) with formate dehydrogenase (FDH) [162].

Inserting bio-originated channel proteins is straightforward. However, the intrinsic incompatibility between synthetic polymer membranes and natural fragile proteins usually induces inefficient insertions [163]. Recently, a study intending to better quantify the mismatches in the insertion of proteins into polymeric membranes was conducted [164]. In this work, two types of mismatches were taken into account. One is physical mismatch, a dimensional difference between the length of the hydrophobic region of protein and the thickness of the hydrophobic polymeric membrane. The other is chemical mismatch, which indicates the polarity difference between the

surface of protein and the polymeric membrane. This investigation gave some clues when choosing optimal membrane proteins for a specific polymersome membrane, or tailored-preparing polymers for a specific membrane protein, which is inspiring. However, the trial-and-error investigations are somewhat costly.

## (2) Insertion of synthetic nanochannels

Membrane proteins (MPs) are naturally optimized for biological membranes. Generally, MPs are too small to completely span the thicker polymer membranes. In addition, it is difficult to obtain structural or orientational information of the reconstituted MPs in polymer membranes. Instead, synthetic nanochannels, possessing tunable size and chemical composition, as well as the good structural stability, are thought to be more easily inserted in polymer membranes with maintained nanochannel structures.

Synthetic nanochannels are generally constructed by one or multiple scaffold molecules, forming unimolecular or multimolecular channels. The later can further be classified into barrel-stave, barrel-hoop, and barrel-rosette shaped nanochannels according to the stacked shape of the multiple units [165]. To assay the channel-forming capacity and the properties of the formed channels, the scaffold molecules are usually inserted in planar lipid bilayer or three-dimensional (3D) lipid vesicles [166,167]. In contrast to the enormous systems of synthetic channels-in-lipid membranes, the ones of synthetic nanochannels-in-polymersome membranes have been rarely reported.

Carbon nanotube porins (CNTP) is a unique class of biomimetic nanopores because carbon nanotubes are robust and highly chemically resistant. CNTPs have been inserted into lipid membranes, forming defined unimolecular-typed membrane pores, with atomically smooth hydrophobic walls, supporting the transport of protons and water [168,169]. Recently, CNTPs were integrated into PB-PEG polymersome membranes to mimic the biological membranes in an all-synthetic architecture [170]. Proton and water transport measurements showed that these CNTPs maintained their high permeability in the polymer membrane environment. Interestingly, CNTPs could also mimic the behavior of biological gap junctions by forming bridges between vesicular compartments.

Multimolecular nanochannels-equipped polymersomes have also been reported: helical synthetic nanopores, formed via self-assembly of dendritic dipeptides or dendritic esters were incorporated in PB-PEG membranes [171]. The fully synthetic systems demonstrated great stability over a wide pH range and one-month of storage. The transport study showed that both the incorporated pores facilitated the transport of protons, while the dendritic ester-incorporated polymersomes had a greater proton transport capacity. Additionally, it was interesting to find that neither dendritic dipeptides nor dendritic esters could be integrated in PMOXA-PDMS-PMOXA

polymersome membrane. It was supposed that the result was originated from the worse solubility of dendritic molecules in PDMS membrane compared to PB membrane. The difference between diblock and triblock architectures was also thought to contribute to the result to some extent.

**In summary**, the fully synthetic cell-mimetic compartmental systems, constructed by inserting synthetic nanochannels into polymersome membranes, is of great advantages. Therefore, in the next section,  $\beta$ CD-based derivatives and polymers will be introduced, focusing on their applications in the construction of synthetic nanochannels and polymersomes.

#### 4. $\beta$ CD-based Amphiphiles and Applications

Cyclodextrin (CD) is a family of cyclic oligosaccharides composed of several D-glucose units linked via  $\alpha$ -1,4-glycosidic bonds. Commonly, the number of glucose units is 6, 7, or 8, and accordingly named as  $\alpha$ -,  $\beta$ -, or  $\gamma$ -CD (Figure 14) [172,173]. There are three sets of hydroxyl groups in the glucose units, including the primary hydroxyls at position 6, and the secondary hydroxyls at positions 2 and 3. The hydrogen bondings between secondary hydroxyls make CD a rigid bucket-like shape, with a hydrophilic exterior and a hydrophobic cavity. The diameter of the cavity varies depending on the number of glucoses. But the height is around 0.78 nm independent on the type of CDs.

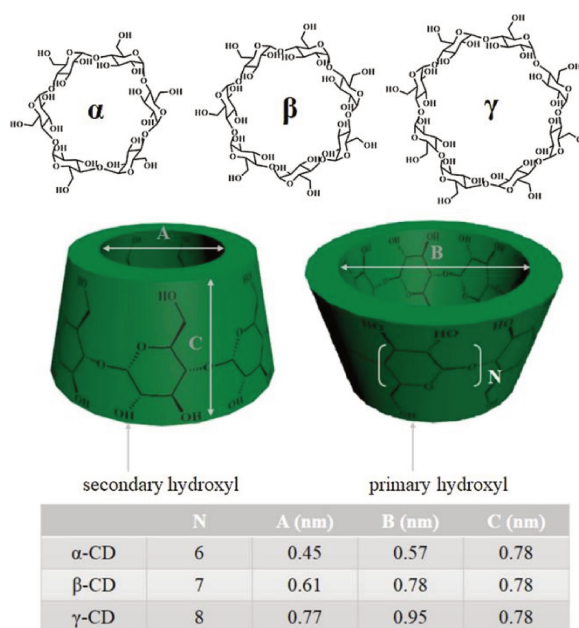


**Figure 14.** Molecular structures and structural parameters of three common cyclodextrins (CDs) [172].

The hydrophobic cavity of CDs is versatile to form complexes with a variety of organic hydrophobic moieties, and thus has been widely applied in solubilizing hydrophobic drugs [174]. Additionally, CDs are widely available, biocompatible and biodegradable, and hence are also explored a great deal in other application fields, in a variety of formulations, such as CD derivatives, CD-based sponges, CD-based host-guest inclusion complexes, and so forth [175–177].

Besides the common merits of CDs,  $\beta$ CD, composed of seven glucose units, shows some unique characteristics, such as the rather rigid and symmetric molecular structure. There are seven hydroxyls on positions 2, 3, and 6, denoted respectively as 2-OH, 3-OH, and 6-OH here. These three classes of hydroxyls can be selectively modified due to their different chemical environments [178,179]. 6-OH is the least sterically hindered, and the most basic and neutrophilic. In contrast, 3-OH is orienting inwards being the most sterically hindered and thus the least accessible. 2-OH is orienting outwards being more acidic and more accessible than 3-OH. There are many reviews dedicated to the selective modifications of  $\beta$ CD. The huge number of  $\beta$ CD derivatives has been widely used in the pharmaceutical, drug, food, cosmetical fields by themselves, by forming inclusion complexes, or by conjugating with polymers [180–182].

Here, only amphiphilic  $\beta$ CD derivatives and  $\beta$ CD-cored amphiphilic star-like copolymers are discussed in terms of their molecular structures and their applications in the constructions of synthetic nanochannels and self-assembled nanoparticles. Some achievements on  $\alpha$ CD and  $\gamma$ CD are also taken into account here.

#### 4.1 Amphiphilic $\beta$ CD derivatives

Native  $\beta$ CD is intrinsically amphiphilic because of the hydrophilic exterior and the hydrophobic cavity. However, the hydrophobic interior cavity is usually adopted to form complexes with small hydrophobic organic molecules. In order to have a lipid-like amphiphilicity,  $\beta$ CD is usually decorated with alkyl tails on one side. Taking advantage of the hydrophilicity of the cavity exterior, these amphiphilic  $\beta$ CD derivatives can form artificial nanochannels in lipid bilayers or form 3D nanostructures via self-assembly.

##### (1) $\beta$ CD derivatives acting as synthetic nanochannels

Due to the unique characteristics of the cavity (rigidity, hydrophobicity and presence of plenty of oxygen moieties),  $\beta$ CD is greatly attractive to build artificial ion channels. For instance, the earliest reported  $\beta$ CD derivative formed hemi-channels in the lipid bilayer and facilitated the transport of  $\text{Co}^{2+}$  [183]. Afterwards, a tremendous number of artificial nanochannels were designed and characterized. It is commonly thought that there are two requirements for efficient formation of nanochannels in lipid bilayer:

the amphiphilicity of the scaffold and the dimensional match between the length of the hydrophobic part of the scaffold and the thickness of the lipid membrane [184]. To fulfill these two requirements,  $\beta$ CD was modified with hydrophilic oligoPEG at position 6 and decorated with hydrophobic heptyl tails at positions 2 and 3 which could span half of the lipid bilayer [184]. The derivatives formed dynamic hemi-channels. The effective transmembranar channels were formed when two of the halves encountered each other. Such nanochannels were found to have short lifetime decided by the occurrences and the probability of facing. These hemi-channel scaffolds were later refined by the incorporation of triazole functional groups between  $\beta$ CD cavity and hydrophilic mPEG [185]. Interestingly, the  $\beta$ CD derivatives formed defined isolated unitary pores at pH 3, while at pH 7 both ill-aggregates and isolated pores were formed. It was guessed that in acidic conditions, the protonated cationic triazole moieties imparted electrostatic hindrance between pores and thus prevented from aggregation, as shown in Figure 15.

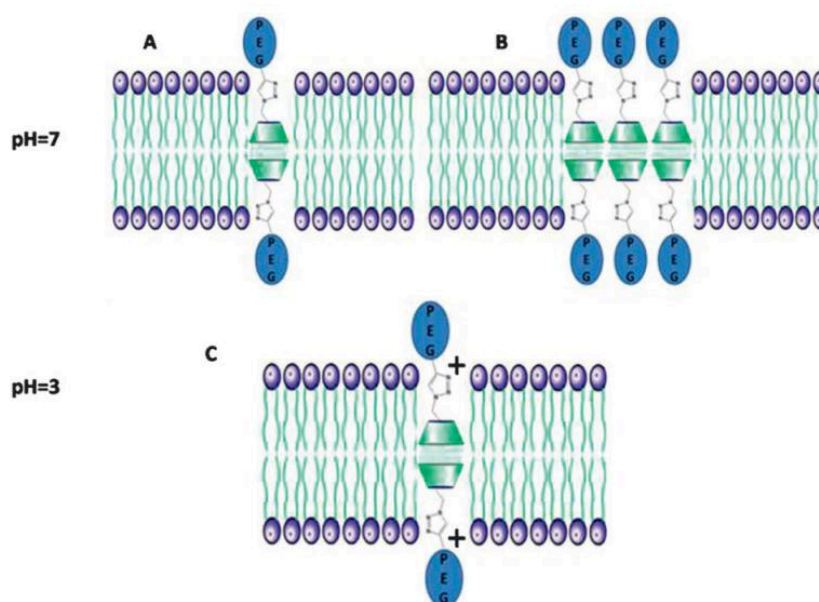


**Figure 15.** The triazole-incorporated  $\beta$ CD derivatives formed different types of pores in lipid bilayers under different pH conditions [185].

In comparison to the dynamic nanochannels formed by two of hemi-channels, more recently, a class of ion channels was prepared by covalently linking two  $\alpha$ CD onto a middle pillararene [186]. The three-rings system formed unimolecular channels in liposome membrane exhibiting a selectivity on the transmembranar translocation of  $K^+$  over  $Na^+$ .

In a similar way,  $\alpha$ CD rings were covalently linked resulting in cyclodextrin nanotubes (CDNTs) which formed unimolecular nanochannels in lipid membranes [187]. The CDNTs of  $\alpha$ CDs were prepared via several steps: first, the polyrotaxanes

of  $\alpha$ CD threading  $\alpha,\omega$ -dimethacrylate PEG were prepared. The polyrotaxanes were then capped with pyrene derivatives to stabilize the structure, and the  $\alpha$ CD rings were connected using epichlorohydrin. At last, the inner PEG chains were removed resulting in short CDNTs. This procedure was demonstrated efficient to synthesize CDNTs with well-controlled length, diameter, and the number of  $\alpha$ CDs. Additionally, these short CDNTs formed well-defined biomimetic ion-conducting channels in lipid membrane possessing similar ion transport dynamics and sensitivity to the natural channels. This method was also successfully extended with  $\beta$ CD and  $\gamma$ CD [188]. The structural parameters of the obtained CDNTs were tunable, showing the versatility of the method. This method is also promising for biotechnology and industrial applications by mass production.

## (2) Cyclodextrin bilayered vesicles (CDVs)

The low-molar-mass amphiphilic  $\beta$ CD derivatives can self-assemble into vesicles with appropriate modifications. The formed cyclodextrin bilayered vesicles (CDVs) have been widely explored and applied in the fields of biosensor, glue and so on. The first reported CDVs were made of per(2,3-di-O-hydroxyethyl-6-alkylthio)- $\beta$ CD via self-assembly in water [189]. Later on, this series of amphiphilic  $\beta$ CD derivatives was optimized, but it always ensures that the wider secondary face is exposed to the outer aqueous surrounding and the narrower face is modified with hydrophobic alkyl chains to construct the bilayer membrane.

A most interesting character of such  $\beta$ CD vesicles is that the exposed hydrophobic cavities maintain their host-guest ability in great extent, and thus the vesicles are promising for many applications. For example, such vesicles retained the characteristic affinity of  $\beta$ CD for adamantane carboxylate [190]. This property was further applied to combine adamantane-ended poly(acrylic acid) (Ad-PAA) onto the  $\beta$ CD vesicle. After crosslinking PAA chains and removing the  $\beta$ CD-based template, hydrophilic PAA polymer cages were manufactured [191]. More recently, a type of magnetic CDVs was prepared by embedding super-paramagnetic nanoparticles in the CDVs membrane [192]. The magnetic CDVs were investigated for application as biosensor for thyroxine (T4), taking advantage of the strong affinity between  $\beta$ CD and T4. Benefitting from the enormous binding points, T4 was effectively pre-concentrated which greatly increased the detection sensitivity.

Another interesting characteristic of CDVs is the selective permeation imparted by the CD cavities. CDVs were investigated regarding to their membrane permeability to  $H_2O$  and water-soluble PEG and PPO polymers, via the technique of pulsed field gradient-stimulated echo nuclear magnetic resonance (PFG-NMR) to measure the permeates exchange times through the bilayer [193]. It was found that the permeability decreased with increasing membrane thickness, consistent with the general rules in the cases of liposomes and polymersomes. Interestingly, it was found

that the permeation of polymers through the CD cavities was greatly dependent on the cross-sectional areas of polymers. PEG was able to permeate through both  $\alpha$ CD and  $\beta$ CD vesicles, while PPO was only able to penetrate through the larger cavity of  $\beta$ CD vesicles. The penetration of linear polymers through the defined  $\beta$ CD cavities mimics the DNA translocation through the defined pores of the cell membrane, making CDVs potential biomimetic systems.

*In brief*, low-molar-mass CD derivatives have great potential applications, while more interesting properties can be incorporated with them when they are conjugated with polymer chains. The following part will focus on  $\beta$ CD-based amphiphilic star-like copolymers with  $\beta$ CD as core, namely,  $\beta$ CD-cored amphiphilic star-like copolymers.

#### 4.2 $\beta$ CD-cored amphiphilic star-like copolymers

Amphiphilic  $\beta$ CD derivatives are usually “small” molecules because of the relatively short decoration chains, analogue to lipids, and consequently the self-assembled structures usually lack enough stability and functional groups. In the contrary, amphiphilic  $\beta$ CD-based polymers are expected to self-assemble into nanostructures possessing better stability with more functional groups.

According to the position of  $\beta$ CD moieties relative to the polymer chains,  $\beta$ CD-based polymers can be roughly classified into  $\beta$ CD-cored star-like polymers,  $\beta$ CD-pendant comb-like polymers,  $\beta$ CD-capped linear polymers, and  $\beta$ CD-threaded polyrotaxanes (Figure 16) [172].

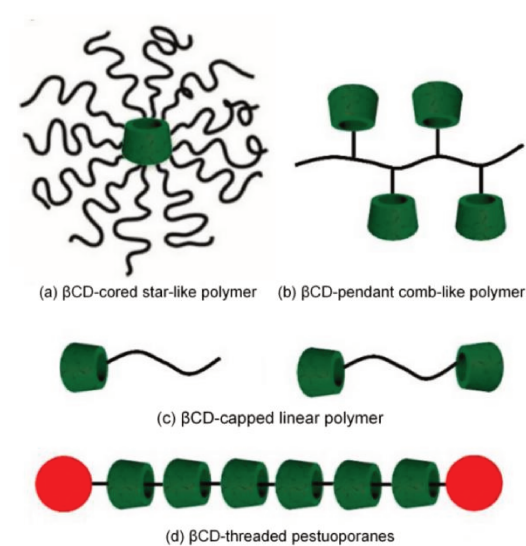


**Figure 16.** Common types of  $\beta$ CD-based polymers, classified according to the position of  $\beta$ CD moieties relative to the polymer chains. Adapted from ref [172].

Herein, only amphiphilic  $\beta$ CD-cored star-like copolymers (Figure 16a) are presented, so as to provide this project a general theoretical background. Thus, in this part, the general synthetic strategies of  $\beta$ CD-cored star-like polymers will be first introduced. Then, the applications of these amphiphilic star-like copolymers for the constructions of artificial nanochannels and self-assembled nanostructures will be discussed.

#### 4.2.1 General synthetic strategies of $\beta$ CD-cored star-like polymers

With  $\beta$ CD as core, star-like polymers can be synthesized by either core-first or grafting-onto strategy.

##### (1) Core-first strategy

In the core-first methodology,  $\beta$ CD is appropriately modified into a macroinitiator for polymerizations. The polymerization strategies widely used are ATRP, RAFT and ROP. As stated, there are three types of hydroxyls in  $\beta$ CD that can be selectively modified, thus, the  $\beta$ CD core can be modified into macroinitiators with 7, 14 and 21 active sites, with some other number of active sites also being reported [194,195]. The active sites can be identical for the initiation of a specific polymerization to produce homoarm star polymers, or be different to orthogonally initiate different types of polymerizations to obtain miktoarm star polymers.

To prepare  $\beta$ CD-cored homoarm star polymers, the hydroxyls of  $\beta$ CD can be used directly, or can be selectively modified for a specific polymerization method. For example,  $\beta$ CD is generally modified via esterification reaction with 2-bromoisobutyryl bromide (BIBB) or chloroacetyl chloride to bear 7 or 21 initiating sites for ATRP, such as per(2,3,6-tri-O-(2-bromo-2-methylpropionyl)- $\beta$ CD ( $\beta$ CD-Br<sub>21</sub>) [196–198]. It is worth noting that in such a crowded environment, side reactions such as star–star coupling usually occur for radical polymerizations [199]. The primary hydroxyls of  $\beta$ CD can easily be modified into azide or alkyne functional groups. The azide- or alkyne- modified  $\beta$ CD moiety is further modified into macromolecular chain transfer agent (macroCTA) via copper-catalyzed azide-alkyne cycloaddition (CuAAC) for the preparation of 7-armed  $\beta$ CD-cored star polymers via RAFT polymerization [200].

ROP is a method more commonly applied. For example, native  $\beta$ CD was directly used to ROP of L-lactide producing 21-armed  $\beta$ CD-cored poly(L-lactide) [201]. The <sup>1</sup>H NMR spectra showed that all the seven primary hydroxyls and all the fourteen secondary hydroxyls were consumed to initiate ROP. SEC results also showed unimodal and symmetric peaks, indicating the absence of linear homopolymers. However, when native  $\beta$ CD was used for ROP of ethylene oxide (EO), the reaction rate was slow with bad control over the molar mass of arms concerning each arm was initiated by the different hydroxylate functions of the glucopyranose unit [202].

In order to get controlled architectures, it seems to be more efficient to selectively protect some of the hydroxyls with inert groups such as methyl, benzyl, acetyl and trimethylsilyl groups, and to initiate ROP with the unprotected hydroxyls. In this way, the arm number of the resultant star-like polymers can be precisely controlled [203,204]. For example, per(2,3-di-O-acetyl)- $\beta$ CD was used for sequential ROP of two cyclic carbonate monomers to prepare 7-armed star-like polycarbonates [205]. This method is very suitable for preparation of 7-armed star polymers based on the fact that the three types of hydroxyls are different in reactivity. Alternatively, defined star polymers bearing 14 or 21 arms are usually prepared by using the  $\beta$ CD-based initiators which are selectively modified to ensure the initiating sites of identical reactivity. For example, per(2,6-di-O-(3-hydropropyl)-3-O-methyl)- $\beta$ CD was synthesized and was verified to have 14 identical initiating sites for ROP of EO [194,202]. The isomer, per(2-O-methyl-3,6-di-O-(3-hydropropyl))- $\beta$ CD, was also used to prepare well-defined star PBO via ROP [54]. Furthermore, the primary hydroxyls of  $\beta$ CD can be converted to amino, iodine or thiol groups as initiating sites of ROP to synthesize  $\beta$ CD-cored 7-armed star polymers [206–208].

To prepare miktoarm star copolymers using the core-first strategy, several protection–deprotection steps are required. For instance, it was reported that the primary hydroxyls could be protected by *tert*-butyldimethylsilyl (TBDMS) groups, and the left fourteen secondary hydroxyls could be used for ROP of  $\epsilon$ -caprolactone ( $\epsilon$ -CL) [209]. The obtained PCL arms were acetylated at the chain ends, and the TBDMS groups were selectively removed to recover the seven primary hydroxyls. The recovered primary hydroxyls were esterified with BIBB, producing an ATRP macroinitiator for the further polymerization of *tert*-butyl acrylate (tBA) monomers. After selective hydrolysis of *tert*-butyl ester groups, the final miktoarm star polymer, PAA<sub>7</sub>- $\beta$ CD-PCL<sub>14</sub>, was obtained.

## (2) Grafting-onto strategy

Grafting-onto strategy is also an effective approach to prepare defined  $\beta$ CD-cored star-like polymers, especially miktoarm star copolymers. Grafting-onto method consists in grafting the pre-synthesized end-functionalized arms onto the complementarily functionalized  $\beta$ CD core via chemical coupling reactions or via non-covalent complexation.

In general, efficient coupling reactions, such as click reactions and condensation reactions, are used to get  $\beta$ CD-cored star polymers [210,211]. As an example, 7-armed and 21-armed  $\beta$ CD-cored star polymers were synthesized by click reaction between alkyne-terminated PNIPAM and azide-functionalized  $\beta$ CDs [211]. In this method (grafting-onto), the arm number has a wide distribution in the finally obtained product due to unreacted sites of  $\beta$ CD-based derivatives, especially when the targeted arm number is large, and the arms are long. In this respect, the specific host–guest

interaction is a good alternative to chemical couplings. For example, a series of miktoarm star copolymers consisting of 21 PLLA arms and one PEG arm was prepared via the complexation between 21-armed  $\beta$ CD-PLLA ( $\beta$ CD-PLLA<sub>21</sub>) and Azo-capped mPEG (Azo-PEG) [201]. Taking advantage of the specific host-guest interaction between  $\beta$ CD and Azo group, the star-like copolymer complex ( $\beta$ CD-PLLA@Azo-PEG) was easily formed via mixing equal molar equivalent of two components in DMF, a good solvent for both polymers.

A combination of core-first and grafting-onto strategies is useful to prepare some complicated structures. For example, a linear trimethylsilyl (TMS)-protected alkyne-functionalized polystyrene (TMS-PS-alkyne) was grafted onto an azide-modified monofunctionalized  $\beta$ CD core ( $\beta$ CD-N<sub>3</sub>) via click reaction [212]. The remaining twenty hydroxyls of the  $\beta$ CD core were esterified by BIBB, generating an ATRP macroinitiator, which was used to polymerize tBA, resulting in a 21-armed miktoarm star polymer, PS<sub>1</sub>- $\beta$ CD-PtBA<sub>20</sub>. After a sequential ATRP of styrene (St) monomers, the miktoarm star copolymer PS<sub>1</sub>- $\beta$ CD-(PtBA-PS)<sub>20</sub> was obtained. Another miktoarm star PS<sub>1</sub>- $\beta$ CD-(PtBA-PEG)<sub>20</sub> was also obtained, via the click reaction between azide-modified PS<sub>1</sub>- $\beta$ CD-(PtBA)<sub>20</sub> and alkyne-terminated PEG.

In short,  $\beta$ CD is a versatile core moiety for construction of a variety of star-like copolymers with the aid of living/controlled polymerization methodologies, like ATRP, RAFT and ROP.

#### **4.2.2. $\beta$ CD-cored amphiphilic star-like polymers acting as artificial nanochannel scaffolds**

As aforementioned, two requirements for effective insertion of synthetic nanochannel scaffolds in lipid bilayer are the amphiphilicity of the scaffold and the dimensional match between the height of the scaffold and the thickness of lipid membrane. Conventional lipid bilayers are *c.a.* 4 nm-thick, that is why  $\beta$ CD is generally modified with short hydrophobic tails to match the thickness of lipid bilayers forming hemichannels or unimolecular channels [194,202].

It has to check, when long decoration chains are connected on  $\beta$ CD, that the long polymer chains do not block the cavity, via inclusion complexation with the hydrophobic cavity, or by collapsing at the entrances of cavities. For example, per(2,6-di-O-(3-hydropropyl)-3-O-methyl)- $\beta$ CD was used for ROP of EO, producing a set of star PEOs ( $\beta$ CD-PEO<sub>14</sub>) with varying DP of PEO arms (DP = 6, 26, and 36) [194]. These polymers were studied regarding to their channel-forming ability in lipid bilayer with the hydrophobic alkyl chains spanning the lipid bilayer. It was found that lasting and stable channels were obtained only when DP of PEO was 6. Thus, it is

more accurate to design amphiphilic  $\beta$ CD-cored copolymers to bear short polymer segments so as to form efficient nanochannels in lipid bilayers.

Recently, amphiphilic star copolymers,  $\beta$ CD-(PBO-PGL)<sub>14</sub>, were synthesized, with the DP of the middle hydrophobic PBO segment being around 6 to 7 to match the thickness of lipid bilayer, and the DP of hydrophilic PGL segment being 6 or 18. The amphiphilic copolymers were characterized in terms of their channel-forming ability by BLM method. However, the results showed mere irregular channels in the membrane together with membrane defects, regardless of the length of PGL segment [54].

#### 4.2.3 Self-assemblies of $\beta$ CD-cored amphiphilic star-like copolymers

$\beta$ CD-cored amphiphilic star-like copolymers can self-assemble into diverse nanostructures in aqueous solution, including micelles and vesicles, with or without stimuli-responsiveness. The morphology of self-assemblies is mainly determined by the hydrophilic-to-hydrophobic ratio and the chemical nature of arm polymers, as stated in Sections 2.1 and 2.2. For example, a library of 7-armed  $\beta$ CD-cored amphiphilic star copolymers was synthesized, with drug molecules (ibuprofen) grafted onto the side chain of the hydrophobic segment, denoted as  $\beta$ CD-P(CL-co-DTC)-D-PEG [213]. These drug-grafted amphiphilic star copolymers self-assembled into various morphologies in water, including spherical micelles, worm-like micelles and vesicles. It was found that the morphology was crucially related with the weight fraction of the hydrophilic PEG segment ( $w_{\text{PEG}}$ ): when  $w_{\text{PEG}}$  was 40.2% and 25.7%, spherical micelles were obtained, when  $w_{\text{PEG}}$  was 23.9% and 20.2%, worm-like micelles were observed, vesicles were formed when  $w_{\text{PEG}}$  was 13.6%, and when  $w_{\text{PEG}}$  further decreased to 11.4%, the copolymers formed precipitates in water. This self-assembly behavior was in agreement with the general rules.

Unusual morphologies have been observed using the aforementioned amphiphilic AB<sub>21</sub> miktoarm star copolymer,  $\beta$ CD-PLLA@Azo-PEG, prepared via host-guest complexation between star  $\beta$ CD-PLLA<sub>21</sub> and linear Azo-PEG [201]. This kind of linear-star supramolecular amphiphilic copolymers could self-assemble into a variety of morphologies, including sphere- and carambola-like micelles, shuttle-like and random curled-up lamellae, closely dependent on the length of each block and the block ratio. More exactly, by changing the length of PLLA chains, the self-assemblies could transfer from micelles to lamellae. Whereas, with fixed PLLA chains, changing PEG length could only lead to the change of morphologies under the same catalogue, either micelles or lamellae, originating from the linear-star topology.

More recently, protein-like multicompartamental nanoparticles (MCNs), possessing separated hydrophilic and hydrophobic subdomains, were obtained via self-assembly

of  $\beta$ CD-cored A(BC)<sub>20</sub> miktoarm star copolymer (PEG-(PAA-PS)<sub>20</sub>) in aqueous solution [214]. In this work, the water-soluble PAA blocks were specially confined in the core of the miktoarm star to favor PS shell to collapse around PAA core when the polymer was suspended in aqueous solution, which was thought critical to form MCNs. Additionally, the hyperbranched topology was also thought as a favorable factor for the construction of multicompartments. The morphology of MCNs was found to be greatly determined by the volume ratio of PS to PAA ( $V_{PS}/V_{PAA}$ ), as expected.

Stimuli-responsive nanoparticles can also be obtained from  $\beta$ CD-cored star-like copolymers with stimuli-responsive moieties integrated into the polymer. Such self-assemblies may undergo morphology transition upon stimuli and then could be used for some special applications. For example, pH-responsive PDEA block was integrated into a 21-armed  $\beta$ CD-cored star triblock copolymers (STBP) ( $\beta$ CD-(PMMA-PDEA-PPEGMA)<sub>21</sub>) [215]. Three STBPs, with fixed length of PMMA block and varied lengths of PDEA and PPEGMA blocks, were synthesized and studied regarding to their pH-sensitivity. It was found that the three STBPs self-assembled into different morphologies and responded differently to pH variation, originating from the different compositions (*i.e.*, PDEA fraction and hydrophilic-to-hydrophobic ratio) (Figure 17): in pure water (neutral pH),  $\beta$ CD-(PMMA<sub>63</sub>-PDEA<sub>15</sub>-PPEGMA<sub>9</sub>)<sub>21</sub> (STBP1) self-assembled into reversed micelles possessing a hydrophilic core, while  $\beta$ CD-(PMMA<sub>63</sub>-PDEA<sub>15</sub>-PPEGMA<sub>14</sub>)<sub>21</sub> (STBP2) self-assembled into vesicles, and  $\beta$ CD-(PMMA<sub>63</sub>-PDEA<sub>20</sub>-PPEGMA<sub>17</sub>)<sub>21</sub> (STBP3) self-assembled into micelles having a hydrophobic core. Of the three self-assemblies, STBP1 assemblies showed the highest sensitivity to pH, which changed from micelles to vesicles when pH increased from 5.0 to 9.0, as a result of the increased hydrophobicity of PDEA block. However, the pH variation had less influences on the morphologies of STBP2 vesicles and STBP3 micelles.

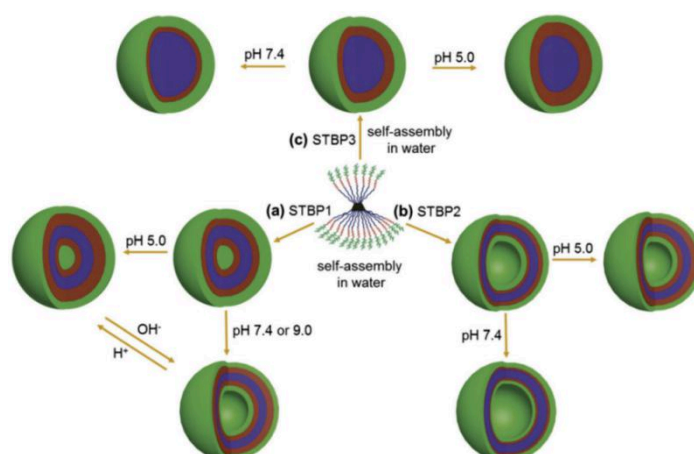


**Figure 17.** pH-responsiveness of star triblock copolymers (STBPs), being respectively  $\beta$ CD-(PMMA<sub>63</sub>-PDEA<sub>15</sub>-PPEGMA<sub>9</sub>)<sub>21</sub> (STBP1),  $\beta$ CD-(PMMA<sub>63</sub>-PDEA<sub>15</sub>-PPEGMA<sub>14</sub>)<sub>21</sub> (STBP2), and  $\beta$ CD-(PMMA<sub>63</sub>-PDEA<sub>20</sub>-PPEGMA<sub>17</sub>)<sub>21</sub> (STBP3) [215].

Thermo-responsive segments, poly(N,N-diethylacrylamide) (PEAAm) and poly(N,N-dimethylacrylamide) (PMAAm), were reported to gather onto one  $\beta$ CD core, via the host-guest interaction between  $\beta$ CD-terminated PEAAm and mid-chain AD-capped PMAAm [216]. The produced 3-armed AB<sub>2</sub>-type miktoarm star copolymer showed two-staged temperature-sensitivity due to the different LCSTs of PEAAm and PMAAm (PEAAm < PMAAm): at a temperature lower than the LCST of PEAAm, both PEAAm and PMAAm were hydrophilic and the copolymers were dissolved in water as unimers. When temperature elevated, hydrophilic PEAAm became hydrophobic, while PMAAm remained hydrophilic, leading to the self-assembly of copolymers into micelles. Further increase of temperature made PMAAm also hydrophobic, resulting in complex micelles. In a later research work, PEAAm and PMAAm were integrated into X- and H-shaped architectures, taking advantage of the host-guest interaction between  $\beta$ CD and AD (Figure 18) [217]. The aforementioned two-staged temperature-sensitivity was also observed with the X- and H-shaped polymers.

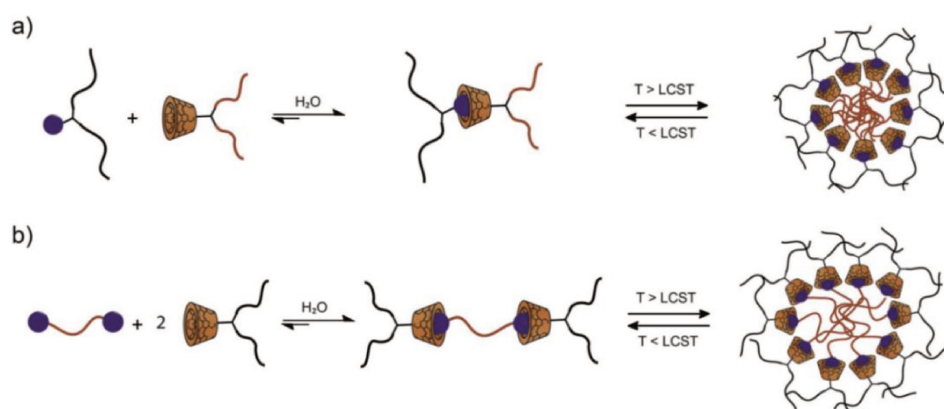


**Figure 18.**  $\beta$ CD-cored miktoarm star copolymers with (A) X- and (B) H-shaped architectures built via  $\beta$ CD-driven supramolecular host-guest interaction. Black chain: PDMA; red chain: PDEA; blue sphere: adamantyl; orange truncated cone:  $\beta$ CD) [217].

Above results showed the versatility of the supramolecular host-guest chemistry to construct polymers with defined architectures of low degree of branching. A more complicated structure of higher branching degree was recently obtained via the host-guest interaction between  $\beta$ CD and Ad, with an integration of thermo-responsive PNIPAM segment [218]. The supramolecular complex had a defined dumbbell-like architecture constructed by the complexation between 7-armed  $\beta$ CD-cored star PEG ( $\beta$ CD-PEG<sub>7</sub>) and  $\alpha,\omega$ -di-Ad-functionalized PNIPAM (Ad-PNIPAM-Ad) (Figure 19). The structure of the supramolecular complexes was interestingly found to be governed by the concentrations of polymers and the temperature of solution. When

the concentrations were rather low and the temperature was below the phase transfer temperature (PTT) of Ad-PNIPAM-Ad, both polymers were soluble in water and apart from each other. When concentrations increased the dumbbell-like structure was obtained. However, these defined dumbbell-like structures would assemble into a cluster having PEG corona and collapsed PNIPAM core, when the temperature was elevated above the PTT of Ad-PNIPAM-Ad. The clustering process also resulted in a release of  $\beta$ CD-PEG<sub>7</sub> into the bulk solution. Interestingly, the temperature-induced dumbbell-cluster transformation was reversible, as evidenced by light scattering, microcalorimetry, and DOSY NMR results.

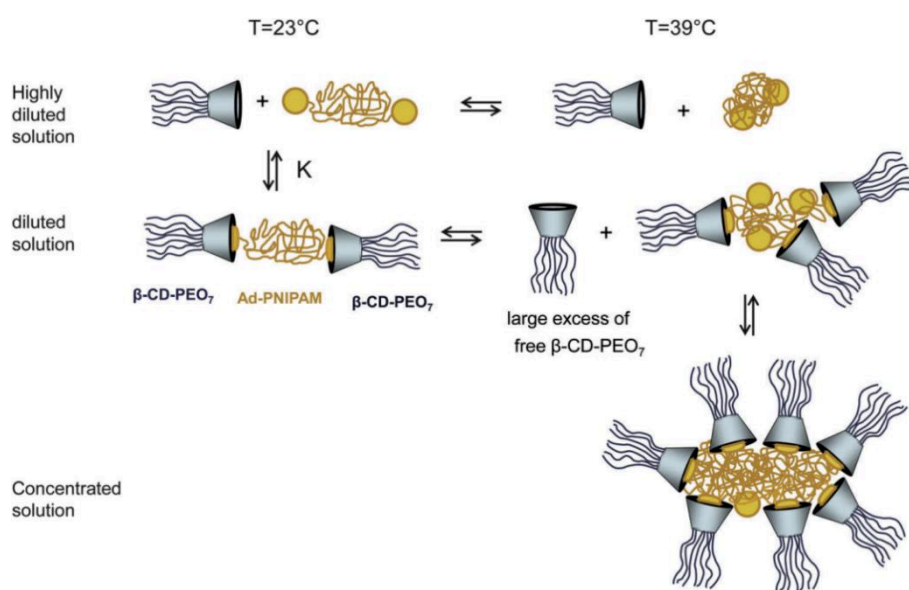


**Figure 19.** Illustration of the assembly of Ad-PNIPAM-Ad and  $\beta$ CD-PEG<sub>7</sub> under different polymer concentrations and temperatures [218].

A dual-responsive system was also achieved by combining pH-responsive PDEA and thermo-responsive PNIPAM onto one  $\beta$ CD core [219]. The produced Janus-type  $\beta$ CD-cored star copolymer PDEA<sub>7</sub>- $\beta$ CD-PNIPAM<sub>14</sub> exhibited dual-responsiveness to both pH and temperature (Figure 20): at pH 4 and 25 °C, both types of segments were hydrophilic and the copolymers were soluble as unimers in water. When pH increased to pH 10, the copolymers self-assembled into vesicles having a PDEA membrane, due to the hydrophilic-to-hydrophobic transfer of PDEA blocks. Similarly, when temperature increased to 45 °C, above the LCST of PNIPAM, the copolymers also self-assembled into vesicles induced by the hydrophilic-to-hydrophobic transfer of PNIPAM, but in this case, the vesicles had a PNIPAM membrane and a PDEA corona. These results showed that the corona and the membrane of the vesicles could be reversibly switched, by adjusting the pH of solution and temperature.

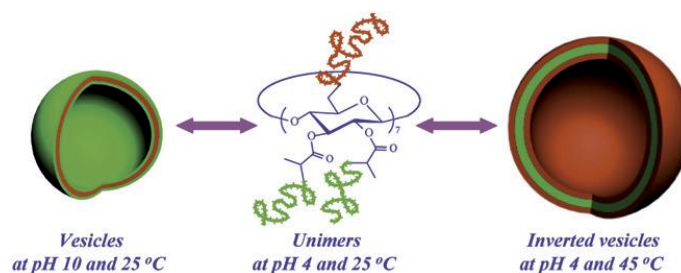


**Figure 20.** A dual-responsive Janus-type  $\beta$ CD-cored star copolymer PDEA<sub>7</sub>- $\beta$ CD-PNIPAM<sub>14</sub> which could reversibly self-assemble into two types of vesicles with “inverted” nanostructures in aqueous solution depending on the pH of solution and temperature [219].

One can see that  $\beta$ CD-cored star-like amphiphilic copolymers can self-assemble into diverse morphologies by tuning the molecular topology, the chemical nature of arm polymers, and the hydrophilic-to-hydrophobic ratio. Defined spherical micelles and vesicles are the most reported nanostructures for a wide range of applications, such as drug delivery systems.

When applied for drug delivery,  $\beta$ CD-based polymer platforms exhibit several merits. One of the advantages is the enhanced drug loading efficiency, because the drugs can be incorporated into polymer by chemically grafting onto polymer [213], and via host-guest complexation with  $\beta$ CD cavities, besides being physically encapsulated into the nanoparticles [220]. It was reported that DOX·HCl was loaded into the polymersomes made of 3-armed  $\beta$ CD-cored mPEG-PLA copolymers ( $\beta$ CD-(mPEG-PLA)<sub>3</sub>) with rather high encapsulation efficiency [220]. Compared with mPEG-PLA polymersomes (without  $\beta$ CD moieties), the increased loading efficiency was found due to the fact that DOX·HCl was loaded in both the  $\beta$ CD cavities sited in membrane and the aqueous interior of polymersomes.

Additionally, the hyperbranched structure of  $\beta$ CD-cored star-like copolymers provides plenty of modifiable sites for efficient integration of stimuli-responsiveness, which can increase the controllability over the release of therapeutic agents. For instance, 21-armed  $\beta$ CD-cored star polymers, with pH-sensitive PDPA-POEGMA arms ( $\beta$ CD-(PDPA-POEGMA)<sub>21</sub>) and fluorescent dye cyanine 5 (Cy5), were prepared for Cy5-labelling and pH-triggered release of DOX [221]: at pH 7.4, the PDPA blocks were hydrophobic, enabling the loading of hydrophobic drugs (DOX). While in an acidic condition, PDPA blocks underwent hydrophobic-to-hydrophilic transition, inducing the rapid release of drugs. Furthermore, the incorporation of the near-infrared fluorescent Cy5 imparted the pH-triggered drug release system with diagnostic functions.

*In short*,  $\beta$ CD is a versatile core for preparation of diverse  $\beta$ CD-cored star-like copolymers via core-first and grafting-onto strategies. Amphiphilic  $\beta$ CD-cored star-like copolymers can self-assemble into various morphologies, governed by many factors, including the hydrophilic-to-hydrophobic ratio and the chemical nature of arm polymers. Micelle is the most reported nanostructure for application as drug delivery system, showing some advantages like the higher drug loading capacity benefiting from the host–guest complexation of  $\beta$ CD with drugs and the hyperbranched structure. Polymersome is less reported so far, but it can be foreseen that  $\beta$ CD-based polymersomes have a huge potential in a wider range of applications by the combination of vesicular structure and  $\beta$ CD.

## 5. Conclusion and Objectives

In this chapter, literature reviews on the self-assembly of amphiphilic copolymers, polymersome nanoreactors, and  $\beta$ CD-based amphiphilic systems were performed.

By overviewing the self-assembly behaviours of non-ionic amphiphilic copolymers in aqueous solution, it can be concluded that self-assembly process is controlled by the interactions between different segments and the interactions between each segment and solvent. Therefore, the resultant morphology is affected by many factors, including the hydrophilic-to-hydrophobic ratio, the chemical nature and the architecture of copolymer. Considering the effect of polymer topology, the self-assembly of star-like amphiphilic copolymers was studied. It was found that the topology effect is observed more as the changes in particle size and the enhanced particle stability than the variation of morphology, compared to the linear analogues of the same compositions.

Among the diverse self-assembled nanostructures, polymersome is the most intriguing one for its numerous reported and potent applications. Construction of polymersome nanoreactors by incorporating functional enzymes with the vesicular compartments is one of the most attractive research topics, full of opportunities and challenges. One of the challenges is to construct a versatile platform for diverse functional nanoreactors. To achieve this goal, polymersome membrane is required to be permeable enough to the substrates and products of enzymatic reactions, but to be able to retain the enzymes inside at the same time. The reported intrinsically permeable polymersomes are limited to date. Therefore, different permeabilization strategies have been suggested, such as permeabilization by stimuli-triggering. Insertion of bio-originated membrane proteins was also proposed, as a straightforward method. However, it is found that the membrane proteins are naturally thought for lipid bilayers, and encounter both physical and chemical mismatches when being inserted in polymeric membranes. In contrast to the natural nanochannels, the synthetic nanochannels are

more suitable to be integrated into polymeric membranes to construct biomimetic systems.

$\beta$ CD-based amphiphiles exhibit versatility in the constructions of both artificial nanochannels and polymeric vesicles. On one hand, amphiphilic  $\beta$ CD derivatives of low molar masses have been successfully inserted in lipid bilayers, forming nanochannels. On the other hand,  $\beta$ CD is a versatile core for the preparation of diverse  $\beta$ CD-cored star-like copolymers. Amphiphilic  $\beta$ CD-cored star-like copolymers can self-assemble into various morphologies, including micelles and vesicles. Micelle is the most reported nanostructure for the application as drug delivery system. Polymersome is less reported so far but is foreseen to have enormous potential in a wider range of applications by the combination of vesicular structure and  $\beta$ CD.

Based on the literature analyses, a fully synthetic system consisting in  $\beta$ CD-based artificial nanochannels inserting in polymersome membrane seems of great interest, from the points of view of both academic investigations and practical applications. Therefore, in this project, the components, namely polymersomes and  $\beta$ CD-based artificial nanochannel scaffolds, will be first prepared and characterized. Subsequently, these two components will be integrated into the targeted  $\beta$ CD-based artificial nanochannels-equipped polymersomes, as graphically shown in Figure 21.

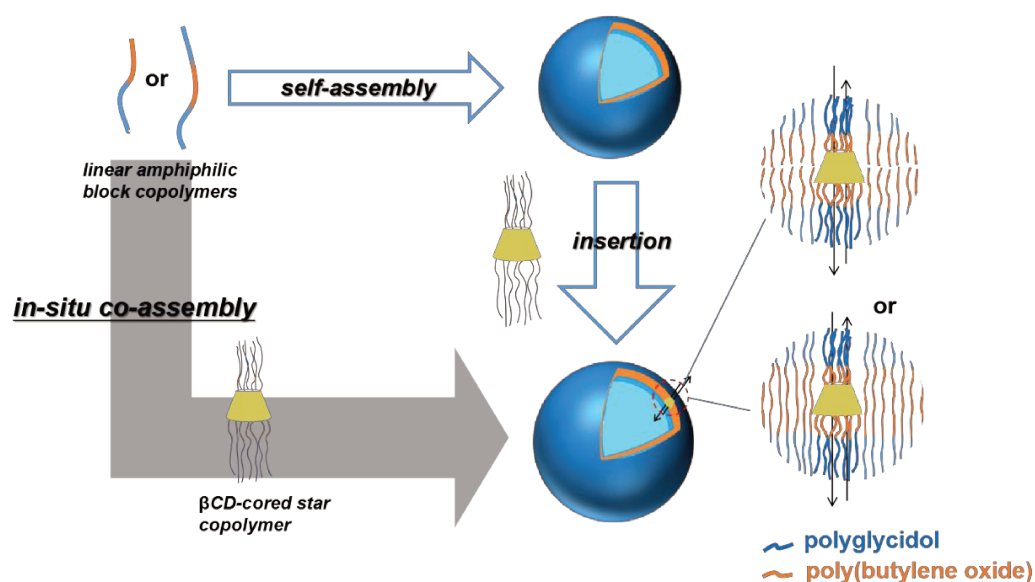


**Figure 21.** Illustration of the aim of my project: to construct a versatile platform with  $\beta$ CD-based artificial nanochannels being inserted in polymersome membrane.

## 6. References

1. Doncom K E B, Blackman L D, Wright D B, et al. Dispersity effects in polymer self-assemblies: a matter of hierarchical control[J]. *Chemical Society Reviews*, 2017, 46(14): 4119-4134.
2. Israelachvili J N. Theoretical considerations on the asymmetric distribution of charged phospholipid molecules on the inner and outer layers of curved bilayer membranes[J]. *Biochimica et Biophysica Acta (BBA)-Biomembranes*, 1973, 323(4): 659-663.
3. Tritschler U, Pearce S, Gwyther J, et al. 50th anniversary perspective: Functional nanoparticles from the solution self-assembly of block copolymers[J]. *Macromolecules*, 2017, 50(9): 3439-3463.
4. Hayward R C, Pochan D J. Tailored assemblies of block copolymers in solution: it is all about the process[J]. *Macromolecules*, 2010, 43(8): 3577-3584.
5. Discher D E, Ahmed F. Polymersomes[J]. *Annu. Rev. Biomed. Eng.*, 2006, 8: 323-341.
6. Smart T, Lomas H, Massignani M, et al. Block copolymer nanostructures[J]. *Nano Today*, 2008, 3(3-4): 38-46.
7. Chen S, Cheng S X, Zhuo R X. Self-assembly strategy for the preparation of polymer-based nanoparticles for drug and gene delivery[J]. *Macromolecular bioscience*, 2011, 11(5): 576-589.
8. Lombardo D, Kiselev M A, Magazù S, et al. Amphiphiles self-assembly: basic concepts and future perspectives of supramolecular approaches[J]. *Advances in Condensed Matter Physics*, 2015, 2015.
9. Brendel J C, Schacher F H. Block Copolymer Self-Assembly in Solution—Quo Vadis?[J]. *Chemistry—An Asian Journal*, 2018, 13(3): 230-239.
10. Karayianni M, Pispas S. Block copolymer solution self-assembly: Recent advances, emerging trends, and applications[J]. *Journal of Polymer Science*, 2021, 59(17): 1874-1898.
11. Wu D, Huang Y, Xu F, et al. Recent advances in the solution self-assembly of amphiphilic “rod-coil” copolymers[J]. *Journal of Polymer Science Part A: Polymer Chemistry*, 2017, 55(9): 1459-1477.
12. Xu F, Zhang J, Zhang P, et al. “Rod-coil” copolymers get self-assembled in solution[J]. *Materials Chemistry Frontiers*, 2019, 3(11): 2283-2307.
13. Qin S, Li H, Yuan W, et al. Hierarchical self-assembly of fluorine-containing diblock copolymer: from onion-like nanospheres to superstructured microspheres[J]. *Polymer*, 2011, 52(4): 1191-1196.
14. Feng H, Lu X, Wang W, et al. Block copolymers: Synthesis, self-assembly, and applications[J]. *Polymers*, 2017, 9(10): 494.
15. Satoh Y, Matsuno H, Yamamoto T, et al. Synthesis of well-defined three- and four-armed cage-shaped polymers via “topological conversion” from trefoil- and quatrefoil-shaped polymers[J]. *Macromolecules*, 2017, 50(1): 97-106.
16. Zhang B, Zhang H, Li Y, et al. Exploring the effect of amphiphilic polymer architecture: synthesis, characterization, and self-assembly of both cyclic and linear poly(ethylene glycol)-*b*-polycaprolactone[J]. *ACS Macro Letters*, 2013, 2(10): 845-848.
17. Honda S, Yamamoto T, Tezuka Y. Topology-directed control on thermal stability: micelles formed from linear and cyclized amphiphilic block copolymers[J]. *Journal of the American Chemical Society*, 2010, 132(30): 10251-10253.

18. Gou P F, Zhu W P, Zhu N, et al. Synthesis and characterization of novel resorcinarene-centered amphiphilic star-block copolymers consisting of eight ABA triblock arms by combination of ROP, ATRP, and click chemistry[J]. *Journal of Polymer Science Part A: Polymer Chemistry*, 2009, 47(11): 2905-2916.
19. Li C, Dong Q, Li W. Largely Tunable Asymmetry of Phase Diagrams of A (AB) *n* Miktoarm Star Copolymer[J]. *Macromolecules*, 2020, 53(24): 10907-10917.
20. Yang J, Wang R, Xie D. Aqueous self-assembly of amphiphilic cyclic brush block copolymers as asymmetry-tunable building blocks[J]. *Macromolecules*, 2019, 52(18): 7042-7051.
21. Wessels M G, Jayaraman A. Molecular dynamics simulation study of linear, bottlebrush, and star-like amphiphilic block polymer assembly in solution[J]. *Soft Matter*, 2019, 15(19): 3987-3998.
22. Battaglia G, Ryan A J. Effect of amphiphile size on the transformation from a lyotropic gel to a vesicular dispersion[J]. *Macromolecules*, 2006, 39(2): 798-805.
23. Lee J C M, Bermudez H, Discher B M, et al. Preparation, stability, and in vitro performance of vesicles made with diblock copolymers[J]. *Biotechnology and bioengineering*, 2001, 73(2): 135-145.
24. Arifin D R, Palmer A F. Polymersome encapsulated hemoglobin: a novel type of oxygen carrier[J]. *Biomacromolecules*, 2005, 6(4): 2172-2181.
25. Yildiz M E, Prud'homme R K, Robb I, et al. Formation and characterization of polymersomes made by a solvent injection method[J]. *Polymers for Advanced Technologies*, 2007, 18(6): 427-432.
26. Wehr R, Gaitzsch J, Daubian D, et al. Deepening the insight into poly (butylene oxide)-block-poly (glycidol) synthesis and self-assemblies: micelles, worms and vesicles[J]. *RSC advances*, 2020, 10(38): 22701-22711.
27. Kelly J M, Gross A L, Martin D R, et al. Polyethylene glycol-b-poly(lactic acid) polymersomes as vehicles for enzyme replacement therapy[J]. *Nanomedicine*, 2017, 12(23): 2591-2606.
28. Ghellab S E, Mu W, Li Q, et al. Prediction of the size of electroformed giant unilamellar vesicle using response surface methodology[J]. *Biophysical chemistry*, 2019, 253: 106217.
29. Shum H C, Kim J W, Weitz D A. Microfluidic fabrication of monodisperse biocompatible and biodegradable polymersomes with controlled permeability[J]. *Journal of the American Chemical Society*, 2008, 130(29): 9543-9549.
30. Jahn A, Vreeland W N, Gaitan M, et al. Controlled vesicle self-assembly in microfluidic channels with hydrodynamic focusing[J]. *Journal of the American Chemical Society*, 2004, 126(9): 2674-2675.
31. Huo M, Xu Z, Zeng M, et al. Controlling vesicular size via topological engineering of amphiphilic polymer in polymerization-induced self-assembly[J]. *Macromolecules*, 2017, 50(24): 9750-9759.
32. Shi P, Qu Y, Liu C, et al. Redox-responsive multicompartiment vesicles of ferrocene-containing triblock terpolymer exhibiting on-off switchable pores[J]. *ACS Macro Letters*, 2016, 5(1): 88-93.
33. Chen X, Liu L, Huo M, et al. Direct synthesis of polymer nanotubes by aqueous dispersion polymerization of a cyclodextrin/styrene complex[J]. *Angewandte Chemie*

- International Edition, 2017, 56(52): 16541-16545.
34. Razavi B, Abdollahi A, Roghani-Mamaqani H, et al. Light-, temperature-, and pH-responsive micellar assemblies of spiropyran-initiated amphiphilic block copolymers: Kinetics of photochromism, responsiveness, and smart drug delivery[J]. *Materials Science and Engineering: C*, 2020, 109: 110524.
  35. C. Ji, Y. Deng, H. Yuan, W. Yuan, Y. Song, Z. Li, *Macromol. Mater. Eng.* 2021, 306, 2100073 (not found)
  36. Kanto R, Yonenuma R, Yamamoto M, et al. Mixed Polyplex Micelles with Thermoresponsive and Lysine-Based Zwitterionic Shells Derived from Two Poly (vinyl amine)-Based Block Copolymers[J]. *Langmuir*, 2021, 37(10): 3001-3014.
  37. Feng G, Chen H, Li J, et al. Gene therapy for nucleus pulposus regeneration by heme oxygenase-1 plasmid DNA carried by mixed polyplex micelles with thermo-responsive heterogeneous coronas[J]. *Biomaterials*, 2015, 52: 1-13.
  38. Tezuka Y. Topological polymer chemistry by electrostatic self - assembly[J]. *Journal of Polymer Science Part A: Polymer Chemistry*, 2003, 41(19): 2905-2917.
  39. Ge Z, Liu S. Supramolecular self-assembly of nonlinear amphiphilic and double hydrophilic block copolymers in aqueous solutions[J]. *Macromolecular rapid communications*, 2009, 30(18): 1523-1532.
  40. Yamamoto T, Tezuka Y. Cyclic polymers revealing topology effects upon self-assemblies, dynamics and responses[J]. *Soft Matter*, 2015, 11(38): 7458-7468.
  41. Isono T. Synthesis of functional and architectural polyethers via the anionic ring-opening polymerization of epoxide monomers using a phosphazene base catalyst[J]. *Polymer Journal*, 2021, 53(7): 753-764.
  42. Iatrou H, Avgeropoulos A, Sakellariou G, et al. Miktoarm Star ( $\mu$ -Star) Polymers: A Successful Story[J]. 2017.
  43. Khanna K, Varshney S, Kakkar A. Miktoarm star polymers: advances in synthesis, self-assembly, and applications[J]. *Polymer Chemistry*, 2010, 1(8): 1171-1185.
  44. Nieto-Orellana A, Di Antonio M, Conte C, et al. Effect of polymer topology on non-covalent polymer-protein complexation: Miktoarm versus linear mPEG-poly (glutamic acid) copolymers[J]. *Polymer Chemistry*, 2017, 8(14): 2210-2220.
  45. Christodoulou E, Klonos P, Tsachouridis K, et al. Amphiphilic Poly ( $\epsilon$ -caprolactone) Copolyesters of Different Architectures for Drug Delivery Applications: Synthesis, Characterization and Molecular Dynamics[J]. 2020.
  46. Zhao Y. Facile synthesis and topological transformation of multicomponent miktoarm star copolymers[J]. *Macromolecular rapid communications*, 2019, 40(6): 1800571.
  47. Yong H W, Kakkar A. Nanoengineering Branched Star Polymer-Based Formulations: Scope, Strategies, and Advances[J]. *Macromolecular Bioscience*, 2021: 2100105.
  48. Tran N Q, Hoang T K D, Nguyen C K. Synthesis of star-shaped poly (methyl acrylate) via ATRP and preliminary evaluation of its reinforcing properties for PVC[J]. *Journal of Polymer Research*, 2012, 19(2): 1-6.
  49. Chen Q, Xu Y, Cao X, et al. Core cross-linked star (CCS) polymers with temperature and salt dual responsiveness: synthesis, formation of high internal phase emulsions (HIPEs) and triggered demulsification[J]. *Polymer Chemistry*, 2014, 5(1): 175-185.
  50. Sun P, Chen D, Deng H, et al. "Bottom-up" construction of multi-polyprodrug-arm

hyperbranched amphiphiles for cancer therapy[J]. *Bioconjugate chemistry*, 2017, 28(5): 1470-1480.

51. Mori H, Ishikawa K, Abiko Y, et al. Water-soluble poly (N-vinyl-1,2,4-triazole) star and amphiphilic star block copolymers by RAFT polymerization[J]. *Polymer*, 2013, 54(8): 2001-2010.

52. Ren J M, Fu Q, Blencowe A, et al. Organic catalyst-mediated ring-opening polymerization for the highly efficient synthesis of polyester-based star polymers[J]. *ACS Macro Letters*, 2012, 1(6): 681-686.

53. Shaver M P, Cameron D J A. Tacticity control in the synthesis of poly (lactic acid) polymer stars with dipentaerythritol cores[J]. *Biomacromolecules*, 2010, 11(12): 3673-3679.

54. Faye I, Huin C, Illy N, et al.  $\beta$ -Cyclodextrin-Based Star Amphiphilic Copolymers: Synthesis, Characterization, and Evaluation as Artificial Channels[J]. *Macromolecular Chemistry and Physics*, 2019, 220(2): 1800308.

55. Soliman G M, Sharma R, Choi A O, et al. Tailoring the efficacy of nimodipine drug delivery using nanocarriers based on A2B miktoarm star polymers[J]. *Biomaterials*, 2010, 31(32): 8382-8392.

56. Shang Y, Guo L, Wang Z. Tetraphenylsilane-Cored Star-Shaped Amphiphilic Block Copolymers for pH-Responsive Anticancer Drug Delivery[J]. *Macromolecular Chemistry and Physics*, 2019, 220(19): 1900248.

57. Alhoranta A M, Lehtinen J K, Urtti A O, et al. Cationic amphiphilic star and linear block copolymers: synthesis, self-assembly, and in vitro gene transfection[J]. *Biomacromolecules*, 2011, 12(9): 3213-3222.

58. Kikuchi S, Chen Y, Fuchise K, et al. Thermoresponsive properties of 3-, 4-, 6-, and 12-armed star-shaped poly [2-(dimethylamino) ethyl methacrylate]s prepared by core-first group transfer polymerization[J]. *Polymer Chemistry*, 2014, 5(16): 4701-4709.

59. Hwang J, Foster M D, Quirk R P. Synthesis of 4-, 8-, 12-arm star-branched polybutadienes with three different chain-end functionalities using a functionalized initiator[J]. *Polymer*, 2004, 45(3): 873-880.

60. Baek K Y, Kamigaito M, Sawamoto M. Star-shaped polymers by metal-catalyzed living radical polymerization. 1. Design of Ru (II)-based systems and divinyl linking agents[J]. *Macromolecules*, 2001, 34(2): 215-221.

61. Gao H, Matyjaszewski K. Synthesis of functional polymers with controlled architecture by CRP of monomers in the presence of cross-linkers: From stars to gels[J]. *Progress in Polymer Science*, 2009, 34(4): 317-350.

62. Gao H, Matyjaszewski K. Modular Approaches to Star and Miktoarm Star Polymers by ATRP of Cross-Linkers[C]//*Macromolecular symposia*. Weinheim: WILEY - VCH Verlag, 2010, 291(1): 12-16.

63. Nabid M R, Bide Y. H40-PCL-PEG unimolecular micelles both as anchoring sites for palladium nanoparticles and micellar catalyst for Heck reaction in water[J]. *Applied Catalysis A: General*, 2014, 469: 183-190.

64. Mai Y, Eisenberg A. Self-assembly of block copolymers[J]. *Chemical Society Reviews*, 2012, 41(18): 5969-5985.

65. Ree B J, Satoh Y, Jin K S, et al. Well-defined and stable nanomicelles self-assembled from brush cyclic and tadpole copolymer amphiphiles: a versatile smart carrier platform[J].

- NPG Asia Materials, 2017, 9(12): e453-e453.
66. Štěpánek M, Uchman M, Procházka K. Self-assemblies formed by four-arm star copolymers with amphiphilic diblock arms in aqueous solutions[J]. *Polymer*, 2009, 50(15): 3638-3644.
  67. Wu W, Wang W, Li J. Star polymers: Advances in biomedical applications[J]. *Progress in Polymer Science*, 2015, 46: 55-85.
  68. Iqbal S, Blenner M, Alexander-Bryant A, et al. Polymersomes for therapeutic delivery of protein and nucleic acid macromolecules: from design to therapeutic applications[J]. *Biomacromolecules*, 2020, 21(4): 1327-1350.
  69. Jin X, Sun P, Tong G, et al. Star polymer-based unimolecular micelles and their application in bio-imaging and diagnosis[J]. *Biomaterials*, 2018, 178: 738-750.
  70. Gu D, Ladewig K, Klimak M, et al. Amphiphilic core cross-linked star polymers as water-soluble, biocompatible and biodegradable unimolecular carriers for hydrophobic drugs[J]. *Polymer Chemistry*, 2015, 6(36): 6475-6487.
  71. Chen G, Wang L, Cordie T, et al. Multi-functional self-fluorescent unimolecular micelles for tumor-targeted drug delivery and bioimaging[J]. *Biomaterials*, 2015, 47: 41-50.
  72. Zhang P, Zhang Z, Jiang X, et al. Unimolecular micelles from POSS-based star-shaped block copolymers for photodynamic therapy[J]. *Polymer*, 2017, 118: 268-279.
  73. Qiu F, Wang D, Zhu Q, et al. Real-time monitoring of anticancer drug release with highly fluorescent star-conjugated copolymer as a drug carrier[J]. *Biomacromolecules*, 2014, 15(4): 1355-1364.
  74. Wang M, Zhang X, Peng H, et al. Optimization of amphiphilic miktoarm star copolymers for anticancer drug delivery[J]. *ACS Biomaterials Science & Engineering*, 2018, 4(8): 2903-2910.
  75. Lombardo D, Calandra P, Pasqua L, et al. Self-assembly of organic nanomaterials and biomaterials: The bottom-up approach for functional nanostructures formation and advanced applications[J]. *Materials*, 2020, 13(5): 1048.
  76. Yin H, Kang H C, Huh K M, et al. Biocompatible, pH-sensitive AB<sub>2</sub> miktoarm polymer-based polymersomes: preparation, characterization, and acidic pH-activated nanostructural transformation[J]. *Journal of materials chemistry*, 2012, 22(36): 19168-19178.
  77. Yang C, Liu S Q, Venkataraman S, et al. Structure-directing star-shaped block copolymers: supramolecular vesicles for the delivery of anticancer drugs[J]. *Journal of Controlled Release*, 2015, 208: 93-105.
  78. Liu H, Zhang J, Dai W, et al. Synthesis and self-assembly of a dual-responsive monocleavable ABCD star quaterpolymer[J]. *Polymer Chemistry*, 2017, 8(44): 6865-6878.
  79. Li Z, Kesselman E, Talmon Y, et al. Multicompartment micelles from ABC miktoarm stars in water[J]. *Science*, 2004, 306(5693): 98-101.
  80. Liu J, Ding Y, Liu X, et al. Self-assembly of tunable ABC miktoarm terpolymers with semi-fluorinated segment for the discovery of a rich diversity of multicompartment micelles[J]. *European Polymer Journal*, 2019, 118: 465-473.
  81. Zhu Y, Yang B, Chen S, et al. Polymer vesicles: Mechanism, preparation, application, and responsive behavior[J]. *Progress in Polymer Science*, 2017, 64: 1-22.
  82. Zartner L, Muthwill M S, Dinu I A, et al. The rise of bio-inspired polymer compartments responding to pathology-related signals[J]. *Journal of Materials Chemistry B*, 2020, 8(29):

6252-6270.

83. Mu X, Gan S, Wang Y, et al. Stimulus-responsive vesicular polymer nano-integrators for drug and gene delivery[J]. *International journal of nanomedicine*, 2019, 14: 5415.
84. Che H, van Hest J C M. Adaptive polymersome nanoreactors[J]. *ChemNanoMat*, 2019, 5(9): 1092-1109.
85. Buddingh' B C, van Hest J C M. Artificial cells: synthetic compartments with life-like functionality and adaptivity[J]. *Accounts of chemical research*, 2017, 50(4): 769-777.
86. Vance J A, Devaraj N K. Membrane Mimetic Chemistry in Artificial Cells[J]. *Journal of the American Chemical Society*, 2021.
87. Du J, O'Reilly R K. Advances and challenges in smart and functional polymer vesicles[J]. *Soft Matter*, 2009, 5(19): 3544-3561.
88. Balasubramanian V, Onaca O, Ezhevskaya M, et al. A surprising system: polymeric nanoreactors containing a mimic with dual-enzyme activity[J]. *Soft Matter*, 2011, 7(12): 5595-5603.
89. Meeuwissen S A, Rioz-Martínez A, de Gonzalo G, et al. Cofactor regeneration in polymersome nanoreactors: enzymatically catalysed Baeyer–Villiger reactions[J]. *Journal of Materials Chemistry*, 2011, 21(47): 18923-18926.
90. Vriezema D M, Garcia P M L, Sancho Oltra N, et al. Positional assembly of enzymes in polymersome nanoreactors for cascade reactions[J]. *Angewandte chemie*, 2007, 119(39): 7522-7526.
91. Wang L, Chierico L, Little D, et al. Encapsulation of biomacromolecules within polymersomes by electroporation[J]. *Angewandte Chemie International Edition*, 2012, 51(44): 11122-11125.
92. Neumann E, Schaefer - Ridder M, Wang Y, et al. Gene transfer into mouse lyoma cells by electroporation in high electric fields[J]. *The EMBO journal*, 1982, 1(7): 841-845.
93. Aranda-Espinoza H, Bermudez H, Bates F S, et al. Electromechanical limits of polymersomes[J]. *Physical review letters*, 2001, 87(20): 208301.
94. Martino C, deMello A J. Droplet-based microfluidics for artificial cell generation: a brief review[J]. *Interface focus*, 2016, 6(4): 20160011.
95. Wehr R, dos Santos E C, Muthwill M S, et al. Fully amorphous atactic and isotactic block copolymers and their self-assembly into nano- and microscopic vesicles[J]. *Polymer Chemistry*, 2021.
96. Brown L, McArthur S L, Wright P C, et al. Polymersome production on a microfluidic platform using pH sensitive block copolymers[J]. *Lab on a Chip*, 2010, 10(15): 1922-1928.
97. Perro A, Nicolet C, Angly J, et al. Mastering a double emulsion in a simple co-flow microfluidic to generate complex polymersomes[J]. *Langmuir*, 2011, 27(14): 9034-9042.
98. Tan J, Bai Y, Zhang X, et al. Room temperature synthesis of poly (poly (ethylene glycol) methyl ether methacrylate)-based diblock copolymer nano-objects via Photoinitiated Polymerization-Induced Self-Assembly (Photo-PISA)[J]. *Polymer Chemistry*, 2016, 7(13): 2372-2380.
99. Blackman L D, Varlas S, Arno M C, et al. Permeable protein-loaded polymersome cascade nanoreactors by polymerization-induced self-assembly[J]. *ACS macro letters*, 2017, 6(11): 1263-1267.
100. Ma C, Liu X, Wu G, et al. Efficient way to generate protein-based nanoparticles by in-

- situ photoinitiated polymerization-induced self-assembly[J]. *ACS Macro Letters*, 2017, 6(7): 689-694.
101. Napoli A, Boerakker M J, Tirelli N, et al. Glucose-oxidase based self-destructing polymeric vesicles[J]. *Langmuir*, 2004, 20(9): 3487-3491.
102. Ranquin A, Versées W, Meier W, et al. Therapeutic nanoreactors: combining chemistry and biology in a novel triblock copolymer drug delivery system[J]. *Nano letters*, 2005, 5(11): 2220-2224.
103. Broz P, Driamov S, Ziegler J, et al. Toward intelligent nanosize bioreactors: a pH-switchable, channel-equipped, functional polymer nanocontainer[J]. *Nano letters*, 2006, 6(10): 2349-2353.
104. Axthelm F, Casse O, Koppenol W H, et al. Antioxidant nanoreactor based on superoxide dismutase encapsulated in superoxide-permeable vesicles[J]. *The Journal of Physical Chemistry B*, 2008, 112(28): 8211-8217.
105. Chen Q, Schönherr H, Vancso G J. Block-Copolymer Vesicles as Nanoreactors for Enzymatic Reactions[J]. *Small*, 2009, 5(12): 1436-1445.
106. Van Dongen S F M, Nallani M, Cornelissen J J L M, et al. A three-enzyme cascade reaction through positional assembly of enzymes in a polymersome nanoreactor[J]. 2009.
107. Dobrunz D, Toma A C, Tanner P, et al. Polymer nanoreactors with dual functionality: simultaneous detoxification of peroxynitrite and oxygen transport[J]. *Langmuir*, 2012, 28(45): 15889-15899.
108. Tanner P, Balasubramanian V, Palivan C G. Aiding nature's organelles: artificial peroxisomes play their role[J]. *Nano letters*, 2013, 13(6): 2875-2883.
109. Louzao I, van Hest J C M. Permeability effects on the efficiency of antioxidant nanoreactors[J]. *Biomacromolecules*, 2013, 14(7): 2364-2372.
110. Peters R J R W, Marguet M, Marais S, et al. Cascade reactions in multicompartmentalized polymersomes[J]. *Angewandte chemie*, 2014, 126(1): 150-154.
111. Spulber M, Baumann P, Saxer S S, et al. Poly (N-vinylpyrrolidone)-poly (dimethylsiloxane)-based polymersome nanoreactors for laccase-catalyzed biotransformations[J]. *Biomacromolecules*, 2014, 15(4): 1469-1475.
112. Gräfe D, Gaitzsch J, Appelhans D, et al. Cross-linked polymersomes as nanoreactors for controlled and stabilized single and cascade enzymatic reactions[J]. *Nanoscale*, 2014, 6(18): 10752-10761.
113. Siti W, de Hoog H P M, Fischer O, et al. An intercompartmental enzymatic cascade reaction in channel-equipped polymersome-in-polymersome architectures[J]. *Journal of Materials Chemistry B*, 2014, 2(18): 2733-2737.
114. Chen H, Tian J, He W, et al. H<sub>2</sub>O<sub>2</sub>-activatable and O<sub>2</sub>-evolving nanoparticles for highly efficient and selective photodynamic therapy against hypoxic tumor cells[J]. *Journal of the American Chemical Society*, 2015, 137(4): 1539-1547.
115. Einfalt T, Goers R, Dinu I A, et al. Stimuli-triggered activity of nanoreactors by biomimetic engineering polymer membranes[J]. *Nano letters*, 2015, 15(11): 7596-7603.
116. Nishimura T, Sasaki Y, Akiyoshi K. Biotransporting self-assembled nanofactories using polymer vesicles with molecular permeability for enzyme prodrug cancer therapy[J]. *Advanced Materials*, 2017, 29(36): 1702406.
117. Klermund L, Poschenrieder S T, Castiglione K. Biocatalysis in polymersomes:

improving multienzyme cascades with incompatible reaction steps by compartmentalization[J]. *ACS Catalysis*, 2017, 7(6): 3900-3904.

118. Li J, Li Y, Wang Y, et al. Polymer prodrug-based nanoreactors activated by tumor acidity for orchestrated oxidation/chemotherapy[J]. *Nano letters*, 2017, 17(11): 6983-6990.

119. Baumann P, Spulber M, Fischer O, et al. Investigation of Horseradish Peroxidase Kinetics in an “Organelle-Like” Environment[J]. *Small*, 2017, 13(17): 1603943.

120. Blackman L D, Varlas S, Arno M C, et al. Permeable protein-loaded polymersome cascade nanoreactors by polymerization-induced self-assembly[J]. *ACS macro letters*, 2017, 6(11): 1263-1267.

121. Edlinger C, Einfalt T, Spulber M, et al. Biomimetic strategy to reversibly trigger functionality of catalytic nanocompartments by the insertion of pH-responsive biovalves[J]. *Nano letters*, 2017, 17(9): 5790-5798.

122. Lomora M, Gunkel-Grabole G, Mantri S, et al. Bio-catalytic nanocompartments for in situ production of glucose-6-phosphate[J]. *Chemical Communications*, 2017, 53(73): 10148-10151.

123. Einfalt T, Witzigmann D, Edlinger C, et al. Biomimetic artificial organelles with in vitro and in vivo activity triggered by reduction in microenvironment[J]. *Nature communications*, 2018, 9(1): 1-12.

124. Gami M, Einfalt T, Goers R, et al. Live follow-up of enzymatic reactions inside the cavities of synthetic giant unilamellar vesicles equipped with membrane proteins mimicking cell architecture[J]. *ACS synthetic biology*, 2018, 7(9): 2116-2125.

125. Belluati A, Craciun I, Liu J, et al. Nanoscale enzymatic compartments in tandem support cascade reactions in vitro[J]. *Biomacromolecules*, 2018, 19(10): 4023-4033.

126. Varlas S, Foster J C, Georgiou P G, et al. Tuning the membrane permeability of polymersome nanoreactors developed by aqueous emulsion polymerization-induced self-assembly[J]. *Nanoscale*, 2019, 11(26): 12643-12654.

127. He J, Cao J, Chen Y, et al. Thermoresponsive block copolymer vesicles by visible light-initiated seeded polymerization-induced self-assembly for temperature-regulated enzymatic nanoreactors[J]. *ACS Macro Letters*, 2020, 9(4): 533-539.

128. Moreno S, Sharan P, Engelke J, et al. Light-Driven Proton Transfer for Cyclic and Temporal Switching of Enzymatic Nanoreactors[J]. *Small*, 2020, 16(37): 2002135.

129. Wang X, Moreno S, Boye S, et al. Feedback-Induced and Oscillating pH Regulation of a Binary Enzyme–Polymersomes System[J]. *Chemistry of Materials*, 2021.

130. Wang Y, Zhang S, Wang J, et al. Ferrocene-containing polymersome nanoreactors for synergistically amplified tumor-specific chemodynamic therapy[J]. *Journal of Controlled Release*, 2021, 333: 500-510.

131. LoPresti C, Lomas H, Massignani M, et al. Polymersomes: nature inspired nanometer sized compartments[J]. *Journal of Materials Chemistry*, 2009, 19(22): 3576-3590.

132. Palivan C G, Goers R, Najer A, et al. Bioinspired polymer vesicles and membranes for biological and medical applications[J]. *Chemical society reviews*, 2016, 45(2): 377-411.

133. Hanneschlaeger C, Horner A, Pohl P. Intrinsic membrane permeability to small molecules[J]. *Chemical reviews*, 2019, 119(9): 5922-5953.

134. Alexandridis P, Lindman B. Amphiphilic block copolymers: self-assembly and applications[M]. Elsevier, 2000.

135. Blackman L D, Varlas S, Arno M C, et al. Permeable protein-loaded polymersome cascade nanoreactors by polymerization-induced self-assembly[J]. *ACS macro letters*, 2017, 6(11): 1263-1267.
136. Bleul R, Thiermann R, Maskos M. Techniques to control polymersome size[J]. *Macromolecules*, 2015, 48(20): 7396-7409.
137. Paxton W F, Price D, Richardson N J. Hydroxide ion flux and pH-gradient driven ester hydrolysis in polymer vesicle reactors[J]. *Soft Matter*, 2013, 9(47): 11295-11302.
138. Le Meins J F, Sandre O, Lecommandoux S. Recent trends in the tuning of polymersomes' membrane properties[J]. *The European Physical Journal E*, 2011, 34(2): 1-17.
139. Battaglia G, Ryan A J, Tomas S. Polymeric vesicle permeability: a facile chemical assay[J]. *Langmuir*, 2006, 22(11): 4910-4913.
140. Megens M, Korman C E, Ajo-Franklin C M, et al. Faster-than-anticipated Na<sup>+</sup>/Cl<sup>-</sup> diffusion across lipid bilayers in vesicles[J]. *Biochimica et Biophysica Acta (BBA)-Biomembranes*, 2014, 1838(10): 2420-2424.
141. Schroeder T B H, Leriche G, Koyanagi T, et al. Effects of lipid tethering in extremophile-inspired membranes on H<sup>+</sup>/OH<sup>-</sup> flux at room temperature[J]. *Biophysical journal*, 2016, 110(11): 2430-2440.
142. Elamrani K, Blume A. Effect of the lipid phase transition on the kinetics of H<sup>+</sup>/OH<sup>-</sup> diffusion across phosphatidic acid bilayers[J]. *Biochimica et Biophysica Acta (BBA)-Biomembranes*, 1983, 727(1): 22-30.
143. Nozaki Y, Tanford C. Proton and hydroxide ion permeability of phospholipid vesicles[J]. *Proceedings of the National Academy of Sciences*, 1981, 78(7): 4324-4328.
144. Blackman L D, Varlas S, Arno M C, et al. Permeable protein-loaded polymersome cascade nanoreactors by polymerization-induced self-assembly[J]. *ACS macro letters*, 2017, 6(11): 1263-1267.
145. Canning S L, Smith G N, Armes S P. A critical appraisal of RAFT-mediated polymerization-induced self-assembly[J]. *Macromolecules*, 2016, 49(6): 1985-2001.
146. do Nascimento D F, Arriaga L R, Eggersdorfer M, et al. Microfluidic fabrication of Pluronic vesicles with controlled permeability[J]. *Langmuir*, 2016, 32(21): 5350-5355.
147. Yan L, Higbee E, Tsourkas A, et al. A simple method for the synthesis of porous polymeric vesicles and their application as MR contrast agents[J]. *Journal of Materials Chemistry B*, 2015, 3(48): 9277-9284.
148. Bueno C Z, Apolinario A C, Duro-Castano A, et al. L-Asparaginase Encapsulation into Asymmetric Permeable Polymersomes[J]. *ACS Macro Letters*, 2020, 9(10): 1471-1477.
149. Renggli K, Baumann P, Langowska K, et al. Selective and responsive nanoreactors[J]. *Advanced Functional Materials*, 2011, 21(7): 1241-1259.
150. De las Heras Alarcón C, Pennadam S, Alexander C. Stimuli responsive polymers for biomedical applications[J]. *Chemical Society Reviews*, 2005, 34(3): 276-285.
151. Hu X, Zhang Y, Xie Z, et al. Stimuli-responsive polymersomes for biomedical applications[J]. *Biomacromolecules*, 2017, 18(3): 649-673.
152. Thambi T, Park J H, Lee D S. Hypoxia-responsive nanocarriers for cancer imaging and therapy: recent approaches and future perspectives[J]. *Chemical Communications*, 2016, 52(55): 8492-8500.
153. Gaitzsch J, Appelhans D, Wang L, et al. Synthetic bio-nanoreactor: mechanical and

chemical control of polymersome membrane permeability[J]. *Angewandte Chemie International Edition*, 2012, 51(18): 4448-4451.

154. Kim K T, Cornelissen J J L M, Nolte R J M, et al. A Polymersome nanoreactor with controllable permeability induced by stimuli-responsive block copolymers[J]. *Advanced materials*, 2009, 21(27): 2787-2791.

155. Rifaie-Graham O, Ulrich S, Galensowske N F B, et al. Wavelength-selective light-responsive DASA-functionalized polymersome nanoreactors[J]. *Journal of the American Chemical Society*, 2018, 140(25): 8027-8036.

156. Spulber M, Najer A, Winkelbach K, et al. Photoreaction of a hydroxyalkylphenone with the membrane of polymersomes: a versatile method to generate semipermeable nanoreactors[J]. *Journal of the American Chemical Society*, 2013, 135(24): 9204-9212.

157. Deng Y, Chen H, Tao X, et al. Oxidation-Sensitive Polymersomes Based on Amphiphilic Diblock Copolypeptides[J]. *Biomacromolecules*, 2019, 20(9): 3435-3444.

158. Deng Z, Qian Y, Yu Y, et al. Engineering intracellular delivery nanocarriers and nanoreactors from oxidation-responsive polymersomes via synchronized bilayer cross-linking and permeabilizing inside live cells[J]. *Journal of the American Chemical Society*, 2016, 138(33): 10452-10466.

159. Kim J, Kim K T. Polymersome-Based Modular Nanoreactors with Size-Selective Transmembrane Permeability[J]. *ACS applied materials & interfaces*, 2020, 12(20): 23502-23513.

160. Broz P, Driamov S, Ziegler J, et al. Toward intelligent nanosize bioreactors: a pH-switchable, channel-equipped, functional polymer nanocontainer[J]. *Nano letters*, 2006, 6(10): 2349-2353.

161. Kumar M, Grzelakowski M, Zilles J, et al. Highly permeable polymeric membranes based on the incorporation of the functional water channel protein Aquaporin Z[J]. *Proceedings of the National Academy of Sciences*, 2007, 104(52): 20719-20724.

162. Schwarzer T S, Klermund L, Wang G, et al. Membrane functionalization of polymersomes: Alleviating mass transport limitations by integrating multiple selective membrane transporters for the diffusion of chemically diverse molecules[J]. *Nanotechnology*, 2018, 29(44): 44LT01.

163. Belluati A, Mikhalevich V, Yorulmaz Avsar S, et al. How do the properties of amphiphilic polymer membranes influence the functional insertion of peptide pores?[J]. *Biomacromolecules*, 2019, 21(2): 701-715.

164. Ren T, Erbakan M, Shen Y, et al. Membrane protein insertion into and compatibility with biomimetic membranes[J]. *Advanced Biosystems*, 2017, 1(7): 1700053.

165. Matile S, Jentzsch A V, Montenegro J, et al. Recent synthetic transport systems[J]. *Chemical Society Reviews*, 2011, 40(5): 2453-2474.

166. Zheng S, Huang L, Sun Z, et al. Self-assembled artificial ion-channels toward natural selection of functions[J]. *Angewandte Chemie International Edition*, 2021, 60(2): 566-597.

167. Howorka S. Building membrane nanopores[J]. *Nature nanotechnology*, 2017, 12(7): 619-630.

168. Tunuguntla R H, Allen F I, Kim K, et al. Ultrafast proton transport in sub-1-nm diameter carbon nanotube porins[J]. *Nature nanotechnology*, 2016, 11(7): 639-644.

169. Tunuguntla R H, Henley R Y, Yao Y C, et al. Enhanced water permeability and tunable

- ion selectivity in subnanometer carbon nanotube porins[J]. *Science*, 2017, 357(6353): 792-796.
170. Sanborn J R, Chen X, Yao Y C, et al. Carbon nanotube porins in amphiphilic block copolymers as fully synthetic mimics of biological membranes[J]. *Advanced Materials*, 2018, 30(51): 1803355.
171. Kim A J, Kaucher M S, Davis K P, et al. Proton transport from dendritic helical - pore - incorporated polymersomes[J]. *Advanced Functional Materials*, 2009, 19(18): 2930-2936.
172. Yao X, Huang P, Nie Z. Cyclodextrin-based polymer materials: from controlled synthesis to applications[J]. *Progress in Polymer Science*, 2019, 93: 1-35.
173. Przybyla M A, Yilmaz G, Becer C R. Natural cyclodextrins and their derivatives for polymer synthesis[J]. *Polymer Chemistry*, 2020, 11(48): 7582-7602.
174. Davis M E, Brewster M E. Cyclodextrin-based pharmaceuticals: past, present and future[J]. *Nature reviews Drug discovery*, 2004, 3(12): 1023-1035.
175. Fernández M A, Silva O F, Vico R V, et al. Complex systems that incorporate cyclodextrins to get materials for some specific applications[J]. *Carbohydrate research*, 2019, 480: 12-34.
176. Antoniuk I, Amiel C. Cyclodextrin-mediated hierarchical self-assembly and its potential in drug delivery applications[J]. *Journal of pharmaceutical sciences*, 2016, 105(9): 2570-2588.
177. Tejashri G, Amrita B, Darshana J. Cyclodextrin based nanosponges for pharmaceutical use: A review[J]. *Acta pharmaceutica*, 2013, 63(3): 335-358.
178. Khan A R, Forgo P, Stine K J, et al. Methods for selective modifications of cyclodextrins[J]. *Chemical Reviews*, 1998, 98(5): 1977-1996.
179. Jia Yue L I U, Zhang X, Tian B R. Selective modifications at the different positions of cyclodextrins: a review of strategies[J]. *Turkish Journal of Chemistry*, 2020, 44(2): 261.
180. Chaudhary V B, Patel J K. Cyclodextrin inclusion complex to enhance solubility of poorly water soluble drugs: A review[J]. *International Journal of Pharmaceutical Sciences and Research*, 2013, 4(1): 68.
181. Astray G, Gonzalez-Barreiro C, Mejuto J C, et al. A review on the use of cyclodextrins in foods[J]. *Food Hydrocolloids*, 2009, 23(7): 1631-1640.
182. Seidi F, Shamsabadi A A, Amini M, et al. Functional materials generated by allying cyclodextrin-based supramolecular chemistry with living polymerization[J]. *Polymer Chemistry*, 2019, 10(27): 3674-3711.
183. Tabushi I, Kuroda Y, Yokota K. A, B, D, F-tetrasubstituted  $\beta$ -cyclodextrin as artificial channel compound[J]. *Tetrahedron Letters*, 1982, 23(44): 4601-4604.
184. Badi N, Auvray L, Guégan P. Synthesis of Half-Channels by the Anionic Polymerization of Ethylene Oxide Initiated by Modified Cyclodextrin[J]. *Advanced Materials*, 2009, 21(40): 4054-4057.
185. El Ghouli Y, Renia R, Faye I, et al. Biomimetic artificial ion channels based on beta-cyclodextrin[J]. *Chemical Communications*, 2013, 49(99): 11647-11649.
186. Xin P, Kong H, Sun Y, et al. Artificial  $K^+$  Channels Formed by Pillararene-Cyclodextrin Hybrid Molecules: Tuning Cation Selectivity and Generating Membrane Potential[J]. *Angewandte Chemie*, 2019, 131(9): 2805-2810.
187. Mamad-Hemouch H, Ramoul H, Abou Taha M, et al. Biomimetic nanotubes based on

- cyclodextrins for ion-channel applications[J]. *Nano letters*, 2015, 15(11): 7748-7754.
188. Mamad-Hemouch H, Bacri L, Huin C, et al. Versatile cyclodextrin nanotube synthesis with functional anchors for efficient ion channel formation: design, characterization and ion conductance[J]. *Nanoscale*, 2018, 10(32): 15303-15316.
189. Ravoo B J, Darcy R. Cyclodextrin bilayer vesicles[J]. *Angewandte Chemie*, 2000, 112(23): 4494-4496.
190. Falvey P, Lim C W, Darcy R, et al. Bilayer vesicles of amphiphilic cyclodextrins: host membranes that recognize guest molecules[J]. *Chemistry—a European journal*, 2005, 11(4): 1171-1180.
191. Samanta A, Tesch M, Keller U, et al. Fabrication of hydrophilic polymer nanocontainers by use of supramolecular templates[J]. *Journal of the American Chemical Society*, 2015, 137(5): 1967-1971.
192. Muñoz J, Crivillers N, Ravoo B J, et al. Cyclodextrin-based superparamagnetic host vesicles as ultrasensitive nanobiocarriers for electrosensing[J]. *Nanoscale*, 2020, 12(17): 9884-9889.
193. Himmelein S, Sporenberg N, Schönhoff M, et al. Size-selective permeation of water-soluble polymers through the bilayer membrane of cyclodextrin vesicles investigated by PFG-NMR[J]. *Langmuir*, 2014, 30(14): 3988-3995.
194. Eskandani Z, Le Gall T, Montier T, et al. Polynucleotide transport through lipid membrane in the presence of starburst cyclodextrin-based poly (ethylene glycol)s[J]. *The European Physical Journal E*, 2018, 41(11): 1-7.
195. Normand M, Kirillov E, Carpentier J F, et al. Cyclodextrin-centered polyesters: controlled ring-opening polymerization of cyclic esters from  $\beta$ -cyclodextrin-diol[J]. *Macromolecules*, 2012, 45(2): 1122-1130.
196. Liu Y Y, Zhong Y B, Nan J K, et al. Star polymers with both temperature sensitivity and inclusion functionalities[J]. *Macromolecules*, 2010, 43(24): 10221-10230.
197. Gao Z, Chen M, Hu Y, et al. Tunable assembly and disassembly of responsive supramolecular polymer brushes[J]. *Polymer Chemistry*, 2017, 8(18): 2764-2772.
198. Pang X, Zhao L, Akinc M, et al. Novel amphiphilic multi-arm, star-like block copolymers as unimolecular micelles[J]. *Macromolecules*, 2011, 44(10): 3746-3752.
199. Ohno K, Wong B, Haddleton D M. Synthesis of well-defined cyclodextrin-core star polymers[J]. *Journal of Polymer Science Part A: Polymer Chemistry*, 2001, 39(13): 2206-2214.
200. Xie C, Zhang P, Zhang Z, et al. Drug-loaded pseudo-block copolymer micelles with a multi-armed star polymer as the micellar exterior[J]. *Nanoscale*, 2015, 7(29): 12572-12580.
201. Wang J, Wang X, Yang F, et al. Self-assembly behavior of a linear-star supramolecular amphiphile based on host-guest complexation[J]. *Langmuir*, 2014, 30(43): 13014-13020.
202. Huin C, Eskandani Z, Badi N, et al. Anionic ring-opening polymerization of ethylene oxide in DMF with cyclodextrin derivatives as new initiators[J]. *Carbohydrate polymers*, 2013, 94(1): 323-331.
203. Gou P F, Zhu W P, Xu N, et al. Synthesis and characterization of well-defined cyclodextrin-centered seven-arm star poly ( $\epsilon$ -caprolactone)s and amphiphilic star poly ( $\epsilon$ -caprolactone-*b*-ethylene glycol)s[J]. *Journal of Polymer Science Part A: Polymer Chemistry*, 2008, 46(19): 6455-6465.

204. Li Y K, Jiang M W, Wang L, et al. Heat-Induced Supramolecular Organogels Composed of  $\alpha$ -Cyclodextrin and “Jellyfish-Like”  $\beta$ -Cyclodextrin-Poly ( $\epsilon$ -caprolactone)[J]. *Journal of Polymer Science Part B: Polymer Physics*, 2013, 51(22): 1598-1606.
205. Yang C, Krishnamurthy S, Liu J, et al. Broad-Spectrum Antimicrobial Star Polycarbonates Functionalized with Mannose for Targeting Bacteria Residing inside Immune Cells[J]. *Advanced healthcare materials*, 2016, 5(11): 1272-1281.
206. Yang W, Yu C, Wu C, et al. Cell-penetrating poly (disulfide)-based star polymers for simultaneous intracellular delivery of miRNAs and small molecule drugs[J]. *Polymer Chemistry*, 2017, 8(27): 4043-4051.
207. Yong D, Luo Y, Du F, et al. CDDP supramolecular micelles fabricated from adamantane terminated mPEG and  $\beta$ -cyclodextrin based seven-armed poly (L-glutamic acid)/CDDP complexes[J]. *Colloids and Surfaces B: Biointerfaces*, 2013, 105: 31-36.
208. Zhang P, Qian X, Zhang Z, et al. Supramolecular amphiphilic polymer-based micelles with seven-armed polyoxazoline coating for drug delivery[J]. *ACS applied materials & interfaces*, 2017, 9(7): 5768-5777.
209. Gou P F, Zhu W P, Xu N, et al. Synthesis and self-assembly of well-defined cyclodextrin-centered amphiphilic A14B7 multimiktoarm star copolymers based on poly ( $\epsilon$ -caprolactone) and poly (acrylic acid)[J]. *Journal of Polymer Science Part A: Polymer Chemistry*, 2010, 48(14): 2961-2974.
210. Pereira G, Huin C, Morariu S, et al. Synthesis of poly (2-methyl-2-oxazoline) star polymers with a  $\beta$ -cyclodextrin core[J]. *Australian Journal of Chemistry*, 2012, 65(8): 1145-1155.
211. Xu J, Liu S. Synthesis of well-defined 7-arm and 21-arm poly (N-isopropylacrylamide) star polymers with  $\beta$ -cyclodextrin cores via click chemistry and their thermal phase transition behavior in aqueous solution[J]. *Journal of Polymer Science Part A: Polymer Chemistry*, 2009, 47(2): 404-419.
212. Huang B, Chen M, Zhou S, et al. Synthesis and properties of clickable A (BbC) 20 miktoarm star-shaped block copolymers with a terminal alkyne group[J]. *Polymer Chemistry*, 2015, 6(21): 3913-3917.
213. Gou P F, Zhu W P, Shen Z Q. Drug-grafted seven-arm amphiphilic star poly ( $\epsilon$ -caprolactone-co-carbonate)-b-poly (ethylene glycol)s based on a cyclodextrin core: synthesis and self-assembly behavior in water[J]. *Polymer Chemistry*, 2010, 1(8): 1205-1214.
214. Huo H, Liu J, Kannan S, et al. Multicompartment Nanoparticles Bearing Hydrophilic/Hydrophobic Subdomains by Self-Assembly of Star Polymers in Aqueous Solution[J]. *Macromolecules*, 2020, 54(1): 35-43.
215. Niu L, Liu Y, Hou Y, et al. Self-assembly and micelle-to-vesicle transition from star triblock ABC copolymers based on a cyclodextrin core[J]. *Polymer Chemistry*, 2016, 7(20): 3406-3415.
216. Schmidt B V K J, Hetzer M, Ritter H, et al. Miktoarm star polymers via cyclodextrin-driven supramolecular self-assembly[J]. *Polymer Chemistry*, 2012, 3(11): 3064-3067.
217. Schmidt B V K J, Barner-Kowollik C. Supramolecular X-and H-shaped star block copolymers via cyclodextrin-driven supramolecular self-assembly[J]. *Polymer Chemistry*, 2014, 5(7): 2461-2472.
218. Bennevault V, Huin C, Guegan P, et al. Temperature sensitive supramolecular self

assembly of per-6-PEO- $\beta$ -cyclodextrin and  $\alpha,\omega$ -di-(adamantylethyl) poly (N-isopropylacrylamide) in water[J]. *Soft matter*, 2015, 11(32): 6432-6443.

219. Ge Z, Xu J, Hu J, et al. Synthesis and supramolecular self-assembly of stimuli-responsive water-soluble Janus-type heteroarm star copolymers[J]. *Soft Matter*, 2009, 5(20): 3932-3939.

220. Hu M, Shen Y, Zhang L, et al. Polymersomes via self-assembly of amphiphilic  $\beta$ -cyclodextrin-centered triarm star polymers for enhanced oral bioavailability of water-soluble chemotherapeutics[J]. *Biomacromolecules*, 2016, 17(3): 1026-1039.

221. Shi X, Ma X, Hou M, et al. pH-Responsive unimolecular micelles based on amphiphilic star-like copolymers with high drug loading for effective drug delivery and cellular imaging[J]. *Journal of Materials Chemistry B*, 2017, 5(33): 6847-6859.

## **Chapter 2.**

### **Linear Amphiphilic Copolymers:**

**Syntheses, structural characterizations and self-assemblies**

## Content

<b>1. Introduction.....</b>	<b>79</b>
<b>2. Materials and Methods.....</b>	<b>80</b>
2.1 Materials.....	80
2.2 Syntheses of EEGE monomer.....	81
2.3 Syntheses and structural characterizations of the block copolymers.....	82
2.3.1 Syntheses of the diblock copolymers.....	82
2.3.2 Syntheses of the triblock copolymers.....	83
2.3.3 Structural characterizations of the block copolymers.....	84
2.4 Self-assembly behaviors of the block copolymers.....	84
2.4.1 Preparation of the self-assemblies.....	84
2.4.2 Characterizations of the self-assemblies.....	85
2.5 Antifouling behaviors of the self-assemblies.....	88
<b>3. Results and Discussions.....</b>	<b>88</b>
3.1 Synthesis of EEGE monomer.....	88
3.2 Syntheses and characterizations of the block copolymers.....	90
3.2.1 Syntheses and characterizations of the diblock copolymers.....	90
3.2.2 Syntheses and characterizations of the triblock copolymers.....	94
3.3 Self-assembly behaviors of the block copolymers.....	99
3.3.1 Self-assembly behaviors of the diblock copolymers.....	100
3.3.2 Self-assembly behaviors of the triblock copolymers.....	103
3.4 Antifouling behaviors of the self-assemblies.....	110
<b>4. Conclusions.....</b>	<b>120</b>
<b>5. References.....</b>	<b>121</b>

## 1. Introduction

Amphiphilic block copolymers have been widely studied especially on their self-assembly behaviors as well as the properties and applications of the resultant self-assemblies. Amphiphilic block copolymer comprises of hydrophilic and hydrophobic blocks and could self-assemble into a variety of morphologies in aqueous solution, driven by the minimization of the free energy between different blocks and of the free energy between each block with the surrounding solvent [1].

From an academic point of view, the self-assembly behaviors of amphiphilic copolymers, usually portrayed as morphological phase diagrams, are useful tools to understand the interactions in a specific amphiphilic copolymer system and the differences between varied systems [2,3]. From a practical point of view, the diverse morphologies (*e.g.*, spherical micelle, worm-like micelle and vesicle) allow amphiphilic copolymers to be applied in a broad variety of fields. Vesicle is especially the most intriguing nanostructure and has been widely explored.

Polymeric vesicle (*i.e.*, polymersome) is featured by an aqueous interior enclosed by a hydrophobic membrane which is further stabilized by an outer hydrophilic corona. Thus, both hydrophilic and hydrophobic molecules can be loaded in the available space in aqueous lumen and hydrophobic membrane, respectively. Besides the high loading efficiency, the nanometric dimension allows them to be efficiently accumulated in solid tumors via the enhanced permeability and retention (EPR) effect. Therefore, polymersomes are of great interest for biotechnological applications as drug delivery systems, therapeutic nanosystems, and so forth [4].

In biotechnological applications, the protein-repelling capacity of these nanoparticles should be taken into account, because protein adsorption and the resultant protein coronas on the nanoparticles would introduce several shortcomings towards the application of nanoparticles in medicine, by impacting their targeting ability, toxicity, cellular uptake, circulation lifetime, biodistribution, and so on [5]. In this respect, poly(ethylene glycol) (PEG) has been widely used to solve this problem to some extent, via PEGylation of the nanoparticles. However, PEG-relevant shortcomings have been encountered, for instance, PEG can trigger the activation of the complement system and the produced antibody (anti-PEG) greatly affects the therapeutic effects of such PEGylated nanoparticles [6]. Accordingly, a diversity of polymers has been investigated trying to find solutions to overcome the limitations in PEGylation. Polyglycidol (PGL) has been anticipated as a good alternative to PEG, since it possesses similar biocompatibility to PEG, and some PGL-based surfaces have been reported to resist protein adsorptions [7]. Additionally, well-defined linear PGL can be tailor-made via ring-opening polymerization of protected glycidol monomers (*e.g.*, *tert*-butylglycidyl ether (tBuGE) and ethoxyethyl glycidyl ether (EEGE)) and a sequential deprotection in mild acidic conditions [8]. The synthetic

procedures are safer and more versatile than those involving the volatile ethylene oxide (EO) monomers.

Then, to construct PGL-based amphiphilic block copolymers, poly(butylene oxide) (PBO) is a good option for the hydrophobic block. Firstly, PBO shares the same polyether backbone with PGL and can also be synthesized via ring-opening polymerization [9]. In other words, the block copolymers comprising PBO and PGL blocks can be prepared via sequential ring-opening polymerizations of two epoxide monomers, efficiently and facily [10]. Secondly, PBO has low glass transition temperature ( $T_g$ ) [11], enabling PBO-contained amphiphilic copolymers to self-assemble at relatively low temperature compared to the widely studied poly(lactic acid) (PLA) and poly( $\epsilon$ -caprolactone) (PCL). Additionally, PBO-contained self-assemblies have also been reported to have better cytocompatibility than the nanoparticles made of more hydrophobic blocks [12].

Taking into account all the aspects mentioned above, hydrophobic PBO and hydrophilic PGL blocks are used as the basic components of the amphiphilic copolymers studied in the whole PhD project herein.

As the first part of this project, linear amphiphilic copolymers are targeted. First, the synthetic strategies of diblock copolymers (PBO-PGL) and triblock copolymers (PGL-PBO-PGL), as well as their structural characterizations by  $^1\text{H}$  NMR and SEC will be discussed. Subsequently, the self-assembly behaviors of these copolymers will be systematically studied by dynamic light scattering (DLS), static light scattering (SLS), transmission electron microscopy (TEM), and small-angle X-ray scattering (SAXS), thanks to a collaboration with Pr. Fernando Carlos Giacomelli of Universidade Federal do ABC (São Paulo, Brésil). At last, the PGL-stabilized self-assemblies will be investigated focusing on their protein-repelling capacity, via the methods of DLS, isothermal titration calorimetry (ITC), fluorescence and circular dichroism (CD) spectroscopy.

## 2. Materials and Methods

### 2.1 Materials

The chemicals for polymerization include butylene oxide (BO, 99%, Sigma–Aldrich), ethoxyethyl glycidyl ether (EEGE, prepared by a published method [13]), benzyl alcohol (BA, anhydrous, 99.8%, Sigma–Aldrich), 1,4-benzene dimethanol (BDM, 99%, Sigma–Aldrich), phosphazene base tBuP4 ( $\sim 0.8 \text{ mol L}^{-1}$  in *n*-hexane, Sigma–Aldrich), anhydrous toluene, and anhydrous THF. BO and EEGE were dried twice over  $\text{CaH}_2$  and stored in the glovebox before use. BA and tBuP4 were stored in glovebox before opening and used as received. Anhydrous toluene and THF were collected from the solvent purification system (MB SPS COMPACT, consisting of an

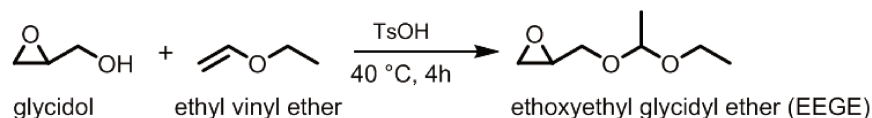
activated alumina column and an activated copper catalyst column) in the glovebox. The addition of these chemicals into the reaction container was performed in the glovebox (MBRAUN) which is equipped with a gas purification system (molecular sieves and copper catalyst) and dry argon atmosphere ensuring the moisture content (H<sub>2</sub>O) less than 0.5 ppm monitored by an MB-MO-SE1 moisture probe. BDM was stored as the manufacturer suggested and used as received.

The chemicals for common uses include CaH<sub>2</sub> (*c.a.* 93%, ACROS), neutral alumina (Sigma–Aldrich), dichloromethane (DCM, VWR Chemical), methanol (MeOH, VWR Chemical), HCl (37%, Sigma–Aldrich), NaHCO<sub>3</sub> (VWR), and MgSO<sub>4</sub> (VWR). All these chemicals were used as received.

## 2.2 Syntheses of EEGE monomer

Ethoxyethyl glycidyl ether (EEGE) was synthesized with a published method [13] following the procedure shown in Scheme 1.

**Scheme 1.** Synthetic Procedure of Ethoxyethyl Glycidyl Ether (EEGE).



Typically, TsOH•H<sub>2</sub>O (0.828 g, 4.4 mmol, 0.01 eq) was added little by little into the mixture of glycidol (30 g, 0.41 mol, 1 eq) and ethylvinyl ether (120 mL, 1.25 mol, 3 eq) at 0 °C under stirring. After feeding, the reaction mixture was stirred at 0 °C for 0.5 h and then at 40 °C for 4 h. At the end of the reaction, a saturated NaHCO<sub>3</sub> aqueous solution (60 mL) was added. The organic phase was separated and dried with MgSO<sub>4</sub>. After filtration, the organic solution was collected and concentrated by rotavapor to remove the excess of ethylvinyl ether. The remaining mixture was then applied to vacuum distillation to collect the product EEGE as a colorless liquid (23 g, yield 38%).

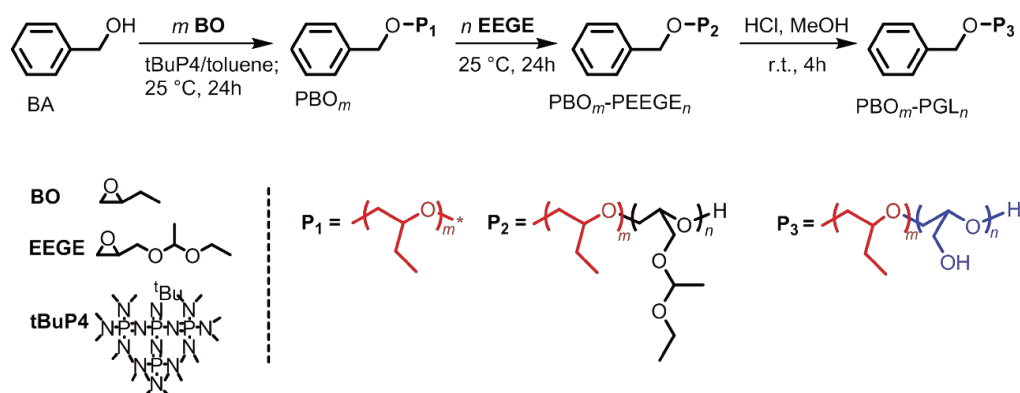
The product was characterized on a Bruker Ultra Shield 300 NMR spectrometer routinely (300 K). All the <sup>1</sup>H NMR, <sup>13</sup>C NMR and COSY spectra were analyzed with MestReNova 9.1.0 software and internally referenced to the residual proton signals of the deuterated solvents.

## 2.3 Syntheses and structural characterizations of block copolymers

### 2.3.1 Syntheses of diblock copolymers

Diblock copolymers  $\text{PBO}_m\text{-PGL}_n$ , where  $m$  and  $n$  are respectively the values of the degree of polymerization (DP) of PBO and PGL blocks, were synthesized via a  $\text{tBuP4}$ -catalyzed sequential anionic ring-opening copolymerization followed with a deprotection in acidic conditions, as shown in Scheme 2.

**Scheme 2.** Synthetic Procedure for Diblock Copolymer  $\text{PBO}_m\text{-PGL}_n$ .



A typical procedure is described for the preparation of  $\text{PBO}_{13}\text{-PGL}_{47}$  (Entry HQ029): BO (0.1879 g, 2.6 mmol, 13 eq) and  $\text{tBuP4}$  ( $0.8\text{ mol L}^{-1}$  in  $n$ -hexane;  $125\text{ }\mu\text{L}$ , 0.1 mmol, 0.5 eq) were sequentially added into the solution of BA ( $20.8\text{ }\mu\text{L}$ , 0.2 mmol, 1 eq) in toluene (0.5 mL) to start the homopolymerization of BO. The mixture was stirred at  $25\text{ }^\circ\text{C}$  for 24 hours, then an aliquot of the reaction medium was withdrawn and applied to  $^1\text{H}$  NMR characterization to check the conversion of BO. After confirming the consumption of BO, the second monomer, EEGE (1.3775 g, 9.4 mmol, 47 eq) was added. The mixture was stirred at  $25\text{ }^\circ\text{C}$  for another 24 hours. After confirming the consumption of EEGE by  $^1\text{H}$  NMR characterizing the copolymerization medium, drops of DI water was added. The mixture was concentrated giving a brown viscous liquid, which was then eluted by DCM through a neutral alumina column to remove  $\text{tBuP4}$  (mass ratio of alumina-to- $\text{tBuP4}$   $\sim 100$ ). The eluent was collected and concentrated giving the diblock copolymer  $\text{PBO}_{13}\text{-PEEGE}_{47}$ , as a colorless viscous liquid (1.55 g, yield 97%).

At last, the  $\text{PBO}\text{-PEEGE}$  intermediate was treated in acidic conditions to reveal hydroxyl functions: A desired amount of  $\text{HCl}$  solution ( $2\text{ mol L}^{-1}$  in  $\text{MeOH}$ ; 2.4 mL, 4.8 mmol) was added into the solution of  $\text{PBO}_{13}\text{-PEEGE}_{47}$  ( $M_n\ 7.6\text{ kg mol}^{-1}$ ; 0.76 g, 0.1 mmol) in  $\text{MeOH}$  (7.1 mL). The mixture was stirred at room temperature (r.t.) for 4 hours and then was neutralized by  $\text{NaHCO}_3$  (1.21 g, 14.4 mmol). The resultant solid

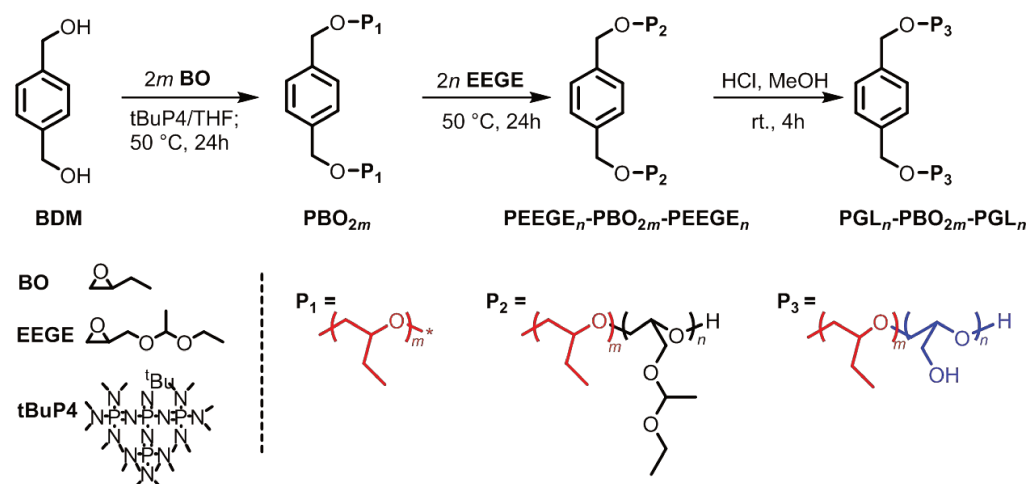
was removed by filtration. The filtrate was collected and concentrated giving the product PBO<sub>13</sub>-PGL<sub>47</sub> (Entry HQ029) as a white solid (0.32g, yield 71%).

Diblock copolymers PBO<sub>*m*</sub>-PGL<sub>*n*</sub> with varied values of *m* and *n* were synthesized following the same procedure but with varied monomer feeding ratios ([BO]<sub>0</sub>/[EEGE]<sub>0</sub>/[BA]<sub>0</sub>).

### 2.3.2 Syntheses of triblock copolymers

Triblock copolymers PGL<sub>*n*</sub>-PBO<sub>2*m*</sub>-PGL<sub>*n*</sub>, where 2*m* and *n* are respectively the values of DP of PBO and PGL blocks, were synthesized via an adapted synthetic procedure shown in Scheme 3.

**Scheme 3.** Synthetic Procedure for Triblock Copolymers PGL<sub>*n*</sub>-PBO<sub>2*m*</sub>-PGL<sub>*n*</sub>.



A typical procedure is described for the synthesis of PGL<sub>12</sub>-PBO<sub>84</sub>-PGL<sub>12</sub> (Entry HQ033): BO (1.2106 g, 16.8 mmol, 84 eq) and tBuP4 (~ 0.8 mol L<sup>-1</sup> in *n*-hexane; 125 μL, 0.1 mmol, 0.5 eq) were sequentially added into the solution of BDM (29.0 mg, 0.2 mmol, 1 eq) in THF (1.3 mL). The mixture was stirred at 50 °C for 24 hours. At the end, BO conversion was checked by characterizing the homopolymerization medium by <sup>1</sup>H NMR. After confirming the consumption of BO, EEGE (0.7060 g, 4.8 mmol, 23 eq) was added. The reaction medium was stirred at 50 °C for another 24 hours. The copolymerization medium was characterized by <sup>1</sup>H NMR to check EEGE conversion. After confirming the absence of EEGE monomer, drops of DI water was added. The mixture was subsequently concentrated giving a brown viscous liquid. The obtained crude product was purified by chromatography via being eluted with DCM through a neutral alumina column to remove tBuP4. The eluent was collected

and concentrated to give the triblock copolymer PEEGE<sub>12</sub>-PBO<sub>84</sub>-PEEGE<sub>12</sub> as a colorless viscous liquid (1.54 g, yield 81%).

At last, the PEEGE-PBO-PEEGE intermediate was treated in acidic conditions: An amount of HCl solution (2 mol L<sup>-1</sup> in MeOH; 1.2 mL, 2.4 mmol) was added into the solution of PEEGE<sub>12</sub>-PBO<sub>84</sub>-PEEGE<sub>12</sub> ( $M_n$  9.2 kg mol<sup>-1</sup>; 0.92 g, 0.1 mmol) in MeOH (3.5 mL). The mixture was stirred at r.t. for 4 hours, and then was neutralized by NaHCO<sub>3</sub> (0.60g, 7.2 mmol). The resultant solid was removed by filtration. The filtrate was concentrated giving the product PGL<sub>12</sub>-PBO<sub>84</sub>-PGL<sub>12</sub> (Entry HQ033) as a white solid (0.76 g, yield 97%).

Triblock copolymers PGL<sub>*n*</sub>-PBO<sub>2*m*</sub>-PGL<sub>*n*</sub> with varying values of *m* and *n* were synthesized following the same procedures but with varying monomer feeding ratios ( $[BO]_0/[EEGE]_0/[BDM]_0$ ).

### 2.3.3 Structural characterizations of block copolymers

<sup>1</sup>H NMR spectra were recorded on a Bruker Ultra Shield 300 NMR spectrometer routinely (300 K). All the <sup>1</sup>H NMR spectra were analyzed with MestReNova 9.1.0 software and internally referenced to the residual proton signals of the deuterated solvents.

Size exclusion chromatography (SEC) were performed at 60 °C in DMF (containing 1.0 g L<sup>-1</sup> lithium bromide as an additive at a flow rate of 0.8 mL min<sup>-1</sup>) using a Viscotek gel permeation chromatography system (TDA 305) equipped with one PSS-GRAM 30 Å column (8 mm × 300 mm) and two PSS GRAM 1000 Å columns (8 mm × 300 mm). All polymers were injected at a concentration of 5 mg mL<sup>-1</sup> after filtration through a 0.2 μm syringe filter. OmniSEC 5.12 software was used to acquire and analyze SEC data. Number-average molar mass ( $M_{nSEC}$ ), weight-average molar mass ( $M_{wSEC}$ ) and polymer dispersity index ( $\mathcal{D} = M_{wSEC}/M_{nSEC}$ ) were determined on the basis of poly(methyl methacrylate) (PMMA) standards (provided by Polymer Standard Services) using an RI detector.

## 2.4 Self-assembly behaviors of block copolymers

### 2.4.1 Preparation of self-assemblies

The self-assemblies were manufactured via the well-studied thin-film rehydration method [14,15]. Typically, block copolymer (5.0 mg), PBO<sub>*m*</sub>-PGL<sub>*n*</sub> or PGL<sub>*n*</sub>-PBO<sub>2*m*</sub>-PGL<sub>*n*</sub>, was dissolved with MeOH (2.5 mL) in a glass vial. Then, the organic solvent was evaporated with the aid of rotavapor (40 °C, 5 mbar, 30 min) resulting in a polymer film on the inner wall of the glass vial. The polymer film was hydrated by

the addition of 5.0 mL of DI water. The mixture was stirred at r.t. until the film totally detached from the inner wall producing a suspension of self-assemblies. The suspension was subsequently extruded through a PTFE syringe filter (0.45  $\mu\text{m}$ ) repeatedly in one direction, typically for 5 times, to remove dust and/or ill aggregates following the characterization criteria/suggestions.

### 2.4.2 Characterizations of self-assemblies

The self-assemblies were characterized by dynamic light scattering (DLS), static light scattering (SLS), electrophoretic light scattering (ELS), transmission electron microscopy (TEM) and small-angle X-ray scattering (SAXS).

#### (1) Dynamic light scattering (DLS)

DLS measurements were performed using a ZetaSizer Nano ZS90 at 20 °C. The averaged intensity autocorrelation functions were evaluated using non-negative least-squares (NNLS) analysis implemented in the Zetasizer software to produce the intensity-weighted particle size distribution (PSD) curves.

The hydrodynamic radius ( $R_H$ ) of assemblies was determined by using Stokes–Einstein equation:

$$R_H = \frac{k_B T}{6\pi\eta D} \quad (1)$$

where  $k_B$  is the Boltzmann constant,  $T$  is the absolute temperature,  $\eta$  is the viscosity of solvent, and  $D$  is the diffusion coefficient defined as  $D = \tau^{-1}q^{-2}$  with  $\tau$  being the mean relaxation time related to the diffusion of nanoparticles and  $q$  being the scattering vector.

The autocorrelation functions were also analyzed using the cumulant method [16].

$$\lg g_1(t) = \ln C - \Gamma t + \frac{\mu_2}{2} t^2 \dots \quad (2)$$

wherein  $C$  is the amplitude,  $\Gamma$  is the relaxation frequency ( $\tau^{-1}$ ), and the parameter  $\mu_2$  is known as the second-order cumulant. The polydispersity index of particles (PDI) was computed as  $\text{PDI} = \mu_2/\Gamma^2$ .

The values of  $R_H$  and PDI were reported as the Z-average radius and PDI given by the Zetasizer software on the basis of five measurements.

#### (2) Static light scattering (SLS)

SLS measurements were performed on a ZetaSizer Nano ZS90 at 20 °C, by acquiring

the light scattering intensities monitored at a set scattering angle ( $\theta = 90^\circ$ ) as a function of polymer concentrations.

The molecular weight of assemblies/nanoparticles ( $M_{W_{NPs}}$ ), were estimated by the Debye plot:

$$\frac{Kc}{R_\theta} = \frac{1}{M_{W_{NPs}}} + 2A_2c \quad (3)$$

where  $R_\theta$  (Rayleigh ratio) is the normalized scattered intensity with toluene as the standard solvent,  $c$  is the concentration given in  $\text{mg mL}^{-1}$ , and  $K$  is the optical constant expressed by

$$K = \frac{4\pi^2 n^2 \left(\frac{dn}{dc}\right)^2}{N_A \lambda^4} \quad (4)$$

wherein  $n$  is the refractive index of solvent,  $N_A$  is Avogadro's number, and  $dn/dc$  is the specific refractive index increment of the polymer solution. Specially, the  $dn/dc$  value is a crucial parameter to accurately determine the molecular weight of particles ( $M_{W_{NPs}}$ ) in SLS measurements [17]. Hence, the calculation of the  $dn/dc$  value of the polymer aqueous solution is emphasized herein.

The  $dn/dc$  value of the polymer aqueous solution was estimated from the  $dn/dc$  values of PBO and PGL blocks and their weight fractions ( $w$ ) taking into account the additive rule [17]:

$$\frac{dn}{dc} = \left(\frac{dn}{dc}\right)_{PBO} \times w_{PBO} + \left(\frac{dn}{dc}\right)_{PGL} \times w_{PGL} \quad (5)$$

wherein,  $w_{PBO}$  and  $w_{PGL}$  are the weight fractions of the individual components, and the respective  $dn/dc$  values were estimated based on the  $n$  values of the components.

Therefore, Equation 5 is simplified as

$$\frac{dn}{dc} = (n_{PBO} \times w_{PBO} + n_{PGL} \times w_{PGL}) - n_{\text{water}} \quad (6)$$

with the refractive indexes of PBO ( $n_{PBO}$ ), PGL ( $n_{PGL}$ ), and water ( $n_{\text{water}}$ ) being respectively 1.454, 1.474, and 1.333.

Then, taking into account Equation 3, by plotting  $Kc/R_\theta$  against  $c$ ,  $M_{W_{NPs}}$  could be extracted from the inverse of the intercept. Accordingly, the number of aggregation ( $N_{agg}$ ) is estimated using the following equation:

$$N_{agg} = \frac{Mw_{NPS}}{Mw_{polymer}} \quad (7)$$

wherein,  $Mw_{polymer}$  is the molar mass of copolymer unimer.

### (3) Electrophoretic light scattering (ELS)

ELS data were acquired on a ZetaSizer Nano ZS90 at 20 °C to provide the average zeta potential ( $\zeta$ ) of the nanoparticles. The value of electrophoretic mobility ( $U_E$ ) was converted to the value of  $\zeta$  through the Henry's equation:

$$U_E = \frac{2\varepsilon\zeta f(ka)}{3\eta} \quad (8)$$

where  $\varepsilon$  and  $\eta$  are respectively the dielectric constant and the viscosity of the medium, and  $f(ka)$  is the Henry's function, which is calculated through the Smoluchowski approximation with  $f(ka) = 1.5$ .

ELS data were analyzed using the Zetasizer software, and reported as the average results on the basis of three measurements.

### (4) Transmission electron microscopy (TEM)

TEM images were obtained by using a Tecnai G2 Spirit Twin 120 kV microscope (FEI, Czech Republic), thanks to a collaboration with Fernando. 2  $\mu$ L of the aqueous solution of self-assemblies was dropped onto a copper TEM microscopic grid (400 mesh) which was pre-coated with a thin electron-transparent carbon film. The excess of sample was removed by touching the bottom of the grid with filtering paper. This fast removal of solution was performed after 5 min of sedimentation in order to minimize oversaturation during the drying process. The assemblies were negatively stained with uranyl acetate (2  $\mu$ L of 2 wt% solution dropped onto not completely dried nanoparticles and removed after 30 s in the same way as described above). The samples were left to dry completely at environment temperature and then observed by TEM. Under these conditions, the micrographs displayed negatively stained background with bright nanoparticles.

### (5) Small-angle X-ray scattering (SAXS)

SAXS measurements were performed, thanks to a collaboration with Guillaume Tresset, in the SWING beamline at SOLEIL synchrotron facility (Gif-sur-Yvette, France). The wavelength was set to 1 Å, and the sample-to-detector distance was 2 m, which provided scattering wavenumbers ranging from about  $5 \times 10^{-3}$  to  $0.5 \text{ \AA}^{-1}$ . The samples were automatically injected into a through-flow capillary, and for each sample, about 30 two-dimensional scattering images were recorded on an Eiger 4 M Dectris detector with an exposure time of 1 s while pushing the sample to avoid

radiation damages. The scattering intensities were converted into absolute units after subtracting the contribution of buffer using the FOXTROT software package. The produced SAXS data were analyzed by using the SASfit software (Paul Scherrer Institute, Switzerland).

## **2.5 Antifouling behaviors of the self-assemblies**

The antifouling behaviors of the self-assemblies were conducted, with Fernando, by incubating the self-assemblies in a protein environment, and subsequently evaluated by DLS, isothermal titration calorimetry (ITC), fluorescence and circular dichroism (CD) spectroscopy. DLS measurements were performed in the same method as mentioned above and is not repeated here.

### **(1) Isothermal titration calorimetry (ITC)**

ITC measurements were performed at 25 °C using a MicroCal iTC200 calorimeter. The reference cell was filled with water, the sample cell was filled with 2.0 mg mL<sup>-1</sup> of block copolymer solution, and the syringe was filled with 1.6 mg mL<sup>-1</sup> of protein solution. The titrations were performed by injecting the protein solution into the sample cell every predetermined interval of time. The ITC raw data were integrated from a baseline to give the heat per injection as a function of the protein-to-nanoparticle weight ratio. The heat of dilution of protein solution was determined in a blank experiment where protein solution was injected into the sample cell containing only PBS buffer.

### **(2) Fluorescence spectroscopy**

Fluorescence spectra were recorded on a Varian Cary Eclipse fluorescence spectrophotometer. The spectra of protein solution were recorded after the progressive additions of nanoparticles into the protein solution, with excitation wavelength as 280 nm, emission wavelength scanning from 300 to 450 nm, and using a quartz cell with 10.0 mm optical path at 296 K.

### **(3) Circular dichroism spectroscopy (CD)**

CD data were acquired on a Jasco J-815 circular dichroism spectrometer using a quartz cuvette with 1.0 mm optical path. CD spectra were collected in the range of 200–260 nm at r.t. and corrected by subtracting the solvent background.

## **3. Results and Discussions**

### **3.1 Synthesis of EEGE monomer**

Many studies showed that the ring-opening polymerization of glycidol results in

random hyper-branched polyglycidol (hb-PGL), while the well-defined linear polyglycidol, shortened as PGL herein, is usually prepared by polymerization of the protected glycidol monomer followed with a deprotection treatment. In this respect, acetal group is the commonly used protection group in the form of ethoxyethyl glycidyl ether (EEGE), since it can be easily removed under mild acidic conditions [18,19]. Therefore, EEGE was used in this work to prepare PGL blocks in the amphiphilic block copolymers.

EEGE monomer was prepared with a published method [13] and its quality was assayed by NMR spectrometer. Figure 1A gives the  $^1\text{H}$  NMR spectrum, showing the characteristic peaks belonging to the epoxide protons, including protons 1 ( $\delta$  2.56 ppm, *ddd*, and  $\delta$  2.73 ppm, *ddd*) and proton 2 ( $\delta$  3.08 ppm, *dqd*). The methine proton of acetal group (proton 4,  $\delta$  4.69 ppm, *qd*) was also detected. With the methine proton (proton 4) as the integration reference, the integrals of the other protons were determined as indicated in Figure 1A, in agreement with the molecular formula. The  $^{13}\text{C}$  NMR spectrum also indicated the defined peaks of each carbon atom as identified in Figure 1B. To note, with the exception of the methyl carbon (carbon 7,  $\delta$  15.23 ppm), each carbon had two peaks meaning each was in two chemical environments, consistent with the  $^1\text{H}$  NMR spectrum. Additionally, the COSY spectrum (Figure 1C) demonstrated the expected correlations between the protons. Altogether, the NMR spectra evidenced that the synthesized EEGE monomer had the expected molecular structure with a high purity.

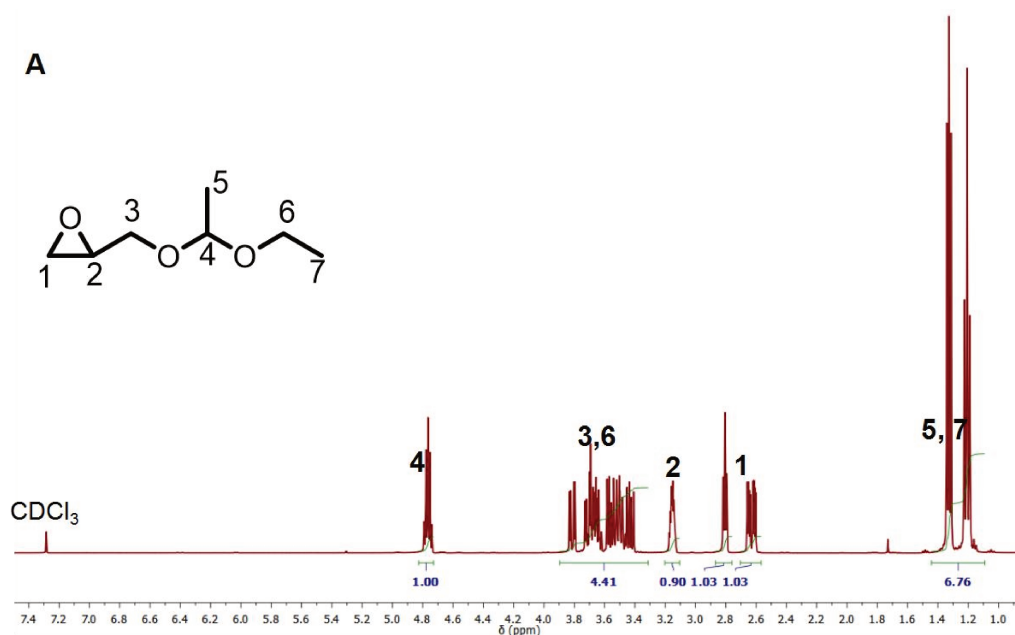


**Figure 1.** (A) Representative  $^1\text{H}$  NMR spectrum of EEGE, recorded in  $\text{CDCl}_3$ , at 300 K.

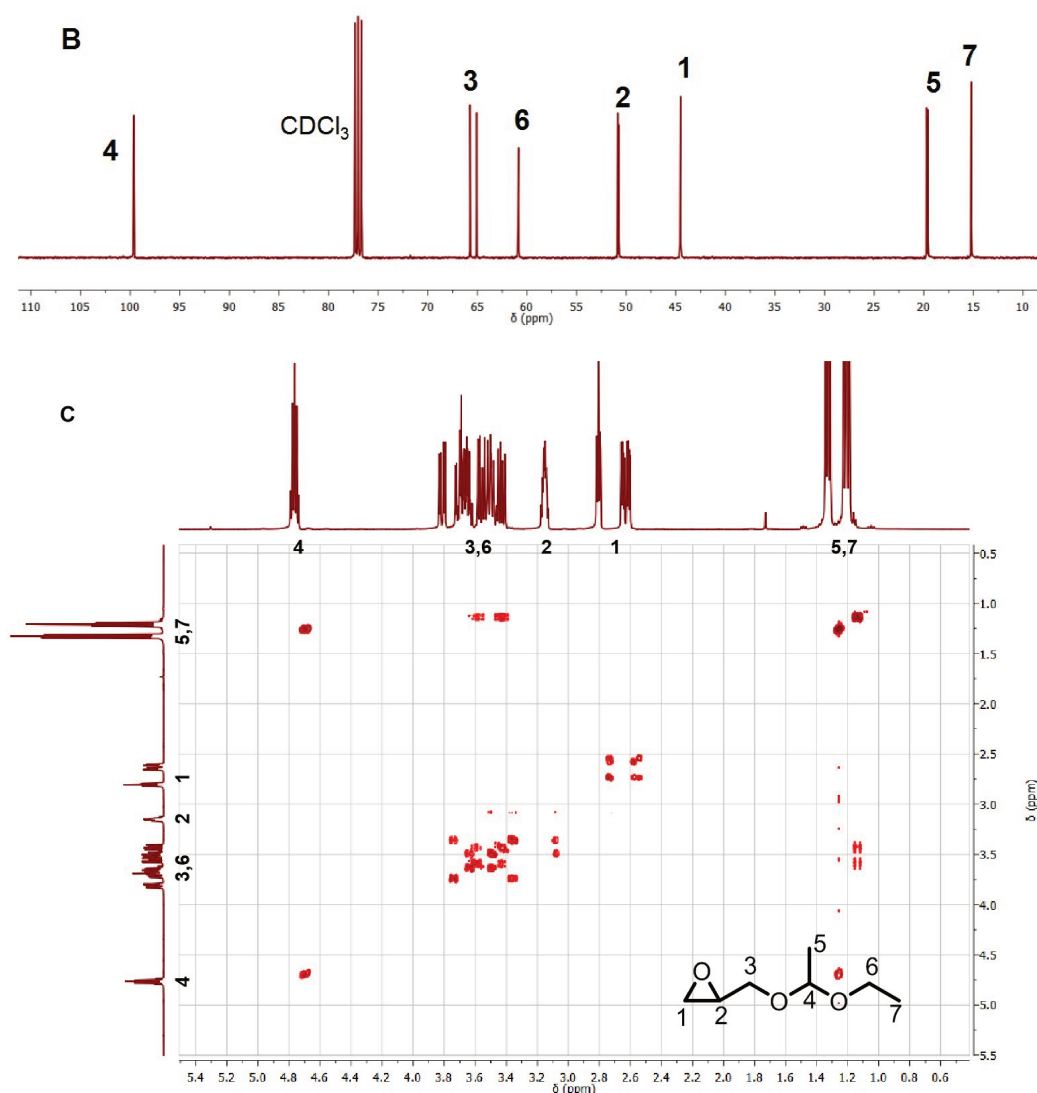


**Figure 1 (continued).** Representative (B)  $^{13}\text{C}$  NMR and (C) COSY spectra of EEGE, recorded in  $\text{CDCl}_3$ , at 300 K.

### 3.2 Syntheses and characterizations of the block copolymers

The block copolymers, including diblock  $\text{PBO}_m\text{-PGL}_n$  and triblock  $\text{PGL}_n\text{-PBO}_{2m}\text{-PGL}_n$ , were synthesized via a tBuP4-catalyzed sequential copolymerization of BO and EEGE followed with a deprotection in acidic conditions to reveal the hydroxyl groups, as depicted in Scheme 2 and Scheme 3, respectively.

#### 3.2.1 Syntheses and characterizations of diblock copolymers

In a standard synthetic procedure (Scheme 2), the PBO block bearing living center at the chain end was obtained first. Sequentially the polymer chain was extended by the addition of PEEGE block giving the diblock copolymer PBO-PEEGE. At last, the

acetal groups in EEGE units were removed to result in the final copolymer PBO-PGL. The intermediates and the final product obtained in the synthetic procedure were characterized by  $^1\text{H}$  NMR and SEC.

As an example, the results for the synthesis of  $\text{PBO}_{13}\text{-PGL}_{47}$  (Entry HQ029) are discussed here. Figure 2 displays the  $^1\text{H}$  NMR characterization results.

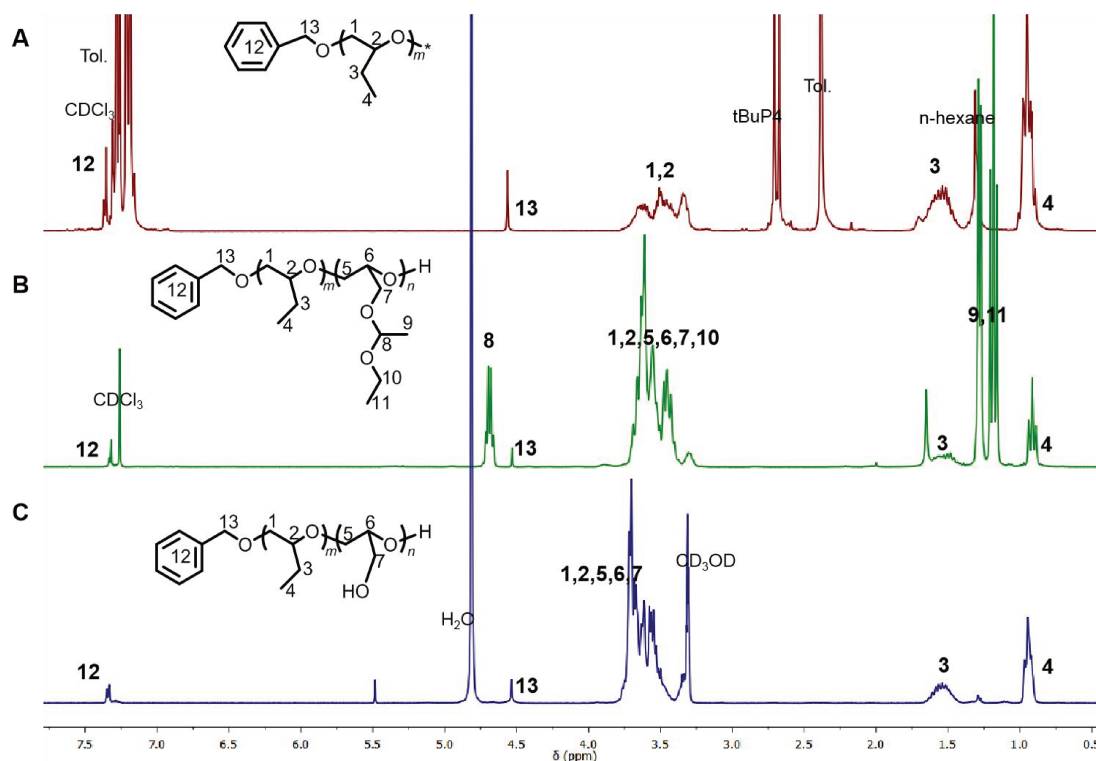


**Figure 2.**  $^1\text{H}$  NMR spectra of (A) PBO (reaction medium), (B) PBO-PEEGE (without tBuP4) and (C) PBO-PGL obtained in the synthetic process of  $\text{PBO}_{13}\text{-PGL}_{47}$  (Entry HQ029). A and B were in  $\text{CDCl}_3$  and C was in  $\text{CD}_3\text{OD}$ , all at 300 K.

Figure 2A gives the  $^1\text{H}$  NMR spectrum of the homopolymerization medium sampled at the end of homopolymerization, to determine BO conversion. In this spectrum, the peaks assigned to the protons of the benzyl group of initiator [proton 12 ( $\delta$  7.34 ppm, *d*) and proton 13 ( $\delta$  4.55 ppm, *s*)], the protons in polyether backbone (protons 1,2,  $\delta$  3.83–3.03 ppm, *m*) and the protons in the pendant ethyl groups of BO repeat units [protons 3 ( $\delta$  1.52 ppm, *s*) and protons 4 ( $\delta$  0.93 ppm, *s*)] were detected, while the protons of the epoxide ring in BO monomer were not detected, confirming the total consumption of BO, with a 100% BO conversion ( $p_{\text{BO}} = 1$ ). Sequentially, EEGE was added into the homopolymerization medium to extend the polymer chains with PEEGE block. At the end, the consumption of EEGE ( $p_{\text{EEGE}} = 1$ ) was also confirmed

by <sup>1</sup>H NMR spectrum with the absence of the protons in the epoxide ring of EEGE monomer (data was not shown here).

Figure 2B shows the <sup>1</sup>H NMR spectrum of the PBO-PEEGE intermediate (after the removal of tBuP4). The peaks assigned to the initiator (protons 12 and 13), BO repeat units (protons 3 and protons 4) and polyether backbone (protons 1,2,5,6, δ 4.02–3.18 ppm, *m*) were detected together with the characteristic peaks belonging to the protons of EEGE repeat units, including the methine proton (proton 8, δ 4.69 ppm, *d*) and the methyl protons [protons 9 (δ 1.27 ppm, *s*) and protons 11 (δ 1.18 ppm, *s*)].

Figure 2C provides the <sup>1</sup>H NMR spectrum of the deprotected product. It clearly shows that the aforementioned characteristic peaks belonging to the protons in EEGE units (protons 8, 9 and 11) disappeared, indicating the targeted PBO-PGL product was obtained.

The <sup>1</sup>H NMR spectra were also used to determine the average composition of the intermediates and the final product. The value of the DP of PBO block, *i.e.*, *m* in PBO<sub>*m*</sub>, was determined from the integrals of methyl protons in BO unit (proton 4) and the methylene protons in the initiator (proton 13) using the formula of  $m = (I_4/3)/(I_{13}/2)$ . The DP of PEEGE block, namely the value of *n* in PBO<sub>*m*</sub>-PEEGE<sub>*n*</sub>, was calculated from the integrals of methine proton in EEGE unit (proton 8) and the methylene protons in the initiator (proton 13) using the formula of  $n = (I_8/1)/(I_{13}/2)$ . The DP of PGL block, *i.e.*, the value of *n* in PBO<sub>*m*</sub>-PGL<sub>*n*</sub>, was computed based on the integrals of the protons in the backbone (protons 1,2,5,6,7) and the methylene protons in the initiator (proton 13) using the formula of  $n = [(I_{1,2,5,6,7}-I_4)/5]/(I_{13}/2)$ . The results were summarized in Table 1, with comparison of the theoretical compositions of each polymer calculated on the basis of monomer feeding ratio and monomer conversions.

**Table 1.** Characteristics of the Intermediates and Product in the Synthetic Process of PBO<sub>13</sub>-PGL<sub>47</sub> (Entry HQ029).

Polymer	Theoretical results <sup>a</sup>			<sup>1</sup> H NMR results <sup>b</sup>			SEC results <sup>c</sup>	
	<i>m</i> <sub>theo.</sub>	<i>n</i> <sub>theo.</sub>	<i>Mn</i> <sub>theo.</sub> (kg mol <sup>-1</sup> )	<i>m</i> <sub>NMR</sub>	<i>n</i> <sub>NMR</sub>	<i>Mn</i> <sub>NMR</sub> (kg mol <sup>-1</sup> )	<i>Mn</i> <sub>SEC</sub> (kg mol <sup>-1</sup> )	<i>D</i>
PBO <sub><i>m</i></sub>	13	--	1.0	13	--	1.0	1.0	1.17
PBO <sub><i>m</i></sub> -PEEGE <sub><i>n</i></sub>	13	47	7.9	12	44	7.3	6.8	1.08
PBO <sub><i>m</i></sub> -PGL <sub><i>n</i></sub>	13	47	4.5	14	57	5.3	5.2	1.13

<sup>a</sup>Theoretical DP values (*m*<sub>theo.</sub> and *n*<sub>theo.</sub>) were calculated based on the monomer feeding ratio ([BO]<sub>0</sub>/[EEGE]<sub>0</sub>/[BA]<sub>0</sub>) and monomer conversions (100% for both BO and EEGE herein); theoretical molar mass (*Mn*<sub>theo.</sub>) was calculated on the basis of the theoretical DP values. <sup>b</sup>NMR results were derived from the <sup>1</sup>H NMR spectrum of each polymer; <sup>c</sup>SEC was performed in DMF using an RI detector, and the results were determined with PMMA as the standard.

One can see that the results derived from  $^1\text{H}$  NMR spectra were close to the theoretical values calculated based on monomer feeding ratio and monomer conversions, indicating the synthetic procedure was defined.

The intermediates and the product were characterized by SEC as well. The traces were shown in Figure 3 and the characterization results were listed in Table 1.

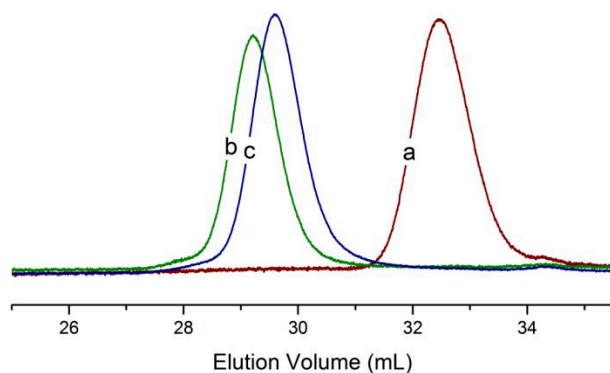


**Figure 3.** SEC traces of (a) PBO (reaction medium), (b) PBO-PEEGE (without tBuP4) and (c) PBO-PGL in the synthetic process of  $\text{PBO}_{13}\text{-PGL}_{47}$  (Entry HQ029), performed in DMF using an RI detector.

All the traces were unimodal and narrowly distributed, giving low polydispersity indexes ( $\mathcal{D}$ , Table 1), indicating the polymers were of high purity. Traces *a* (centered at 32.5 mL) and *b* (centered at 29.2 mL) were respectively the trace of PBO and PBO-PEEGE. It can be seen that, from *a* to *b*, the elution volume decreased, due to the increase of molar mass from PBO to PBO-PEEGE. Trace *c* (centered at 29.6 mL) portrays the PBO-PGL product, indicating an increase in the elution volume compared to that of trace *b* (29.2 mL), in agreement with the decrease of molar mass resulting from the removal of acetal groups from the EEGE units. The number-average molar mass ( $M_{n\text{SEC}}$ ) of each polymer was determined with linear PMMA as the standard and was listed in Table 1. The data showed that the characterization results from SEC were close to the theoretical values and the values derived from  $^1\text{H}$  NMR spectra, demonstrating the reactions in this synthetic procedure were well controlled.

Furthermore, the same synthetic procedure was adopted to prepare other diblock copolymers,  $\text{PBO}_m\text{-PGL}_n$  with different values of  $m$  and  $n$ , by varying the monomer feeding ratio ( $[\text{BO}]_0/[\text{EEGE}]_0/[\text{BA}]_0$ ). All the products were characterized by  $^1\text{H}$  NMR and SEC, and the results were listed in Table 2, together with the theoretical values.

**Table 2.** Characteristics of the Diblock Copolymers According to the Weight Fraction of PGL Block ( $w_{\text{PGL}}^a$ ).

Entry	[BO] <sub>0</sub> /[EEGE] <sub>0</sub> / [BA] <sub>0</sub> <sup>b</sup>	Theoretical results <sup>b</sup>			<sup>1</sup> H NMR results <sup>c</sup>			SEC results <sup>d</sup>	
		Formula	$w_{\text{PGL}}$	$Mn_{\text{theo.}}$ (kg mol <sup>-1</sup> )	Formula	$w_{\text{PGL}}$	$Mn_{\text{NMR}}$ (kg mol <sup>-1</sup> )	$Mn_{\text{SEC}}$ (kg mol <sup>-1</sup> )	$\bar{D}$
HQ021B	10/3/1	PBO <sub>10</sub> - PGL <sub>3</sub>	0.22	1.1	PBO <sub>10</sub> - PGL <sub>3</sub>	0.19	1.2	1.3	1.13
HQ021A	21/6/1	PBO <sub>21</sub> - PGL <sub>6</sub>	0.23	2.1	PBO <sub>21</sub> - PGL <sub>6</sub>	0.22	2.1	2.5	1.16
HQ020	39/16/1	PBO <sub>39</sub> - PGL <sub>16</sub>	0.28	4.1	PBO <sub>48</sub> - PGL <sub>23</sub>	0.33	5.2	6.0	1.17
HQ029	13/47/1	PBO <sub>13</sub> - PGL <sub>47</sub>	0.77	4.5	PBO <sub>14</sub> - PGL <sub>57</sub>	0.79	5.3	5.2	1.13

<sup>a</sup>The weight fraction of PGL block ( $w_{\text{PGL}}$ ) in PBO<sub>m</sub>-PGL<sub>n</sub> is calculated as  $w_{\text{PGL}} = Mr_{\text{GL}} \times n / (Mr_{\text{BO}} \times m + Mr_{\text{GL}} \times n + Mr_{\text{BA}})$ , in which  $Mr_{\text{GL}}$ ,  $Mr_{\text{BO}}$  and  $Mr_{\text{BA}}$  are the molar masses of GL (74 g mol<sup>-1</sup>), BO (72 g mol<sup>-1</sup>) and BA (108 g mol<sup>-1</sup>), respectively. <sup>b</sup>Theoretical results are calculated on the basis of monomer feeding ratio ([BO]<sub>0</sub>/[EEGE]<sub>0</sub>/[BA]<sub>0</sub>) and the monomer conversions (100% for both BO and EEGE in all cases herein). <sup>c</sup>NMR results were derived from <sup>1</sup>H NMR spectra. <sup>d</sup>SEC was performed in DMF using an RI detector and the results were determined with PMMA as the standard.

One can see that, for each copolymer, the <sup>1</sup>H NMR and SEC characterization results were comparable with each other and in agreement with theoretical value, indicating the synthetic procedure for diblock copolymer was defined and reproducible.

### 3.2.2 Syntheses and characterizations of triblock copolymers

The aforementioned synthetic procedure for diblock copolymers was proved defined and thus was adapted to synthesize triblock copolymers by using a bifunctional initiator, 1,4-benzenedimethanol (BDM). In the standard procedure (Scheme 3), the PBO block bearing two living centers at the chain ends was first obtained, the chain was subsequently extended with the addition of PEEGE blocks at both ends giving PEEGE-PBO-PEEGE intermediate. At last, under acidic conditions, the acetal groups in PEEGE blocks were removed to give the PGL-PBO-PGL product. All the intermediates and the product were characterized by <sup>1</sup>H NMR and SEC so to evaluate the synthetic procedure.

Here are the results of the intermediates and product in the synthetic process of PGL<sub>12</sub>-PBO<sub>84</sub>-PGL<sub>12</sub> (Entry HQ033). The polymers were first characterized by <sup>1</sup>H NMR (Figure 4).

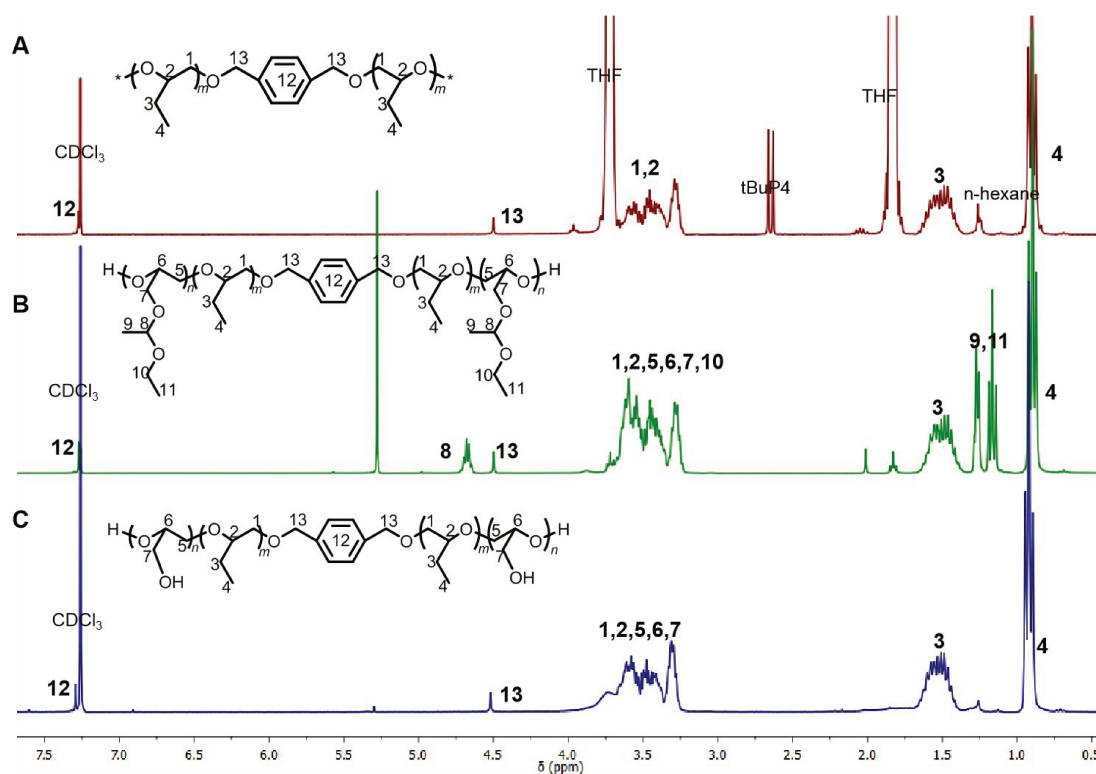


**Figure 4.**  $^1\text{H}$  NMR spectra of (A) PBO (reaction medium), (B) PEEGE-PBO-PEEGE (without tBuP4) and (C) PGL-PBO-PGL in the synthetic process of PGL<sub>12</sub>-PBO<sub>84</sub>-PGL<sub>12</sub> (Entry HQ033), recorded in  $\text{CDCl}_3$  at 300 K.

Figure 4A displays the  $^1\text{H}$  NMR spectrum of the homopolymerization medium. The peaks assigned to the protons of the initiator moiety [proton 12 ( $\delta$  7.27 ppm, *s*) and proton 13 ( $\delta$  4.50 ppm, *s*)], the protons of the pendent ethyl group of BO repeat unit [protons 3 ( $\delta$  1.51 ppm, *s*) and protons 4 ( $\delta$  0.90 ppm, *s*)], as well as the protons in the polyether backbone [protons 1,2,  $\delta$  3.82–3.12 ppm, *m* (overlapping with THF,  $\delta$  3.72 ppm, *s*)] were detected. At the same time, the epoxide protons of BO monomer were not detected, indicating the consumption of the monomers ( $p_{\text{BO}} = 1$ ). Afterwards, EEGE units were added to extend the living PBO chain from both ends forming the linear triblock architecture. At the end of copolymerization, EEGE was consumed ( $p_{\text{EEGE}} = 1$ ), as confirmed by  $^1\text{H}$  NMR with the absence of epoxide protons of EEGE monomer (data was not shown here).

Figure 4B indicates the PEEGE-PBO-PEEGE intermediate after the removal of tBuP4. This  $^1\text{H}$  NMR spectrum showed the characteristic peaks assigned to the PEEGE blocks, including the methine protons (protons 8,  $\delta$  4.58 ppm, *s*), and the methyl protons [protons 9 ( $\delta$  1.27 ppm, *s*) and protons 11 ( $\delta$  1.17 ppm, *s*)], besides the peaks belonging to PBO block (protons 3 and 4) and polyether backbone (protons 1,2,5,6,7,10). Figure 4C shows the  $^1\text{H}$  NMR spectrum of the final product, which

evidenced the removal of acetal groups by the disappearance of the peaks belonging to the methine (proton 8) and methyl groups (protons 9 and 11) of EEGE units, indicating the PGL-PBO-PGL product was obtained.

Deriving from <sup>1</sup>H NMR spectra, the DP of PBO block (*i.e.*,  $2m$  in PBO<sub>2m</sub>) was calculated on the basis of the integrals of methyl protons in BO units (proton 4) and the methylene protons in the initiator moiety (proton 13), using the formula of  $2m = (I_4/6)/(I_{13}/4) \times 2$ . The DP of PEEGE block (*i.e.*,  $n$  in PEEGE<sub>n</sub>-PBO<sub>2m</sub>-PEEGE<sub>n</sub>) was calculated on the basis of the integrals of the methine proton in EEGE units (proton 8) and the methylene protons in the initiator moiety (proton 13), with the formula of  $n = (I_8/2)/(I_{13}/4)$ . The DP of PGL block (*i.e.*,  $n$  in PGL<sub>n</sub>-PBO<sub>2m</sub>-PGL<sub>n</sub>) was determined from the integrals of the protons in backbone (protons 1,2,5,6,7) and the methylene protons in the initiator (proton 13), with the formula of  $n = [(I_{1,2,5,6,7}-I_4)/10]/(I_{13}/4)$ . The values derived from <sup>1</sup>H NMR spectra were listed in Table 3.

**Table 3.** Characteristics of the Intermediates and the Product in the Synthetic Process of PGL<sub>12</sub>-PBO<sub>84</sub>-PGL<sub>12</sub> (Entry HQ033).

Polymer	Theoretical results <sup>a</sup>			<sup>1</sup> H NMR results <sup>b</sup>			SEC results <sup>c</sup>	
	$2m_{\text{theo.}}$	$n_{\text{theo.}}$	$Mn_{\text{theo.}}$ (kg mol <sup>-1</sup> )	$2m_{\text{NMR}}$	$n_{\text{NMR}}$	$Mn_{\text{NMR}}$ (kg mol <sup>-1</sup> )	$Mn_{\text{SEC}}$ (kg mol <sup>-1</sup> )	$\bar{D}$
PBO <sub>2m</sub>	84	--	6.2	93	--	6.8	5.9	1.08
PEEGE <sub>n</sub> -PBO <sub>2m</sub> - PEEGE <sub>n</sub>	84	12	9.7	70	10	8.2	8.8	1.07
PGL <sub>n</sub> -PBO <sub>2m</sub> - PGL <sub>n</sub>	84	12	8.0	88	10	7.9	8.7	1.10

<sup>a</sup>Theoretical DP values ( $2m_{\text{theo.}}$  and  $n_{\text{theo.}}$ ) were calculated on the basis of the monomer feeding ratio ( $[\text{BO}]_0/[\text{EEGE}]_0/[\text{BDM}]_0$ ) and monomer conversions (100% for both BO and EEGE herein); theoretical molar mass ( $Mn_{\text{theo.}}$ ) was calculated based on the theoretical DP values. <sup>b</sup>NMR results were derived from the <sup>1</sup>H NMR spectrum of each polymer; <sup>c</sup>SEC was performed in DMF using an RI detector and the results were determined with PMMA as the standard.

It can be seen that the characterization results by <sup>1</sup>H NMR were close to the theoretical ones derived from monomer feeding ratio and monomer conversions, indicating the reactions in the synthetic procedure were defined.

The intermediates and the product were characterized by SEC. The traces were shown in Figure 5 and the characterization results were listed in Table 3.

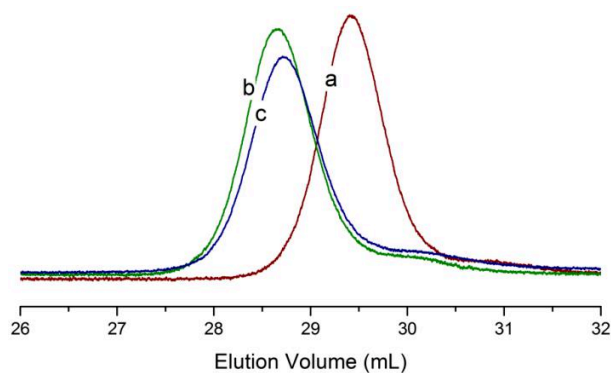


**Figure 5.** SEC traces of (a) PBO (reaction medium), (b) PEEGE-PBO-PEEGE (without tBuP4) and (c) PGL-PBO-PGL in the synthetic process of PGL<sub>12</sub>-PBO<sub>84</sub>-PGL<sub>12</sub> (Entry HQ033), performed in DMF using an RI detector.

Figure 5 clearly shows that all the traces were unimodal and narrowly distributed corresponding to the low polydispersity values ( $\bar{D}$ , Table 3), indicating all the polymers were of high purity. The number-average molar mass ( $M_{nSEC}$ ) of each polymer was determined with PMMA as the standard, and the values were in agreement with the theoretical ones as well as those derived from <sup>1</sup>H NMR (Table 3), evidencing the reactions were controlled.

Applying the same procedure, a set of triblock copolymers PGL<sub>n</sub>-PBO<sub>2m</sub>-PGL<sub>n</sub> with different values of  $m$  and  $n$  was synthesized by varying the monomer feeding ratio ( $[BO]_0/[EEGE]_0/[BDM]_0$ ). All the products were characterized by <sup>1</sup>H NMR and SEC, with the results being gathered in Table 4.

**Table 4.** Characteristics of the Triblock Copolymers According to the Weight Fraction of PGL Blocks ( $w_{PGL}^a$ ).

Entry	$[BO]_0/[EEGE]_0/[BDM]_0$	Theoretical results <sup>b</sup>			<sup>1</sup> H NMR results <sup>c</sup>			SEC results <sup>d</sup>	
		Formula	$w_{PGL}$	$M_{ntheo.}$ (kg mol <sup>-1</sup> )	Formula	$w_{PGL}$	$M_{nNMR}$ (kg mol <sup>-1</sup> )	$M_{nSEC}$ (kg mol <sup>-1</sup> )	$\bar{D}$
HQ134	84/14/1	PGL <sub>7</sub> -PBO <sub>84</sub> -PGL <sub>7</sub>	0.14	7.2	PGL <sub>6</sub> -PBO <sub>86</sub> -PGL <sub>6</sub>	0.12	7.2	8.3	1.08
HQ132	81/19/1	PGL <sub>10</sub> -PBO <sub>81</sub> -PGL <sub>10</sub>	0.19	7.4	PGL <sub>10</sub> -PBO <sub>89</sub> -PGL <sub>10</sub>	0.18	7.9	10.6	1.03
HQ153	85/22/1	PGL <sub>11</sub> -PBO <sub>85</sub> -PGL <sub>11</sub>	0.21	7.9	PGL <sub>11</sub> -PBO <sub>97</sub> -PGL <sub>11</sub>	0.18	8.7	8.6	1.07
HQ035	20/6/1	PGL <sub>3</sub> -PBO <sub>20</sub> -PGL <sub>3</sub>	0.22	2.1	PGL <sub>4</sub> -PBO <sub>21</sub> -PGL <sub>4</sub>	0.25	2.2	3.0	1.08

**Table 4. Continued.**

Entry	[BO] <sub>0</sub> /[EEGE] <sub>0</sub> /[BDM] <sub>0</sub>	Theoretical results <sup>b</sup>			<sup>1</sup> H NMR results <sup>c</sup>			SEC results <sup>d</sup>	
		Formula	w <sub>PGL</sub>	M <sub>n,theo.</sub> (kg mol <sup>-1</sup> )	Formula	w <sub>PGL</sub>	M <sub>n,NMR</sub> (kg mol <sup>-1</sup> )	M <sub>n,SEC</sub> (kg mol <sup>-1</sup> )	Đ
HQ033	84/24/1	PGL <sub>12</sub> -PBO <sub>84</sub> - PGL <sub>12</sub>	0.22	8.0	PGL <sub>10</sub> -PBO <sub>88</sub> - PGL <sub>10</sub>	0.18	7.9	8.7	1.10
HQ031	40/12/1	PGL <sub>6</sub> -PBO <sub>40</sub> - PGL <sub>6</sub>	0.23	3.9	PGL <sub>7</sub> -PBO <sub>43</sub> - PGL <sub>7</sub>	0.23	4.2	5.4	1.07
HQ081 B	84/41/1	PGL <sub>21</sub> -PBO <sub>84</sub> - PGL <sub>21</sub>	0.33	9.2	PGL <sub>18</sub> -PBO <sub>89</sub> - PGL <sub>18</sub>	0.29	9.2	10.1	1.09
HQ112	63/32/1	PGL <sub>16</sub> -PBO <sub>63</sub> - PGL <sub>16</sub>	0.34	7.1	PGL <sub>6</sub> -PBO <sub>68</sub> - PGL <sub>6</sub>	0.15	5.9	4.3	1.34
HQ034	20/11/1	PGL <sub>6</sub> -PBO <sub>20</sub> - PGL <sub>6</sub>	0.35	2.4	PGL <sub>6</sub> -PBO <sub>21</sub> - PGL <sub>6</sub>	0.35	2.5	3.6	1.09
HQ119 B	62/36/1	PGL <sub>18</sub> -PBO <sub>62</sub> - PGL <sub>18</sub>	0.37	7.3	PGL <sub>18</sub> -PBO <sub>70</sub> - PGL <sub>18</sub>	0.34	7.9	10.1	1.05
HQ077	80/50/1	PGL <sub>25</sub> -PBO <sub>80</sub> - PGL <sub>25</sub>	0.39	9.6	PGL <sub>25</sub> -PBO <sub>96</sub> - PGL <sub>25</sub>	0.34	10.8	9.2	1.19
HQ113	61/39/1	PGL <sub>19</sub> -PBO <sub>61</sub> - PGL <sub>19</sub>	0.39	7.4	PGL <sub>11</sub> -PBO <sub>70</sub> - PGL <sub>11</sub>	0.24	6.9	6.4	1.24
HQ119 A	59/40/1	PGL <sub>20</sub> -PBO <sub>59</sub> - PGL <sub>20</sub>	0.40	7.4	PGL <sub>21</sub> -PBO <sub>66</sub> - PGL <sub>21</sub>	0.38	7.9	9.9	1.05
HQ099	41/32/1	PGL <sub>16</sub> -PBO <sub>41</sub> - PGL <sub>16</sub>	0.43	5.5	PGL <sub>15</sub> -PBO <sub>44</sub> - PGL <sub>15</sub>	0.40	5.5	7.6	1.08
HQ038 B	14/13/1	PGL <sub>7</sub> -PBO <sub>14</sub> - PGL <sub>7</sub>	0.46	2.1	PGL <sub>7</sub> -PBO <sub>14</sub> - PGL <sub>7</sub>	0.47	2.2	3.1	1.12
HQ098	21/20/1	PGL <sub>10</sub> -PBO <sub>21</sub> - PGL <sub>10</sub>	0.47	3.1	PGL <sub>11</sub> -PBO <sub>22</sub> - PGL <sub>11</sub>	0.49	3.4	4.9	1.09
HQ038 A	13/44/1	PGL <sub>22</sub> -PBO <sub>13</sub> - PGL <sub>22</sub>	0.75	4.3	PGL <sub>29</sub> -PBO <sub>14</sub> - PGL <sub>29</sub>	0.78	4.8	5.9	1.14

<sup>a</sup>The weight fraction of PGL blocks (w<sub>PGL</sub>) in PGL<sub>n</sub>-PBO<sub>2m</sub>-PGL<sub>n</sub> was calculated as  $w_{PGL} = M_{rGL} \times 2n / (M_{rBO} \times 2m + M_{rGL} \times 2n + M_{rBDM})$ , in which  $M_{rGL}$ ,  $M_{rBO}$  and  $M_{rBDM}$  are the molar masses of GL (74 g mol<sup>-1</sup>), BO (72 g mol<sup>-1</sup>) and BDM (138 g mol<sup>-1</sup>), respectively. <sup>b</sup>Theoretical results were calculated on the basis of monomer feeding ratio ([BO]<sub>0</sub>/[EEGE]<sub>0</sub>/[BDM]<sub>0</sub>) and monomer conversions (100% for both BO and EEGE in all cases herein). <sup>c</sup>NMR results were derived from <sup>1</sup>H NMR spectra. <sup>d</sup>SEC was performed in DMF using an RI detector and the results were determined with PMMA as the standard.

One can see that most of the copolymers (15 of 17) were well defined as evidenced by the comparable <sup>1</sup>H NMR and SEC characterization results to the theoretical values, as well as the low polydispersity values (Đ ~ 1.1). The undefined copolymers, Entry

HQ112 ( $\bar{M}_w \sim 1.34$ ) and Entry HQ113 ( $\bar{M}_w \sim 1.24$ ), were supposed to result from deteriorated EEGE (for unclear reasons). In general, the synthetic procedure for triblock copolymers was also demonstrated as defined and reproducible.

Another evidence on the feasibility and reproducibility of this synthetic procedure for the triblock copolymers was provided by the work of Sandra Kalem (Master de Chimie de Paris Centre). In her work, a library of PGL<sub>n</sub>-PBO<sub>2m</sub>-PGL<sub>n</sub> copolymers, with the value of  $n$  focusing around 10 and  $2m$  varying from 30 to 80, were prepared following the same synthetic procedure (Scheme 3). The characterization results (Table 5) of the PGL-PBO-PGL products and the respective PEEGE-PBO-PEEGE intermediates clearly showed that the polymers were well defined, as evidenced by the comparable characterization results to the theoretical values and the low polydispersity values ( $\bar{M}_w \sim 1.04$ ).

**Table 5.** Characteristics of the Triblock Copolymers Synthesized by Sandra Kalem According to the Weight Fraction of PGL Blocks ( $w_{\text{PGL}}^a$ ).

Entry	PGL-PBO-PGL			PEEGE-PBO-PEEGE			
	Formula <sup>b</sup>	$w_{\text{PGL,theo.}}^c$	$w_{\text{PGL,NMR}}^d$	$M_n^{\text{theo.}}^c$ (kg mol <sup>-1</sup> )	$M_n^{\text{NMR}}^d$ (kg mol <sup>-1</sup> )	$M_n^{\text{SEC}}^e$ (kg mol <sup>-1</sup> )	$\bar{M}_w^e$
SK1	PGL <sub>8</sub> -PBO <sub>78</sub> -PGL <sub>8</sub>	0.20	0.17	8.5	8.0	8.7	1.04
SK2	PGL <sub>9</sub> -PBO <sub>68</sub> -PGL <sub>9</sub>	0.22	0.21	7.9	7.5	9.0	1.04
SK3	PGL <sub>8</sub> -PBO <sub>59</sub> -PGL <sub>8</sub>	0.25	0.21	7.2	6.7	7.8	1.05
SK4	PGL <sub>10</sub> -PBO <sub>49</sub> -PGL <sub>10</sub>	0.28	0.27	6.7	6.4	7.5	1.03
SK5	PGL <sub>8</sub> -PBO <sub>42</sub> -PGL <sub>8</sub>	0.33	0.27	5.7	5.4	6.5	1.04
SK6	PGL <sub>9</sub> -PBO <sub>33</sub> -PGL <sub>9</sub>	0.38	0.33	5.3	5.0	6.0	1.04

<sup>a</sup>The weight fraction of PGL blocks ( $w_{\text{PGL}}$ ) in PGL<sub>n</sub>-PBO<sub>2m</sub>-PGL<sub>n</sub> was calculated as  $w_{\text{PGL}} = M_{\text{rGL}} \times 2n / (M_{\text{rBO}} \times 2m + M_{\text{rGL}} \times 2n + M_{\text{rBDM}})$ , in which  $M_{\text{rGL}}$ ,  $M_{\text{rBO}}$  and  $M_{\text{rBDM}}$  are the molar masses of GL (74 g mol<sup>-1</sup>), BO (72 g mol<sup>-1</sup>) and BDM (138 g mol<sup>-1</sup>), respectively. <sup>b</sup>Formula were reported as the ones determined by <sup>1</sup>H NMR. <sup>c</sup>Theoretical results were calculated on the basis of monomer feeding ratio ( $[\text{BO}]_0/[\text{EEGE}]_0/[\text{BDM}]_0$ ) and monomer conversions (100% for both BO and EEGE in all cases herein). <sup>d</sup>NMR results were derived from <sup>1</sup>H NMR spectra. <sup>e</sup>SEC was performed in DMF using an RI detector and the results were determined with PMMA as the standard.

### 3.3 Self-assembly behaviors of block copolymers

The defined block copolymers, both diblock and triblock copolymers, were further systematically investigated on their self-assembly behaviors by DLS, SLS, TEM, and SAXS.

### 3.3.1 Self-assembly behaviors of diblock copolymers

The self-assemblies of diblock copolymers (Table 2) were prepared by thin-film rehydration method, namely rehydrating the polymer films which were pre-coated on the inner wall of sample vials. After being sufficiently rehydrated, the polymer films detached from the surfaces, giving the suspensions.

By appearance, the suspensions were different from each other. In the suspension of PBO<sub>10</sub>-PGL<sub>3</sub> (Entry HQ021B), the film formed oily drops adhering to the inner wall or suspending in the aqueous solution. However, the film of PBO<sub>20</sub>-PGL<sub>6</sub> (Entry HQ021A) formed large visible aggregates. The undefined aggregates (different in size and shape seen by eyes) would precipitate quickly without stirring and could be removed when extruded through a 0.45  $\mu$ m syringe filter, resulting in a clear aqueous solution of rather low light scattering intensity (measured by DLS), indicating the loss of sample. On the contrary, the suspension of PBO<sub>39</sub>-PGL<sub>16</sub> (Entry HQ020) was homogeneous with a white-bluish appearance, while the suspension of PBO<sub>13</sub>-PGL<sub>47</sub> (Entry HQ029) was transparent. Both suspensions were stable as a function of time, and no sample loss after being extruded through the 0.45  $\mu$ m syringe filter as no decrease in the light scattering intensity measured by DLS.

Therefore, the assemblies of PBO<sub>10</sub>-PGL<sub>3</sub> (Entry HQ021B) and PBO<sub>20</sub>-PGL<sub>6</sub> (Entry HQ021A) were not further characterized, while the assemblies of PBO<sub>39</sub>-PGL<sub>16</sub> (Entry HQ020) and PBO<sub>13</sub>-PGL<sub>47</sub> (Entry HQ029) were then characterized by DLS and SLS to acquire information on the sizes and the molecular weights of the self-assemblies.

Figure 6 gives the autocorrelation functions acquired by DLS which were mathematically treated by using the NNLS analysis, as well as the respective intensity-weighted particle size distribution (PSD) curves.

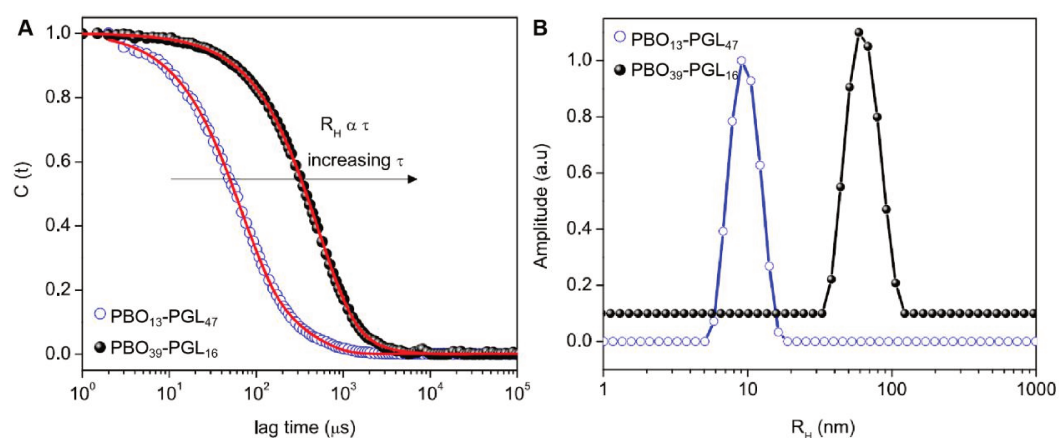


**Figure 6.** (A) Autocorrelation functions (dots) and corresponding cumulant fittings (solid lines), and (B) the respective particle size distribution curves of the assemblies of PBO<sub>39</sub>-PGL<sub>16</sub> (Entry HQ020) and PBO<sub>13</sub>-PGL<sub>47</sub> (Entry HQ029), according to the legend.

Figure 6A clearly showed that the cumulant fit autocorrelation functions resulted in single populations of relaxation times, consistent with the monomodal PSD curves which indicated the particles were of single populations (Figure 6B). To note, the presence of the monomodal distribution of relaxation time is essential to determine the hydrodynamic radius ( $R_H$ ) and polydispersity ( $PDI = \mu_2/I^2$ ) via the cumulant method.

The molecular weight ( $M_{WNPs}$ ) and aggregation number ( $N_{agg}$ ) of the self-assembled nanoparticles were determined by DLS data. Using the Debye plot (Equation 3), by plotting  $Kc/R_\theta$  against  $c$ , the value of  $M_{WNPs}$  was extracted from the inverse of the intercept. Accordingly,  $N_{agg}$  was calculated using the relation of  $N_{agg} = M_{WNPs}/M_{W_{polymer}}$  (Equation 6). The results derived from DLS and SLS measurements were listed in Table 6.

**Table 6.** Scattering Data for the Assemblies of the Diblock Copolymers According to the Weight Fraction of PGL block ( $w_{PGL}^a$ ).

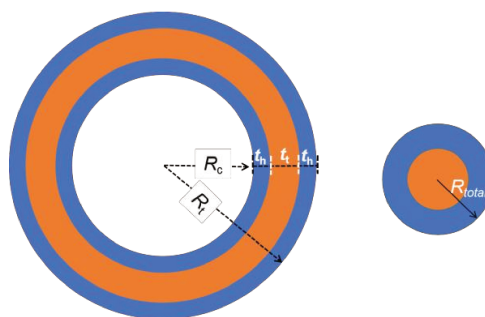
Entry	Formula <sup>a</sup>	$w_{PGL}^a$	$R_H$ (nm)	PDI	$M_{WNPs}$ (kDa)	$N_{agg}$
<b>Aggregates</b>						
HQ021B	PBO <sub>10</sub> -PBO <sub>3</sub>	0.22	-- <sup>b</sup>			
HQ021A	PBO <sub>21</sub> -PGL <sub>6</sub>	0.23				
<b>Polymersomes</b>						
HQ020	PBO <sub>39</sub> -PGL <sub>16</sub>	0.28	67.2	0.26	$4.89 \times 10^4$	12300
<b>Spherical micelles</b>						
HQ029	PBO <sub>13</sub> -PGL <sub>47</sub>	0.77	9.7	0.24	$3.62 \times 10^2$	77

<sup>a</sup> $w_{PGL}$  and formula were reported as the theoretical vaules; <sup>b</sup>No data, because the undefined aggregates were not suitable for DLS or SLS measurements as mentioned in the text.

As the results show that the values of  $R_H$  and  $N_{agg}$  for the assemblies of PBO<sub>39</sub>-PGL<sub>16</sub> (Entry HQ020) were respectively ten-fold and two orders of magnitude larger than those for the assemblies of PBO<sub>13</sub>-PGL<sub>47</sub> (Entry HQ020), indicating the former was much of a vesicle character while the latter was supposed to be micelles [20].

The assemblies were further probed by SAXS. The acquired SAXS pattern was analyzed using the SAXfit software and fitted with the form factor of bilayered vesicle in the context of vesicles suggested by DLS (schematically shown in the left panel of Scheme 4), or with the former factor of spherical shell in the context of spherical micelles suggested by DLS (the right panel of Scheme 4), to acquire respective structural parameters.

**Scheme 4.** Form Factors of Bilayered Vesicle (left) and Spherical Shell (right) with Respective Structural Parameters. Blue layer indicates the hydrophilic PGL layer while the orange is the hydrophobic PBO layer.



It shows that the SAXS profile for PBO<sub>39</sub>-PGL<sub>16</sub> (Entry HQ020) assemblies (Figure 7A) was well-fitted by using the bilayered vesicle form factor, giving  $t_1 = 6.6$  nm. The value of  $t_1$ , *i.e.*, the thickness of the hydrophobic PBO layer agreed with the reported thickness of a monolayer of PBO block in the work of Riccardo Wehr et al., wherein the self-assembly behaviors of PBO-PGL were deeply investigated [21]. Figure 7B profiles the SAXS pattern of the PBO<sub>13</sub>-PGL<sub>47</sub> (Entry HQ029) assemblies which was well-fitted by using the core-shell spherical form factor with  $R_{total} = 6$  nm, also consistent with the thickness a monolayer of PBO block [21].

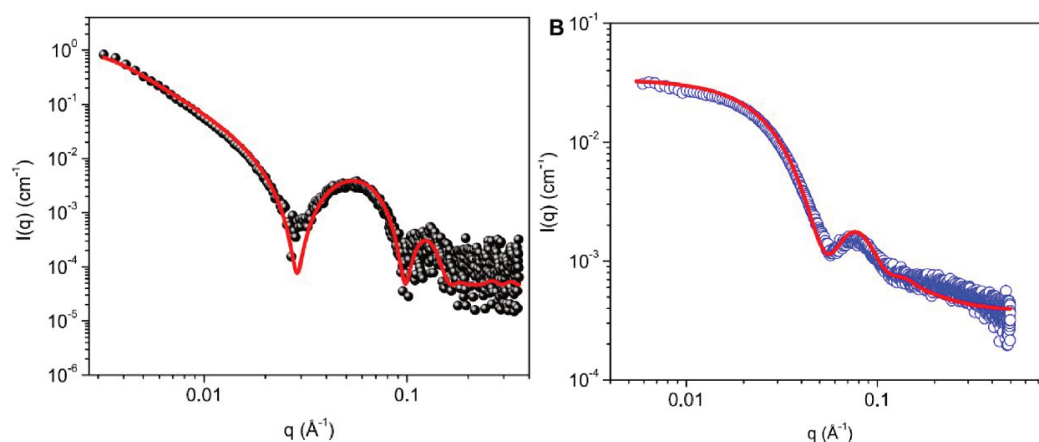


**Figure 7.** (A) SAXS profile of the assemblies of PBO<sub>39</sub>-PGL<sub>16</sub> (Entry HQ020) and the corresponding fitting curve by using the bilayered vesicle form factor (solid line). (B) SAXS profile of the assemblies of PBO<sub>13</sub>-PGL<sub>47</sub> (Entry HQ029) and the fitting curve by using the core-shell spherical form factor (solid line).

Furthermore, the assemblies were observed by TEM (Figure 8). Figures 8A and B display respectively the TEM images of the PBO<sub>39</sub>-PGL<sub>16</sub> (Entry HQ020) and PBO<sub>13</sub>-PGL<sub>47</sub> (Entry HQ029) assemblies. The images straightforward evidenced that the

morphologies of the assemblies were respectively vesicles and spherical micelles, in accordance with the SAXS data.

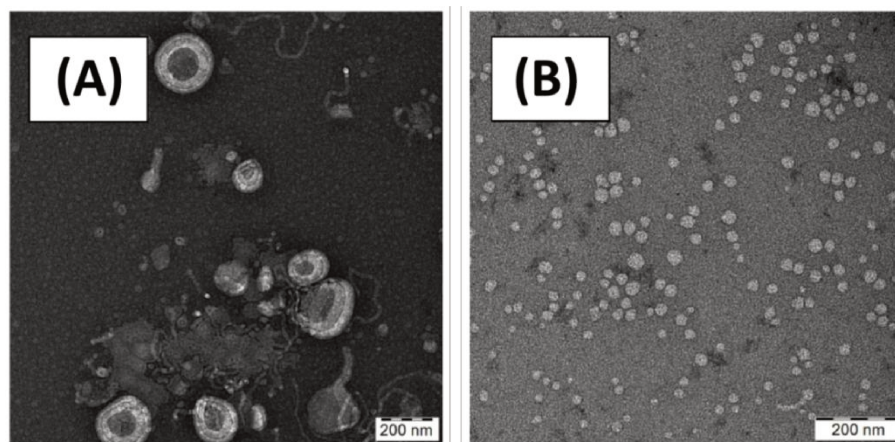


**Figure 8.** TEM images of the assemblies of (A) PBO<sub>39</sub>-PGL<sub>16</sub> (Entry HQ020) and PBO<sub>13</sub>-PGL<sub>47</sub> (Entry HQ029).

In conclusion, the morphology of the diblock PBO-PGL copolymers was mainly determined by the weight fraction of PGL block ( $w_{\text{PGL}}$ ): when  $w_{\text{PGL}}$  was as small as 0.22 or 0.23, the polymer formed undefined aggregates, resulting from the relatively small portion of PGL to stabilize the assemblies. Riccardo Wehr et al. also observed PBO<sub>67</sub>-PGL<sub>14</sub> ( $w_{\text{PGL}} = 0.18$ ) formed aggregates [21]; when  $w_{\text{PGL}}$  increased to 0.28, the polymer self-assembled into vesicles. These data are similar to the reported results that PBO<sub>50</sub>-PGL<sub>18</sub> ( $w_{\text{PGL}} = 0.27$ ) formed deformed vesicles and PBO<sub>42</sub>-PGL<sub>21</sub> ( $w_{\text{PGL}} = 0.33$ ) formed pure vesicles [21]; at last, when  $w_{\text{PGL}}$  was as large as 0.77, the polymer formed spherical micelles. This also agreed with the published result that PBO<sub>42</sub>-PGL<sub>77</sub> ( $w_{\text{PGL}} = 0.65$ ) formed pure micelles [21]. To mention that in Riccardo Wehr's work [21] the assemblies were prepared via the solvent-exchange method and were extensively characterized by TEM enabling to provide detailed information on the transformation in morphologies as well as the differences between the extruded and unextruded samples. Taking into account the results in both works, it can be concluded that the hydrophobic-to-hydrophilic ratio is the crucial parameter deciding the self-assembled morphology.

### 3.3.2 Self-assembly behaviors of the triblock copolymers

The self-assemblies of all the defined triblock copolymers were also prepared via thin-film rehydration except the polymer PGL<sub>3</sub>-PBO<sub>20</sub>-PGL<sub>3</sub> (Entry HQ035) which degraded during storage. The undefined PGL<sub>16</sub>-PBO<sub>63</sub>-PGL<sub>16</sub> (Entry HQ112) and PGL<sub>18</sub>-PBO<sub>61</sub>-PGL<sub>19</sub> (Entry HQ113) were not applied to this study either.

The suspensions obtained after the sufficient rehydration of polymer film were observed by eyes first. According to the appearance, the suspensions were classified into two groups, having undefined visible aggregates or not. The first group included the suspensions of PGL<sub>7</sub>-PBO<sub>84</sub>-PGL<sub>7</sub> (Entry HQ134), PGL<sub>10</sub>-PBO<sub>81</sub>-PGL<sub>10</sub> (Entry HQ132) and PGL<sub>11</sub>-PBO<sub>85</sub>-PGL<sub>11</sub> (Entry HQ153) assemblies, having undefined aggregates which would precipitate quickly without stirring and could be removed by extrusion through a 0.45  $\mu\text{m}$  syringe filter producing a clear aqueous solution with very low light scattering intensities (by DLS), indicating the loss of sample.

The other suspensions were homogeneous and stable with a white-bluish or colorless transparent appearance. These suspension solutions were extruded through the syringe filter (0.45  $\mu\text{m}$ ) to remove dust before being analyzed by DLS and SLS following the characterization suggestions. To note, the extrusions did not cause sample loss verified by the unchanged light scattering intensity of the extruded solutions (by DLS).

Figure 9 provides the representative DLS measurement results of the assemblies of PGL<sub>12</sub>-PBO<sub>84</sub>-PGL<sub>12</sub> (Entry HQ081B;  $w_{\text{PGL}} = 0.22$ ), PGL<sub>16</sub>-PBO<sub>41</sub>-PGL<sub>16</sub> (Entry HQ099;  $w_{\text{PGL}} = 0.43$ ), and PGL<sub>10</sub>-PBO<sub>21</sub>-PGL<sub>10</sub> (Entry HQ098;  $w_{\text{PGL}} = 0.47$ ). It can be seen that the cumulant fit autocorrelation functions had single populations of relaxation time (Figure 9A) which resulted in the monomodal PSD curves (Figure 9B) and produced the values of  $R_{\text{H}}$  and PDI.

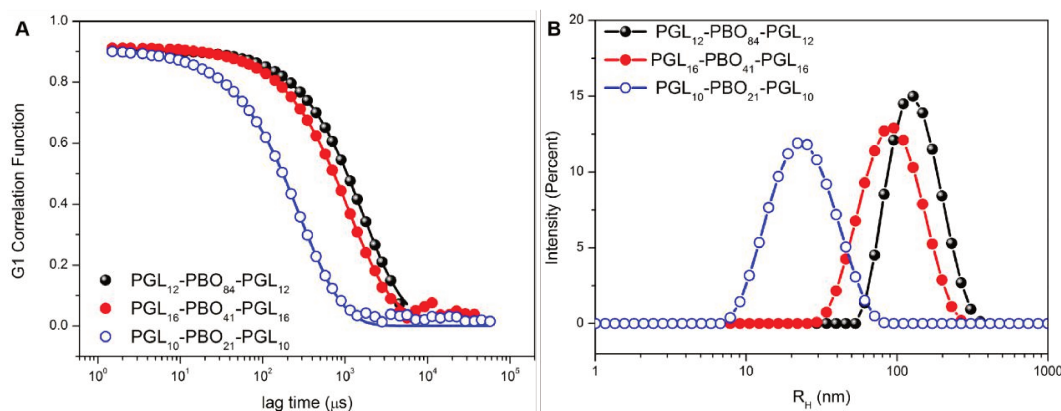


**Figure 9.** Representative DLS data of the assemblies of PGL<sub>12</sub>-PBO<sub>84</sub>-PGL<sub>12</sub> (Entry HQ033), PGL<sub>16</sub>-PBO<sub>41</sub>-PGL<sub>16</sub> (Entry HQ099) and PGL<sub>10</sub>-PBO<sub>21</sub>-PGL<sub>10</sub> (Entry HQ098), according to the legend: (A) Autocorrelation functions and corresponding cumulant fittings (solid lines), and (B) the respective intensity-weighted particle size distribution curves.

Moreover, using the Debye plot (Equation 3) by plotting  $Kc/R_{\theta}$  against  $c$  at a given angle, the value of  $M_{\text{WNPs}}$  was extracted from the inverse of the intercept.

Accordingly, the value of  $N_{agg}$  was determined using the relation  $N_{agg} = M_{WNPS}/M_{W_{polymer}}$  (Equation 6). The light scattering results of the triblock copolymer self-assemblies were gathered in Table 7.

**Table 7.** Scattering Data for the Assemblies of Triblock Copolymers According to the Weight Fraction of PGL Blocks ( $w_{PGL}^a$ ).

Entry	Formula <sup>a</sup>	$w_{PGL}^a$	$R_H$ (nm)	PDI	$M_{WNPS}$ (kDa)	$N_{agg}$
<b>Aggregates</b>						
HQ134	PGL <sub>7</sub> -PBO <sub>84</sub> -PGL <sub>7</sub>	0.14				
HQ132	PGL <sub>10</sub> -PBO <sub>81</sub> -PGL <sub>10</sub>	0.19	-- <sup>b</sup>			
HQ153	PGL <sub>11</sub> -PBO <sub>85</sub> -PGL <sub>11</sub>	0.21				
<b>Polymersomes</b>						
HQ033	PGL <sub>12</sub> -PBO <sub>84</sub> -PGL <sub>12</sub>	0.22	124	0.12	$9.71 \times 10^4$	12100
HQ031	PGL <sub>6</sub> -PBO <sub>40</sub> -PGL <sub>6</sub>	0.23	109	0.10	$6.17 \times 10^4$	15800
HQ081B	PGL <sub>21</sub> -PBO <sub>84</sub> -PGL <sub>21</sub>	0.33	111	0.18	$7.64 \times 10^4$	8300
HQ034	PGL <sub>6</sub> -PBO <sub>20</sub> -PGL <sub>6</sub>	0.35	87.8	0.21	$1.61 \times 10^5$	67200
HQ119B	PGL <sub>18</sub> -PBO <sub>62</sub> -PGL <sub>18</sub>	0.37	133	0.20	$3.76 \times 10^4$	5150
HQ077	PGL <sub>25</sub> -PBO <sub>80</sub> -PGL <sub>25</sub>	0.39	89.7	0.08	$8.30 \times 10^4$	8640
HQ119A	PGL <sub>20</sub> -PBO <sub>59</sub> -PGL <sub>20</sub>	0.40	79.5	0.10	$6.48 \times 10^4$	8760
<b>Spherical and Cylindrical Micelles</b>						
HQ099	PGL <sub>16</sub> -PBO <sub>41</sub> -PGL <sub>16</sub>	0.43	83.3	0.21	$3.07 \times 10^4$	4040
<b>Spherical micelles</b>						
HQ038B	PGL <sub>7</sub> -PBO <sub>14</sub> -PGL <sub>7</sub>	0.46	11.3	0.19	$7.58 \times 10^2$	361
HQ098	PGL <sub>10</sub> -PBO <sub>21</sub> -PGL <sub>10</sub>	0.47	20.5	0.21	$4.60 \times 10^3$	933
HQ038A	PGL <sub>22</sub> -PBO <sub>13</sub> -PGL <sub>22</sub>	0.75	13.4	0.21	$6.68 \times 10^2$	155

<sup>a</sup> $w_{PGL}$  and formula were reported as the theoretical values; <sup>b</sup>No data because the undefined aggregates were not suitable for DLS or SLS measurements herein.

The data showed that when  $w_{PGL}$  was 0.22–0.43, the resultant assemblies were featured by the much larger values of  $R_H$  and  $M_{WNPS}$  than those obtained with  $w_{PGL}$  ranging 0.46–0.75 (the last three samples in Table 7). The larger assemblies were suggested as vesicles while the smaller ones as micelles, based on the results with PBO-PGL. The anticipated nanostructures need to be further probed with other characterizations, such as TEM.

Figure 10 shows the TEM images of some representatives of each catalog of the morphologies suggested by DLS.

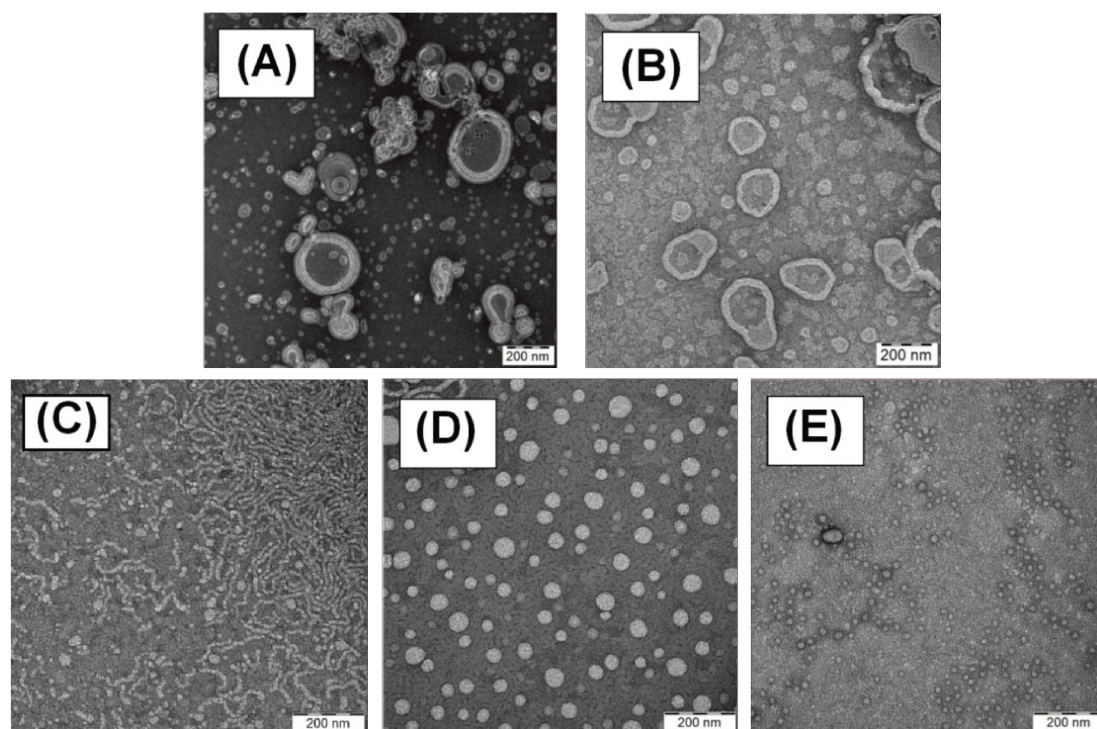


**Figure 10.** Representative TEM images of the assemblies of triblock copolymers: (A) PGL<sub>12</sub>-PBO<sub>84</sub>-PGL<sub>12</sub> (Entry HQ033), (B) PGL<sub>21</sub>-PBO<sub>84</sub>-PGL<sub>21</sub> (Entry HQ081B), (C) PGL<sub>16</sub>-PBO<sub>41</sub>-PGL<sub>16</sub> (Entry HQ099), (D) PGL<sub>10</sub>-PBO<sub>21</sub>-PGL<sub>10</sub> (Entry HQ098) and (E) PGL<sub>22</sub>-PBO<sub>13</sub>-PGL<sub>22</sub> (Entry HQ038A).

The TEM images agreed with the scattering results with the exception of the PGL<sub>16</sub>-PBO<sub>41</sub>-PGL<sub>16</sub> (Entry HQ099) assemblies (Figure 10C) which were priority of cylindrical micelles and not distinguishable by DLS because the basic equations used to calculate  $R_H$  in DLS measurement are originated from the correlation function cumulant analysis based on the assumption that the particles are non-interacting spheres and not anisotropic objects [22].

In Figure 10, from A to E, the  $w_{PGL}$  value of the assemblies-forming triblock copolymer increased and the morphology transitioned from polymersomes to cylindrical micelles to spherical micelles. Furthermore, comparing the images of Figure 10A and B, it can be seen that, in Figure 10A, there were a few undefined aggregates and the polymersomes were somewhat heterogeneous in size; while the polymersomes in Figure 10B were relatively homogeneous. Generally, with the increase of  $w_{PGL}$ , the particle size decreased, and the morphology transformed from vesicles to micelles. This kind of transformation in morphology was also observed in various works [21,23,24].

By systematically analyzing the triblock copolymers, it could conclude that, for the PGL-PBO-PGL prepared herein, when  $w_{PGL} \leq 0.21$ , the assemblies are undefined

aggregates; when  $0.22 \leq w_{\text{PGL}} \leq 0.40$  the assemblies are dominated by polymersomes; when  $w_{\text{PGL}} \sim 0.43$ , the assemblies are mostly cylindrical micelles; and when  $w_{\text{PGL}} \geq 0.46$ , the assemblies are defined spherical micelles.

As an extension of this work, the PGL-PBO-PGL copolymers prepared by Sandra (Table 5) were also studied in terms of their self-assembly behaviors, conducted by Sandra. The self-assemblies were also manufactured by thin-film rehydration method and subsequently studied by DLS and SLS. The light scattering data were listed in Table 8, with the permission of Sandra.

**Table 8.** Scattering Data for the Assemblies of the Triblock Copolymers Synthesized by Sandra Kalem According to the Weight Fraction of PGL Blocks ( $w_{\text{PGL}}^a$ ).

Entry	Formula <sup>a</sup>	$w_{\text{PGL}}^a$	$R_{\text{H}}$ (nm)	PDI	$M_{\text{WNPs}}$ (kDa)	$N_{\text{agg}}$
<b>Aggregates<sup>b</sup></b>						
SK1	PGL <sub>8</sub> -PBO <sub>78</sub> -PGL <sub>8</sub>	0.17	75	0.23	$0.01 \times 10^4$	12
<b>Mixture of Aggregates and Polymersomes<sup>c</sup></b>						
SK2	PGL <sub>9</sub> -PBO <sub>68</sub> -PGL <sub>9</sub>	0.21	65	0.18	$0.70 \times 10^4$	835
SK3	PGL <sub>8</sub> -PBO <sub>59</sub> -PGL <sub>8</sub>	0.21	85	0.12	$1.3 \times 10^4$	2164
<b>Polymersomes<sup>d</sup></b>						
SK4	PGL <sub>10</sub> -PBO <sub>49</sub> -PGL <sub>10</sub>	0.27	89	0.13	$7.6 \times 10^4$	12300
SK5	PGL <sub>8</sub> -PBO <sub>42</sub> -PGL <sub>8</sub>	0.27	95	0.13	$5.5 \times 10^4$	8898
SK6	PGL <sub>9</sub> -PBO <sub>33</sub> -PGL <sub>9</sub>	0.33	51	0.26	$3.3 \times 10^4$	5270

<sup>a</sup>Formula and  $w_{\text{PGL}}$  were the results derived from <sup>1</sup>H NMR characterizations. <sup>b</sup>The rehydrated mixture, containing some undefined aggregates, was filter through a syringe filter (0.45  $\mu\text{m}$ ) before the DLS and SLS characterizations resulting in a rather clear and transparent solution. <sup>c</sup>The rehydrated mixtures, containing a few undefined aggregates, became more homogeneous after the extrusion through the syringe filter (0.45  $\mu\text{m}$ ). <sup>d</sup>The rehydrated mixtures were homogeneous and stable both before and after the extrusion through the syringe filter (0.45  $\mu\text{m}$ ).

One can see that, the results in Tables 7 and 8 were consistent with each other, and altogether, were in full agreement with the well-known phase diagram for the self-assembly of amphiphilic block copolymers in aqueous solution, where polymersomes are expected at relative low weight ratios of the hydrophilic segment(s) [23].

Among the varieties of morphologies, polymersomes are of great interest due to their versatile applications [25,26]. The characters of their membranes are of critical importance, for example the membrane thickness is a most important parameter which decides many membrane properties such as the membrane permeability [24].

Therefore, the polymersomes listed in Table 7 were probed by SAXS to determine the thicknesses of the hydrophobic layers as a function of the DP of PBO block. Figure 11 displays the SAXS profiles and the respective fitting curves by using the bilayered vesicle form factor. The well-fitted curves indicated the polymersomes were mostly well-defined. To note it that the SAXS profile for the PGL<sub>6</sub>-PBO<sub>40</sub>-PGL<sub>6</sub> polymersomes (Entry HQ031, Figure 11B) in accordance with the pattern of vesicles in large extent, however the low- $q$  range (left part of the scattering profile) diverged indicating the sample was comprised mostly of vesicles and some ill-aggregates.

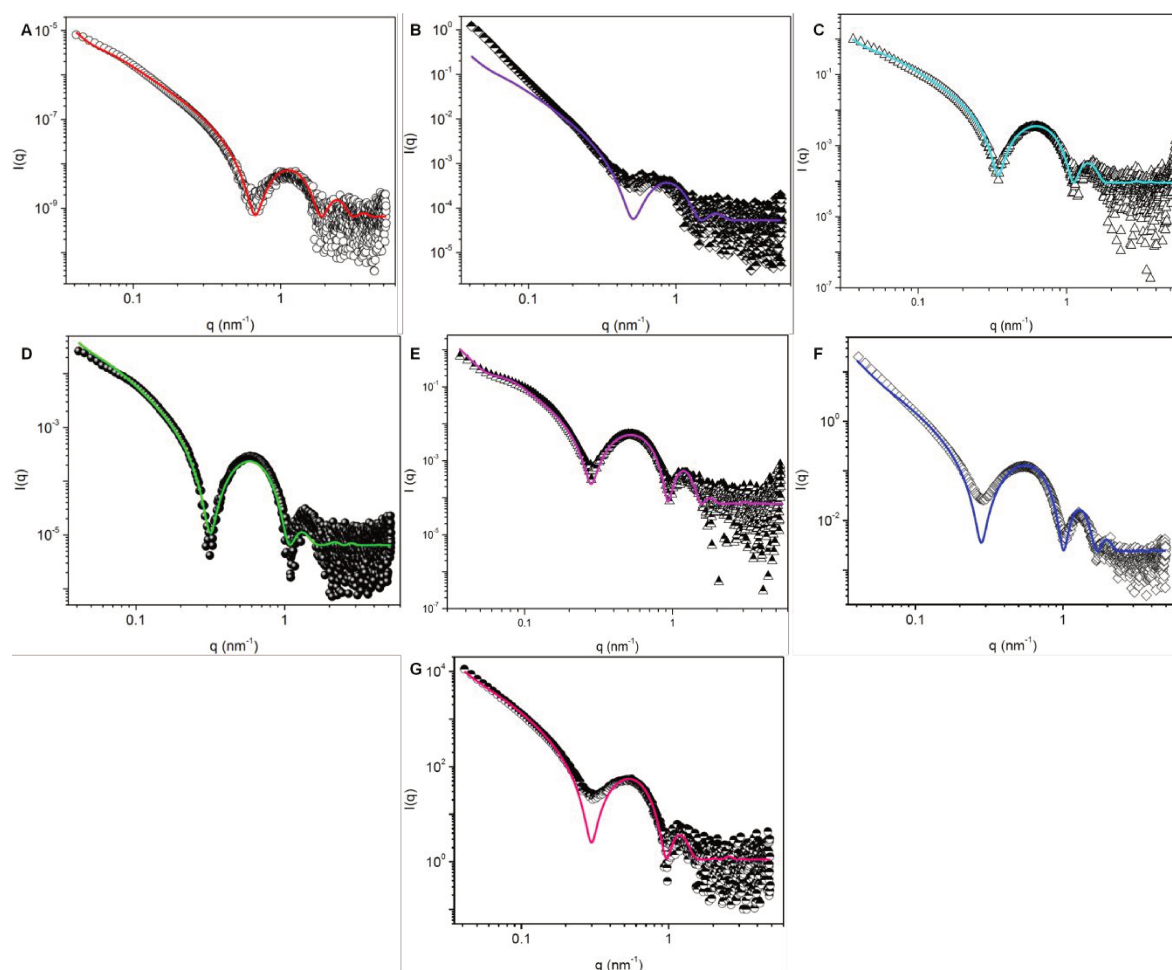


**Figure 11.** SAXS profiles and the respective fitting curves (solid lines) by using the bilayered vesicle form factor for the assemblies of (A) PGL<sub>6</sub>-PBO<sub>20</sub>-PGL<sub>6</sub> (Entry HQ034), (B) PGL<sub>6</sub>-PBO<sub>40</sub>-PGL<sub>6</sub> (Entry HQ031), (C) PGL<sub>20</sub>-PBO<sub>59</sub>-PGL<sub>20</sub> (Entry HQ119A), (D) PGL<sub>18</sub>-PBO<sub>62</sub>-PGL<sub>18</sub> (Entry HQ119B), (E) PGL<sub>25</sub>-PBO<sub>80</sub>-PGL<sub>25</sub> (Entry HQ077), (F) PGL<sub>12</sub>-PBO<sub>84</sub>-PGL<sub>12</sub> (Entry HQ033) and (G) PGL<sub>21</sub>-PBO<sub>84</sub>-PGL<sub>21</sub> (Entry HQ081B).

Based on the fitting curves, the structural parameters were acquired and summarized in Table 9.

**Table 9.** Structural Parameters of the Polymersomes as Determined by SAXS Measurements According to the DP of PBO block.

Polymersomes		$t_t^a$	$t_h^a$	$d^b$	$R_c^a$	$R_t^a$
		(nm)	(nm)	(nm)	(nm)	(nm)
HQ034	PGL <sub>6</sub> -PBO <sub>20</sub> -PGL <sub>6</sub>	2.9	1.8	6.5	52.5	59.0
HQ031	PGL <sub>6</sub> -PBO <sub>40</sub> -PGL <sub>6</sub>	4.3	2.0	8.3	44.4	52.7
HQ119A	PGL <sub>20</sub> -PBO <sub>59</sub> -PGL <sub>20</sub>	5.7	2.7	11.2	54.8	66.0
HQ119B	PGL <sub>18</sub> -PBO <sub>62</sub> -PGL <sub>18</sub>	6.1	3.6	13.3	61.0	74.3
HQ077	PGL <sub>25</sub> -PBO <sub>80</sub> -PGL <sub>25</sub>	7.3	2.8	12.8	42.8	55.6
HQ033	PGL <sub>12</sub> -PBO <sub>84</sub> -PGL <sub>12</sub>	6.7	2.9	12.5	56.1	68.6
HQ081B	PGL <sub>21</sub> -PBO <sub>84</sub> -PGL <sub>21</sub>	6.8	3.6	14.0	51.9	65.9

<sup>a</sup> $t_t$ ,  $t_h$ ,  $R_c$  and  $R_t$  are the structural parameters illustrated in Scheme 4; <sup>b</sup> $d = t_h + t_t + t_h$ .

To elucidate the dependence of the thickness of hydrophobic layer ( $t_t$ ) on the DP of PBO block,  $t_t$  was plotted against DP, producing the curve depicted in Figure 12.

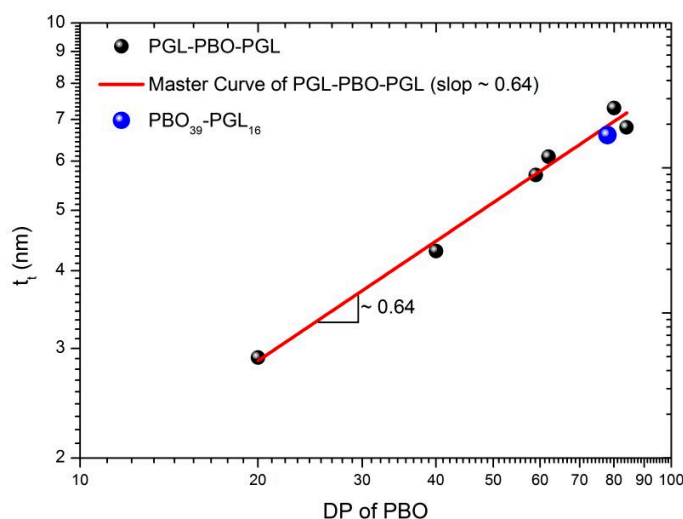


**Figure 12.** Master curve of the evolution of the thickness of the hydrophobic layer ( $t_t$ ) with the DP of PBO in the context of PGL-PBO-PGL polymersomes. The blue dot indicates the “double layer” of the polymersome made of the diblock PBO<sub>39</sub>-PGL<sub>16</sub> (Entry HQ020, DP = 78 in total, and  $t_t = 6.6$  nm)

The master curve produced a scaling law around 0.64, reflecting the PBO chains were stretched in some extent when the DP ranged from 20 to 84 and the thickness was below 8 nm. This result was consistent with the reported results in the case of poly(butylene oxide)-*block*-poly(ethylene oxide) (PBO-PEO) polymersomes in the same ranges of DP and thickness [24]. On the other hand, the  $t_t$  value of the PBO<sub>39</sub>-

PGL<sub>16</sub> polymersomes was compared with the master curve (the blue dot in Figure 12) taken the middle hydrophobic layer as two PBO monolayers, namely the DP of PBO is doubled as 78 in total. One can see that this point fitted well into the master curve for the PGL-PBO-PGL polymersomes, agreeing with the reported results in the case of PEG-PBO-PEG vs PEO-PBO [27]. This result also indicated the two monolayers were somewhat stretched. The somewhat elongated chain conformation of PBO was also reported in Riccardo Wehr's work [21]. This master curve is of tutorial importance to modulate the polymersome membrane thickness and correspondingly the polymersome permeability according to the first Fick's law [28]. This will be discussed in the future chapter.

### 3.4 Antifouling behaviors of the self-assemblies<sup>1</sup>

The antifouling behaviors of certain self-assembled nanoparticles were investigated by incubating the nanoparticles in protein environments. This work was performed with Fernando Giacomelli, who was interested in this research topic. The structural parameters of the nanoparticles and the model proteins used in these investigations were listed in Table 10.

**Table 10.** Characteristics of the Polymeric Nanoparticles and Model Proteins Used in the Antifouling Investigations.

Particles		$R_H$ (nm)	$M_{WNPs}$ (kDa)	$\zeta^a$ (mV)	Charge density <sup>b</sup> (mV nm <sup>-2</sup> )
<b>Spherical Micelles</b>					
HQ029	PBO <sub>13</sub> -PGL <sub>47</sub>	9.7	$3.62 \times 10^2$	-8.4	$-2.2 \times 10^{-3}$
HQ038A	PGL <sub>22</sub> -PBO <sub>13</sub> -PGL <sub>22</sub>	13.4	$6.68 \times 10^2$	-22.4	$-2.2 \times 10^{-3}$
HQ098	PGL <sub>10</sub> -PBO <sub>21</sub> -PGL <sub>10</sub>	24.0	$4.60 \times 10^3$	-8.4	$-1.2 \times 10^{-3}$
<b>Polymersomes</b>					
HQ020	PBO <sub>39</sub> -PGL <sub>16</sub>	67.2	$4.89 \times 10^4$	-24.3	$-1.9 \times 10^{-5}$
HQ081B	PGL <sub>21</sub> -PBO <sub>84</sub> -PGL <sub>21</sub>	79.6	$3.76 \times 10^4$	-21.2	$-1.0 \times 10^{-5}$
HQ033	PGL <sub>12</sub> -PBO <sub>84</sub> -PGL <sub>12</sub>	85.9	$15.1 \times 10^4$	-10.3	$-3.9 \times 10^{-6}$
<b>Model proteins</b>					
BSA		4.2	66.4	<i>pI</i> 4.9	
IgG		6.5	150	<i>pI</i> 7.0	
lysozyme		2.1	14	<i>pI</i> 10.5	

<sup>a</sup> $\zeta$  was the zeta potential of the polymer assemblies measured by ELS or the *pI* value of protein. <sup>b</sup>The charge density of the polymer assemblies was defined as the ratio of  $\zeta/(4\pi R_H^2)$ .

<sup>1</sup> These results were published, referring to *doi/10.1021/acs.langmuir.9b03687*.

All the polymer assemblies herein were negatively charged with high values of  $\zeta$  regardless the morphology, although the nanoparticles were made from neutral organic polymer. Indeed, it seems to be a more general phenomenon that negative  $\zeta$ -potentials have been measured for many different non-ionic particles [29–31]. Herein, the negative  $\zeta$ -potentials on the self-assembled nanoparticles were supposed to arise from the preferential accumulation of  $\text{OH}^-$  ions at the interface between water and the outer PGL shell. It is worth noting that such a feature imparted electrostatic stability to the assemblies as they were stable for months when stored at 4 °C.

The protein-adsorption study was performed by incubating the polymeric nanoparticles in a protein environment. First, the number of each protein required to cover the produced spherical nanoparticles ( $N_{\text{protein}}$ ) was estimated by using the following equations:

$$N_{\text{protein}} = \frac{4R_{\text{H,NPs}}^2}{R_{\text{H,protein}}^2} \quad (9)$$

wherein  $R_{\text{H,NPs}}$  and  $R_{\text{H,protein}}$  were the radii of the polymeric nanoparticles and the protein, respectively.

$$\text{Also, } N_{\text{protein}} = \frac{[\text{protein}]}{[\text{NPs}]} \quad (10)$$

wherein  $[\text{protein}]$  is the molar concentration of protein, and  $[\text{NPs}]$  is the molar concentration of the polymeric nanoparticles which is calculated using the following equations:

$$[\text{NPs}] = \frac{[\text{polymer}]}{[N_{\text{agg}}]} \quad (11)$$

$$\text{and } [\text{polymer}] = \frac{m_{\text{polymer}}}{M_{\text{w,polymer}} V} \quad (12)$$

wherein  $N_{\text{agg}}$  is the aggregation number obtained by SLS,  $M_{\text{w,polymer}}$  was the molar mass of the copolymer chain.

For each pair of nanoparticle–protein, the concentrations of the polymeric nanoparticle and the protein were estimated (Table 11).

**Table 11.** The Number of Proteins Required for Full Cover on the Surfaces of the Assemblies ( $N_{\text{protein}}$ ) as well as the Molar Concentrations of the Assemblies ([NPs]) and the Proteins ([protein]) Applied in the Antifouling Investigation.

Assemblies		[NPs] (nM)	BSA		IgG		lysozyme	
			$N_{\text{BSA}}$	[BSA] (μM)	$N_{\text{IgG}}$	[IgG] (μM)	$N_{\text{Lz}}$	[Lz] (μM)
<b>Spherical Micelles</b>								
HQ029	PBO <sub>13</sub> -PGL <sub>47</sub>	2760	21	58.0	85	234.6	7.5	20.7
HQ038A	PGL <sub>22</sub> -PBO <sub>13</sub> -PGL <sub>22</sub>	1500	41	61.5	163	244.5	14	21.0
HQ098	PGL <sub>10</sub> -PBO <sub>21</sub> -PGL <sub>10</sub>	219	131	28.7	522	114.3	46	10.1
<b>Polymersomes</b>								
HQ020	PBO <sub>39</sub> -PGL <sub>16</sub>	27.2	768	20.9	3072	83.6	269	7.3
HQ081B	PGL <sub>21</sub> -PBO <sub>84</sub> -PGL <sub>21</sub>	26.6	1437	38.2	5747	152.9	503	13.4
HQ033	PGL <sub>12</sub> -PBO <sub>84</sub> -PGL <sub>12</sub>	13.0	2309	30.0	9234	120.0	808	10.5

Based on the estimated values (Table 11), the antifouling behaviors of the assemblies were investigated by incubating the polymeric nanoparticles in a protein environment, where the protein concentration was two times higher than  $N_{\text{protein}}$  (*i.e.*,  $2N_{\text{protein}}$ ), with the methods of DLS, ITC, fluorescence and CD spectroscopy.

First, DLS was used to probe the change in  $R_{\text{H}}$  of nanoparticles after contacting proteins induced by the interactions between protein and the polymeric nanoparticles. For example, the PGL<sub>12</sub>-PBO<sub>84</sub>-PGL<sub>12</sub> (Entry HQ033) polymersomes were incubated in the lysozyme solution with a concentration of  $2N_{\text{lysozyme}}$ . And the autocorrelation functions and the  $R_{\text{H}}$  distributions of the polymersomes with or without lysozymes were acquired and compared, as depicted in Figure 13.

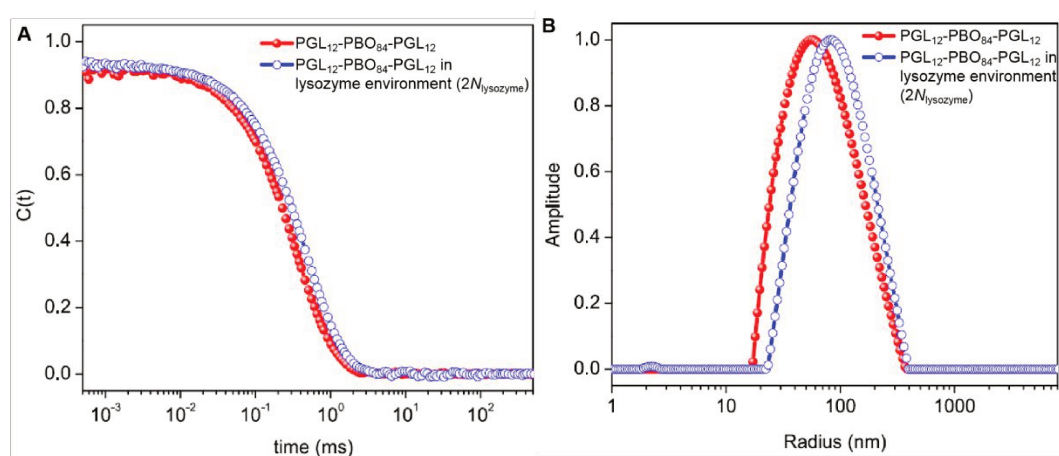


**Figure 13.** (A) Autocorrelation functions and (B)  $R_{\text{H}}$  distribution curves of the PGL<sub>12</sub>-PBO<sub>84</sub>-PGL<sub>12</sub> polymersomes (Entry HQ033) in a lysozyme-free or a lysozyme environment, according to the legend.

It clearly showed that both the mean decay of the autocorrelation function (Figure 13A) and the  $R_H$  distribution curve (Figure 13B) of the nanoparticles shifted towards the right-hand in the lysozyme environment. These shifts suggested lysozymes were adsorbed onto the surface of the PGL<sub>12</sub>-PBO<sub>84</sub>-PGL<sub>12</sub> (Entry HQ033) polymersomes and resulted in the increase in size.

For PGL<sub>10</sub>-PBO<sub>21</sub>-PGL<sub>10</sub> (Entry HQ098) micelles, the  $R_H$  distribution curve shifted towards the right-hand side at the presence of lysozymes (Figure 14A), indicating the protein adsorptions. On the contrary, the size of the micelles remained essentially the same at IgG environment with IgG giving a separated size distribution located at the left-hand (Figure 14B), suggesting no IgG adsorption onto the surface of the micelles.

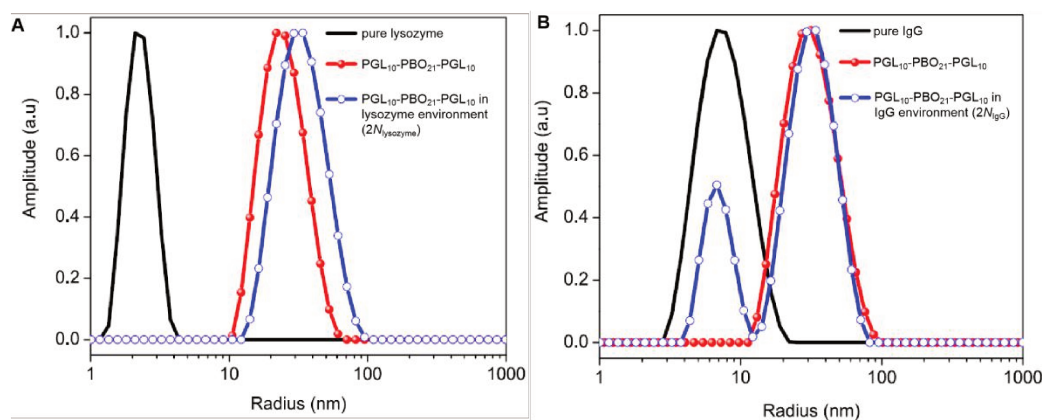


**Figure 14.**  $R_H$  distribution curves of the micelles of PGL<sub>10</sub>-PBO<sub>21</sub>-PGL<sub>10</sub> (Entry HQ098) in (A) lysozyme and (B) IgG environments.

Using this methodology, the nanoparticle–protein pairs (Table 11) were investigated to probe the possible adsorptions of the model proteins onto the surfaces of the self-assembled polymeric nanoparticles. The size variation of the polymeric nanoparticles after being in contact with proteins ( $\Delta R_H$ ) were calculated and listed in Table 12.

**Table 12.** Size Variation of the Assemblies ( $\Delta R_H$ ) after Contacting the Model Proteins.

Assemblies		$\Delta R_H$ (nm)		
		BSA	IgG	lysozyme
<b>Spherical Micelles</b>				
HQ029	PBO <sub>13</sub> -PGL <sub>47</sub>	0 ± 1	1 ± 1	2 ± 1
HQ038A	PGL <sub>22</sub> -PBO <sub>13</sub> -PGL <sub>22</sub>	-1 ± 2	3 ± 2	0 ± 1
HQ098	PGL <sub>10</sub> -PBO <sub>21</sub> -PGL <sub>10</sub>	-2 ± 3	2 ± 2	9 ± 2
<b>Polymersomes</b>				
HQ020	PBO <sub>39</sub> -PGL <sub>16</sub>	2 ± 2	-2 ± 1	7 ± 2
HQ081B	PGL <sub>21</sub> -PBO <sub>84</sub> -PGL <sub>21</sub>	3 ± 2	6 ± 2	2 ± 1
HQ033	PGL <sub>12</sub> -PBO <sub>84</sub> -PGL <sub>12</sub>	2 ± 1	16 ± 1	8 ± 1

Herein,  $\Delta R_H$  was defined as the size variation of the nanoparticles before and after the contact with proteins at a concentration of  $2N_{\text{protein}}$ , *i.e.*,  $\Delta R_H = R_{H,\text{NPs-protein}} - R_{H,\text{NPs}}$ . Under current investigation conditions, it was thought that protein adsorptions took place when  $\Delta R_H$  was larger than the dimension of the protein (*i.e.*,  $2R_{H,\text{protein}}$ ). Therefore, the values (Table 12) indicated that no evidence of BSA adsorption was observed regardless the morphology. The absence of adsorptions was attributed to the electrostatic repulsions between the negatively charged polymer assemblies and BSA.

Similarly, in the case of IgG, adsorption was avoided except onto the PGL<sub>12</sub>-PBO<sub>84</sub>-PGL<sub>12</sub> assemblies (Entry HQ033) which has relatively short PGL segments producing the lowest surface charge density (Table 10). These results indicated that the electrostatic repulsion may also contribute to the IgG-repelling characteristic of the assemblies to some extent when the PGL shell was adequately long.

The importance of the length of PGL in shell to the protein-repelling characteristic was further proved by the results acquired at the lysozyme environment. Lysozyme ( $pI$  10.5) is positively charged at pH 7.4, and then presumably enables to be adsorbed onto the negatively charged assemblies due to the electrostatic attractions. However, the adsorption phenomena were not observed on the assemblies which had relatively long PGL shell ( $DP_{\text{PGL}} \sim 20$ ), such as the PBO<sub>13</sub>-PGL<sub>47</sub> micelles (Entry HQ029) and PGL<sub>21</sub>-PBO<sub>84</sub>-PGL<sub>21</sub> polymersomes (Entry HQ081B).

The protein adsorption events suggested by the DLS results (Table 12) were further investigated by ITC (Figure 15).

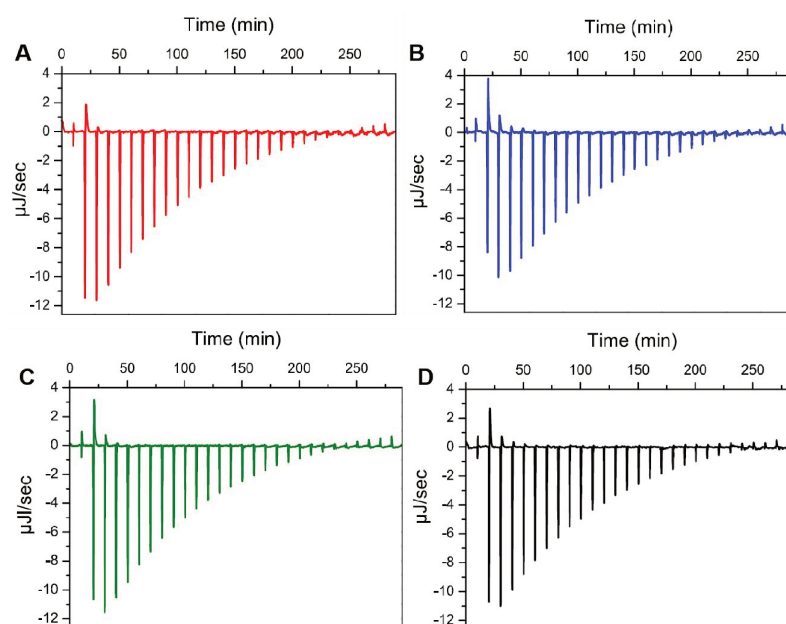


**Figure 15.** ITC raw data for the titration of protein into the polymer assemblies. The protein–nanoparticle pairs were respectively (A) IgG–PGL<sub>12</sub>-PBO<sub>84</sub>-PGL<sub>12</sub> (Entry HQ033), (B) lysozyme–PGL<sub>12</sub>-PBO<sub>84</sub>-PGL<sub>12</sub> (Entry HQ033), (C) lysozyme–PGL<sub>10</sub>-PBO<sub>21</sub>-PGL<sub>10</sub> (Entry HQ098) and (D) lysozyme–PBO<sub>39</sub>-PGL<sub>16</sub> (Entry HQ020).

Figure 15 displays the raw data recorded in the process of gradual addition of protein solution into the nanoparticle suspension. It clearly shows that all the ITC raw data gave strong signals resulting from the energy transfer in the titration processes, which evidenced the interactions between proteins with the polymer assemblies, consistent with DLS results.

The ITC raw data were interpreted into the curves of enthalpy change against the protein-to-nanoparticle ratio, as shown in Figure 16.

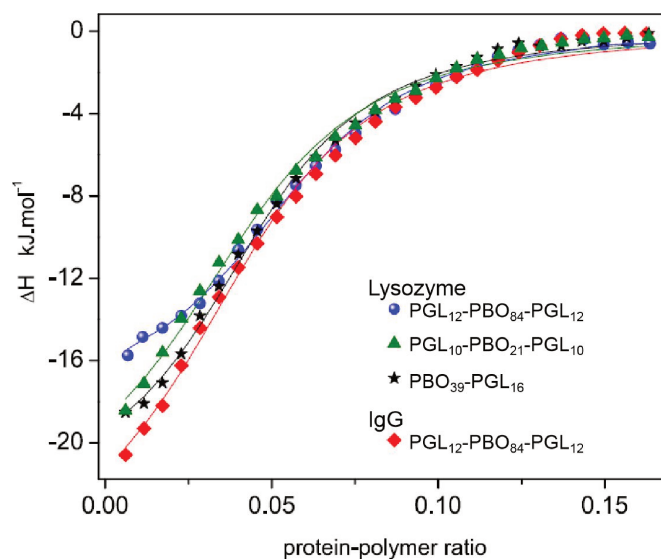


**Figure 16.** The curves of the enthalpy per weight of injection as a function of protein-to-nanoparticle ratio, for the titrations of protein into the polymer assemblies, according to the legend.

The resultant curves (Figure 16) were fitted by using the straightforward one set of binding site model (Equation 13).

$$Q = \frac{NM_t \Delta H V_{\text{cell}}}{2} \left( 1 + \frac{1}{NK_A M_t} + \frac{X_t}{NM_t} - \sqrt{\left( 1 + \frac{1}{NK_A M_t} \right)^2 - \frac{4X_t}{NM_t}} \right) \quad (13)$$

wherein  $Q$  is the measured heat content after each injection,  $V_{\text{cell}}$  is the cell volume, and  $M_t$  and  $X_t$  are respectively the molar concentrations of nanoparticles and protein. The thermodynamic parameters, namely  $N$ ,  $K_A$  and  $\Delta H$  are the fitting parameters, with the meanings being respectively the number of protein molecules per nanoparticle, the equilibrium association constant and the molar enthalpy change in the adsorption process.

Furthermore, the molar free energy change ( $\Delta G$ ) and the molar entropy change ( $\Delta S$ ) of the binding events were determined by using the following fundamental

thermodynamic equations:

$$\Delta G = -RT \ln K_A \quad (14)$$

$$\text{and } \Delta S = \frac{\Delta H - \Delta G}{T} \quad (15)$$

The thermodynamic parameters obtained from the fitting approaches were provided in Table 13.

**Table 13.** Thermodynamic Parameters Derived from ITC Titrations and Stern–Volmer Quenching Constants ( $K_{SV}$ ) Derived from Fluorescence Spectra for the Adsorption Events of IgG and Lysozyme onto Polymer Assemblies.

		$\Delta H$ (kJ mol <sup>-1</sup> )	$K_A$ (10 <sup>4</sup> M <sup>-1</sup> )	$N$ (protein /NP)	$\Delta S$ (J mol <sup>-1</sup> K <sup>-1</sup> )	$\Delta G$ (kJ mol <sup>-1</sup> )	$K_{SV}$ (M <sup>-1</sup> )
<b>IgG</b>							
HQ033	PGL <sub>12</sub> -PBO <sub>84</sub> -PGL <sub>12</sub>	-26.4	4.10	0.0457	-0.3	-26.3	1.36 × 10 <sup>6</sup>
<b>lysozyme</b>							
HQ033	PGL <sub>12</sub> -PBO <sub>84</sub> -PGL <sub>12</sub>	-18.0	5.89	0.0570	30.9	-27.2	1.07 × 10 <sup>9</sup>
HQ098	PGL <sub>10</sub> -PBO <sub>21</sub> -PGL <sub>10</sub>	-22.7	5.41	0.0471	14.5	-27.0	8.58 × 10 <sup>7</sup>
HQ020	PBO <sub>39</sub> -PGL <sub>16</sub>	-23.6	3.99	0.0445	8.9	-26.2	1.38 × 10 <sup>8</sup>

The results showed that all the processes were exothermic ( $\Delta H < 0$ ), implying certainly the non-covalent binding of proteins onto the surfaces of the assemblies. The non-covalent intermolecular forces may include electrostatic interactions, hydrophobic interactions, hydrogen bondings and Van der Waals force. Accordingly, to make conclusions on the dominating intermolecular forces responsible for the protein fouling, the signals of thermodynamic parameters are useful. In an endothermic and entropically driven process ( $\Delta H > 0$  and  $\Delta S > 0$ ), the hydrophobic interactions are dominant, whereas the exothermic signals and positive entropy changes ( $\Delta H < 0$  and  $\Delta S > 0$ ) are attributed to the dominating electrostatic forces. The Van der Waals and hydrogen bondings are usually the main operating forces when  $\Delta H < 0$  and  $\Delta S < 0$ . Thus, it was concluded that Van der Waals force and hydrogen bondings were the main forces in the IgG adsorption process, while the processes of lysozyme adsorptions were driven by the electrostatic interactions.

Additionally, the assemblies-protein pairs without protein adsorptions suggested by DLS (Table 12) were also confirmed by ITC measurements with the fact that the ITC raw data highlighted the negligible energy transfer (Figure 17).

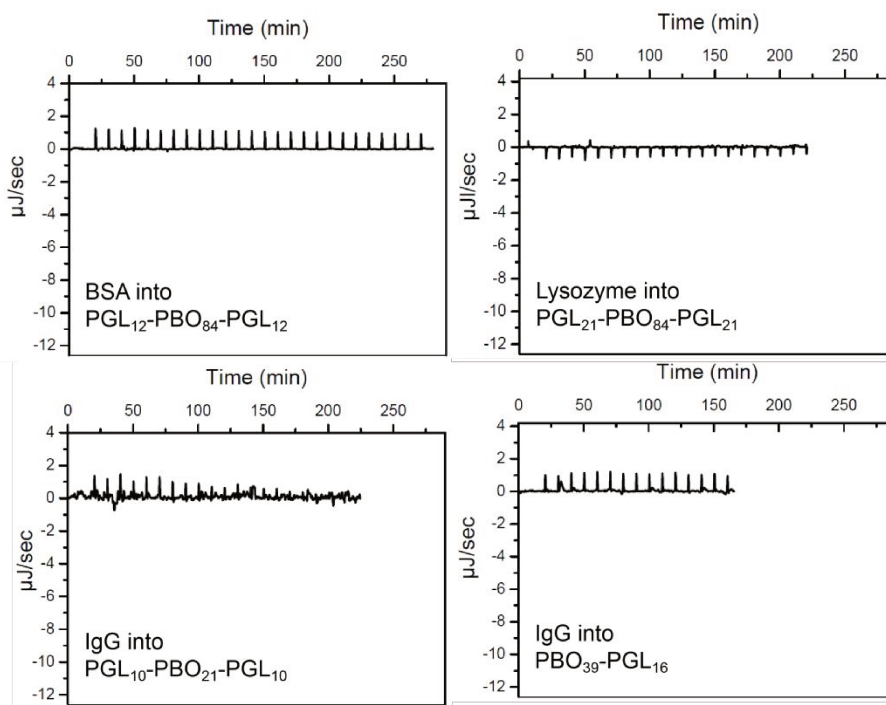


**Figure 17.** Representative ITC raw data for the titrations of protein into the polymer assemblies, according to the legends.

The results of DLS and ITC altogether robustly confirmed that the protein adsorption was  $DP_{\text{PGL}}$ -dependent, and that  $DP_{\text{PGL}} \sim 20$  was already sufficient to provide the PGL-shelled assemblies with protein-repelling characteristics, regardless the morphology.

Furthermore, fluorescence data were acquired when polymer assemblies were gradually added into the protein solution, so as to evaluate the mechanism of protein quenching by polymeric assemblies in the adsorption phenomena [32]. As an example, the fluorescence spectra of IgG as a function of the concentration of  $\text{PBO}_{39}\text{-PGL}_{16}$  assemblies (Entry HQ020) were portrayed in Figure 18A. One can see that the fluorescence spectra of IgG remained the same when the concentration of the nanoparticles increased, indicating the absence of IgG adsorption onto the assemblies. For other protein-assemblies pairs where protein adsorptions had not been suggested by DLS (Table 12), the similar results were obtained that the spectrum of the protein remained the same when the assemblies were successively added.

On the contrary, as shown in Figure 18B, the fluorescence intensity of lysozyme was progressively quenched with the increased concentration of the  $\text{PGL}_{12}\text{-PBO}_{84}\text{-PGL}_{12}$  assemblies (Entry HQ033). This fluorescence quenching indicated again the adsorption event in the pair of lysozyme– $\text{PGL}_{12}\text{-PBO}_{84}\text{-PGL}_{12}$  (Entry HQ033), which agreed with the DLS and ITC data. Protein quenching was observed in other protein–assemblies pairs involving protein adsorptions as suggested by DLS and ITC.

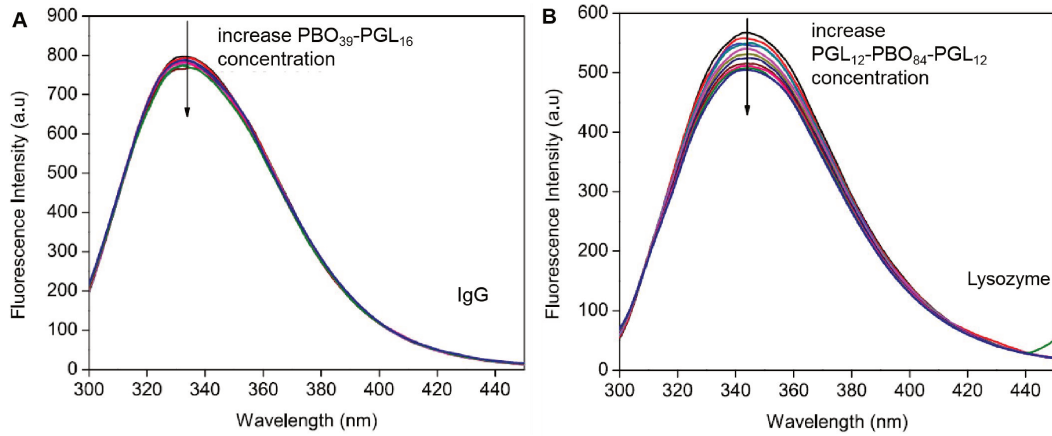


**Figure 18.** Fluorescence spectra of protein as a function of successive addition of polymer assemblies. The protein-assemblies pairs were respectively (A) IgG–PBO<sub>39</sub>-PGL<sub>16</sub> (Entry HQ020), and (B) lysozyme–PGL<sub>12</sub>-PBO<sub>84</sub>-PGL<sub>12</sub> (Entry HQ033).

The fluorescence quenching data was analyzed by Stern–Volmer plot (Equation 16).

$$\frac{F_0}{F} = 1 + K_{SV}[NPs] \quad (16)$$

wherein,  $F_0$  and  $F$  are the fluorescence intensities in the absence and presence of polymeric nanoparticles.  $K_{SV}$  is the Stern–Volmer quenching constant.

The Stern–Volmer plots for the fluorescence quenching of lysozyme and IgG by different polymer assemblies were displayed in Figure 19.

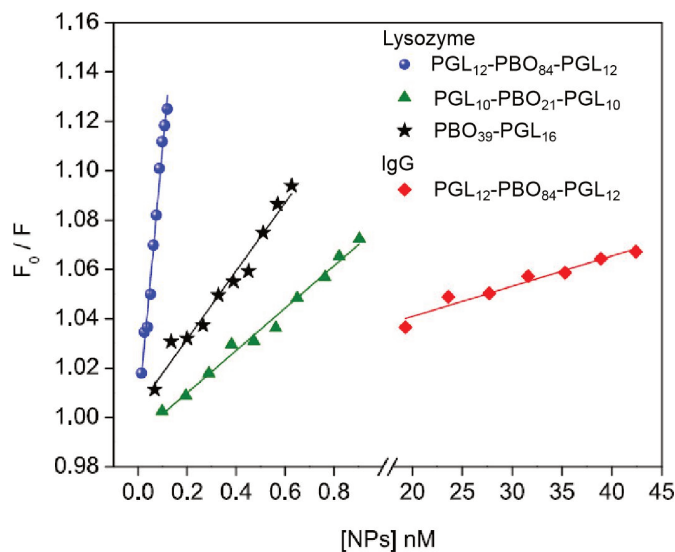


**Figure 19.** Stern–Volmer plots for the fluorescence quenching of lysozyme and IgG by different polymer assemblies, according to the legend.

All Stern–Volmer plots showed good linear relationship, allowing the determination of the  $K_{SV}$  values (Table 13). The linearity also suggested the prevalence of one quenching mechanism involved in the protein adsorption events, either static or dynamic quenching [33]. The static quenching refers to the actual formation of ground state complexes, whereas the dynamic quenching is related to collisional encounters. To figure out the quenching mechanism, the values of the quenching rate constant ( $K_b$ ) were calculated from the relation of  $K_b = K_{SV}/\tau_0$  ( $\tau_0 \sim 10^{-8}$  s, an average value for fluorescence lifetime of proteins in the absence of quenchers [34]). The values of  $K_{SV}$  herein were in the range of  $10^6$ – $10^9$   $M^{-1}$  (Table 13). Accordingly, the values of  $K_b$  were in the range of  $10^{14}$ – $10^{17}$   $M^{-1} s^{-1}$ , which were remarkably greater than the threshold value for the diffusion collision rate constant of quenchers to proteins ( $2 \times 10^{10}$   $M^{-1} s^{-1}$ ). Therefore, the proteins were quenched by static quenching mechanism where the proteins and the assemblies formed ground state complexes.

Circular dichroism (CD) spectroscopy was applied to probe the possible conformational changes on the proteins induced by the adsorption phenomena [32]. For example, for the lysozyme–PGL<sub>12</sub>–PBO<sub>84</sub>–PGL<sub>12</sub> (Entry HQ033) pair, where protein adsorption was thoroughly verified by DLS, ITC and fluorescence spectroscopy, Figure 20 portrays the CD spectra of lysozyme recorded in the absence and presence of the PGL<sub>12</sub>–PBO<sub>84</sub>–PGL<sub>12</sub> assemblies (Entry HQ33). In the absence of nanoparticles, the CD spectrum was characteristic of biomacromolecules with certain degree of  $\alpha$ -helix content as evidenced by the minima at 208 and 207 nm. In the presence of nanoparticles, the CD profile remained the same in the aspects of shape and peak positions. This result highlighted that even when the adsorption took place, it did not cause major alterations in the conformation of proteins. The same conclusion was made on the other protein–nanoparticle pairs where the adsorption was confirmed by DLS, ITC and fluorescence spectroscopy.

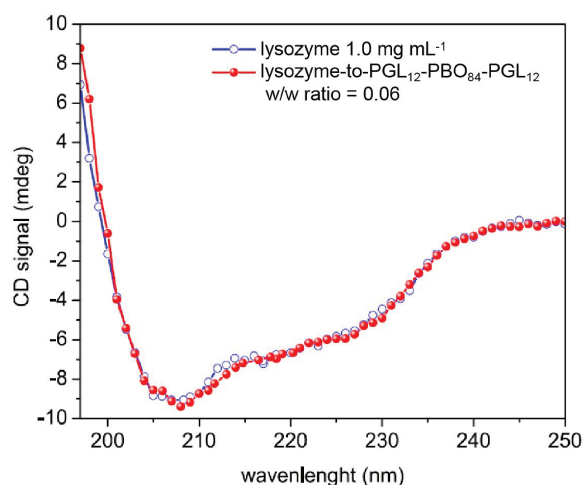


**Figure 20.** Circular dichroism (CD) spectra of lysozyme in the absence and presence of PGL<sub>12</sub>–PBO<sub>84</sub>–PGL<sub>12</sub> assemblies (Entry HQ033).

In summary, the protein-repelling behaviors of the polymer assemblies were investigated by DLS, ITC, fluorescence and CD spectroscopy. The results showed that protein adsorptions were observed only when the assemblies had rather short PGL segments in the outer shell, and moreover, that proteins were efficiently resisted from binding onto the assemblies when the PGL segments were as long as  $DP_{\text{PGL}} \sim 20$ . This finding was exciting in comparison with PEG-based analogues. In the context of the PEG-stabilized surfaces, it is well documented and accepted that  $M_{\text{WPEG}} \sim 5000 \text{ g mol}^{-1}$  (*i.e.*,  $DP_{\text{PEG}} \sim 115$ ) is required to render the PEGylated nanoparticles protein-repelling. For example, the studies on the PEG-stabilized and poly(lactic acid) (PLA)- or poly( $\epsilon$ -caprolactone) (PCL)-based assemblies showed that negligible protein adsorptions were observed when the nanoparticles were stabilized by much longer PEG chains ( $DP_{\text{PEG}} \sim 113$ ). These results were in agreement with those reported by Gref et al. that maximal reduction in protein adsorption was achieved when PLA-based nanoparticles were stabilized by PEG with  $M_{\text{WPEG}} \sim 5000 \text{ g mol}^{-1}$  and no considerable benefits for the values above such a threshold [35]. In this aspect, the results herein highlighted that much shorter PGL chains ( $DP_{\text{PGL}} \sim 20$ ) were apparently adequate to provide the nanoparticle surfaces with the protein-repelling characteristics, and these findings may be promising in the design of non-fouling nanoparticles for a wide range of applications.

#### 4. Conclusions

As to prepare polymeric membranes for the whole PhD project, in this part, the amphiphilic linear block copolymers, PBO-PGL and PGL-PBO-PGL were focused on. The block copolymers were synthesized via defined and reproducible procedures, which included a tBuP4-catalyzed sequential anionic ring-opening block copolymerization of BO and EEGE and a deprotection treatment in acidic conditions. The copolymers were defined in structure and of good purity, as confirmed by  $^1\text{H}$  NMR and SEC.

The copolymers were investigated first on their self-assembly behaviors with the methods of DLS, SLS, TEM and SAXS. The characterization results showed that PGL-PBO-PGL self-assembled into different morphologies greatly depending on the weight ratio of PGL blocks ( $w_{\text{PGL}}$ ): when  $w_{\text{PGL}} \leq 0.21$  the assemblies were undefined aggregates; when  $0.22 \leq w_{\text{PGL}} \leq 0.40$  the assemblies dominantly were polymersomes; and spherical micelles were formed when  $w_{\text{PGL}} \geq 0.46$ . This was in full agreement with the phase diagram for the self-assembly of non-ionic amphiphilic block copolymers in aqueous solution. Moreover, in the context of polymersomes, the thickness of hydrophobic layer ( $t_t$ ) increased with the DP of PBO block ( $DP_{\text{PBO}}$ ) in a relation of  $t_t \sim DP_{\text{PBO}}^{0.64}$ , verifying the PBO chains were somewhat stretched in the membrane.

Then the assemblies, both micelles and polymersomes, were studied regarding their protein-repelling features via DLS, ITC, fluorescence and CD spectroscopy. The data firmly evidenced that the PGL-stabilized assemblies were protein-repelling even by using short shells ( $DP_{\text{PGL}} \sim 20$ ), which was considerably shorter than the requirement for the well-known PEG ( $DP_{\text{PEG}} \sim 100$ ) [23].

## 5. References

1. Doncom K E B, Blackman L D, Wright D B, et al. Dispersity effects in polymer self-assemblies: a matter of hierarchical control[J]. *Chemical Society Reviews*, 2017, 46(14): 4119-4134.
2. Qin S, Li H, Yuan W, et al. Hierarchical self-assembly of fluorine-containing diblock copolymer: from onion-like nanospheres to superstructured microspheres[J]. *Polymer*, 2011, 52(4): 1191-1196.
3. Smart T, Lomas H, Massignani M, et al. Block copolymer nanostructures[J]. *Nano Today*, 2008, 3(3-4): 38-46.
4. Leong J, Teo J Y, Aakalu V K, et al. Engineering polymersomes for diagnostics and therapy[J]. *Advanced healthcare materials*, 2018, 7(8): 1701276.
5. Caracciolo G, Farokhzad O C, Mahmoudi M. Biological identity of nanoparticles in vivo: clinical implications of the protein corona[J]. *Trends in biotechnology*, 2017, 35(3): 257-264.
6. Zhang P, Sun F, Liu S, et al. Anti-PEG antibodies in the clinic: Current issues and beyond PEGylation[J]. *Journal of Controlled Release*, 2016, 244: 184-193.
7. Utrata-Wesołek A, Wałach W, Anioł J, et al. Multiple and terminal grafting of linear polyglycidol for surfaces of reduced protein adsorption[J]. *Polymer*, 2016, 97: 44-54.
8. Thomas A, Müller S S, Frey H. Beyond poly (ethylene glycol): linear polyglycerol as a multifunctional polyether for biomedical and pharmaceutical applications[J]. *Biomacromolecules*, 2014, 15(6): 1935-1954.
9. Dentzer L, Bray C, Noinville S, et al. Phosphazene-promoted metal-free ring-opening polymerization of 1, 2-epoxybutane initiated by secondary amides[J]. *Macromolecules*, 2015, 48(21): 7755-7764.
10. Misaka H, Tamura E, Makiguchi K, et al. Synthesis of end-functionalized polyethers by phosphazene base-catalyzed ring-opening polymerization of 1, 2-butylene oxide and glycidyl ether[J]. *Journal of Polymer Science Part A: Polymer Chemistry*, 2012, 50(10): 1941-1952.
11. Gerstl C, Schneider G J, Pyckhout-Hintzen W, et al. Segmental and normal mode relaxation of poly (alkylene oxide) s studied by dielectric spectroscopy and rheology[J]. *Macromolecules*, 2010, 43(11): 4968-4977.
12. Villar-Alvarez E, Figueroa-Ochoa E, Barbosa S, et al. Reverse poly(butylene oxide)-poly(ethylene oxide)-poly(butylene oxide) block copolymers with lengthy hydrophilic blocks as efficient single and dual drug-loaded nanocarriers with synergistic toxic effects on cancer cells[J]. *RSC Advances*, 2015, 5(64): 52105-52120.
13. Zhang Y, Wang G, Huang J. A new strategy for synthesis of “umbrella-like” poly (ethylene glycol) with monofunctional end group for bioconjugation[J]. *Journal of Polymer Science Part A: Polymer Chemistry*, 2010, 48(24): 5974-5981.

14. Hope M J, Bally M B, Webb G, et al. Production of large unilamellar vesicles by a rapid extrusion procedure. Characterization of size distribution, trapped volume and ability to maintain a membrane potential[J]. *Biochimica et Biophysica Acta (BBA)-Biomembranes*, 1985, 812(1): 55-65.
15. Kamata Y, Parnell A J, Gutfreund P, et al. Hydration and ordering of lamellar block copolymer films under controlled water vapor[J]. *Macromolecules*, 2014, 47(24): 8682-8690.
16. Stepanek P. Dynamic light scattering: the method and some applications[J]. W. Brown, Clarendon Press Oxford, UK, 1993: 177.
17. Striegel A M. Specific refractive index increment ( $\partial n/\partial c$ ) of polymers at 660 nm and 690 nm[J]. *Chromatographia*, 2017, 80(6): 989-996.
18. Backes M, Messenger L, Mourran A, et al. Synthesis and thermal properties of well-defined amphiphilic block copolymers based on polyglycidol[J]. *Macromolecules*, 2010, 43(7): 3238-3248.
19. Faye I, Huin C, Illy N, et al. β-Cyclodextrin-Based Star Amphiphilic Copolymers: Synthesis, Characterization, and Evaluation as Artificial Channels[J]. *Macromolecular Chemistry and Physics*, 2019, 220(2): 1800308.
20. Letchford K, Burt H. A review of the formation and classification of amphiphilic block copolymer nanoparticulate structures: micelles, nanospheres, nanocapsules and polymersomes[J]. *European journal of pharmaceutics and biopharmaceutics*, 2007, 65(3): 259-269.
21. Wehr R, Gaitzsch J, Daubian D, et al. Deepening the insight into poly (butylene oxide)-block-poly (glycidol) synthesis and self-assemblies: micelles, worms and vesicles[J]. *RSC Advances*, 2020, 10(38): 22701-22711.
22. Gou P F, Zhu W P, Shen Z Q. Synthesis, self-assembly, and drug-loading capacity of well-defined cyclodextrin-centered drug-conjugated amphiphilic A14B7 miktoarm star copolymers based on poly (ε-caprolactone) and poly (ethylene glycol)[J]. *Biomacromolecules*, 2010, 11(4): 934-943.
23. Blanz A, Armes S P, Ryan A J. Self-assembled block copolymer aggregates: from micelles to vesicles and their biological applications[J]. *Macromolecular rapid communications*, 2009, 30(4-5): 267-277.
24. Le Meins J F, Sandre O, Lecommandoux S. Recent trends in the tuning of polymersomes' membrane properties[J]. *The European Physical Journal E*, 2011, 34(2): 1-17.
25. Rideau E, Dimova R, Schwille P, et al. Liposomes and polymersomes: a comparative review towards cell mimicking[J]. *Chemical society reviews*, 2018, 47(23): 8572-8610.
26. LoPresti C, Lomas H, Massignani M, et al. Polymersomes: nature inspired nanometer sized compartments[J]. *Journal of Materials Chemistry*, 2009, 19(22): 3576-3590.
27. Battaglia G, Ryan A J. Bilayers and interdigitation in block copolymer vesicles[J]. *Journal of the American Chemical Society*, 2005, 127(24): 8757-8764.
28. Battaglia G, Ryan A J, Tomas S. Polymeric vesicle permeability: a facile chemical assay[J]. *Langmuir*, 2006, 22(11): 4910-4913.
29. de Castro C E, Mattei B, Riske K A, et al. Understanding the structural parameters of biocompatible nanoparticles dictating protein fouling[J]. *Langmuir*, 2014, 30(32): 9770-9779.
30. de Castro C E, Bonvent J J, da Silva M C C, et al. Influence of Structural Features on the Cellular Uptake Behavior of Non-Targeted Polyester-Based Nanocarriers[J]. *Macromolecular*

bioscience, 2016, 16(11): 1643-1652.

31. Ribeiro C A S, de Castro C E, Albuquerque L J C, et al. Biodegradable nanoparticles as nanomedicines: are drug-loading content and release mechanism dictated by particle density?[J]. Colloid and Polymer Science, 2017, 295(8): 1271-1280.

32. Hao C, Xu G, Feng Y, et al. Fluorescence quenching study on the interaction of ferroferric oxide nanoparticles with bovine serum albumin[J]. Spectrochimica Acta Part A: Molecular and Biomolecular Spectroscopy, 2017, 184: 191-197.

33. Chakraborty S, Joshi P, Shanker V, et al. Contrasting effect of gold nanoparticles and nanorods with different surface modifications on the structure and activity of bovine serum albumin[J]. Langmuir, 2011, 27(12): 7722-7731.

34. Chakraborti S, Joshi P, Chakravarty D, et al. Interaction of polyethyleneimine-functionalized ZnO nanoparticles with bovine serum albumin[J]. Langmuir, 2012, 28(30): 11142-11152.

35. Gref R, Lück M, Quellec P, et al. 'Stealth' corona-core nanoparticles surface modified by polyethylene glycol (PEG): influences of the corona (PEG chain length and surface density) and of the core composition on phagocytic uptake and plasma protein adsorption[J]. Colloids and Surfaces B: Biointerfaces, 2000, 18(3-4): 301-313.



## **Chapter 3.**

### **$\beta$ CD-cored Star Amphiphilic Copolymers:**

#### **Syntheses, structural characterizations and self-assemblies**

## Content

<b>1. Introduction.....</b>	<b>127</b>
<b>2. Materials and Methods.....</b>	<b>128</b>
2.1 Materials.....	128
2.2 Synthesis of per(2-O-methyl-3,6-di-O-(3-hydroxypropyl))- $\beta$ CD.....	129
2.3 Synthesis of $\beta$ CD-(PBO <sub>m</sub> -PGL <sub>n</sub> ) <sub>14</sub> with $m \leq 10$ .....	132
2.4 Synthesis of $\beta$ CD-(PBO <sub>m</sub> -PGL <sub>n</sub> ) <sub>14</sub> with $m > 10$ .....	133
2.5 Structural characterizations of the star polymers.....	134
2.6 Self-assembly behaviors of the star copolymers.....	135
2.6.1 Preparation of the self-assemblies.....	135
2.6.2 Characterizations of the self-assemblies.....	135
<b>3. Results and Discussions.....</b>	<b>137</b>
3.1 Synthesis of the initiator, per(2-O-methyl-3,6-di-O-(3-hydroxypropyl))- $\beta$ CD.....	137
3.2 Syntheses of the star copolymers $\beta$ CD-(PBO <sub>m</sub> -PGL <sub>n</sub> ) <sub>14</sub> with $m \leq 10$ .....	140
3.3 Syntheses of the star copolymers $\beta$ CD-(PBO <sub>m</sub> -PGL <sub>n</sub> ) <sub>14</sub> with $m > 10$ .....	145
3.3.1 Syntheses of $\beta$ CD-(PBO <sub>m</sub> ) <sub>14</sub> with $m > 10$ .....	145
3.3.2 Syntheses of $\beta$ CD-(PBO <sub>m</sub> -PGL <sub>n</sub> ) <sub>14</sub> with $m > 10$ .....	152
3.4 Self-assembly behaviors of the star copolymers.....	158
<b>4. Conclusions.....</b>	<b>166</b>
<b>5. Reference.....</b>	<b>166</b>
<b>6. Appendix.....</b>	<b>169</b>
6.1 The intermediates in the synthetic process of per(2-O-methyl-3,6-di-O-(3-hydroxypropyl))- $\beta$ CD.....	169
6.2 Estimation of the theoretical formula of the star copolymer $\beta$ CD-(PBO <sub>m</sub> -PGL <sub>n</sub> ) <sub>14</sub> .....	175

## 1. Introduction

The work in Chapter 2 has investigated the self-assembly behaviors of linear amphiphilic copolymers comprising of hydrophobic poly(butylene oxide) (PBO) block and hydrophilic polyglycidol (PGL) block(s). The results showed that their self-assembly behaviors were well consistent with the phase diagram for the self-assembly of amphiphilic block copolymers in aqueous solution and that hydrophobic-to-hydrophilic ratio decided the morphology [1]. Indeed, when the weight fraction of PGL block(s) ( $w_{\text{PGL}}$ ) ranged from 0.22 to 0.44, the linear copolymers self-assembled into polymersomes.

The linear amphiphilic copolymers dominate the field of polymersome formation [2–4]. However, it was recently suggested that deviation from the linear structure could also provide some interesting self-assembled structures with unique properties. Mikto-arm stars are star-like copolymers composed of branches with different chemical compositions and/or structures by block. Voigt et al. reviewed some of the early works carried out in this field [5]. The hydrophilic-to-hydrophobic ratio remains one of the driving forces to successfully obtain the desired polymersome structure, and the architectures spanning from simple trimiktoarm stars [6] to dendron-based stars [7] allowed for successful polymersome synthesis. The choice of such architecture seems counter-intuitive but it allows to add some specific functions to the polymersomes often related to their membrane permeability. Grafting azobenzene derivatives onto the star polymers has allowed the modulation of the permeability of the polymersomes thanks to a light triggering [8], and the system was then refined by the use of the complexes between azobenzene and Pillar-6-arene that successfully modulated drug release of polymersomes upon light triggering [9].

Triggering complex formation through host–guest systems opens the way to introduce supramolecules into the polymersome membranes to add functionality to the self-assembled systems. Later on, cyclodextrin was used to form the core of a triarm star polymer with amphiphilic arms through a grafting-onto strategy [10]. The control over the number of arms was poor, but the presence of cyclodextrin into the hydrophobic part of the membrane was found to play important roles in the improved loading efficiency of doxorubicin as well as the sustained drug release. The structural aspect of polymersomes, when star polymers are used instead of linear amphiphilic copolymers, have been poorly addressed, even if Plamper et al. reported that in their system, the hydrophobic thickness of the membranes was not affected by the number of branches of the arm part involved in the formation of the hydrophobic domain of the interpolyelectrolyte complexes [11].

The previous studies revealed that the arm number of star-like polymers used in the formation of polymersomes were always kept to low values, typically 3, while in the lipid field, Lehn et al. demonstrated that bouquet-like molecules (actually star-like

polymers with arms of low molar masses) were able to be inserted in liposomes [12]. This was further confirmed by Badi et al. with 7-armed star polymers [13] and Faye et al. with 14-armed star polymers [14], where stable insertion of star polymers in lipid bilayers were demonstrated by black lipid membrane technique. However, the use of cyclodextrin-based star polymers in the polymersome field was scarce and limited to doxorubicine delivery. This oversight is surprising since the translocation of ssDNA through cyclodextrins could be demonstrated [15], opening the way to the modulation of the permeability of polymersome membranes, suitable for further development, either in the field of nanoreactor, or mimicking the cell functions.

In the present part of this manuscript, we aim at investigating the role of a cyclodextrin core onto the self-assembling of star polymers with high number of amphiphilic arms into polymersome. Taking example of results obtained in the domain of the nanopore technology, the star polymers have to be symmetrical in order to reach a high stability [15]. Thus, the *beta*-cyclodextrin ( $\beta$ CD)-based initiator was derivatized to obtain a well-defined symmetric structure, with 14 hydroxyl groups having the same reactivity ( $\beta$ CD-(OH)<sub>14</sub>) [14,15]. Afterwards, the symmetric  $\beta$ CD-cored star block copolymer ( $\beta$ CD-(PBO-PGL)<sub>14</sub>) was synthesized, initiated by the  $\beta$ CD derivative. The synthetic protocol generally included an adapted tBuP4-catalyzed sequential anionic ring-opening block copolymerization of butylene oxide (BO) and ethoxyethyl glycidol ether (EEGE), followed by a deprotection step in acidic conditions to obtain PGL blocks. A discussion about the different synthetic pathways used for the syntheses of star PBO-PGL copolymers was performed, according to the length of the PBO blocks. To assess the synthetic pathways, the intermediates and the final product were well characterized by <sup>1</sup>H NMR and SEC. At last, the symmetric star amphiphilic PBO-PGL copolymers were investigated on their self-assembly behaviors by dynamic light scattering (DLS), static light scattering (SLS), and small-angle X-ray scattering (SAXS).

## 2. Materials and Methods

### 2.1 Materials

The chemicals used for the preparation of per-(2-O-methyl-3,6-di-O-(3-hydroxypropyl))- $\beta$ CD ( $\beta$ CD-(OH)<sub>14</sub>) include native *beta*-cyclodextrin ( $\beta$ CD, Roquette, France; recrystallized in H<sub>2</sub>O and dried at 100 °C for 2 days before use), pyridine (anhydrous, 99.8%, Sigma–Aldrich), DMF (anhydrous, 99.8%, Sigma–Aldrich), 4-(dimethylamino)pyridine (DMAP, 99%, Acros Organics), *tert*-butyldimethylsilyl chloride (TBDMSCl, 98%, Acros Organics), sodium hydride (NaH, 60% dispersion in mineral oil, Sigma–Aldrich), iodomethane (MeI, 99%, contains copper as stabilizer, Sigma–Aldrich), tetrabutylammonium fluoride (TBAF, 1.0 M in

THF, Sigma–Aldrich), allyl bromide (99%, Acros Organics), 9-borabicyclo[3.3.1]nonane (9-BBN, 0.5 M in THF, Sigma–Aldrich), hydrogen peroxide ( $\text{H}_2\text{O}_2$ , 30 wt% in  $\text{H}_2\text{O}$ , contains stabilizer, Sigma–Aldrich), sodium hydroxide (NaOH, 97%, Sigma–Aldrich), and THF (anhydrous, collected from the MB SPS 800 solvent purification system). All of these chemicals were used as received.

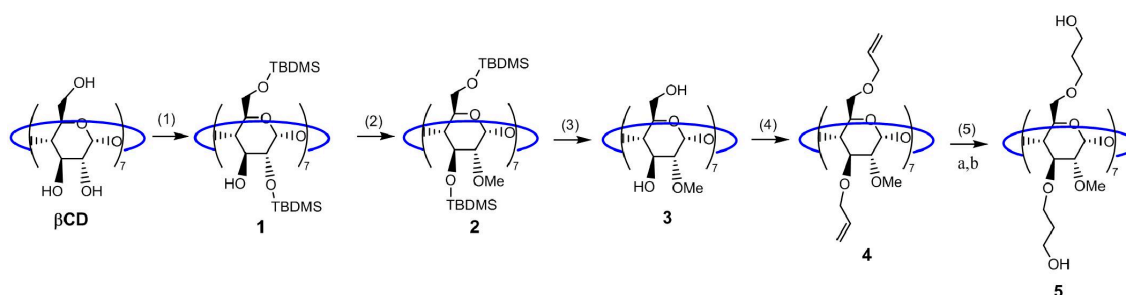
The chemicals used for polymerizations include butylene oxide (BO, 99%, Sigma–Aldrich), ethoxyethyl glycidyl ether (EEGE, home-made with a published method [16], its structure and purity were confirmed by  $^1\text{H}$  NMR,  $^{13}\text{C}$  NMR and COSY spectra as described in Chapter 2), DMF (anhydrous, 99.8%, Sigma–Aldrich), toluene (anhydrous, collected from the solvent MB SPS COMPACT purification system equipped in the glovebox), and tBuP4 (0.8 M in *n*-hexane, Sigma–Aldrich). BO, EEGE and DMF were dried twice over  $\text{CaH}_2$  (Sigma–Aldrich) and stored in the glovebox before use. Toluene was used as received. tBuP4 was stored in the glovebox before use and used as received. All of the chemicals were charged into the reaction container in the glovebox (MBRAUN), which is equipped with a gas purification system (molecular sieves and copper catalyst) and dry argon atmosphere ensuring the moisture content ( $\text{H}_2\text{O}$ ) less than 0.5 ppm monitored by an MB-MO-SE1 moisture probe.

Other chemicals for common uses include  $\text{H}_2\text{SO}_4$  (98%, Sigma–Aldrich), HCl (37%, Sigma–Aldrich),  $\text{NaHCO}_3$  (VWR),  $\text{MgSO}_4$  (VWR), methanol (MeOH, VWR), dichloromethane (DCM, VWR), diethyl ether ( $\text{Et}_2\text{O}$ , VWR), petroleum ether (VWR), and silica gel 60M (Macherey-Nagel). These chemicals were used as received.

## 2.2 Synthesis of per(2-O-methyl-3,6-di-O-(3-hydroxypropyl))- $\beta$ CD

The  $\beta$ CD-based initiator, per(2-O-methyl-3,6-di-O-(3-hydroxypropyl))- $\beta$ CD ( $\beta$ CD-(OH)<sub>14</sub>), was synthesized following a published method [14], as shown in Scheme 1.

**Scheme 1.** Synthetic Procedure for the  $\beta$ CD-based Initiator, Per(2-O-methyl-3,6-di-O-(3-hydroxypropyl))- $\beta$ CD ( $\beta$ CD-(OH)<sub>14</sub>).



The details of each step are described as follows.

**(1) Synthesis of per(2,6-di-O-*tert*-butyldimethylsilyl)- $\beta$ CD (product 1)**

Native  $\beta$ CD (dried at 80 °C overnight before use; 5.00 g, 4.4 mmol, 1 eq) was dissolved in anhydrous DMF (75 mL) and pyridine (50 mL). Into this solution, TBDMSCl (27.75 g, 184 mmol, 42 eq) and DMAP (25 mg, 0.2 mmol, 0.05 eq) were sequentially added. The mixture was stirred at 100 °C (refluxing) for 24 hours under Ar atmosphere. At the end, the mixture was concentrated. The residue mixed with DCM and DI H<sub>2</sub>O to be totally dissolved in two phases. The organic phase was sequentially washed with DI H<sub>2</sub>O, H<sub>2</sub>SO<sub>4</sub> (0.25 M) and DI H<sub>2</sub>O and subsequently dried with MgSO<sub>4</sub>. After filtering out the solid, the organic solution was concentrated. The obtained crude product was purified first via precipitation in MeOH and then by a SiO<sub>2</sub> column (DCM as the eluant). The purified product was obtained after concentrating the collected eluant solutions, as per(2,6-di-O-TBDMS)- $\beta$ CD (white solid; 10.36 g, yield 86%).

**(2) Synthesis of per(2-O-methyl-3,6-di-O-*tert*-butyldimethylsilyl)- $\beta$ CD (product 2)**

NaH (60% dispersion in mineral oil; 10.24 g, 256 mmol, 140 eq) was washed by petroleum ether (250 mL  $\times$  3) and then was suspended in anhydrous THF (85 mL). Into this suspension, the solution of per(2,6-di-O-TBDMS)- $\beta$ CD (product 1, dried at 80 °C overnight before use; 5.00 g, 1.83 mmol, 1 eq) in anhydrous THF (40 mL) was charged under Ar at 0 °C with stirring. After feeding, the mixture was stirred at 0 °C for another 3 hours before the addition of MeI (12.75 mL, 205 mmol, 112 eq). The reaction mixture was stirred at room temperature (r.t.) for 72 hours in dark. At the end, some MeOH was added to quench the excess of NaH and then the solvents were removed by rotavapor. The residue was dissolved in some DCM. Subsequently the solution was washed with DI H<sub>2</sub>O three times then dried with MgSO<sub>4</sub>. The organic solution was collected and concentrated to give the crude product. The crude product was purified via precipitation in MeOH twice. At last, the purified product was collected by vacuum filtration, as per(2-O-Me-3,6-di-O-TBDMS)- $\beta$ CD (white powder; 3.65 g, yield 70%).

**(3) Synthesis of per(2-O-methyl)- $\beta$ CD (product 3)**

Per(2-O-Me-3,6-di-O-TBDMS)- $\beta$ CD (product 2, dried at 80 °C overnight before use; 3.00 g, 1.06 mmol, 1 eq) was dissolved in anhydrous THF (12 mL). Then the solution was added into the solution of TBAF (1 M in THF; 45 mL, 45 mmol, 42 eq). The reaction mixture was stirred at 80 °C (refluxing) for 4 hours, then at 40 °C overnight. At the end, the reaction mixture was concentrated by rotavapor. The residue was dissolved into Et<sub>2</sub>O (ca. 200 mL) with the aid of ultrasound at r.t. for 1 hour. The resultant supernatant was poured out and the precipitate was recrystallized in MeOH to obtain the expected product, as per(2-O-Me)- $\beta$ CD (white solid; 0.72 g, yield 55%).

**(4) Synthesis of per(2-O-methyl-3,6-di-O-allyl)- $\beta$ CD (product 4)**

NaH (60% dispersion in mineral oil; 0.68 g, 17 mmol, 42 eq) was washed by petroleum ether (150 mL  $\times$  3) and suspended in anhydrous DMF (10 mL). Into this suspension, the solution of per(2-O-Me)- $\beta$ CD (product **3**, dried at 80 °C overnight before use; 0.50 g, 0.41 mmol, 1 eq) in anhydrous DMF (2.5 mL) was charged at 0 °C under Ar. The mixture was stirred at 0 °C for 1 hour and then allyl bromide (1.2 mL, 13.9 mmol, 34 eq) was added. The reaction mixture was stirred at 0 °C under Ar for 12 hours. At the end, some MeOH was added to quench the excess of NaH, and the quenched mixture was concentrated. The residue was dissolved in some DCM. The obtained solution was washed by DI H<sub>2</sub>O and dried with MgSO<sub>4</sub>. At last, the solution was collected and concentrated to give the product, as per(2-O-Me-3,6-di-O-Allyl)- $\beta$ CD (brown viscous liquid; 0.65 g, yield 90%).

**(5) Synthesis of per(2-O-methyl-3,6-di-O-(3-hydroxypropyl))- $\beta$ CD (product 5)**

Per(2-O-Methyl-3,6-di-O-Allyl)- $\beta$ CD (product **4**, dried at 80 °C overnight before use; 0.50 g, 0.28 mmol, 1 eq) was dissolved in anhydrous THF (5 mL). The solution was then added into the solution of 9-BBN (0.5 M in THF; 24 mL, 12 mmol, 43 eq) at 0 °C under Ar. After feeding, the mixture was stirred at 0 °C for 1 hour and then at r.t. for 72 hours. Then, a NaOH solution (3 M in H<sub>2</sub>O; 10.42 mL, 31.3 mmol, 112 eq) and a H<sub>2</sub>O<sub>2</sub> solution (30 wt% in H<sub>2</sub>O; 32 mL, 313 mmol, 1120 eq) were simultaneously and slowly added into the reaction mixture. After feeding, the mixture was stirred at 60 °C (refluxing) for 72 hours. At the end, the reaction mixture was concentrated by rotavapor. The remaining aqueous solution was washed by Et<sub>2</sub>O and then freeze-dried. The obtained solid was mixed with some EtOH (ca. 200 mL), with the aid of ultrasound at r.t. for 1 hour. The insoluble solid was removed by vacuum filtration. The collected filtrate was concentrated to give the crude product, which was then purified by dialysis against H<sub>2</sub>O with a regenerated cellulose membrane (MWCO 1 kDa). Finally, the purified product was obtained after freeze-drying, as per(2-O-Me-3,6-di-O-(3-hydroxypropyl))- $\beta$ CD (white solid; 0.21 g, yield 36%).

The products obtained in each step were characterized by <sup>1</sup>H, <sup>13</sup>C and COSY NMR before being used for the next reaction. The spectra were recorded on a Bruker Ultra Shield 300 NMR spectrometer routinely (at 300 K) and were analyzed with MestReNova 9.1.0 software using the residual proton signals of the deuterated solvents as the internal reference.

Additionally, for the convenience of use, the final product (product **5**), namely the  $\beta$ CD-based initiator, was dried at 120 °C overnight and then weighed. The dried and weighed product was then dissolved in anhydrous DMF to a concentration of 50 mg mL<sup>-1</sup> and stored in the glovebox before use. When the initiator was used for polymerization, it was further dried via the following treatment: the required amount

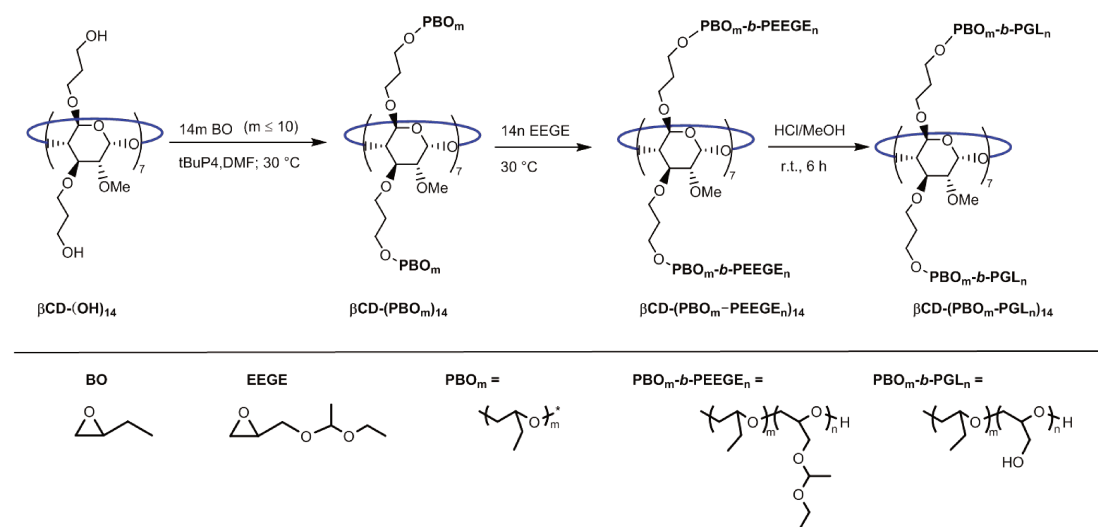
of initiator solution (50 mg mL<sup>-1</sup> in DMF) mixed with an equal volume of anhydrous toluene, performed in glovebox, and the solution was stirred at r.t. overnight. Subsequently, the solvents were removed via distillation on vacuum line and the residue was dried at 120 °C overnight, ready to be used for polymerization.

### 2.3 Synthesis of $\beta$ CD-(PBO<sub>m</sub>-PGL<sub>n</sub>)<sub>14</sub> with $m \leq 10$

$\beta$ CD-cored star copolymers,  $\beta$ CD-(PBO<sub>m</sub>-PGL<sub>n</sub>)<sub>14</sub> with  $m$  and  $n$  being respectively the numbers of the BO and GL units per arm, were synthesized.

First, star copolymers having “short” PBO blocks,  $\beta$ CD-(PBO<sub>m</sub>-PGL<sub>n</sub>)<sub>14</sub> ( $m \leq 10$ ), were synthesized with a reported procedure with minor adaptation [14]. The synthetic procedure is divided into a tBuP4-catalyzed sequential anionic ring-opening block copolymerization and a deprotection step, as shown in Scheme 2.

**Scheme 2.** Synthetic Pathway for  $\beta$ CD-(PBO<sub>m</sub>-PGL<sub>n</sub>)<sub>14</sub> with  $m \leq 10$ .



The synthesis of the star copolymer  $\beta$ CD-(PBO<sub>7</sub>-PGL<sub>5</sub>)<sub>14</sub> (Entry HQ137) is described here as an example: BO (0.2426 g, 3.36 mmol, 112 eq) and tBuP4 (0.8 M in *n*-hexane; 105  $\mu$ L, 0.084 mmol, 2.8 eq) were sequentially added into the solution of  $\beta$ CD-(OH)<sub>14</sub> (61.32 mg, 0.03 mmol, 1 eq) in DMF (0.72 mL). The mixture was stirred at 30 °C for 72 hours. At the end, the conversion of BO was checked by <sup>1</sup>H NMR characterization of the homopolymerization medium. Subsequently, EEGE (0.3420 g, 2.34 mmol, 78 eq) was added and the mixture was stirred at 30 °C for another 72 hours. At the end, the conversion of EEGE was also checked by <sup>1</sup>H NMR. Then drops of DI H<sub>2</sub>O was added into the reaction medium to quench the polymerization.

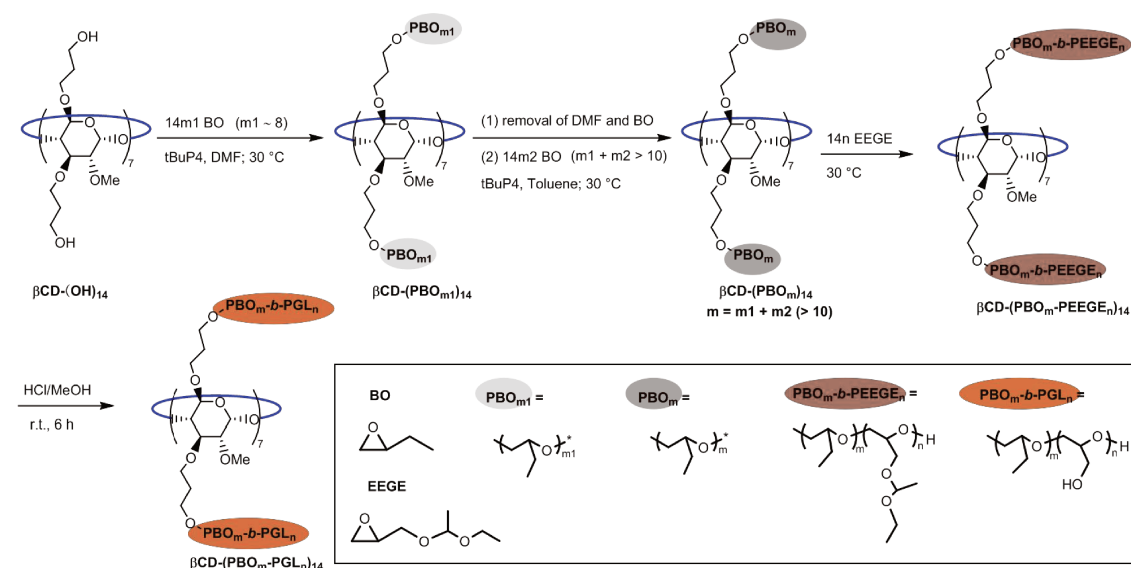
The quenched reaction mixture was concentrated by rotavapor, and the residue was then dissolved in Et<sub>2</sub>O and washed with DI H<sub>2</sub>O. The organic phase was dried by MgSO<sub>4</sub>. After filtration, the organic solution was concentrated to give the intermediate.

Subsequently, the obtained intermediate was treated in acidic conditions to reveal the hydroxyl groups: the previously obtained intermediate, with a composition of BO/EEGE/ $\beta$ CD = 105/76/1 ( $M_n = 20.8 \text{ kg mol}^{-1}$ ; 138.4 mg, 6.7  $\mu\text{mol}$ ), was dissolved in MeOH (2.6 mL). Into this solution, a HCl solution (2 M in MeOH; 0.26 mL, 0.52 mmol) was added. The mixture was stirred at r.t. for 6 hours then was neutralized by NaHCO<sub>3</sub> (0.15 g, 1.75 mmol). The resultant solid was removed by filtration. The filtrate was concentrated by rotavapor, giving the crude product. The crude product was purified by dialysis against MeOH with a regenerated cellulose membrane (MWCO 10 kDa). The final product was obtained after concentration.

## 2.4 Synthesis of $\beta\text{CD}-(\text{PBO}_m\text{-PGL}_n)_{14}$ with $m > 10$

Star copolymers having relatively “long” PBO blocks,  $\beta\text{CD}-(\text{PBO}_m\text{-PGL}_n)_{14}$  ( $m > 10$ ), were synthesized following a refined procedure as shown in Scheme 3. This procedure includes a stepwise homopolymerization of BO, a sequential block copolymerization of EEGE and a final deprotection treatment in acidic conditions.

**Scheme 3.** Synthetic Pathway for  $\beta\text{CD}-(\text{PBO}_m\text{-PGL}_n)_{14}$  with  $m > 10$ .



Here is an example for the synthesis of the star copolymer  $\beta$ CD-(PBO<sub>24</sub>-PGL<sub>6</sub>)<sub>14</sub> (Entry HQ144): BO (0.1124 g, 1.70 mmol, 113 eq) and tBuP4 (0.8 M in *n*-hexane; 52.5  $\mu$ L, 0.042 mmol, 2.8 eq) were sequentially added into the solution of  $\beta$ CD-(OH)<sub>14</sub> (30.66 mg, 0.015 mmol, 1 eq) in DMF (0.26 mL). The reaction mixture was stirred at 30 °C for 48 hours and the conversion of BO was checked by <sup>1</sup>H NMR. Then the solvent DMF and the unreacted monomer BO were removed via distillation on vacuum line. The residue (a brown viscous liquid) was dissolved with toluene (1.2 mL) before the second batch of BO (0.3607 g, 5.00 mmol, 334 eq) and tBuP4 (0.8 M in *n*-hexane; 26.25  $\mu$ L, 0.021 mmol, 1.4 eq) were added sequentially. The reaction mixture was stirred at 30 °C for 72 hours, and the conversion of BO was checked by <sup>1</sup>H NMR at the end. Subsequently, EEGE (0.3052 g, 2.09 mmol, 139 eq) was charged into the reactor. The copolymerization was performed at 30 °C for 72 hours, and the conversion of EEGE was checked by <sup>1</sup>H NMR at the end of the reaction. Then, drops of DI H<sub>2</sub>O was added into the reaction medium. The mixture was concentrated, and the residue was then dissolved in Et<sub>2</sub>O and was washed by DI H<sub>2</sub>O. The organic solution was dried by MgSO<sub>4</sub>. After filtering out the solid, the filtrate was concentrated giving the intermediate.

To reveal the hydroxyl groups, the deprotection step in acidic conditions was performed: the previously obtained intermediate, with a composition of BO/EEGE/ $\beta$ CD = 431/139/1 (*M<sub>n</sub>* = 53.4 kg mol<sup>-1</sup>; 732.7 mg, 0.014 mmol), was dissolved in MeOH (8.6 mL). Then, into this solution, a HCl solution (2 M in MeOH; 0.96 mL, 1.91 mmol) was added. The mixture was stirred at r.t. for 6 hours before the addition of NaHCO<sub>3</sub> (0.48 g, 5.7 mmol). The resultant solid was filtered out, and the collected filtrate was concentrated to give the crude product, which was further purified by dialysis against MeOH with a regenerated cellulose membrane (MWCO 10 kDa). The final product was obtained after removing the solvent.

## 2.5 Structural characterizations of the star polymers

The star polymers were characterized by <sup>1</sup>H NMR and size exclusion chromatography (SEC). <sup>1</sup>H NMR spectra were recorded on a Bruker Ultra Shield 300 NMR spectrometer routinely (300 K) and analyzed with MestReNova 9.1.0 software using the residual proton signals of the deuterated solvents as the internal reference.

SEC were performed in DMF or THF. In DMF, the measurements were carried on a Viscotek gel permeation chromatography system (TDA 305) equipped with one PSS-GRAM 30 Å column (8 mm × 300 mm) and two PSS GRAM 1000 Å columns (8 mm × 300 mm) maintained at 60 °C. DMF (containing 1.0 g L<sup>-1</sup> lithium bromide as an additive) was used as the mobile phase at a flow rate of 0.8 mL min<sup>-1</sup>. All polymers were injected at a concentration of 5 mg mL<sup>-1</sup> after filtration through the

0.2  $\mu\text{m}$  syringe filter. In THF, the measurements were carried out on three PL Gel Mixte C 5  $\mu\text{m}$  columns (7.5  $\times$  300 mm) maintained at 40  $^{\circ}\text{C}$  coupled with 2 modular detectors: a differential refractive index (RI) detector (Viscotek 3580) and a diode array UV detector (Shimadzu SPD20-AV). THF was used as the mobile phase at a flow rate of 1  $\text{mL min}^{-1}$ . All polymers were injected at a concentration of 5  $\text{mg mL}^{-1}$  after filtration through the 0.45  $\mu\text{m}$  syringe filter. In both cases, the OmniSEC 5.12 software was used for data acquisition and data analysis. The number-average molar mass ( $M_{\text{NSEC}}$ ), the weight-average molar mass ( $M_{\text{WSEC}}$ ) and the polydispersity index ( $\mathcal{D} = M_{\text{WSEC}}/M_{\text{NSEC}}$ ) were determined with a calibration curve based on narrowly distributed poly(methyl methacrylate) (PMMA) standards (from Polymer Standard Services), using an RI detector.

## 2.6 Self-assembly behaviors of the star copolymers

### 2.6.1 Preparation of the self-assemblies

The self-assemblies of the star amphiphilic copolymers were manufactured using the thin-film rehydration method [17,18]. Typically, the star copolymer (5.0 mg),  $\beta\text{CD}-(\text{PBO-PGL})_{14}$ , was first dissolved in MeOH (2.5 mL). Subsequently, MeOH was removed by rotavapor (40  $^{\circ}\text{C}$ , 5 mbar, 30 min) to get the polymer film on the inner wall of the vial. The polymer film was then rehydrated by DI  $\text{H}_2\text{O}$  (5.0 mL). After stirring for adequate time, the film sufficiently detached from the inner wall giving a suspension. The suspension was repeatedly extruded through a PTFE syringe filter (0.45  $\mu\text{m}$ ) repeatedly (in one direction) to remove dusts and/or ill-aggregates for light scattering characterizations, usually 5 times.

### 2.6.2 Characterizations of the self-assemblies

The self-assemblies were characterized by dynamic light scattering (DLS), static light scattering (SLS), as well as small-angle X-ray scattering (SAXS).

#### (1) Dynamic light scattering (DLS)

DLS data were acquired using a ZetaSizer Nano ZS90 at 20  $^{\circ}\text{C}$ . The averaged intensity autocorrelation functions were evaluated using non-negative least-squares (NNLS) analysis implemented in the Zetasizer software to produce the particle size distribution curves (Intensity PSD curves). The hydrodynamic radius ( $R_{\text{H}}$ ) of the nanoparticles was determined by using the Stokes–Einstein equation:

$$R_{\text{H}} = \frac{k_{\text{B}}T}{6\pi\eta D} \quad (1)$$

wherein  $k_B$  is the Boltzmann constant,  $T$  is the absolute temperature,  $\eta$  is the viscosity of the solvent, and  $D$  is the diffusion coefficient as  $D = \tau^{-1}q^{-2}$  with  $\tau$  being the mean relaxation time related to the diffusion of the nanoparticles and  $q$  the scattering vector. The autocorrelation functions were also analyzed using the cumulant method [19].

$$\ln g_1(t) = \ln C - \Gamma t + \frac{\mu_2}{2} t^2 \dots \quad (2)$$

wherein  $C$  is the amplitude,  $\Gamma$  is the relaxation frequency ( $\tau^{-1}$ ), and the parameter  $\mu_2$  is known as the second-order cumulant. The polydispersity index of the particles (PDI) was computed as  $\text{PDI} = \mu_2/\Gamma^2$ .

The values of  $R_H$  and PDI were reported as the Z-average radius and corresponding PDI given by the Zetasizer software, based on 5 measurements.

## (2) Static light scattering (SLS)

SLS measurements were performed on a ZetaSizer Nano ZS90 at 20 °C by measuring the light intensities monitored at a scattering angle  $\theta = 90^\circ$ , as a function of the polymer concentration. The molecular weight of the self-assembled nanoparticles ( $M_{W_{\text{NPs}}}$ ) was estimated using the Debye plot:

$$\frac{Kc}{R_\theta} = \frac{1}{M_{W_{\text{NPs}}}} + 2A_2c \quad (3)$$

wherein  $R_\theta$  (Rayleigh ratio) is the normalized scattered intensity with toluene as the standard solvent,  $c$  is the concentration given in  $\text{mg mL}^{-1}$  and  $K$  is the optical constant expressed by

$$K = \frac{4\pi^2 n^2 \left(\frac{dn}{dc}\right)^2}{N_A \lambda^4} \quad (4)$$

wherein  $n$  is the refractive index of the solvent,  $N_A$  is Avogadro's number, and  $dn/dc$  is the specific refractive index increment of the nanoparticle.

Specially, the  $dn/dc$  value of the nanoparticle in aqueous solution was estimated from the  $dn/dc$  values of βCD, PBO and PGL blocks and their weight fractions ( $w$ ) taking into account the additive rule [20]:

$$\frac{dn}{dc} = \left(\frac{dn}{dc}\right)_{\text{PBO}} w_{\text{PBO}} + \left(\frac{dn}{dc}\right)_{\text{PGL}} w_{\text{PGL}} + \left(\frac{dn}{dc}\right)_{\beta\text{CD}} w_{\beta\text{CD}} \quad (5)$$

where  $w_{\text{PBO}}$ ,  $w_{\text{PGL}}$  and  $w_{\beta\text{CD}}$  are the weight fractions of the individual components,

and the respective  $dn/dc$  values were estimated based on the refractive indexes ( $n$ ) of the components. Therefore, Equation 5 is simplified as

$$\frac{dn}{dc} = (n_{\text{PBO}} \times w_{\text{PBO}} + n_{\text{PGL}} \times w_{\text{PGL}} + n_{\beta\text{CD}} \times w_{\beta\text{CD}}) - n_{\text{water}} \quad (6),$$

with the refractive indexes of PBO ( $n_{\text{PBO}}$ ), PGL ( $n_{\text{PGL}}$ ),  $\beta$ CD ( $n_{\beta\text{CD}}$ ) and water ( $n_{\text{water}}$ ) being 1.454, 1.474, 1.478 and 1.333, respectively.

Taking into account the Equation 3, plotting  $Kc/R_\theta$  against  $c$  at a given angle, the molecular weight of the assemblies ( $M_{\text{WNPs}}$ ) is extracted from the reverse of the intercept, and accordingly the aggregation number ( $N_{\text{agg}}$ ) can be determined as

$$N_{\text{agg}} = \frac{M_{\text{WNPs}}}{M_{\text{polymer}}} \quad (7)$$

wherein  $M_{\text{polymer}}$  is the molar mass of the copolymer chain.

### (3) Small-angle X-ray scattering (SAXS)

SAXS measurements were performed, thanks to a collaboration with Guillaume Tresset, in the SWING beamline at SOLEIL synchrotron facility (Gif-sur-Yvette, France). The wavelength was set to 1 Å, and the sample-to-detector distance was 2 m, which provided scattering wavenumbers ranging from about 0.005 to 0.5 Å<sup>-1</sup>. The samples were automatically injected into a through-flow capillary, and for each sample, about 30 two-dimensional scattering images were recorded on an Eiger 4 M Dectris detector with an exposure time of 1 s while pushing the sample to avoid radiation damages. The scattering intensities were converted into absolute units after subtracting the contribution of the buffer using the FOXTROT software package. The produced SAXS data were analyzed by using the SASfit software (Paul Scherrer Institute, Switzerland).

## 3. Results and Discussions

### 3.1 Synthesis of the initiator, per(2-O-methyl-3,6-di-O-(3-hydroxypropyl))- $\beta$ CD

The initiator, per(2-O-methyl-3,6-di-O-(3-hydroxypropyl))- $\beta$ CD ( $\beta$ CD-(OH)<sub>14</sub>), was prepared via a 5-step method [14], as depicted in Scheme 1.

The first step is to protect the hydroxyl (OH) groups at 2- and 6- positions of the glucopyranose of the native  $\beta$ CD by *tert*-butyldimethylsilyl (TBDMS) groups giving per(2,6-di-O-TBDMS)- $\beta$ CD (product 1).

In the following step, *i.e.* the methylation of the 3-position of the glucopyranose units, the TBDMS groups migrated from 2-position to 3-position under basic conditions

and, at the meanwhile, the 2-position was methylated by MeI [21]. Consequently, the OH groups on 3- and 6- positions were protected by TBDMS groups in the form of per(2-O-Me-3,6-di-O-TBDMS)- $\beta$ CD (product **2**). In the native  $\beta$ CD, the OH function at 3-position of the glucopyranose unit is oriented towards the inside of the  $\beta$ CD ring, while the OH function at 2-position is oriented towards the outside. We believe that the properties of the  $\beta$ CD-based initiator and star polymers will not be affected too much by this migration step of the protective residue.

Next, the protective TBDMS groups at 3- and 6- positions were cleaved with the aid of TBAF giving the deprotected product, per(2-O-Me)- $\beta$ CD (product **3**). Then, the OH groups at 3- and 6- positions of the glucopyranose units were modified with allyl bromide giving per(2-O-methyl-3,6-di-O-allyl)- $\beta$ CD (product **4**). At last, allyl groups were oxidized into the end primary OH groups via hydroboration-oxidation reactions producing the final expected product, per(2-O-methyl-3,6-di-O-(3-hydroxypropyl))- $\beta$ CD (product **5**).

The structure and purity of the products in the first four steps were confirmed by their  $^1\text{H}$  NMR,  $^{13}\text{C}$  NMR and COSY spectra (Figures A1–A4, Appendix) before being used in the next step. The structure and purity of the final product (product **5**) were also assessed by the  $^1\text{H}$  NMR,  $^{13}\text{C}$  NMR and COSY spectra (Figure 1).

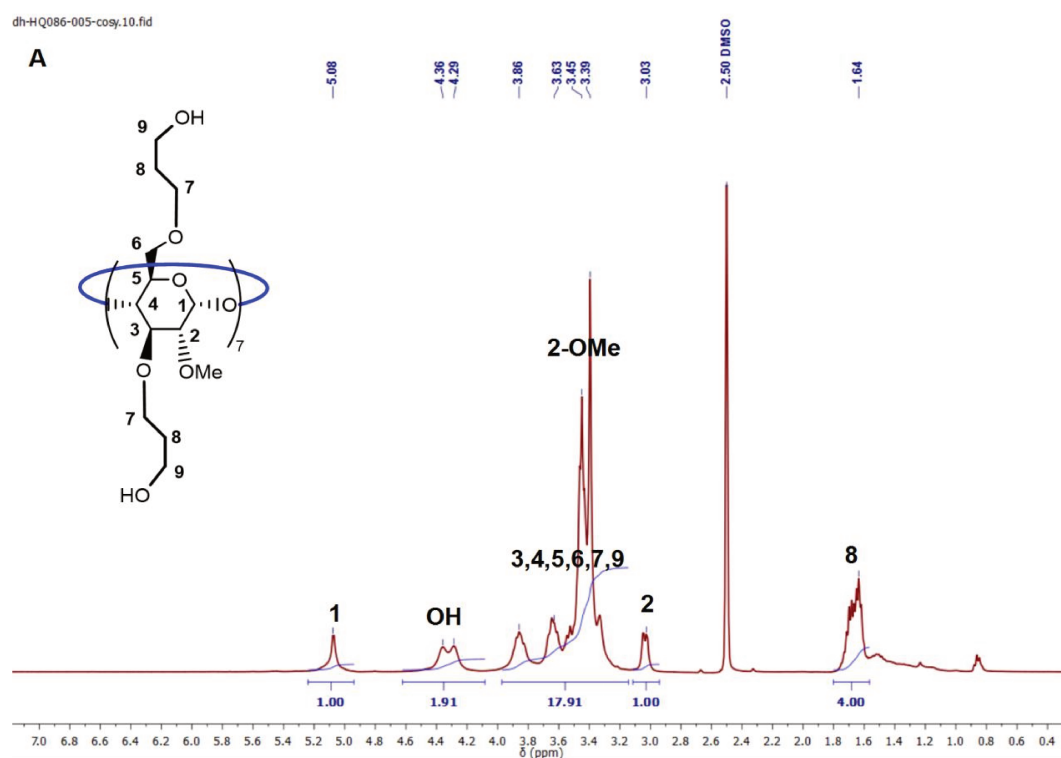


**Figure 1.** (A) Representative  $^1\text{H}$  NMR spectrum of per(2-O-methyl-3,6-di-O-(3-hydroxypropyl))- $\beta$ CD ( $\beta$ CD-(OH)<sub>14</sub>, product **5** in Scheme 1), recorded in DMSO-*d*<sub>6</sub> at 300 K.

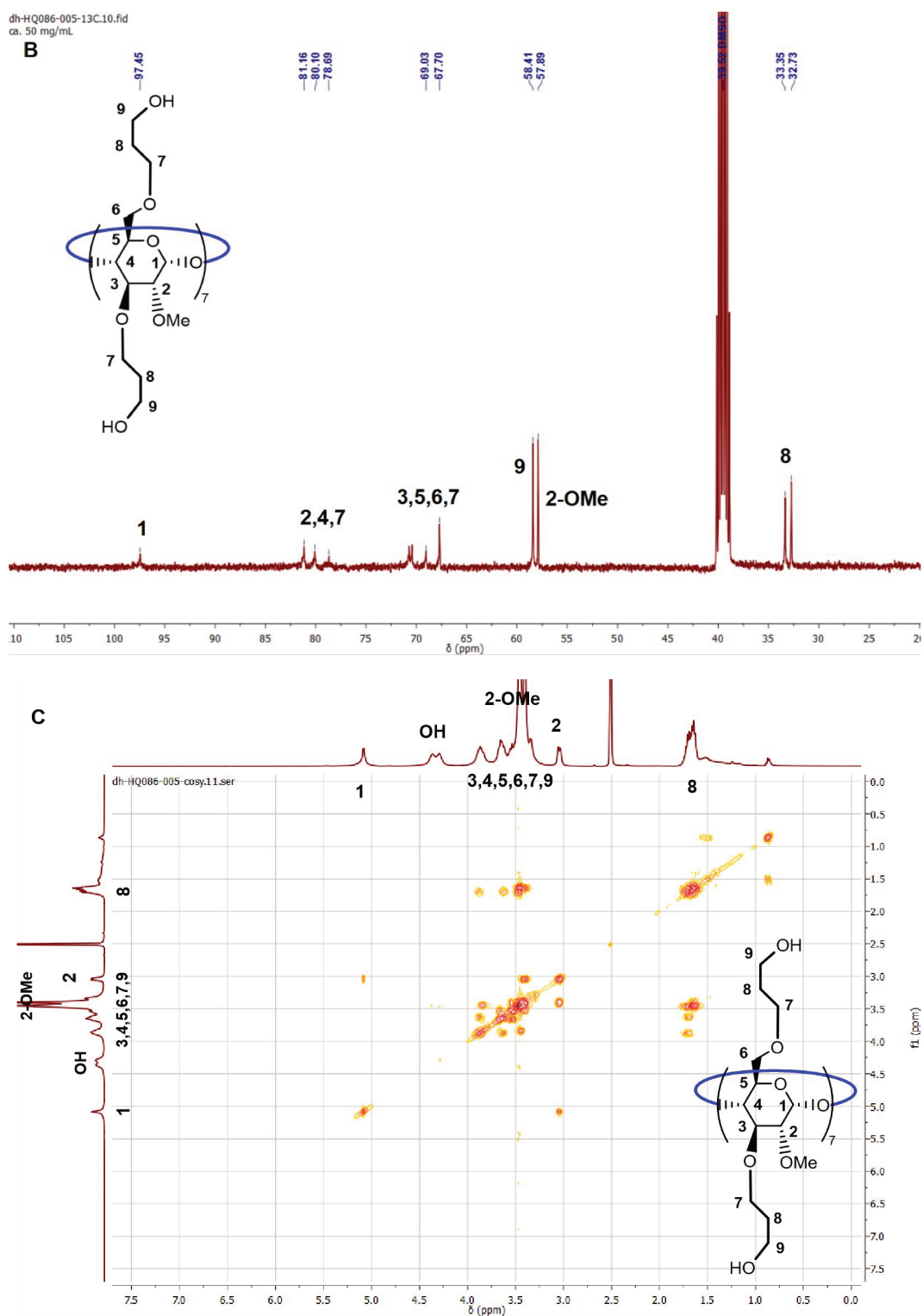


**Figure 1 (continued).** Representative (B)  $^{13}\text{C}$  NMR and (C) COSY spectra of per(2-O-methyl-3,6-di-O-(3-hydroxypropyl))- $\beta$ CD ( $\beta$ CD-(OH) $_{14}$ , product **5** in Scheme 1), recorded in DMSO- $d_6$  at 300 K.

In the  $^1\text{H}$  NMR spectrum (Figure 1A), the defined anomeric proton (proton 1) was detected ( $\delta$  5.08 ppm,  $q$ ). The other protons were also detected at the respective

expected chemical shifts. Setting the integration of anomeric proton as the reference *i.e.*,  $I_1 = 1.00$ , the other proton integrals were calculated, as labeled in the spectrum. The integrals were consistent with the expected chemical formula, indicating a good purity. In the  $^{13}\text{C}$  NMR spectrum (Figure 1B), the anomeric carbon ( $\delta$  97 ppm), as well as the other carbons were identified with the right chemical shifts [15]. The COSY spectrum (Figure 1C) also showed the expected correlations between the protons. Altogether, the spectra indicated that the final product, namely the  $\beta$ CD-based initiator, was obtained with the expected structure and a good purity.

### 3.2 Syntheses of the star copolymers $\beta\text{CD}-(\text{PBO}_m\text{-PGL}_n)_{14}$ with $m \leq 10$

It has been shown in our previous work that the per(2-O-methyl-3,6-di-O-(3-hydroxypropyl))- $\beta$ CD ( $\beta\text{CD}-(\text{OH})_{14}$ ) initiator possesses 14 OH functions of equal reactivity in anionic ring-opening polymerizations [21,22]. Thus, the  $\beta\text{CD}-(\text{OH})_{14}$  initiator was used in the present study to synthesize  $\beta$ CD-cored star copolymers, *i.e.*  $\beta\text{CD}-(\text{PBO}_m\text{-PGL}_n)_{14}$  with  $m$  and  $n$  being respectively the numbers of BO and GL units per arm.

Adapted from the published procedures [14,23,24], the star copolymers with short PBO blocks,  $\beta\text{CD}-(\text{PBO}_m\text{-PGL}_n)_{14}$  ( $m \leq 10$ ) were synthesized via a tBuP4-catalyzed sequential anionic ring-opening block copolymerization of BO and EEGE, followed by a deprotection treatment in acidic conditions (Scheme 2).

For the star copolymer  $\beta\text{CD}-(\text{PBO}_7\text{-PGL}_5)_{14}$  (Entry HQ137), the homopolymerization of BO was first performed, at 30 °C in DMF with the feeding ratio of  $[\text{BO}]_0/[\text{tBuP4}]_0/[\beta\text{CD}]_0 = 112/2.8/1$ . After 72 hours, a sampling of the reaction medium was performed, and the conversion of BO was determined from the  $^1\text{H}$  NMR spectrum as  $p_{\text{BO}} = 0.94$  (Figure 2A), on the basis of the integrates of the epoxide proton (proton a',  $\delta$  2.43 ppm (*dd*)) and the methyl protons (protons d' and d,  $\delta$  0.96 and 0.88 ppm (*t*)). Of the glucopyranose unit, the anomeric proton (proton 1,  $\delta$  5.09 ppm) was clearly shown, while the others were respectively overlapped either by the peak of water or by the peaks of polyether protons. In specific, the peak of the methylene protons ( $-\text{CH}_2\text{-OR}$ , proton 8, around  $\delta$  1.7 ppm), was overlapped by the peak of water (OH), and the peaks of the other protons attributed to the  $\beta$ CD initiator (protons 2,3,4,5,6,7, "H<sub>CD</sub>",  $\delta$  4.0–2.9 ppm), were overlapped by the peaks of the protons of polyether backbone (protons a,b).

Then, EEGE was added into the reactor with a feeding ratio of  $[\text{EEGE}]_0/[\beta\text{CD}]_0 = 78/1$ . After 48 hours, the conversion of EEGE was determined from the  $^1\text{H}$  NMR spectrum of the reaction medium as  $p_{\text{EEGE}} = 0.98$  (Figure 2B), based on the integral ratio of the methine proton of the EEGE monomer (proton h',  $\delta$  4.73 ppm (*q*)) to that of the EEGE repeating unit (proton h,  $\delta$  4.67 ppm (*q*)). The anomeric proton of the

$\beta$ CD ring (proton 1,  $\delta$  5.09 ppm) was detected once more. However, the tiny peak was hard to be integrated in a proper manner, and in consequence, it is unreliable to determine the number-average molar mass of the copolymer from the  $^1\text{H}$  NMR spectrum. It was worth to note that, in this spectrum (Figure 2B), the peaks assigned to BO monomer were again detected (*e.g.*, proton a',  $\delta$  2.46 ppm (*dd*)), implying BO was not consumed in the copolymerization which owes to the much higher reactivity of EEGE than BO [25,26]. At this point, formation of blocks of BO and EEGE was witnessed, however formation of the expected star polymers was not demonstrated.

After quenching and purification the PBO-PEEGE intermediate was obtained (Figure 2C). The peaks attributed to tBuP4 ( $\delta$  2.66 ppm (*d*)) totally disappeared, comparing with the spectrum of the not-purified reaction medium (Figure 2B).

At last, the acetal groups of the PEEGE blocks were cleaved in acidic conditions, producing the crude deprotected PBO-PGL product, as proved by the  $^1\text{H}$  NMR spectrum (Figure 2D). The characteristic peaks of PEEGE (*e.g.*, protons h, i and k, in Figure 2C) entirely disappeared in the  $^1\text{H}$  NMR spectrum of the deprotected product (Figure 2D).

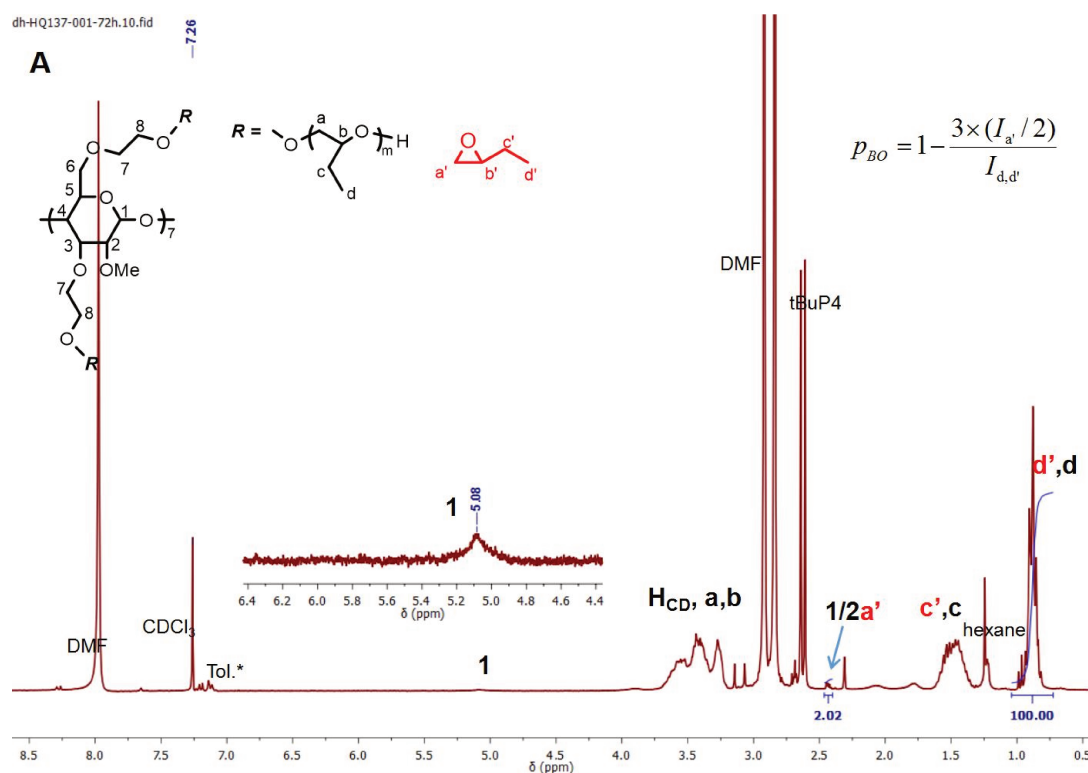


**Figure 2.** (A)  $^1\text{H}$  NMR spectrum of the PBO homopolymerization medium sampled in the synthetic process of the star copolymer  $\beta$ CD-(PBO<sub>7</sub>-PGL<sub>5</sub>)<sub>14</sub> (Entry HQ137). H<sub>CD</sub> are the protons in the  $\beta$ CD moiety including protons 2, 3, 4, 5, 6 and 7. \*Tol. is the residual toluene in the initiator due to the drying process, recorded in CDCl<sub>3</sub>-d<sub>1</sub> at 300 K.

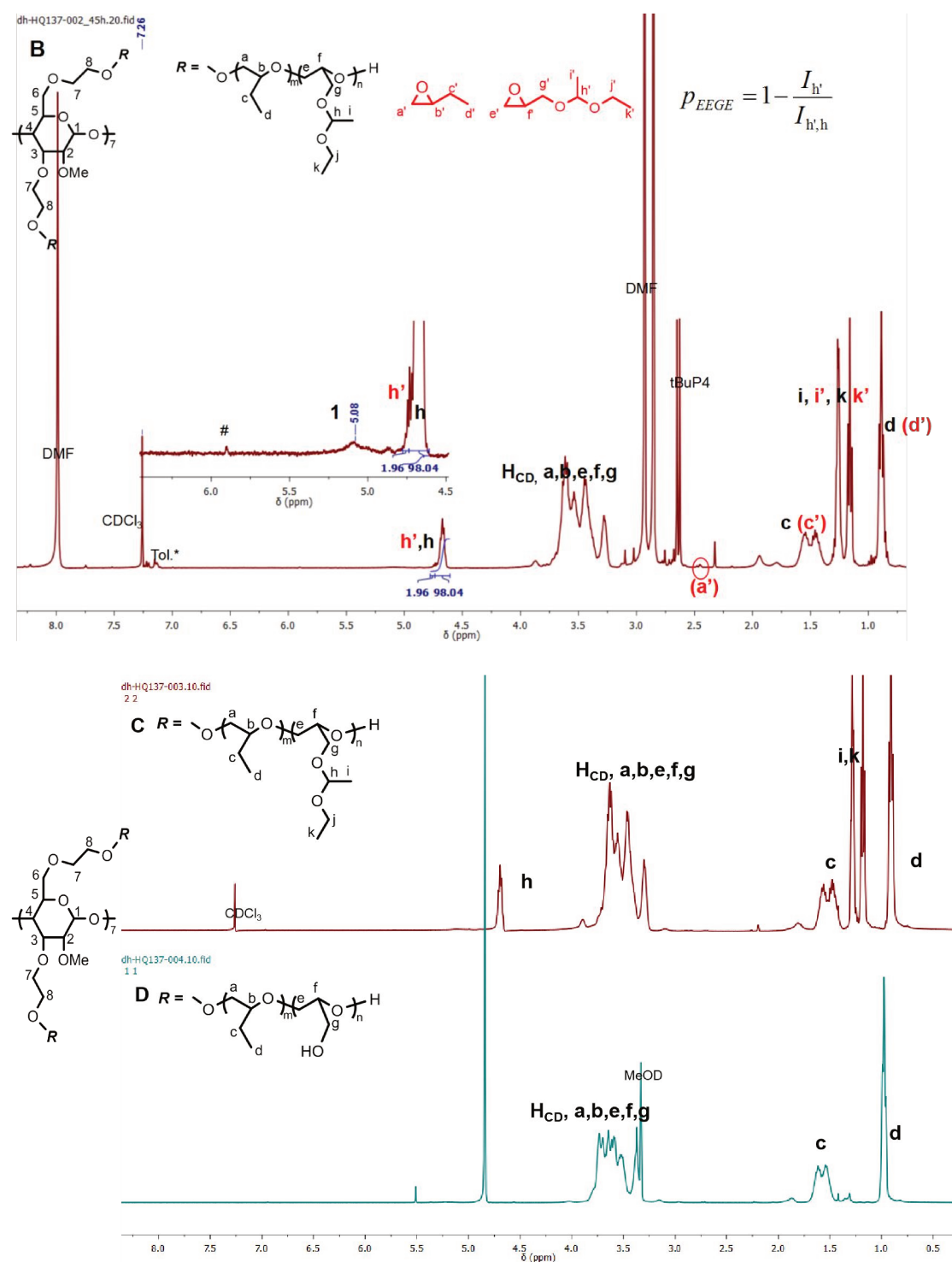


**Figure 2 (continued).**  $^1\text{H}$  NMR spectra of the intermediates and the crude deprotected product in the synthetic process of the star copolymer  $\beta\text{CD}-(\text{PBO}_7\text{-PGL}_5)_{14}$  (Entry HQ137): (B) PBO-PEEGE copolymer (reaction medium), (C) purified PBO-PEEGE copolymer (without tBuP4) and (D) crude PBO-PGL copolymer.  $\text{H}_{\text{CD}}$  are the protons in the  $\beta\text{CD}$  moiety including protons 2, 3, 4, 5, 6, and 7. Spectra B and C were recorded in  $\text{CDCl}_3\text{-d}_1$ , and D was in  $\text{MeOD-d}_4$ , all at 300 K.

The intermediates and the final deprotected products (before and after purification) were characterized by SEC (Figure 3). Trace *a* indicated the PBO homopolymer (reaction medium). The peak at an elution volume around 28.5 mL referred to the star PBO with a molar mass of  $10 \text{ kg mol}^{-1}$  determined using the PMMA standard (Table 1). No specific peak could be attributed to the presence of free cyclodextrin, however a tiny bump around 32.0 mL could hardly be detected and referred to the byproduct resulting from a side reaction issued from an initiation by residual water entrapped in the  $\beta$ CD cavity [21,22], denoted as “HO-PBO-OH”.

Trace *b* was the PBO-PEEGE copolymer resulting from the addition of PEEGE blocks onto the first PBO blocks. The peak at the elution volume of 27.4 mL was assigned to the star-shaped copolymer, an elution volume lower than the one of the PBO star polymer as expected. The bump around 30.9 mL was attributed to the byproducts. The byproducts might consist of linear PBO-PEEGE deriving from linear HO-PBO-OH. Transfer-to-monomer and back-biting reactions in the ring-opening polymerization of EEEGE have been reported [27,28], however the double bond signal at  $\delta$  5.92 ppm (Figure 2B) witnessed for the very low occurrence of such reactions.

Trace *c* profiled the crude deprotected product PBO-PGL copolymers, which was obtained by removing the acetal groups of the PBO-PEEGE intermediate (both the star-shaped copolymer and byproducts) in acidic conditions. Compared with the peaks in trace *b*, the two peaks in trace *c* both shifted to larger elution-volume side, 27.5 mL and 31.6 mL respectively for the star PBO-PGL and the byproducts, in accordance with the loss of protecting groups. Trace *d* portrayed the final PBO-PGL copolymer obtained after purification. It clearly showed the only presence of the star PBO-PGL around 27.5 mL, no shift of elution volume from that one of trace *c*.

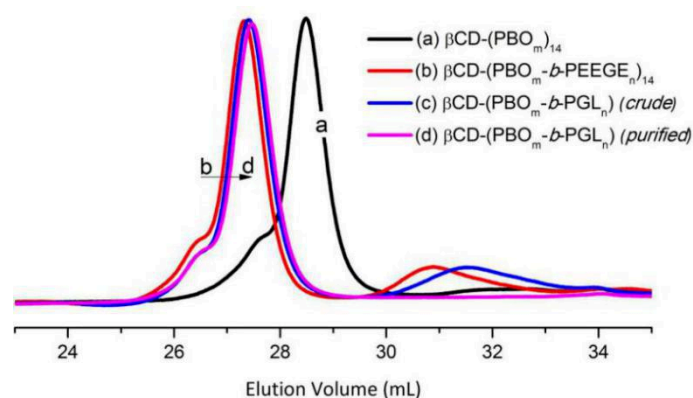


**Figure 3.** SEC traces of the intermediates and the deprotected products (before and after purification) in the synthetic process of the star copolymer  $\beta$ CD-(PBO<sub>7</sub>-PGL<sub>5</sub>)<sub>14</sub> (Entry HQ137): (a) PBO homopolymer (reaction medium), (b) PBO-PEEGE copolymer (without tBuP4), (c) crude deprotected PBO-PGL product, and (d) purified PBO-PGL product, performed in DMF at 60 °C and detected with an RI detector.

The SEC peak areas (using an RI detector) were used to estimate the purity, namely the fraction of the star-shaped polymer in each intermediate and product by following equation:

$$f = \frac{A_s}{A_s + A_b} \quad (8)$$

in which,  $A_s$  and  $A_b$  are the peak areas of the star-shaped polymer and byproduct(s), respectively, reported by the OmniSEC 5.12 software.

Based on product purity, monomer feeding ratio and monomer conversions, the theoretical formula of star polymers, including star PBO ( $\beta\text{CD}-(\text{PBO}_m)_{14}$ ), star PBO-PEEGE ( $\beta\text{CD}-(\text{PBO}_m\text{-PEEGE}_n)_{14}$ ), and star PBO-PGL ( $\beta\text{CD}-(\text{PBO}_m\text{-PGL}_n)_{14}$ ) were estimated (Table 1). (The computation details can be found in the Appendix.)

**Table 1.** Characteristics of the Star-shaped Intermediates and Product for the Synthesis of Star Copolymer  $\beta\text{CD}-(\text{PBO}_7\text{-PGL}_5)_{14}$  (Entry HQ137).

Polymer	$p_{\text{BO}}^a$	$p_{\text{EEGE}}^a$	$f^b$	$m_{\text{theo.}}^c$	$n_{\text{theo.}}^c$	$Mn_{\text{theo.}}^c$ (kg mol <sup>-1</sup> )	$Mn_{\text{SEC}}^d$ (kg mol <sup>-1</sup> )	$\mathcal{D}^d$
$\beta\text{CD}-(\text{PBO}_m)_{14}$	0.94	--	0.93	7.0	--	9.0	10.3	1.09
$\beta\text{CD}-(\text{PBO}_m\text{-PEEGE}_n)_{14}$	0.94	0.98	0.84	7.0	4.7	18.7	17.7	1.05
$\beta\text{CD}-(\text{PBO}_m\text{-PGL}_n)_{14}$ (crude)	--	--	0.84	7.0	4.7	13.9	16.7	1.05
$\beta\text{CD}-(\text{PBO}_m\text{-PGL}_n)_{14}$ (purified)	--	--	0.99	7.0	4.7	13.9	16.3	1.07

<sup>a</sup>Monomer conversions of BO ( $p_{\text{BO}}$ ) and EEGE ( $p_{\text{EEGE}}$ ) were calculated from the <sup>1</sup>H NMR spectra (illustrated in Figure 2A and B); <sup>b</sup>The fraction of the star-shaped polymer in each intermediate and product ( $f$ ) was estimated from the RI peak areas in SEC traces using Equation 8; <sup>c</sup>Theoretical DP values of PBO and PEEGE/PGL blocks per arm ( $m_{\text{theo.}}$  and  $n_{\text{theo.}}$ , respectively) were estimated based on monomer feeding ratio ( $[\text{BO}]_0/[\text{EEGE}]_0/[\beta\text{CD}]_0$ ), monomer conversions ( $p$ ) and the fraction of star-shaped polymer ( $f$ ). Theoretical molar masses ( $Mn_{\text{theo.}}$ ) were derived from the theoretical DP values. <sup>d</sup>SEC measurements were performed in DMF at 60 °C and the results were determined with PMMA as the standard using an RI detector.

The theoretical molar masses ( $Mn_{\text{theo.}}$ ), especially of the hydrophobic polymers (star PBO and star PBO-PEEGE), were consistent with the values determined by SEC (Table 1). All the star-shaped polymers were narrowly distributed considering the low polydispersity indexes ( $\mathcal{D}$ ). The final product was  $\beta\text{CD}-(\text{PBO}_7\text{-PGL}_5)_{14}$  with a purity of 99%, indicating the synthesis procedure was effective to get the narrowly

distributed star PBO-PGL of a high purity. Applying the same procedure (Scheme 2), two other star copolymers were synthesized. Table 2 gathered the theoretical and characterization results of the three star copolymers  $\beta$ CD-(PBO<sub>m</sub>-PGL<sub>n</sub>)<sub>14</sub> ( $m \leq 10$ ).

**Table 2.** Reaction Conditions and Characteristics the Star Copolymers having Short PBO blocks,  $\beta$ CD-(PBO<sub>m</sub>-PGL<sub>n</sub>)<sub>14</sub> ( $m \leq 10$ ), According to Weight Fraction of PGL Blocks ( $w_{\text{PGL}}$ ).

Entry	[BO] <sub>0</sub> /[EEGE] <sub>0</sub> / [ $\beta$ CD] <sub>0</sub>	$p_{\text{BO}}^a$	$p_{\text{EEGE}}^a$	$f^b$	Formula <sup>c</sup>	$w_{\text{PGL}}^c$	$M_{\text{n,theo.}}^c$ (kg mol <sup>-1</sup> )	$M_{\text{n,SEC}}^d$ (kg mol <sup>-1</sup> )	$\mathcal{D}^d$
HQ137	112/78/1	0.94	0.98	0.99	$\beta$ CD-(PBO <sub>7</sub> - PGL <sub>5</sub> ) <sub>14</sub>	0.35	13.9	16.3	1.07
HQ093	158/206/1	1	1	0.97	$\beta$ CD-(PBO <sub>8</sub> - PGL <sub>12</sub> ) <sub>14</sub>	0.57	22.2	28.1	1.05
HQ105	91/211/1	0.98	1	0.94	$\beta$ CD-(PBO <sub>6</sub> - PGL <sub>14</sub> ) <sub>14</sub>	0.62	22.2	25.6	1.07

<sup>a</sup>Monomer conversions of BO ( $p_{\text{BO}}$ ) and EEGE ( $p_{\text{EEGE}}$ ) were calculated on the basis of the <sup>1</sup>H NMR spectra; <sup>b</sup>The fraction of the star-shaped copolymer in the product ( $f$ ) was estimated from the RI peak areas in SEC traces using Equation 8; <sup>c</sup>Theoretical formula of star copolymer was calculated based on monomer feeding ratio ( $[\text{BO}]_0/[\text{EEGE}]_0/[\beta\text{CD}]_0$ ), monomer conversions ( $p$ ) and the fraction of star-shaped polymer ( $f$ ). Theoretical mass fraction of PGL blocks ( $w_{\text{PGL}}$ ) was calculated as  $w_{\text{PGL}} = 14 \times n \times M_{\text{rGL}} / (14 \times m \times M_{\text{rBO}} + 14 \times n \times M_{\text{rGL}} + M_{\text{rI}})$  where  $M_{\text{rGL}}$ ,  $M_{\text{rBO}}$  and  $M_{\text{rI}}$  are respectively the molar masses of GL (74 g mol<sup>-1</sup>), BO (72 g mol<sup>-1</sup>), and initiator (2044 g mol<sup>-1</sup>). Theoretical molar mass ( $M_{\text{n,theo.}}$ ) was derived from the theoretical formula; <sup>d</sup>SEC measurements were performed in DMF at 60 °C and the results were determined with PMMA as the standard using an RI detector.

As shown in Table 2, all the star copolymers were narrowly distributed ( $\mathcal{D} \sim 1.07$ ) with high purity ( $f \geq 0.94$ ). The theoretical molar masses ( $M_{\text{n,theo.}}$ ) and the values determined by SEC ( $M_{\text{n,SEC}}$ ) were close. The results altogether indicated that the procedure (Scheme 2) was reproducible for the syntheses of star copolymers having short PBO blocks,  $\beta$ CD-(PBO<sub>m</sub>-PGL<sub>n</sub>)<sub>14</sub> ( $m \leq 10$ ).

### 3.3 Syntheses of the star copolymers $\beta$ CD-(PBO<sub>m</sub>-PGL<sub>n</sub>)<sub>14</sub> with $m > 10$

#### 3.3.1 Syntheses of $\beta$ CD-(PBO<sub>m</sub>)<sub>14</sub> with $m > 10$

##### (1) The limitation of homopolymerization

As shown above, the synthetic procedure depicted in Scheme 2 was effective to prepare  $\beta$ CD-(PBO<sub>m</sub>-PGL<sub>n</sub>)<sub>14</sub> with  $m = 6, 7$  and  $8$ , in accordance with the published results [14]. Following the same procedure, the star copolymers having relatively long PBO blocks were attempted to be synthesized by increasing the feeding ratio of

BO to the initiator. However, it failed to get the targeted lengths of PBO blocks in the homopolymerization step. In order to figure out this issue, a kinetic study on the homopolymerization of BO was conducted.

The homopolymerization reaction targeting  $\beta$ CD-(PBO<sub>43</sub>)<sub>14</sub> (Entry HQ109-1) was conducted at 30 °C with a feeding ratio of  $[\text{BO}]_0/[\text{tBuP4}]_0/[\beta\text{CD}]_0 = 604/2.8/1$  and an initial monomer concentration of  $[\text{BO}]_0 = 3 \text{ M}$  in DMF. During the reaction, the reaction medium was sampled, and BO conversion ( $p$ ) was measured by <sup>1</sup>H NMR. Figure 4A depicted the stacked <sup>1</sup>H NMR spectra, and from trace *a* to trace *g*, reaction time increased from 6 h to 144 h. It clearly showed that, after 6 h, the polyether backbone formed as proved by the presence of the peaks ranging from 4.0 ppm to 3.2 ppm (trace *a*), and these peaks increased with the increase of reaction time. At the meantime the peaks attributed to the unreacted monomer (protons *a'*, *b'*, *c'* and *d'*) decreased with the reaction time. Based on the integrals of epoxide proton *a'* and methyl protons *d'* and *d*, BO conversion was determined. The values were labeled besides respective reaction times, indicating BO conversion increased along with reaction time.

In order to figure out the reaction kinetics, monomer conversions ( $p$ ) and reaction times ( $t$ ) were then fitted into a pseudo first-order kinetics plot in monomer *i.e.*  $\ln(1/(1-p))$  against  $t$  as shown in Figure 4B. The fitting result showed that the  $\ln(1/(1-p))$  vs  $t$  plot had a good linearity ( $R^2 = 0.9653$ ) up to 24.5 h, and the linear fitting was lost from 48 h.

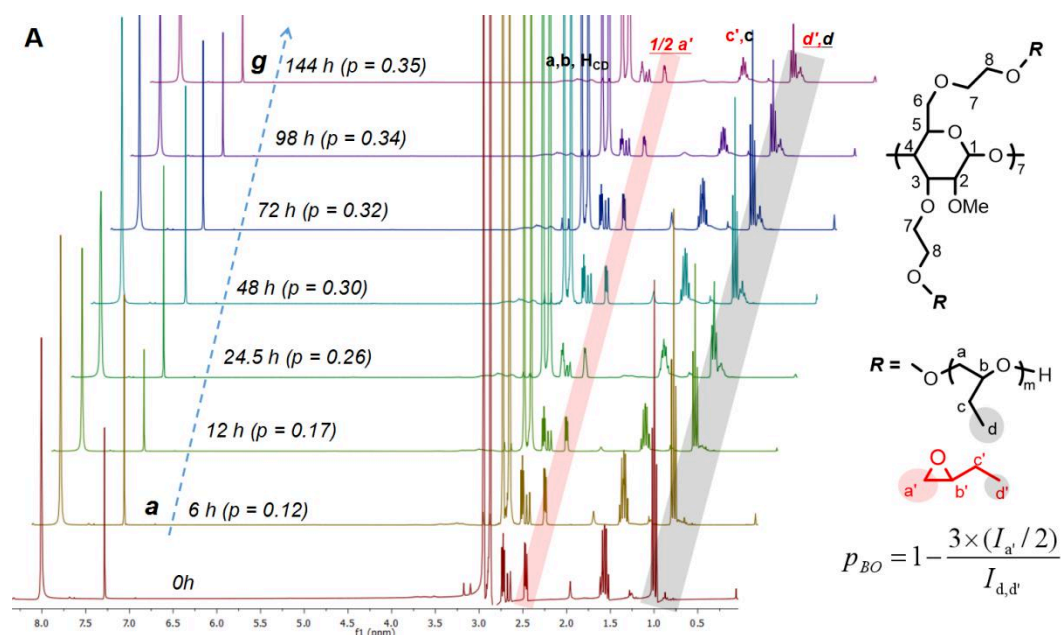


**Figure 4.** (A) Stacked <sup>1</sup>H NMR spectra of the homopolymerization medium sampled at different reaction times. All were recorded in CDCl<sub>3</sub>-d<sub>1</sub>, at 300 K. Reaction conditions were  $[\text{BO}]_0/[\text{tBuP4}]_0/[\beta\text{CD}]_0 = 604/2.8/1$ , and  $[\text{BO}]_0 = 3 \text{ M}$  in DMF at 30 °C (Entry HQ109-1).

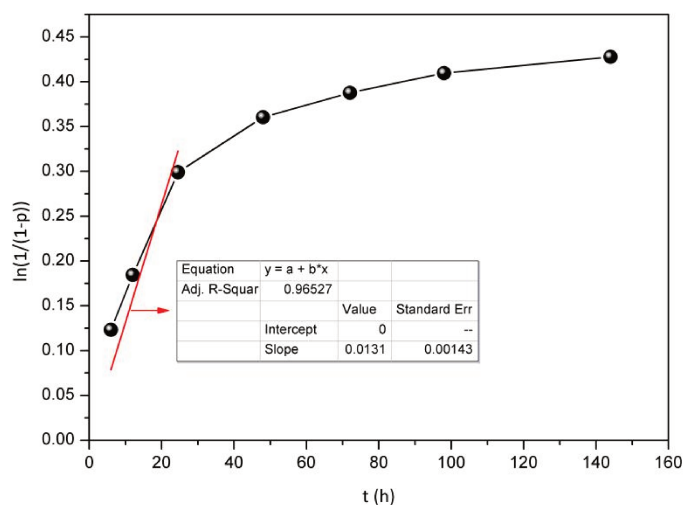


**Figure 4 (continued).** (B) The corresponding plot of  $\ln(1/(1-p))$  against  $t$ . Reaction conditions were  $[\text{BO}]_0/[\text{tBuP4}]_0/[\beta\text{CD}]_0 = 604/2.8/1$ , and  $[\text{BO}]_0 = 3 \text{ M}$  in DMF at  $30 \text{ }^\circ\text{C}$  (Entry HQ109-1).

In parallel, the samples collected at different reaction times were characterized by SEC (Figure 5).

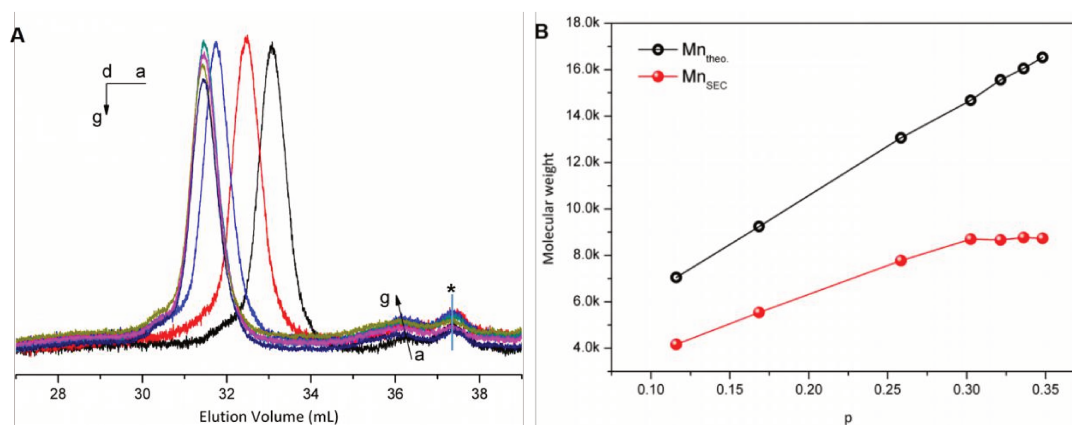


**Figure 5.** (A) Overlaid SEC traces of the homopolymerization intermediates obtained at different reaction times ( $t$ ). From  $a$  to  $g$ ,  $t = 6, 12, 24.5, 48, 72, 98$  and  $144 \text{ h}$ . \*Peak means tBuP4. (B) The corresponding plots of  $Mn_{\text{theo}}$  and  $Mn_{\text{SEC}}$  against  $p$ .  $Mn_{\text{theo}} = Mr_{\text{BO}} \times M_0 \times p \times f + Mr_1$ , with  $M_0$  being feeding ratio of BO to initiator,  $f$  being the fraction of star PBO, and  $Mr_{\text{BO}}$  and  $Mr_1$  being respectively the molar masses of BO and initiator.  $Mn_{\text{SEC}}$  is the number-average molar mass determined by SEC (performed in DMF, at  $60 \text{ }^\circ\text{C}$ ) with PMMA as the standard using an RI detector. Reaction conditions were  $[\text{BO}]_0/[\text{tBuP4}]_0/[\beta\text{CD}]_0 = 604/2.8/1$ , and  $[\text{BO}]_0 = 3 \text{ M}$  in DMF at  $30 \text{ }^\circ\text{C}$  (Entry HQ109-1).

Figure 5A gathered the stacked SEC traces. From trace *a* to trace *g*, reaction time increased from 6 h to 144 h. Trace *a* was the first sample obtained at *t* = 6 h, and two populations were observed, the most abundant one (elution volume centered at 33.1 mL) referred to star PBO while the tiny one (around 36.3 mL) referred to the byproduct resulting from the side reaction initiated by the residual water in the βCD core of initiator as aforementioned. From *a* to *g*, reaction time increased, and accordingly both peaks shifted towards smaller elution volumes until *t* = 48 h (trace *d*), indicating the increase in molar mass. The molar masses of the star PBOs determined with PMMA as the standard ( $M_{nSEC}$ ) were plotted against the monomer conversions (*p*) as shown in Figure 5B. The  $M_{nSEC}$  vs *p* plot had a good linearity up to 48 h. Afterwards,  $M_{nSEC}$  remained constant even though *p* increased slightly. In parallel, the theoretical molar masses ( $M_{ntheo.}$ ) calculated from monomer conversion and product purity were displayed in Figure 5B for comparison. The divergence of  $M_{nSEC}$  from  $M_{ntheo.}$  might result from the differences in polymer architecture and chemical nature between the molar mass calibration standards (linear PMMA) and the analytes herein (βCD-cored star polymers). The Y-intercept of the fit was different from 0 as expected since the initial molar mass of the initiator is high ( $M_{T1} = 2044 \text{ g mol}^{-1}$ ), and this affects the overall initial molar mass.

Based on the <sup>1</sup>H NMR and SEC characterization results, it was found that a star PBO with a theoretical formula of βCD-(PBO<sub>12</sub>)<sub>14</sub> was obtained at the end. In other words, the theoretical DP of PBO arms is 12, which is much smaller than the targeted value (*m* = 43). The limitations of BO conversion and the corresponding DP of PBO block were observed in other homopolymerizations performed in DMF in various reaction conditions (*i.e.*, temperature and the feeding ratio of tBuP4), as displayed in Table 3.

**Table 3.** Characteristics of the Star PBOs (βCD-(PBO<sub>m</sub>)<sub>14</sub>) Synthesized in DMF at Different Temperatures or with Different Feeding Ratios of tBuP4.

Entry	[BO] <sub>0</sub> /[tBuP4] <sub>0</sub> /[βCD] <sub>0</sub> <sup>a</sup>	T (°C)	<i>p</i> <sub>1</sub> <sup>b</sup>	<i>f</i> <sub>1</sub> <sup>c</sup>	<i>m</i> <sub>theo.</sub> <sup>d</sup>	$M_{ntheo.}$ <sup>d</sup> (kg mol <sup>-1</sup> )	$M_{nSEC}$ <sup>e</sup> (kg mol <sup>-1</sup> )	$\bar{D}$ <sup>e</sup>
HQ107-1	339/2.8/1	25	0.76	0.99	18.2	20.4	15.6	1.03
HQ108-1	588/2.8/1	25	0.38	0.97	15.5	17.6	12.4	1.03
HQ109-1	604/2.8/1	30	0.30	0.96	12.4	16.4	8.8	1.04
HQ133-1	613/2.8/1	30	0.49	0.85	18.2	20.4	17.7	1.04
HQ129-1	589/7.0/1	30	0.44	0.79	14.6	16.8	5.8 <sup>e'</sup>	1.05 <sup>e'</sup>

<sup>a</sup>Various feeding ratios with constant initial monomer concentration as [BO]<sub>0</sub> = 3 M in DMF; <sup>b</sup>BO conversion (*p*<sub>1</sub>) was determined by <sup>1</sup>H NMR; <sup>c</sup>The fraction of the star PBO (*f*<sub>1</sub>) in product was estimated using Equation 8; <sup>d</sup>Theoretical value of *m* ( $m_{theo.}$ ) was calculated based on monomer feeding ratio (*M*<sub>1</sub>), monomer conversion (*p*<sub>1</sub>) and product purity (*f*<sub>1</sub>). Theoretical molar mass ( $M_{ntheo.}$ ) was determined based on  $m_{theo.}$ ; <sup>e,e'</sup>SEC characterizations were performed <sup>e</sup>in DMF at 60 °C or <sup>e'</sup>in THF at 40 °C. The characterization results were determined with PMMA as the standard using an RI detector.

The results showed that either a small increase of reaction temperature (from 25 °C to 30 °C) or an increase of the equivalent of tBuP4 (the catalyst, from 2.8 eq to 7.0 eq) did not allow to increase the value of  $m$  which limited to  $15.8 \pm 2.5$  (“average  $\pm$  StDev” of  $m_{\text{theo.}}$  of the 5 entries listed in Table 3). The increase of tBuP4 seemed to induce more side reactions verified by lower purity of the polymer (Entry HQ129-1, Table 3).

## (2) Extending PBO arms by increasing reaction temperature

In order to extend PBO arms, for the Entries HQ107-1 and HQ108-1, when BO conversion reached the plateau (Table 3), reaction temperature was increased from 25 °C to 50 °C (without other changes) and the reaction was performed for another 69 hours. At the end, the monomer conversions and the molar masses were determined, as listed in Table 4.

**Table 4.** Extending PBO Arms of Star PBOs by Increasing Reaction Temperature.

Entry	Reaction medium <sup>a</sup>	T (°C)	$p_2^b$	$f_2^c$	$m_{\text{theo.}}^d$	$Mn_{\text{theo.}}^d$ (kg mol <sup>-1</sup> )	$Mn_{\text{SEC}}^e$ (kg mol <sup>-1</sup> )	$\bar{D}^e$
HQ107-2	HQ107-1	50	0.99	0.91	21.8	24.0	18.5	1.02
HQ108-2	HQ108-1	50	0.49	0.92	18.9	21.1	12.4	1.04

<sup>a</sup>The reaction media were those in Table 3; <sup>b</sup>BO conversion ( $p_2$ ) was determined by <sup>1</sup>H NMR; <sup>c</sup>The fraction of star PBO in product ( $f_2$ ) was estimated as the peak area ratio in SEC trace using Equation 8; <sup>d</sup>Theoretical value of  $m$  ( $m_{\text{theo.}}$ ) was calculated based on BO feeding ratio ( $M_1$ ), BO conversion ( $p_2$ ) and product purity ( $f_2$ ) using the formulation of  $m_{\text{theo.}} = M_1 \times p_2 \times f_2/14$ . Theoretical molar mass ( $Mn_{\text{theo.}}$ ) was determined as  $Mn_{\text{theo.}} = Mr_{\text{BO}} \times 14 \times m_{\text{theo.}} + Mr_{\text{I}}$ , with  $Mr_{\text{BO}}$  and  $Mr_{\text{I}}$  being respectively the molar masses of BO and initiator; <sup>e</sup>SEC characterizations were performed in DMF at 60 °C and the characterization results were determined with PMMA as the standard using an RI detector.

Comparing the results of Entry HQ107-2 (Table 4) with those of HQ107-1 (Table 3), it can be seen that BO conversion increased from 0.76 to 0.99 by merely increasing reaction temperature, together with  $m_{\text{theo.}}$  increased from 18 to 21.  $Mn_{\text{SEC}}$  increased from 15.6 to 18.5 kg mol<sup>-1</sup> shown as the shift to lower elution volume side of the SEC trace (Figure 6A). Similarly, from Entry HQ108-1 (Table 3) to HQ108-2 (Table 4), BO conversion increased slightly from 0.38 to 0.49, with  $m_{\text{theo.}}$  increased from 16 to 19. However,  $Mn_{\text{SEC}}$  increased little, indicated by the little decreased elution volume of the SEC trace (Figure 6B). Thus, in the case of Entry HQ108-2, it was assumed that at higher temperature, the increased monomer conversion was attributed more to the evaporation of monomer than polymerization. Moreover, the increased

temperature promoted the side reactions at the same time (Figure 6), giving lower product purity ( $f_2$  values, Table 4).

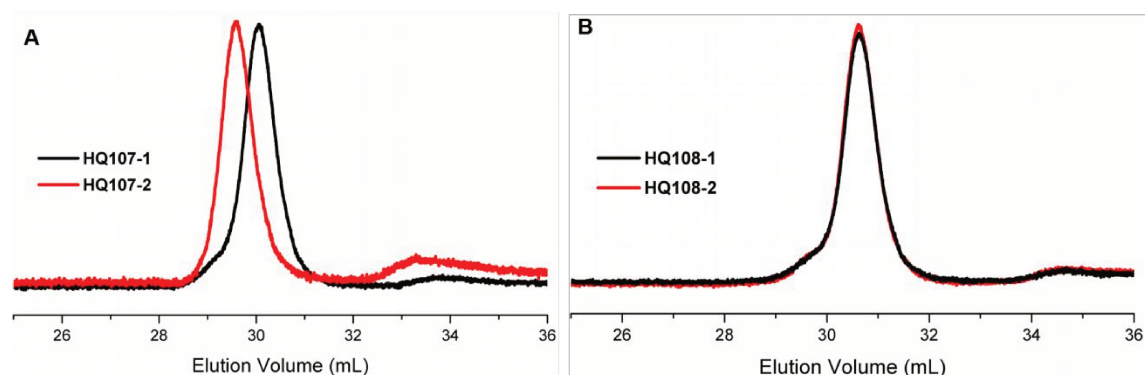
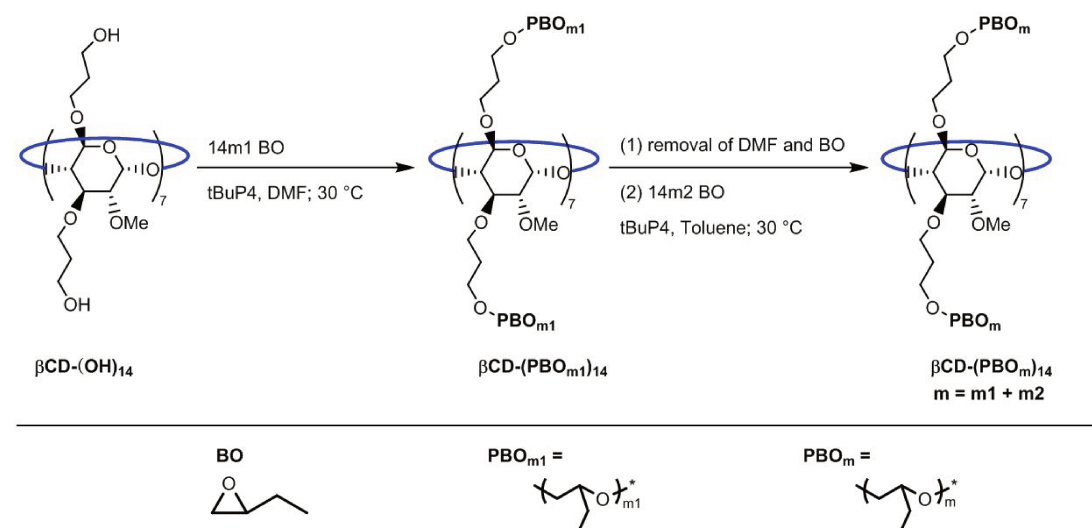


**Figure 6.** SEC traces of the star PBOs listed in Table 4, before (black) and after (red) the second reaction performed at a higher reaction temperature, according to legends. Reaction conditions were described in Table 4. SEC characterizations were performed in DMF at 60 °C with an RI detector.

### (3) Extending PBO arms by changing the solvent

As already discussed, increasing temperature was not a better way to extend the PBO arms, thus an adapted procedure was developed as shown in Scheme 4. The procedure includes two homopolymerization steps: the first step is to form the short living PBO arms grafted on the  $\beta$ CD core conducted in DMF, and the second step is to extend the PBO arms performed in toluene. Before the second homopolymerization, DMF and unreacted BO monomer in the first homopolymerization medium are removed via distillation on vacuum line.

**Scheme 4.** Extending PBO Arms of Star PBO by Changing the Solvent.



Following this procedure, the product of Entry HQ109-1 (Table 3) was used as the macroinitiator in the second homopolymerization step, where toluene and a second batch of BO and tBuP4 were added with the molar ratio of  $[\text{BO}]_2/[\text{tBuP4}]_2/[\beta\text{CD}]_0 = 910/11.2/1$  and  $[\text{BO}]_2 = 3 \text{ M}$  (Table 5). At the end of the second homopolymerization, BO was entirely consumed ( $p_2 = 1$ ) as checked by  $^1\text{H NMR}$  with no residual peaks attributed to the free BO monomer. The product was characterized by SEC (Figure 7A), showing that from Entry HQ109-1 to Entry HQ109-2, the peak of star PBO shifted to lower elution volume side, *i.e.* from 24.0 mL to 22.7 mL, and the peak of byproduct also shifted to the lower elution volume from 27.4 mL to 25.4 mL, witnessing the increase of molar masses. However, the fraction of the star-shaped product decreased a lot from  $f = 0.96$  (Entry HQ109-1, Table 3) to  $f = 0.51$  (Entry HQ109-2, Table 5). Similar phenomena were observed in another reaction (Entry HQ129-2, Table 5 and Figures 7B). In order to suppress the side reactions, in the third reaction (Entry HQ133-2, Table 5), TiBA was added after the charge of the second batch of BO and tBuP4, since TiBA was reported to suppress the side reactions in tBuP4-catalyzed polymerizations [29]. But herein, as soon as TiBA was dropped into the reaction medium, the reaction solution started gelling and finally a homogeneous gel was obtained, resulting in the big bump in the SEC trace (Figure 7C), as well as the slight increase in the molar mass of the star PBO (Table 5).

**Table 5.** Extending PBO Arms of Star PBOs by a Second Homopolymerization in Toluene.

Entry	Reaction medium <sup>a</sup>	$[\text{BO}]_2/[\text{tBuP4}]_2/[\text{TiBA}]/[\beta\text{CD}]_0$	T (°C)	$p_2^b$	$f_2^c$	$m_{\text{theo.}}^d$	$M_{\text{ntheo.}}^d$ (kg mol <sup>-1</sup> )	$M_{\text{nSEC}}^e$ (kg mol <sup>-1</sup> )	$\mathcal{D}^e$
HQ109-2	HQ109-1	910/11.2/0/1	30	1	0.51	40.4	42.8	25.9 <sup>e'</sup>	1.08 <sup>e'</sup>
HQ129-2	HQ129-1	589/11.2/0/1	30	1	0.33	18.7	22.5	29.2 <sup>e'</sup>	1.04 <sup>e'</sup>
HQ133-2	HQ133-1	364/11.2/40.3/1	30	1	0.14	--	--	18.7	1.03

<sup>a</sup>The reaction media were those listed in Table 3; <sup>b</sup>BO conversion in the second homopolymerization step ( $p_2$ ) was determined by  $^1\text{H NMR}$ ; <sup>c</sup>The fraction of star PBO in the product ( $f_2$ ) was estimated as the peak ratio in SEC trace using Equation 8; <sup>d</sup>Theoretical value of  $m$  ( $m_{\text{theo.}}$ ) was calculated based on BO feeding ratios ( $M_1$  and  $M_2$ , respectively in the 1<sup>st</sup> and 2<sup>nd</sup> polymerization steps), BO conversions ( $p_1$  and  $p_2$ ) and the final product purity ( $f_2$ ), using the equation of  $m_{\text{theo.}} = (M_1 \times p_1 + M_2) \times p_2 \times f_2/14$ . Theoretical molar mass ( $M_{\text{ntheo.}}$ ) was determined based on  $m_{\text{theo.}}$  as  $M_{\text{ntheo.}} = M_{\text{rBO}} \times 14 \times m_{\text{theo.}} + M_{\text{rI}}$ , with  $M_{\text{rBO}}$  and  $M_{\text{rI}}$  being respectively the molar masses of BO and initiator; <sup>e,e'</sup>SEC characterizations were performed <sup>e</sup>in DMF at 60 °C or <sup>e'</sup>in THF at 40 °C. Characterization results were determined with PMMA as the standard and using an RI detector.

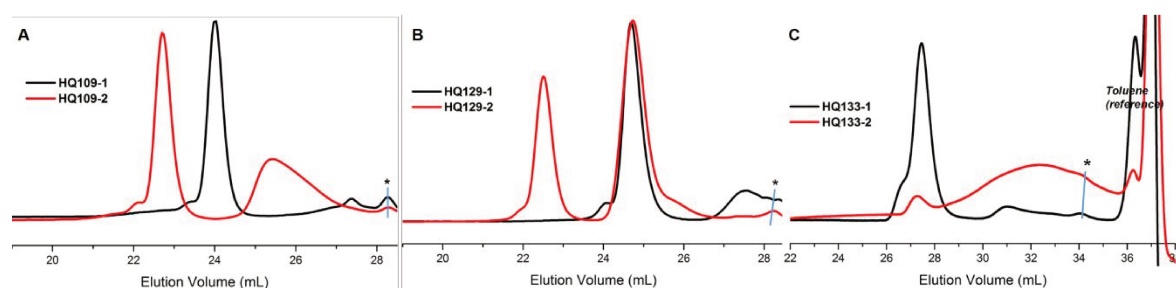


**Figure 7.** SEC traces of the PBOs listed in Table 5, before (black) and after (red) the second homopolymerization conducted in toluene, according to the legends. Reaction conditions were listed in Table 5. \*Peak means tBuP4. SEC characterizations of A and B were performed in DMF at 60 °C, and C was in THF at 40 °C, all used an RI detector.

*In summary*, regarding the synthesis of star PBO, three points could be concluded:

- (1) the homopolymerization performed in DMF at a mild temperature (25 °C or 30 °C) produced  $\beta$ CD-(PBO<sub>m</sub>)<sub>14</sub> with the value of *m* limiting at  $16 \pm 3$  (“average  $\pm$  StDev” of *m*<sub>theo.</sub> of the 5 entries listed in Table 3);
- (2) increasing temperature from 25 °C to 50 °C worked slightly to extend the PBO arms (Table 4);
- (3) via replacing DMF with toluene and performing a second homopolymerization, PBO arms were successfully extended (Table 5). The solubility of the growing star in DMF might be reduced at high BO unit number in the arms, hampering the formation of large-molar-massed star polymers. The collapsed star PBO of large molar mass in DMF impedes the exposure of active centers to the monomers. For reminder, DMF is necessary in the first step to dissolve the initiator [22], although it would be replaced by toluene to get longer PBO arms.

Taking into account all the results, the stepwise homopolymerization procedure is a better way to prepare the star PBO with long PBO arms.

### 3.3.2 Syntheses of $\beta$ CD-(PBO<sub>m</sub>-PGL<sub>n</sub>)<sub>14</sub> with *m* > 10

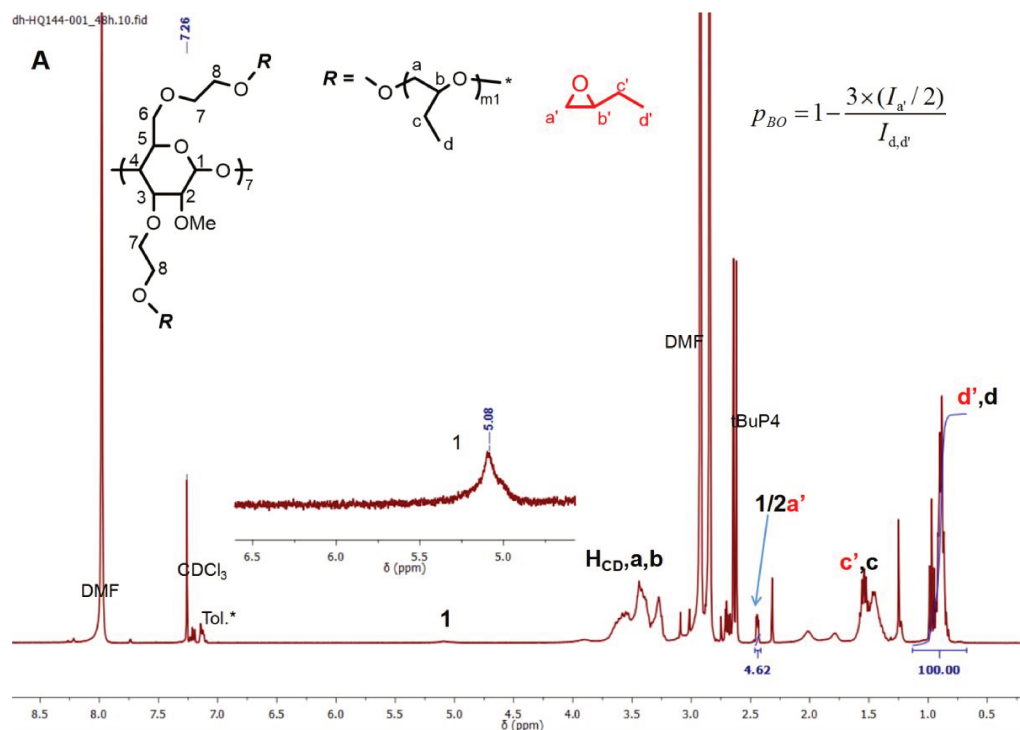
Based on the seminal results of the synthesis of  $\beta$ CD-(PBO<sub>m</sub>)<sub>14</sub> of large molar mass, the star copolymer with relatively long PBO blocks,  $\beta$ CD-(PBO<sub>m</sub>-PGL<sub>n</sub>)<sub>14</sub> (*m* > 10), was prepared via an adapted copolymerization procedure which is featured by the stepwise homopolymerization (Scheme 3).

As an example, the synthesis of star copolymer  $\beta$ CD-(PBO<sub>24</sub>-PGL<sub>6</sub>)<sub>14</sub> (Entry HQ144) was performed by a first homopolymerization of BO in DMF with the feeding ratio of  $[\text{BO}]_1/[\text{tBuP4}]_1/[\beta\text{CD}]_0 = 113/2.8/1$ . After 48 hours, BO conversion was calculated

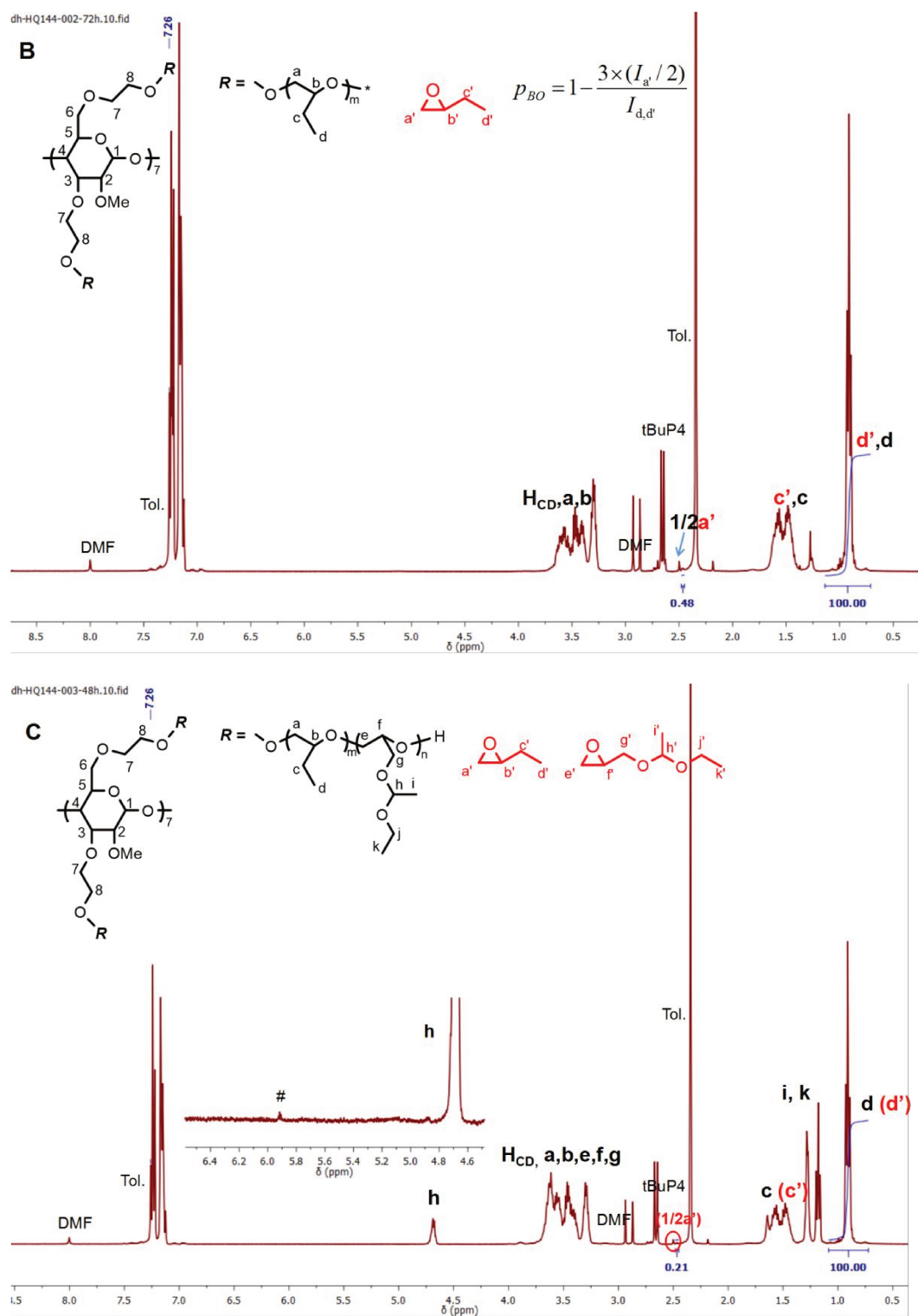
from the  $^1\text{H}$  NMR spectrum, as  $p_{\text{BO}1} = 0.86$ , based on the integrals of the epoxide proton a' and the methyl protons d' and d (Figure 8A). In this spectrum the anomeric proton of the glucopyranose unit (proton 1,  $\delta$  5.1 ppm) was hardly detected and could not be accurately integrated.

Then, the second homopolymerization step was performed with the molar ratio of  $[\text{BO}]_2/[\text{tBuP4}]_2/[\beta\text{CD}]_0 = 334/1.4/1$  and for 72 hours. At the end, nearly all BO monomer was consumed ( $p_{\text{BO}2} = 0.99$ ) as verified by the  $^1\text{H}$  NMR spectrum (Figure 8B). It can be seen that the anomeric proton (proton 1) was undetectable at all due to the large amounts of protons in the polymer, corresponding to a large degree of polymerization of BO.

Subsequently, the sequential copolymerization was conducted with the ratio of  $[\text{EEGE}]_0/[\beta\text{CD}]_0 = 139/1$  and for 48 hours. At the end EEGE was consumed ( $p_{\text{EEGE}} = 1$ ) as confirmed by the  $^1\text{H}$  NMR spectrum (Figure 8C), which only showed the peaks attributed to the protons of EEGE repeating units (protons h, i and k), without any peaks belonging to the free EEGE monomer. After quenching and the removal of tBuP4, the PBO-PEEGE intermediate was obtained (Figure 8D). At last, the acetal groups of EEGE units were cleaved giving the crude deprotected product (Figure 8E), evidenced by the disappearance of the characteristic peaks of EEGE units.



**Figure 8.** (A)  $^1\text{H}$  NMR spectra of the first PBO homopolymerization medium obtained in the synthetic procedure for  $\beta\text{CD}-(\text{PBO}_{24}\text{-PGL}_6)_{14}$  (Entry HQ144).  $\text{H}_{\text{CD}}$  stands for the protons in the  $\beta\text{CD}$ -based initiator (*i.e.*, protons 2, 3, 4, 5, 6 and 7). \*Residual Toluene in the initiator originating from the drying pre-treatments., recorded in  $\text{CDCl}_3\text{-d}_1$  at 300 K.



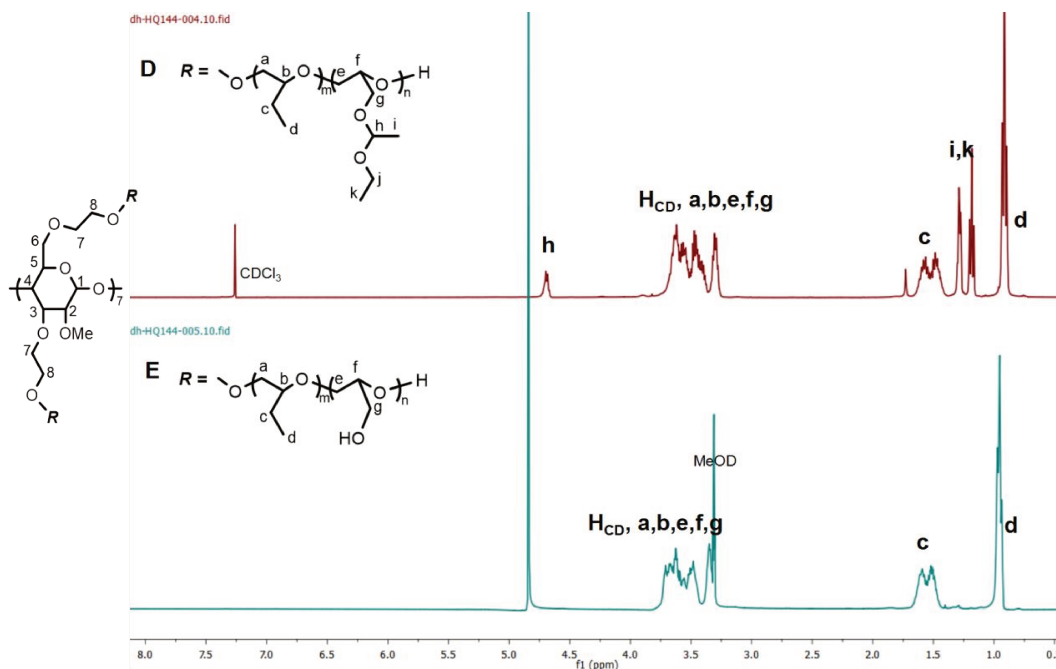


**Figure 8 (continued).**  $^1\text{H}$  NMR spectra of the intermediates and crude deprotected product obtained in the synthetic procedure for the star copolymer  $\beta\text{CD}-(\text{PBO}_{24}\text{-PGL}_6)_{14}$  (Entry HQ144): (D) PBO-PEEGE intermediate (without tBuP4) and (E) crude PBO-PGL product.  $\text{H}_{\text{CD}}$  stands for the protons in the  $\beta\text{CD}$ -based initiator, including protons 2, 3, 4, 5, 6 and 7. Spectra D was recorded in  $\text{CDCl}_3\text{-d}_1$  and E in  $\text{MeOD-d}_4$ , both at 300 K.

The intermediates, the crude deprotected product as well as the final purified product were also characterized by SEC, as displayed in Figure 9.

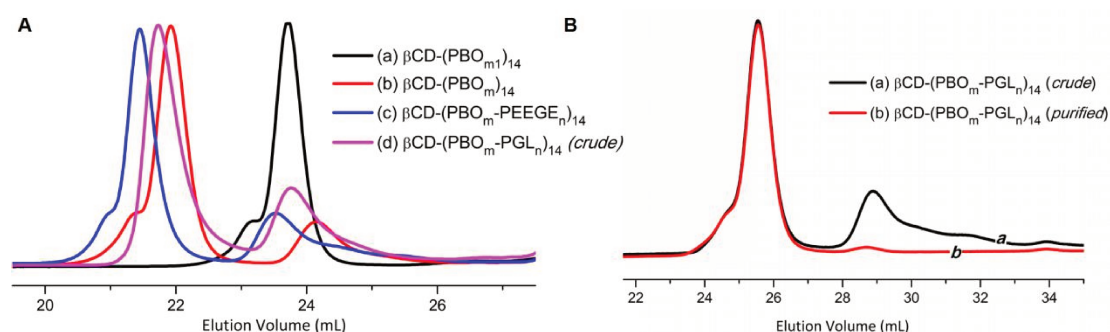


**Figure 9.** SEC traces of the intermediates and the deprotected product in the synthetic process of  $\beta\text{CD}-(\text{PBO}_{24}\text{-PGL}_6)_{14}$  (Entry HQ144): (A) SEC traces of (a) the first PBO homopolymer (reaction medium), (b) the second PBO homopolymer (reaction medium), (c) PBO-PEEGE copolymer (without tBuP4), and (d) crude PBO-PGL product. Characterizations were performed in THF at 40 °C using an RI detector. (B) SEC traces of (a) crude PBO-PGL product and (b) purified PBO-PGL product. Characterizations were performed in DMF at 60 °C using an RI detector.

In Figure 9A, trace *a* profiled the intermediate obtained at the end of the first homopolymerization step of BO. The narrowly distributed peak (centered at 23.7 mL) was star PBO, while a negligible peak around 27.6 mL was attributed to the byproduct initiated by the residual water entrapped in the  $\beta$ CD core. Trace *b* profiled the intermediate obtained at the end the second homopolymerization step of BO. The peak centered around 21.9 mL referred to star PBO, while a small peak around 24.1 mL was attributed to byproduct. Both peaks shifted towards the lower elution volume part, witnessing molar mass increases. Trace *c* showed a further shifted to 21.5 mL of the peak attributed to the star PBO-PEEGE. Similarly, the peak of byproducts shifted to 23.5 mL due to the addition of PEEGE blocks. Trace *d* displayed the crude PBO-PGL deprotected product, showing that the peak of star PBO-PGL shifted to a higher elution volume (around 21.7 mL) witnessing the molar mass loss during the deprotection step. The peak of byproducts also shifted towards the higher elution volume side as expected (around 23.7 mL). Specially, Figure 9B compared the crude and purified PBO-PGL products. It shows that the byproducts were almost removed from the star copolymer (trace *b*), evidenced by the negligible peak around 28.7 mL.

Derived from SEC peak areas, the fraction of each star polymer (*f*) was estimated by using Equation 8. Furthermore, based on the values of *f*, monomer feeding ratios and monomer conversions, the theoretical formulae of the intermediates and the final product were calculated, as gathered in Table 6.

**Table 6.** Characteristics of the Star-shaped Intermediates and Product in the Synthetic Process for  $\beta$ CD-(PBO<sub>24</sub>-PGL<sub>6</sub>)<sub>14</sub> (Entry HQ144).

Polymer	$p_{\text{BO}}^a$	$p_{\text{EEGE}}^a$	$f^b$	$m_{\text{theo.}}^c$	$n_{\text{theo.}}^c$	$Mn_{\text{theo.}}^c$ (kg mol <sup>-1</sup> )	$Mn_{\text{SEC}}^{d'}$ (kg mol <sup>-1</sup> )	$\bar{D}^d$
$\beta$ CD-(PBO <sub>m</sub> ) <sub>14</sub>	0.86	--	0.96	6.7	--	8.8	7.6	1.07
$\beta$ CD-(PBO <sub>m</sub> ) <sub>14</sub>	0.99	--	0.80	24.4	--	26.6	28.8	1.08
$\beta$ CD-(PBO <sub>m</sub> - PEEGE <sub>n</sub> ) <sub>14</sub>	0.99	1	0.72	24.4	5.9	38.6	40.1	1.06
$\beta$ CD-(PBO <sub>m</sub> - PGL <sub>n</sub> ) <sub>14</sub> ( <i>crude</i> )	--	--	0.84	24.4	5.9	32.7	35.5 <sup>d'</sup>	1.05 <sup>d'</sup>
$\beta$ CD-(PBO <sub>m</sub> - PGL <sub>n</sub> ) <sub>14</sub> ( <i>purified</i> )	--	--	0.98	24.4	5.9	32.7	36.1 <sup>d'</sup>	1.05 <sup>d'</sup>

<sup>a</sup>Monomer conversions of BO ( $p_{\text{BO}}$ ) and EEGE ( $p_{\text{EEGE}}$ ) were calculated from <sup>1</sup>H NMR spectra; <sup>b</sup>The fraction of the star-shaped polymer in each product (*f*) was estimated by using Equation 8; <sup>c</sup>Theoretical DP values of PBO and PEEGE/PGL blocks per arm ( $m_{\text{theo.}}$  and  $n_{\text{theo.}}$ , respectively) were estimated based on monomer feeding ratios, the values of *p* and *f*. Theoretical molar mass ( $Mn_{\text{theo.}}$ ) was derived from the theoretical DP values. <sup>d,d'</sup>SEC characterizations were performed <sup>d</sup>in THF at 40 °C or <sup>d'</sup>in DMF at 60 °C. Characterization results were determined with PMMA as the standard and using an RI detector.

Based on the characterization results, a narrowly distributed ( $\mathcal{D} = 1.05$ ) star copolymer with the formulation of  $\beta$ CD-(PBO<sub>24</sub>-PGL<sub>6</sub>)<sub>14</sub> was obtained with high purity ( $f = 0.98$ ) (Entry HQ144).

Above results demonstrated that the synthetic procedure was effective to synthesize the  $\beta$ CD-(PBO<sub>m</sub>-PGL<sub>n</sub>)<sub>14</sub> with long PBO blocks. Therefore, this procedure was extended to the syntheses of other star copolymers having long PBO blocks. The theoretical and characterization results were gathered in Table 7.

**Table 7.** Characteristics of the Star Copolymers  $\beta$ CD-(PBO<sub>m</sub>-PGL<sub>n</sub>)<sub>14</sub> with  $m > 10$  According to the Weight Fraction of PGL Blocks ( $w_{\text{PGL}}$ ).

Entry	$[\text{BO}]_0/[\text{EEG E}]_0/[\beta\text{CD}]_0^a$	$p_{\text{BO}}^b$	$p_{\text{EEGE}}^b$	$f^c$	Formula <sup>d</sup>	$w_{\text{PGL}}^d$	$M_{\text{n,theo.}}^d$ (kg mol <sup>-1</sup> )	$M_{\text{n,SEC}}^e$ (kg mol <sup>-1</sup> )	$\mathcal{D}^e$
HQ152	640/186/1	0.98	1	0.97	$\beta$ CD-(PBO <sub>30</sub> -PGL <sub>4</sub> ) <sub>14</sub>	0.11	35.8	35.3 <sup>e'</sup>	1.08 <sup>e'</sup>
HQ136	416/132/1	1	1	0.77*	$\beta$ CD-(PBO <sub>25</sub> -PGL <sub>5</sub> ) <sub>14</sub>	0.16	32.9	23.2 <sup>e'</sup>	1.09 <sup>e'</sup>
HQ135	435/140/1	0.99	1	0.87*	$\beta$ CD-(PBO <sub>24</sub> -PGL <sub>6</sub> ) <sub>14</sub>	0.19	32.7	25.4 <sup>e'</sup>	1.08 <sup>e'</sup>
HQ144	431/140/1	0.99	1	0.98	$\beta$ CD-(PBO <sub>24</sub> -PGL <sub>6</sub> ) <sub>14</sub>	0.19	32.7	36.1	1.05
HQ107	339/209/1	0.99	1	1	$\beta$ CD-(PBO <sub>22</sub> -PGL <sub>7</sub> ) <sub>14</sub>	0.23	31.2	26.1	1.03
HQ151	252/158/1	0.99	1	0.99	$\beta$ CD-(PBO <sub>13</sub> -PGL <sub>6</sub> ) <sub>14</sub>	0.28	21.4	24.9	1.11

<sup>a</sup>The feeding ratio of BO is the total ratio taking into account both homopolymerization steps using the formula of  $M = M_1 \times p_1 + M_2$ , in which,  $M$  is the total BO feeding ratio;  $M_1$  and  $M_2$  are respectively the feeding ratios in the first and the second homopolymerization steps, and  $p_1$  is BO conversion in the first homopolymerization step; <sup>b</sup>The conversions of BO ( $p_{\text{BO}}$ ) and EEGE ( $p_{\text{EEGE}}$ ) were determined by <sup>1</sup>H NMR. BO conversion ( $p_{\text{BO}}$ ) was the conversion at the end of the second homopolymerization step; <sup>c</sup>The fraction of the star-shaped copolymer in the product ( $f$ ) was estimated from the SEC peak areas using Equation 8. <sup>d</sup>Theoretical formula of the star copolymers were calculated based on the monomer feeding ratios, monomer conversions ( $p$ ) and the fractions of star-shaped copolymer ( $f$ ). Theoretical weight fraction of PGL blocks ( $w_{\text{PGL}}$ ) was defined as  $w_{\text{PGL}} = M_{\text{rGL}} \times 14 \times n / (M_{\text{rBO}} \times 14 \times m + M_{\text{rGL}} \times 14 \times n + M_{\text{rI}})$  with  $M_{\text{rGL}}$ ,  $M_{\text{rBO}}$  and  $M_{\text{rI}}$  being respectively the molar masses of GL (74 g mol<sup>-1</sup>), BO (72 g mol<sup>-1</sup>), and the initiator (2044 g mol<sup>-1</sup>). Theoretical molar mass ( $M_{\text{n,theo.}}$ ) was derived from the theoretical formula; <sup>e,e'</sup>SEC characterizations were performed <sup>e</sup>in DMF at 60 °C or <sup>e'</sup>in THF at 40 °C. Characterization results were determined with PMMA as the standard and using an RI detector. \*Low purity resulted from the inefficient purification via precipitation.

The results indicated that the star copolymer arms were successfully equipped with long PBO blocks (DP ranging from 13 to 30), and all the star-shaped products were narrowly distributed ( $\bar{D} \sim 1.1$ ). Altogether the characterizations results demonstrated that the proposed procedure (Scheme 3) was effective to prepare the star PBO-PGL having long PBO blocks,  $\beta$ CD-(PBO<sub>m</sub>-PGL<sub>n</sub>)<sub>14</sub> with  $m > 10$ .

### 3.4 Self-assembly behaviors of the star copolymers

The star copolymers  $\beta$ CD-(PBO<sub>m</sub>-PGL<sub>n</sub>)<sub>14</sub> consist of hydrophobic PBO and hydrophilic PGL blocks. It has been demonstrated in Chapter 2 that their linear counterparts, PBO-PGL and PGL-PBO-PGL, were able to self-assemble into various morphologies in aqueous solution depending on the weight fraction of PGL block(s) ( $w_{PGL}$ ), such as micelles and vesicles. The self-assemblies of amphiphilic polymers have been investigated for a lot of applications, for instance, both micelles and vesicles are promising drug-carriers [3]. In particular, vesicles have recently been extensively studied in construction of nanoreactors to mimic organelles [4]. In contrast with dominant linear amphiphilic polymer in the self-assembly science, nonlinear polymers gained less attention probably because of the tedious synthetic routes. Nowadays, taking advantage of advanced and controllable polymerization strategies, the non-linear polymers especially star-like polymers have been more and more noticed due to their distinctive configurations and a plenty of modifiable sites for special needs [30]. In this sense, their self-assembly behaviours deserve more investigations.

In the present work, the self-assembly behaviors of the star copolymers  $\beta$ CD-(PBO<sub>m</sub>-PGL<sub>n</sub>)<sub>14</sub> with various hydrophobic-to-hydrophilic ratios (Tables 2 and 7) were systematically studied and compared with their linear analogues. Therefore, the self-assemblies of star copolymers were prepared by the thin-film rehydration method, the same method used to prepare the self-assemblies of the linear copolymers in Chapter 2. Thin-film rehydration method was widely studied and applied mainly because it is friendly to biological macromolecules (without residual organic solvents) than other reported methods, like solvent-exchange method [31] and reverse phase evaporation method [32]. Despite of the different preparation routes the thermodynamically preferred morphology of a specific amphiphile was determined mostly by the hydrophobic-to-hydrophilic ratio [2,3]. Moreover, thin-film rehydration method has been deeply studied in detail on mechanisms and experimental conditions both with lipids and polymers [17,18], which permits to have a more direct comparison of the results obtained here with reported phase diagrams as well as the results obtained from the linear counterparts (Chapter 2).

To perform the thin-film rehydration procedure, the thin film of  $\beta$ CD-(PBO<sub>m</sub>-PGL<sub>n</sub>)<sub>14</sub> was first coated onto the inner wall of a glass vial, by well-dissolving the polymer in methanol and subsequently removing the solvent. The obtained polymer film was then rehydrated by DI water to detach it from the vial inner surface. After an adequate period of time, the suspension solution of the self-assemblies was obtained.

All the star copolymers  $\beta$ CD-(PBO<sub>m</sub>-PGL<sub>n</sub>)<sub>14</sub> (Tables 2 and 7) were used to prepare the suspension solutions of self-assemblies, with the exceptions of  $\beta$ CD-(PBO<sub>25</sub>-PGL<sub>5</sub>)<sub>14</sub> (Entry HQ136, Table 7) and  $\beta$ CD-(PBO<sub>24</sub>-PGL<sub>6</sub>)<sub>14</sub> (Entry HQ135, Table 7), considering their low purities and undefined compositions.

By appearance, the suspensions were classified into three groups:

The first group are the rehydrated suspensions of  $\beta$ CD-(PBO<sub>30</sub>-PGL<sub>4</sub>)<sub>14</sub> (Entry HQ152) and  $\beta$ CD-(PBO<sub>24</sub>-PGL<sub>6</sub>)<sub>14</sub> (Entry HQ144). They were turbid and heterogeneous with many visible aggregates, which were undefined in size and shape (by eye) and tended to precipitate without stirring. Both turbid suspensions turned clear (colorless and transparent), after being extruded once through the 0.45  $\mu$ m syringe filter, in accordance with the rather low light scattering intensities (in terms of count rate) as measured by DLS, indicating the loss of samples.

The second group are the rehydrated suspensions of  $\beta$ CD-(PBO<sub>22</sub>-PGL<sub>7</sub>)<sub>14</sub> (Entry HQ107),  $\beta$ CD-(PBO<sub>13</sub>-PGL<sub>6</sub>)<sub>14</sub> (Entry HQ151) and  $\beta$ CD-(PBO<sub>7</sub>-PGL<sub>5</sub>)<sub>14</sub> (Entry HQ137) which were white-bluish and homogeneous without any aforementioned visible undefined aggregates. The suspensions seemed also to be stable as a function of time. After 5 repeated extrusions through a 0.45  $\mu$ m filter (back and forth), each of the suspensions remained white-bluish and the light scattering intensity (in terms of count rate) was unchanged as observed by DLS indicating the nanoparticles were totally went through the filter membrane without sample loss.

The last group are the rehydrated suspensions of  $\beta$ CD-(PBO<sub>8</sub>-PGL<sub>12</sub>)<sub>14</sub> (Entry HQ093) and  $\beta$ CD-(PBO<sub>6</sub>-PGL<sub>14</sub>)<sub>14</sub> (Entry HQ105) which were clear (colorless and transparent) due to the polymers' good aqueous solubility. Both solutions were stable with no precipitates when stored at r.t. for several months (available time data in records). These solutions had very low light scattering intensities both before and after extrusions as measured by DLS.

The suspensions in the second and third groups had defined self-assemblies and were further characterized by DLS and SLS to get information on the sizes and molecular weights of the self-assembled particles.

Figure 10 displayed the representative DLS characterization results of the self-assemblies of  $\beta$ CD-(PBO<sub>13</sub>-PGL<sub>6</sub>)<sub>14</sub> (Entry HQ151) and  $\beta$ CD-(PBO<sub>6</sub>-PGL<sub>14</sub>)<sub>14</sub> (Entry HQ105). These two star polymers were close in molar mass but significantly

different in the hydrophobic-to-hydrophilic ratio. The weight fraction of PGL blocks ( $w_{\text{PGL}}$ ) was 0.28 for  $\beta\text{CD}-(\text{PBO}_{13}\text{-PGL}_6)_{14}$  (Entry HQ151) and 0.62 for  $\beta\text{CD}-(\text{PBO}_6\text{-PGL}_{14})_{14}$  (Entry HQ105). Keeping the same preparation and characterization conditions allowed a comparison between both copolymers essentially by their different hydrophilic fractions ( $w_{\text{PGL}}$ ).

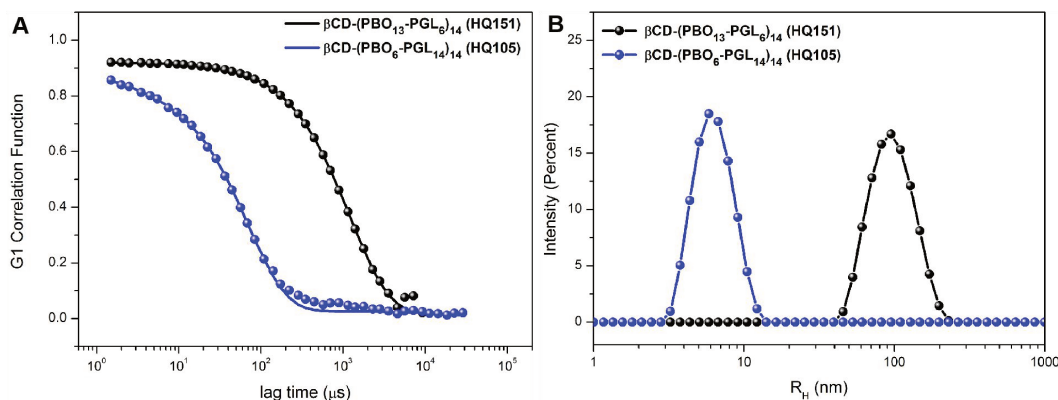


**Figure 10.** (A) Autocorrelation functions of relaxation time (dots) and the corresponding cumulant fittings (lines), and (B) the respective intensity particle distribution curves of the self-assemblies of  $\beta\text{CD}-(\text{PBO}_{13}\text{-PGL}_6)_{14}$  (Entry HQ151) and  $\beta\text{CD}-(\text{PBO}_6\text{-PGL}_{14})_{14}$  (Entry HQ105).

Figure 10A showed the light scattering intensity-derived autocorrelation functions which were mathematically treated by the NNLS analysis. It can be seen both correlation functions were single populations as function of the relaxation time. To note that the monomodal distributions enabled the data to be analyzed via the cumulant method to determine the hydrodynamic radii ( $R_H$ ) and the polydispersity values (PDI). In accordance with the single populations of the relaxation times, both the self-assembled particles presented single populations in size distribution (based on the light scattering intensities), as depicted in Figure 10B.

The self-assemblies made from the other star copolymers also had monomodal correlation functions of relaxation time and one-populated intensity particle size distribution curves (not shown here), permitting the calculations of the sizes and distributions of all the self-assembled particles.

The self-assemblies were all characterized by SLS at the same time, to determine the molecular weights ( $M_{\text{WNPs}}$ ) by using the Debye plot (Equation 3). Plotting  $Kc/R_0$  against  $c$  at a given angle, the value of  $M_{\text{WNPs}}$  was extracted from the reverse of the intercept. Accordingly, the aggregation number ( $N_{\text{agg}}$ ) was determined using Equation 6. The results acquired from the light scattering analyses were gathered in Table 8 according to the weight fraction of PGL blocks ( $w_{\text{PGL}}$ ).

**Table 8.** Scattering Data for the Assemblies of Star Copolymers According to the Weight Fraction of PGL Blocks ( $w_{\text{PGL}}$ ).

Entry	Formula <sup>a</sup>	$w_{\text{PGL}}$ <sup>a</sup>	$R_{\text{H}}$ <sup>b</sup> (nm)	PDI <sup>b</sup>	$M_{\text{WNPs}}$ <sup>c</sup> (kDa)	$N_{\text{agg}}$ <sup>c</sup>
<b>Aggregates</b>						
HQ152	$\beta\text{CD}-(\text{PBO}_{30}\text{-PGL}_4)_{14}$	0.11	-- <sup>d</sup>			
HQ144	$\beta\text{CD}-(\text{PBO}_{24}\text{-PGL}_6)_{14}$	0.19				
<b>Polymersomes</b>						
HQ107	$\beta\text{CD}-(\text{PBO}_{22}\text{-PGL}_7)_{14}$	0.23	111	0.10	$4.11 \times 10^4$	1320
HQ151	$\beta\text{CD}-(\text{PBO}_{13}\text{-PGL}_6)_{14}$	0.28	90	0.10	$2.96 \times 10^4$	1450
HQ137	$\beta\text{CD}-(\text{PBO}_7\text{-PGL}_5)_{14}$	0.35	84	0.16	$5.40 \times 10^4$	3880
<b>Micelles</b>						
HQ093	$\beta\text{CD}-(\text{PBO}_8\text{-PGL}_{12})_{14}$	0.57	7.7	0.28	$2.06 \times 10^2$	9.29
HQ105	$\beta\text{CD}-(\text{PBO}_6\text{-PGL}_{14})_{14}$	0.62	5.6	0.24	$1.61 \times 10^2$	7.27

<sup>a</sup>Polymer formula and  $w_{\text{PGL}}$  value were reported as the theoretical ones; <sup>b</sup>The hydrodynamic radius ( $R_{\text{H}}$ ) and size distribution (PDI) were reported as the Z-average radius and corresponding PDI value based on 5 measurements; <sup>c</sup>The self-assemblies' molecular weight ( $M_{\text{WNPs}}$ ) was determined via the Debye plot (Equation 3) and the aggregation number ( $N_{\text{agg}}$ ) was calculated using Equation 6; <sup>d</sup>Both DLS and SLS were unsuitable to provide these kinds of particle parameters in these cases and detailed descriptions can be found in the text.

First, one can see that, when  $w_{\text{PGL}}$  was as small as 0.11 ( $\beta\text{CD}-(\text{PBO}_{30}\text{-PGL}_4)_{14}$ , Entry HQ152) and 0.19 ( $\beta\text{CD}-(\text{PBO}_{24}\text{-PGL}_6)_{14}$ , Entry HQ144), the amphiphilic polymers precipitated in water.

Then, looking at the values of  $R_{\text{H}}$ ,  $M_{\text{WNPs}}$  and corresponding  $N_{\text{agg}}$ , one can distinguish two sets of values: The set with low values gathered the self-assemblies of  $\beta\text{CD}-(\text{PBO}_8\text{-PGL}_{12})_{14}$  (Entry HQ093) and  $\beta\text{CD}-(\text{PBO}_6\text{-PGL}_{14})_{14}$  (Entry HQ105).  $R_{\text{H}}$  ranged between 5 and 8 nm, values compatible with either micelles or single macromolecules. Looking at the  $N_{\text{agg}}$ , an attribution to micelles was more relevant. A second set of analysis revealed  $R_{\text{H}}$  with values over 80 nm. This set gathered the self-assemblies of  $\beta\text{CD}-(\text{PBO}_{22}\text{-PGL}_7)_{14}$  (Entry HQ107),  $\beta\text{CD}-(\text{PBO}_{13}\text{-PGL}_6)_{14}$  (Entry HQ151), and  $\beta\text{CD}-(\text{PBO}_7\text{-PGL}_5)_{14}$  (Entry HQ137). The  $N_{\text{agg}}$  values of this set were all above 1000 suggesting the presence of vesicles.

To confirm the light scattering analyses, the assemblies were further characterized by SAXS to study deeply the obtained morphologies. Figure 11 displayed the SAXS patterns of star copolymer self-assemblies (scattering dots). The SAXS profiles were fitted into appropriate former factors (implemented in the SASfit software) to obtain the structural parameters. In specific, the SAXS pattern of  $\beta\text{CD}-(\text{PBO}_6\text{-PGL}_{14})_{14}$

assemblies (Entry HQ105), suggested as micelles by DLS, was fit by a core-shell form factor (Figure 11A), and the patterns of the assemblies suggested as vesicles by DLS (Entries HQ137, HQ151 and HQ107) were fit by a bilayered vesicle form factor (Figures 11B–D).

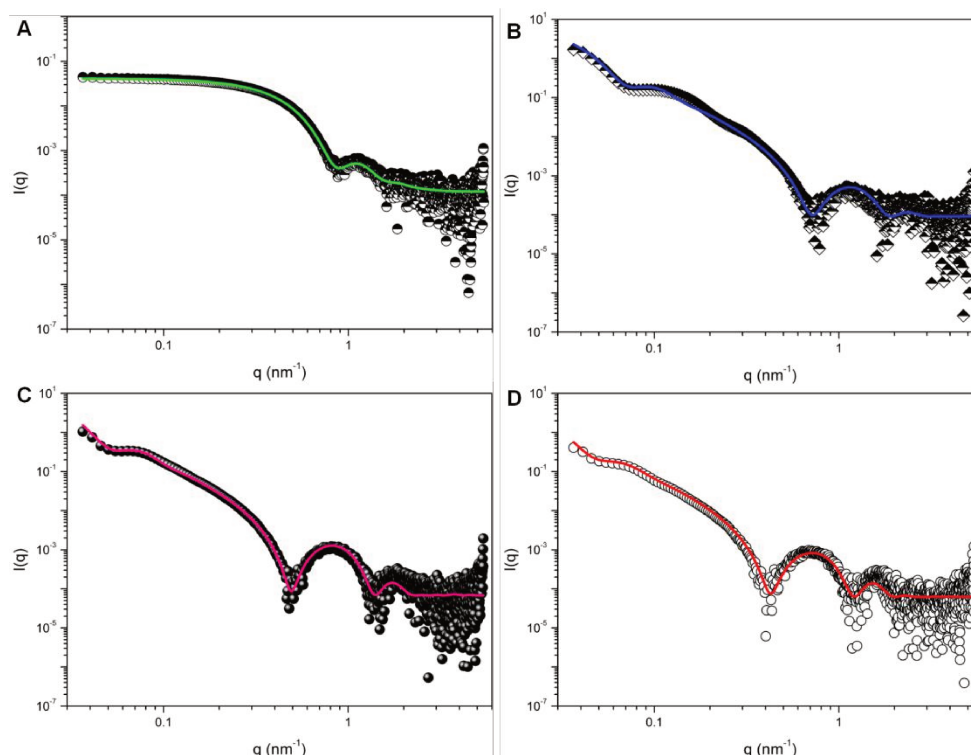


**Figure 11.** SAXS profiles (dots) and the respective fitting curves (lines) of the self-assemblies of (A)  $\beta$ CD-(PBO<sub>6</sub>-PGL<sub>14</sub>)<sub>14</sub> (Entry HQ105), (B)  $\beta$ CD-(PBO<sub>7</sub>-PGL<sub>5</sub>)<sub>14</sub> (Entry HQ137), (C)  $\beta$ CD-(PBO<sub>13</sub>-PGL<sub>6</sub>)<sub>14</sub> (Entry HQ151), and (D)  $\beta$ CD-(PBO<sub>22</sub>-PGL<sub>7</sub>)<sub>14</sub> (Entry HQ107). A was fit by using the core-shell form factor, and B-D were fit by using the bilayered vesicle form factor, with the SASfit software.

From Figure 11, one can see that the suggested fitting form factors matched very well with the SAXS patterns, confirming that the assemblies were spherical micelles (Figure 11A) or well-defined polymersomes (Figure 11B–D). The fitting results also provided detailed structural parameters in each context of form factor. For the micelles of  $\beta$ CD-(PBO<sub>6</sub>-PGL<sub>14</sub>)<sub>14</sub> (Entry HQ105), the fitting results (Figure 11A) depicted a sphere with a core of radius 3.2 nm and a shell of thickness 1.4 nm, namely the entire size was of radius 4.6 nm, consistent with the  $R_H$  measured by DLS as 5.6 nm (Table 8). Regarding the polymersomes (Figures 11B–D), their structural parameters (Scheme 5) were also derived from the SAXS fitting curves and listed in Table 9.

**Scheme 5.** Graphical Descriptions of (left) the Polymersome Made from  $\beta$ CD-cored Star Copolymers and (right) the Structure of the  $\beta$ CD-cored Polymer Unimer. Blue and yellow layers describe the PGL and PBO segments, respectively, and the golden block indicates the  $\beta$ CD core.

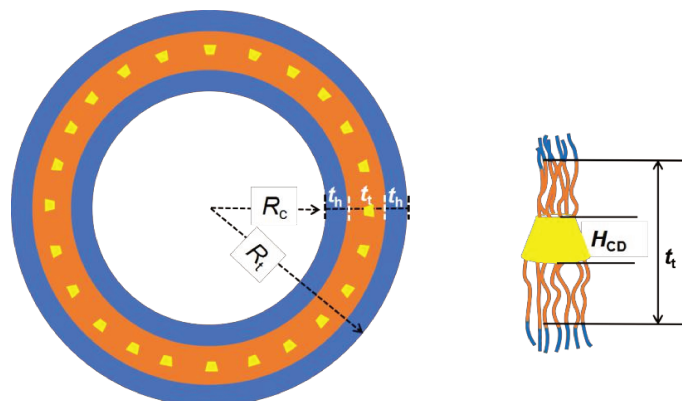


**Table 9.** Structural Parameters of the Polymersomes Obtained from the  $\beta$ CD-cored Star Copolymers Determined by SAXS Measurements According to the DP of PBO block.

Polymersomes		$t_t^a$	$t_h^a$	$d^b$	$R_c^a$	$R_t^a$
		(nm)	(nm)	(nm)	(nm)	(nm)
HQ137	$\beta$ CD-(PBO <sub>7</sub> -PGL <sub>5</sub> ) <sub>14</sub>	3.2	1.7	6.6	36.2	42.8
HQ151	$\beta$ CD-(PBO <sub>13</sub> -PGL <sub>6</sub> ) <sub>14</sub>	4.4	2.3	9.0	49.9	59.0
HQ107	$\beta$ CD-(PBO <sub>22</sub> -PGL <sub>7</sub> ) <sub>14</sub>	5.6	2.2	10.0	52.5	62.6

<sup>a</sup>  $t_t$ ,  $t_h$ ,  $R_c$  and  $R_t$  are the structural parameters illustrated in Scheme 5. <sup>b</sup>  $d = t_h + t_t + t_h$ .

The results evidenced that for these polymersomes, the thickness of the hydrophobic layer ( $t_t$ ) varied in general as a function of the DP of PBO block. Taking into account the attribution of the rigid and non-negligible  $\beta$ CD core to the hydrophobic layer, the thickness merely contributed by the PBO segment ( $t_{PBO}$ ) was taken as the difference between  $t_t$  and  $H_{CD}$ , *i.e.*,  $t_{PBO} = t_t - H_{CD}$ , as illustrated in Scheme 5, with  $H_{CD}$  being the  $\beta$ CD thickness and taken equal to 0.78 nm [33].

For the purpose of comparison, both the thicknesses of the hydrophobic layer ( $t_t$ ) and the mere PBO segment ( $t_t - H_{CD}$ ) were plotted against the DP values of PBO block in log-log scales, allowing the plots depicted in Figure 12. To note that, due to the symmetric structure of  $\beta$ CD-(PBO<sub>*m*</sub>-PGL<sub>*n*</sub>)<sub>14</sub> (Scheme 5, right panel), the DP value of PBO segment in the polymersome membrane is  $2m$  in fact.

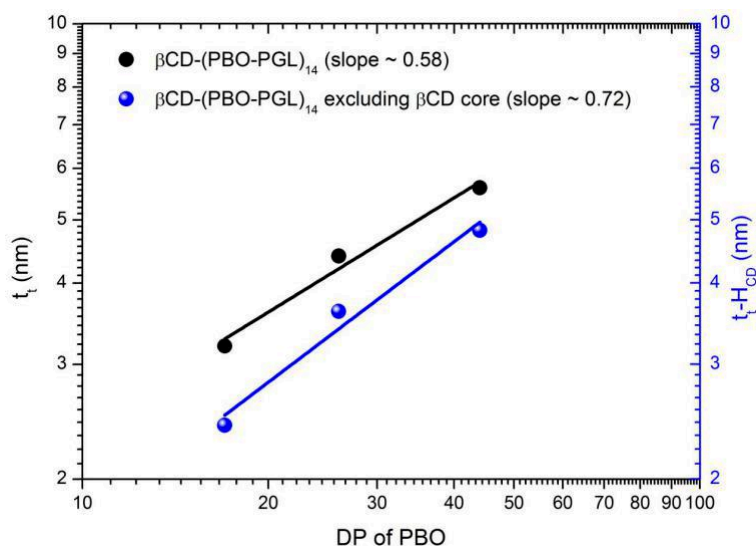


**Figure 12.** The log–log plots of the thicknesses of hydrophobic layer ( $t_t$ , black line) and mere PBO segment ( $t_t - H_{CD}$ , blue line) as a function of the DP of PBO in the context of  $\beta$ CD-(PBO-PGL)<sub>14</sub> polymersomes.

As shown in Figure 12, there was a deviation between the two curves due to the contribution of  $\beta$ CD core to the thickness of the hydrophobic layer. When PBO segment was merely considered, its thickness increased consistently with the DP values, and the log–log plot (blue line, Figure 12) allowed a slope around 0.72, reflecting the PBO chains were stretched to some extent. This slope was a little higher than that in the context of linear triblock copolymer polymersomes which was about 0.64 (red line, Figure 13). It was supposed that the  $\beta$ CD-cored architecture could induce a lateral crowding environment and correspondingly the stretching chains of PBO segment [34]. However, in general, the star copolymers (blue dots, Figure 13) matched the master curve of the linear triblock copolymers (red line, Figure 13). This result demonstrated the PBO chains in both the star copolymers and the linear copolymers had similar configurations and stretching states. These similarities would be interesting when the  $\beta$ CD-cored star copolymers are applied as artificial nanochannel scaffolds to be inserted into the robust polymeric membranes to avoid the mismatching issues between the nature channel/pore proteins and the polymeric membranes as reported in many studies [35–37].

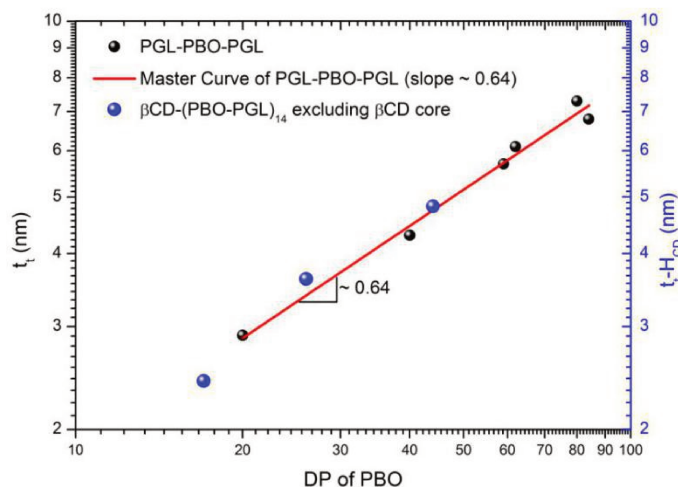
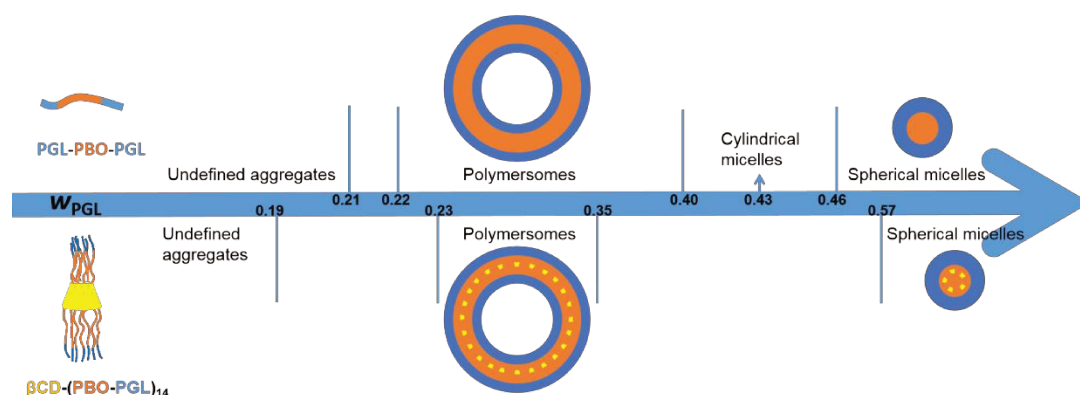


**Figure 13.** Merging the thicknesses of PBO segment in the membrane of the  $\beta$ CD-cored polymersomes ( $t_i$ - $H_{CD}$ , blue dots) with the master curve of the triblock copolymer ( $\log t_i$  vs  $\log DP$ , red line).

Based on above results, it can be concluded that the self-assembled morphology of star copolymer  $\beta$ CD-(PBO-PGL)<sub>14</sub> was also decided by the weight fraction of PGL block ( $w_{PGL}$ ) and obeyed the phase diagram theory for the self-assembly of amphiphilic block copolymers in aqueous solution [1]. More specifically, when  $w_{PGL} \leq 0.19$ , the copolymers precipitated in water; when  $0.23 \leq w_{PGL} \leq 0.35$ , copolymers self-assembled into polymersomes; and when  $w_{PGL} \geq 0.57$ , copolymers formed spherical micelles. These ranges fit pretty well with those of linear analogues, as depicted in Scheme 6.

**Scheme 6.** Morphology Evolution with the Weight Fraction of PGL Blocks ( $w_{PGL}$ ) of the Linear Triblock Copolymers (PGL-PBO-PGL, top) and the Star Copolymers ( $\beta$ CD-(PBO-PGL)<sub>14</sub>, bottom). Based on the available data.



A similar work studied the self-assembly behaviors of the  $\beta$ CD-cored amphiphilic star copolymer having seven poly( $\epsilon$ -caprolactone-*co*-carbonate)-*b*-poly(ethylene glycol) arms on the primary face of  $\beta$ CD, denoted as  $\beta$ CD-[P(CL-*co*-DTC)-*b*-PEG]<sub>7</sub> [38]. These copolymers were prepared via the combination of ring-opening polymerization, esterification and click reactions, having polydispersities ( $\mathcal{D}$ ) ranging from 1.26 to 1.46. The self-assembly results showed that when the weight fraction of PEG ( $w_{\text{PEG}}$ ) was 0.14 polymersomes were obtained. However, in the current work  $\beta$ CD-(PBO-PGL)<sub>14</sub> ( $\mathcal{D} \leq 1.11$ ) was anticipated to form undefined aggregates when the hydrophilic fraction ( $w_{\text{PGL}}$ ) was less than 0.19. The different results might originate from the different chemical compositions and polymer architectures.

#### 4. Conclusions

In this chapter, a set of symmetric star copolymers consisting of hydrophobic PBO and hydrophilic PGL blocks were prepared from the symmetrically modified  $\beta$ CD initiator, per(2-*O*-methyl-3,6-di-*O*-(3-hydroxypropyl))- $\beta$ CD ( $\beta$ CD-(OH)<sub>14</sub>). With this defined macroinitiator, the  $\beta$ CD-cored star copolymers were synthesized via a tBuP4-catalyzed sequential anionic ring-opening block copolymerization, followed by a deprotection treatment in acidic conditions. However, due to the solvent effect, the star homopolymer ( $\beta$ CD-(PBO<sub>*m*</sub>)<sub>14</sub>) had a limitation in the length of PBO arms with the maximum value of *m* being around 16. In order to get longer PBO blocks, a solvent-switch strategy was proposed, and by applying this strategy, a star copolymer  $\beta$ CD-(PBO<sub>*m*</sub>-PGL<sub>*n*</sub>)<sub>14</sub> with the value of *m* as large as 30 was obtained.

The library of defined star copolymers was systematically studied focusing on their self-assembly behaviors by DLS, SLS and SAXS. It was found that the self-assembled morphology in aqueous solution was decided by the weight fraction of the hydrophilic PGL blocks ( $w_{\text{PGL}}$ ): when  $w_{\text{PGL}} \leq 0.19$ , the assemblies were undefined aggregates and precipitated; when  $0.23 \leq w_{\text{PGL}} \leq 0.35$ , the assemblies were stable polymersomes; and when  $w_{\text{PGL}} \geq 0.57$ , the assemblies were stable spherical micelles. These ranges were consistent with those in the case of the linear analogues (PGL-PBO-PGL). Furthermore, the master curve obtained by plotting the thickness of the PBO segment against the DP of PBO blocks into the log-log scales produced a slope around 0.72, a little higher than the one in the context of linear analogues (0.64), which was supposed to be contributed by the rigid  $\beta$ CD core [19].

#### 5. Reference

1. Blanz A, Armes S P, Ryan A J. Self - assembled block copolymer aggregates: from micelles to vesicles and their biological applications[J]. Macromolecular rapid communications, 2009, 30(4-5): 267-277.

2. Discher D E, Ahmed F. Polymersomes[J]. *Annu. Rev. Biomed. Eng.*, 2006, 8: 323-341.
3. Zhang X, Tanner P, Graff A, et al. Mimicking the cell membrane with block copolymer membranes[J]. *Journal of polymer science part A: polymer chemistry*, 2012, 50(12): 2293-2318.
4. dos Santos E C, Angelini A, Hürlimann D, et al. Giant Polymer Compartments for Confined Reactions[J]. *Chemistry*, 2020, 2(2): 470-489.
5. Gaitzsch J, Huang X, Voit B. Engineering functional polymer capsules toward smart nanoreactors[J]. *Chemical reviews*, 2016, 116(3): 1053-1093.
6. Blasco E, Schmidt B V K J, Barner-Kowollik C, et al. A novel photoresponsive azobenzene-containing miktoarm star polymer: Self-assembly and photoresponse properties[J]. *Macromolecules*, 2014, 47(11): 3693-3700.
7. Blasco E, del Barrio J, Sánchez-Somolinos C, et al. Light induced molecular release from vesicles based on amphiphilic linear-dendritic block copolymers[J]. *Polymer Chemistry*, 2013, 4(7): 2246-2254.
8. Blasco E, del Barrio J, Sánchez-Somolinos C, et al. Light induced molecular release from vesicles based on amphiphilic linear-dendritic block copolymers[J]. *Polymer Chemistry*, 2013, 4(7): 2246-2254.
9. Xia D, Yu G, Li J, et al. Photo-responsive self-assembly based on a water-soluble pillar [6] arene and an azobenzene-containing amphiphile in water[J]. *Chemical communications*, 2014, 50(27): 3606-3608.
10. Hu M, Shen Y, Zhang L, et al. Polymersomes via self-assembly of amphiphilic  $\beta$ -cyclodextrin-centered triarm star polymers for enhanced oral bioavailability of water-soluble chemotherapeutics[J]. *Biomacromolecules*, 2016, 17(3): 1026-1039.
11. Steinschulte A A, Gelissen A P H, Jung A, et al. Facile screening of various micellar morphologies by blending miktoarm stars and diblock copolymers[J]. *ACS Macro Letters*, 2017, 6(7): 711-715.
12. Pregel M J, Jullien L, Lehn J M. Towards artificial ion channels: Transport of alkali metal ions across liposomal membranes by “bouquet” molecules[J]. *Angewandte Chemie International Edition in English*, 1992, 31(12): 1637-1640.
13. Badi N, Auvray L, Guégan P. Synthesis of Half - Channels by the Anionic Polymerization of Ethylene Oxide Initiated by Modified Cyclodextrin[J]. *Advanced Materials*, 2009, 21(40): 4054-4057.
14. Faye I, Huin C, Illy N, et al.  $\beta$  - Cyclodextrin - Based Star Amphiphilic Copolymers: Synthesis, Characterization, and Evaluation as Artificial Channels[J]. *Macromolecular Chemistry and Physics*, 2019, 220(2): 1800308.
15. Eskandani Z, Le Gall T, Montier T, et al. Polynucleotide transport through lipid membrane in the presence of starburst cyclodextrin-based poly (ethylene glycol) s[J]. *The European Physical Journal E*, 2018, 41(11): 1-7.
16. Zhang Y, Wang G, Huang J. A new strategy for synthesis of “umbrella - like” poly (ethylene glycol) with monofunctional end group for bioconjugation[J]. *Journal of Polymer Science Part A: Polymer Chemistry*, 2010, 48(24): 5974-5981.
17. Hope M J, Bally M B, Webb G, et al. Production of large unilamellar vesicles by a rapid extrusion procedure. Characterization of size distribution, trapped volume and ability to

maintain a membrane potential[J]. *Biochimica et Biophysica Acta (BBA)-Biomembranes*, 1985, 812(1): 55-65.

18. Kamata Y, Parnell A J, Gutfreund P, et al. Hydration and ordering of lamellar block copolymer films under controlled water vapor[J]. *Macromolecules*, 2014, 47(24): 8682-8690.

19. Kwon W, Rho Y, Kamoshida K, et al. Well-Defined Functional Linear Aliphatic Diblock Copolyethers: A Versatile Linear Aliphatic Polyether Platform for Selective Functionalizations and Various Nanostructures[J]. *Advanced Functional Materials*, 2012, 22(24): 5194-5208.

20. Striegel A M. Specific refractive index increment ( $\partial n/\partial c$ ) of polymers at 660 nm and 690 nm[J]. *Chromatographia*, 2017, 80(6): 989-996.

21. El Ghoul Y, Renia R, Faye I, et al. Biomimetic artificial ion channels based on beta-cyclodextrin[J]. *Chemical Communications*, 2013, 49(99): 11647-11649.

22. Huin C, Eskandani Z, Badi N, et al. Anionic ring-opening polymerization of ethylene oxide in DMF with cyclodextrin derivatives as new initiators[J]. *Carbohydrate polymers*, 2013, 94(1): 323-331.

23. Isono T, Kamoshida K, Satoh Y, et al. Synthesis of star-and figure-eight-shaped polyethers by t-Bu-P4-catalyzed ring-opening polymerization of butylene oxide[J]. *Macromolecules*, 2013, 46(10): 3841-3849.

24. Misaka H, Tamura E, Makiguchi K, et al. Synthesis of end - functionalized polyethers by phosphazene base - catalyzed ring - opening polymerization of 1, 2 - butylene oxide and glycidyl ether[J]. *Journal of Polymer Science Part A: Polymer Chemistry*, 2012, 50(10): 1941-1952.

25. Lee B F, Wolffs M, Delaney K T, et al. Reactivity ratios and mechanistic insight for anionic ring-opening copolymerization of epoxides[J]. *Macromolecules*, 2012, 45(9): 3722-3731.

26. Puchelle V, Du H, Illy N, et al. Polymerization of epoxide monomers promoted by t BuP 4 phosphazene base: a comparative study of kinetic behavior[J]. *Polymer Chemistry*, 2020, 11(21): 3585-3592.

27. Hans M, Keul H, Moeller M. Chain transfer reactions limit the molecular weight of polyglycidol prepared via alkali metal based initiating systems[J]. *Polymer*, 2009, 50(5): 1103-1108.

28. Gervais M, Brocas A L, Cendejas G, et al. Synthesis of linear high molar mass glycidol-based polymers by monomer-activated anionic polymerization[J]. *Macromolecules*, 2010, 43(4): 1778-1784.

29. Tezgel Ö, Puchelle V, Du H, et al. Modification of proline-based 2,5-diketopiperazines by anionic ring-opening polymerization[J]. *Journal of Polymer Science Part A: Polymer Chemistry*, 2019, 57(9): 1008-1016.

30. Ren J M, McKenzie T G, Fu Q, et al. Star polymers[J]. *Chemical reviews*, 2016, 116(12): 6743-6836.

31. Wehr R, Gaitzsch J, Daubian D, et al. Deepening the insight into poly(butylene oxide)-block-poly(glycidol) synthesis and self-assemblies: micelles, worms and vesicles[J]. *RSC advances*, 2020, 10(38): 22701-22711.

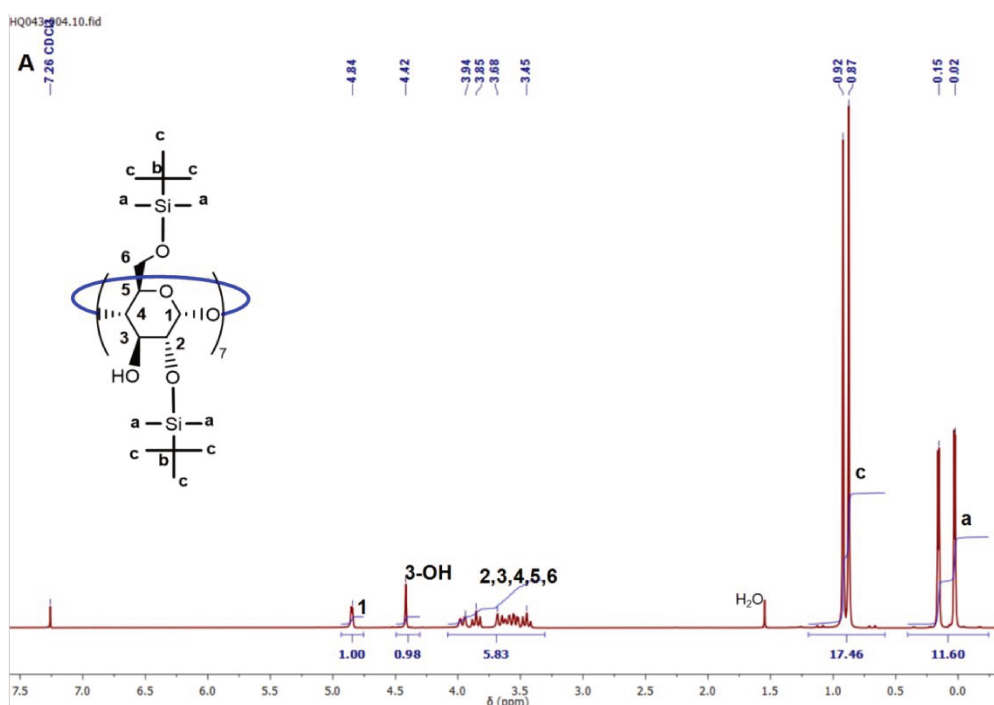
32. Shi N Q, Qi X R. Preparation of drug liposomes by reverse-phase evaporation[J]. *Liposome-Based Drug Delivery Systems*, 2021: 37-46.

33. Van De Manacker F, Vermonden T, Van Nostrum C F, et al. Cyclodextrin-based polymeric materials: synthesis, properties, and pharmaceutical/biomedical applications[J]. *Biomacromolecules*, 2009, 10(12): 3157-3175.
34. Hu M, Shen Y, Zhang L, et al. Polymersomes via self-assembly of amphiphilic  $\beta$ -cyclodextrin-centered triarm star polymers for enhanced oral bioavailability of water-soluble chemotherapeutics[J]. *Biomacromolecules*, 2016, 17(3): 1026-1039.
35. Belluati A, Mikhalevich V, Yorulmaz Avsar S, et al. How do the properties of Amphiphilic polymer membranes influence the functional insertion of peptide pores?[J]. *Biomacromolecules*, 2019, 21(2): 701-715.
36. Lomora M, Garni M, Itel F, et al. Polymersomes with engineered ion selective permeability as stimuli-responsive nanocompartments with preserved architecture[J]. *Biomaterials*, 2015, 53: 406-414.
37. Itel F, Najer A, Palivan C G, et al. Dynamics of membrane proteins within synthetic polymer membranes with large hydrophobic mismatch[J]. *Nano letters*, 2015, 15(6): 3871-3878.
38. Gou P F, Zhu W P, Shen Z Q. Drug-grafted seven-arm amphiphilic star poly( $\epsilon$ -caprolactone-co-carbonate)-b-poly(ethylene glycol)s based on a cyclodextrin core: synthesis and self-assembly behavior in water[J]. *Polymer Chemistry*, 2010, 1(8): 1205-1214.

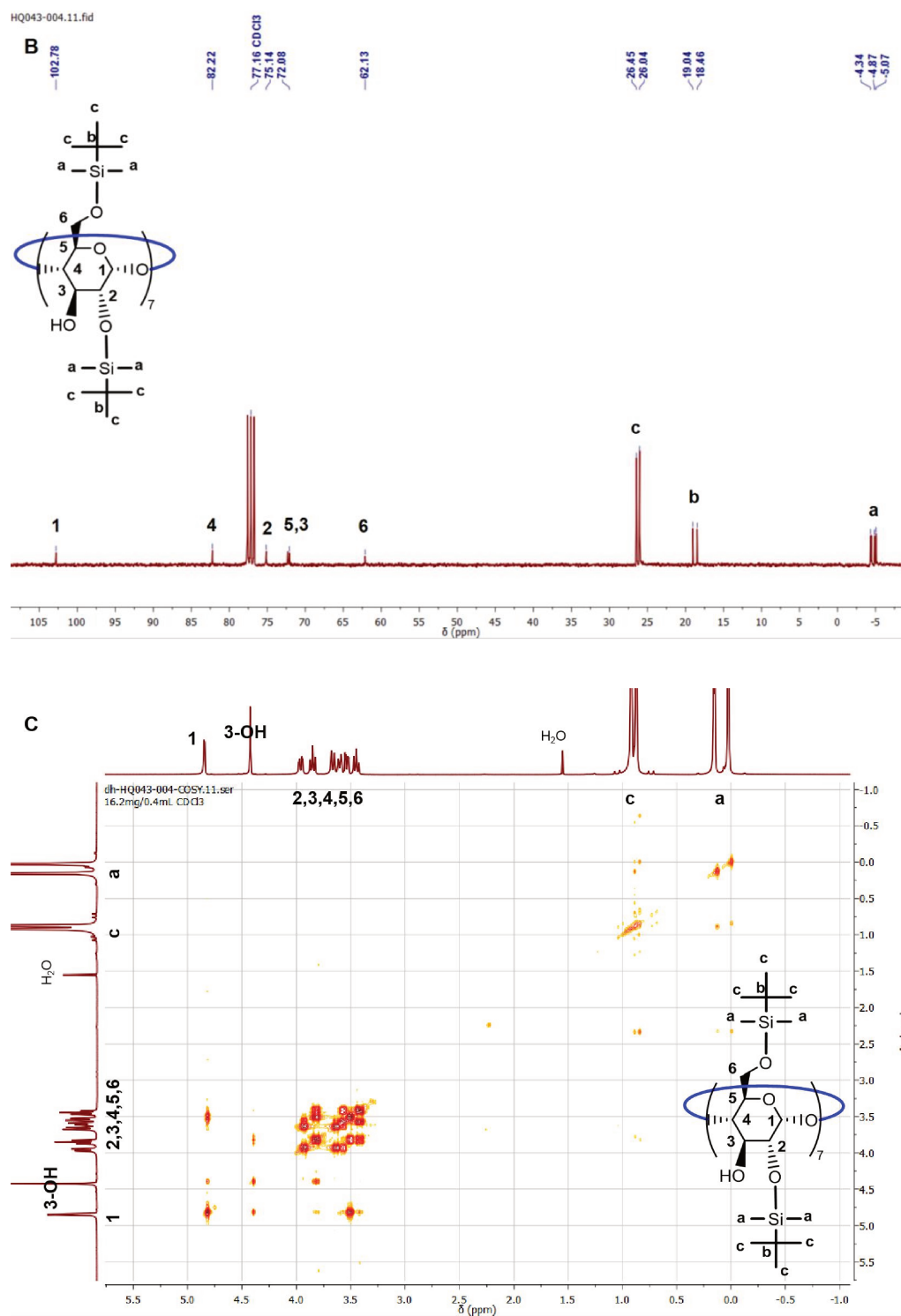
## 6. Appendix

### 6.1 The intermediates in the synthetic process of $\beta$ CD-based initiator

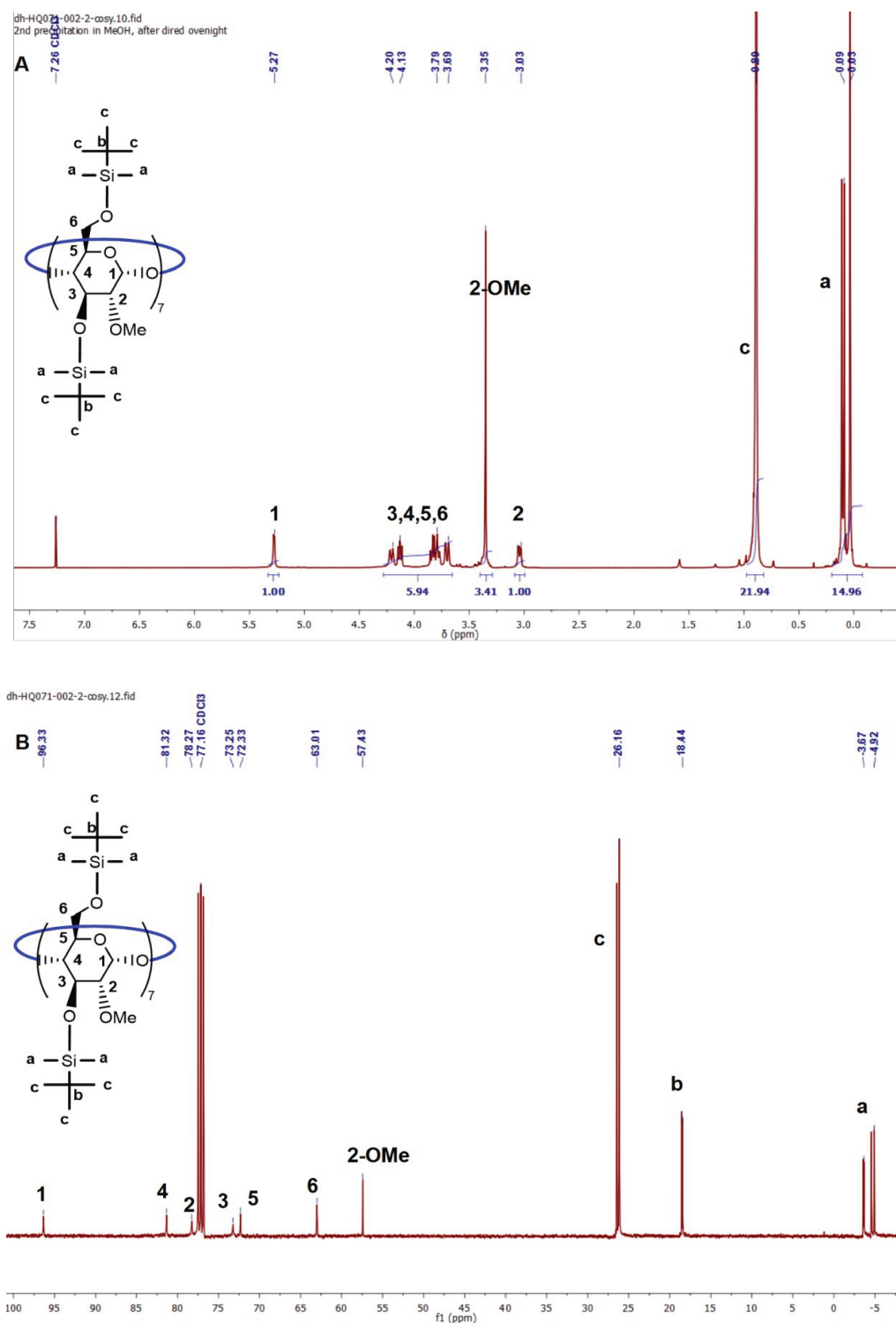
#### (1) per(2,6-di-O-TBDMS)- $\beta$ CD (product 1 in Scheme 1):



**Figure A1.** (A) Representative  $^1\text{H}$  NMR spectrum of per(2,6-di-O-TBDMS)- $\beta$ CD (product 1 in Scheme 1), recorded in  $\text{CDCl}_3\text{-d}_1$ , at 300 K.



**Figure A1 (continued).** Representative (B)  $^{13}\text{C}$  NMR and (C) COSY spectra of per(2,6-di-O-TBDMS)- $\beta$ CD (product **1** in Scheme 1), recorded in  $\text{CDCl}_3\text{-d}_1$ , at 300 K.

(2) per(2-O-Me-3,6-di-O-TBDMS)- $\beta$ CD (product 2 in Scheme 1):

**Figure A2.** Representative (A)  $^1\text{H}$  NMR and (B)  $^{13}\text{C}$  NMR spectra of per(2-O-Me-3,6-di-O-TBDMS)- $\beta$ CD (product 2 in Scheme 1), recorded in  $\text{CDCl}_3\text{-d}_1$ , at 300 K.

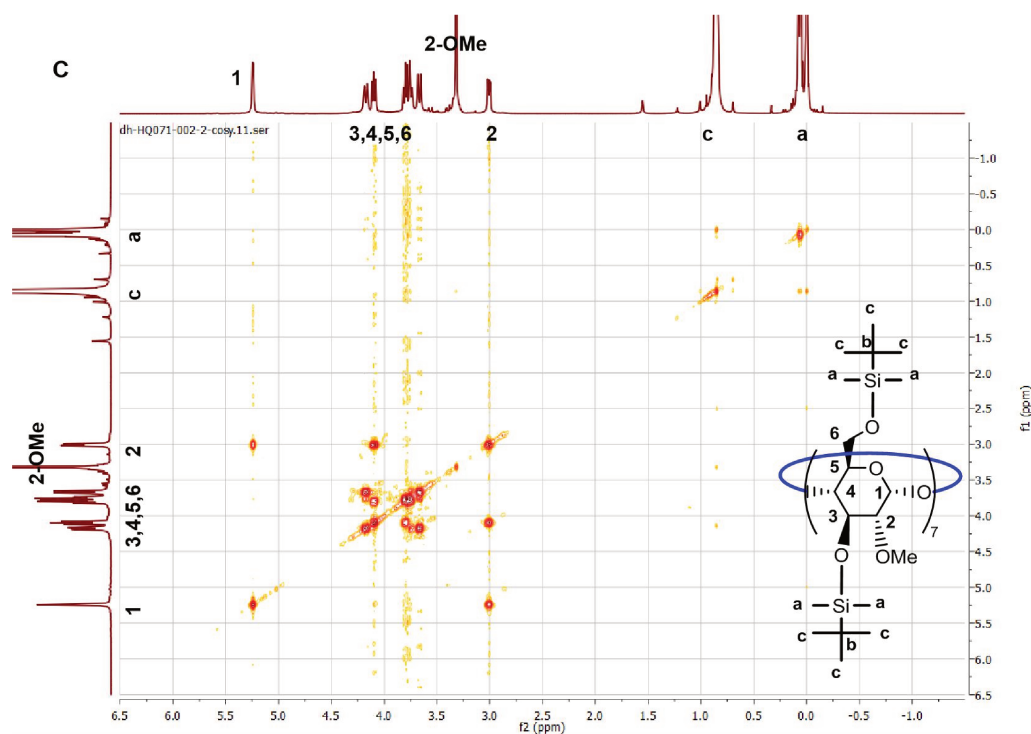


**Figure A2 (continued).** (C) Representative COSY spectrum of per(2-O-Me-3,6-di-O-TBDMS)- $\beta$ CD (product 2 in Scheme 1), recorded in  $\text{CDCl}_3\text{-d}_1$ , at 300 K.

**(3) per(2-O-Me)- $\beta$ CD (product 3 in Scheme 1):**

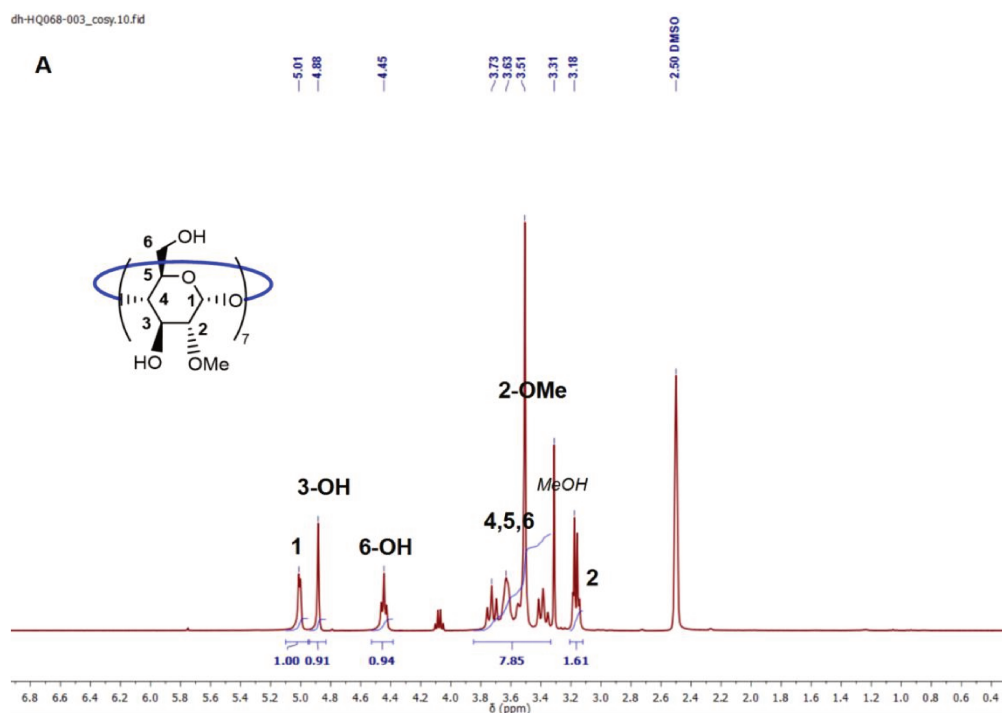


**Figure A3.** (A) Representative  $^1\text{H}$  NMR spectrum of per(2-O-Me)- $\beta$ CD (product 3 in Scheme 1), recorded in  $\text{MeOD-d}_4$ , at 300 K.

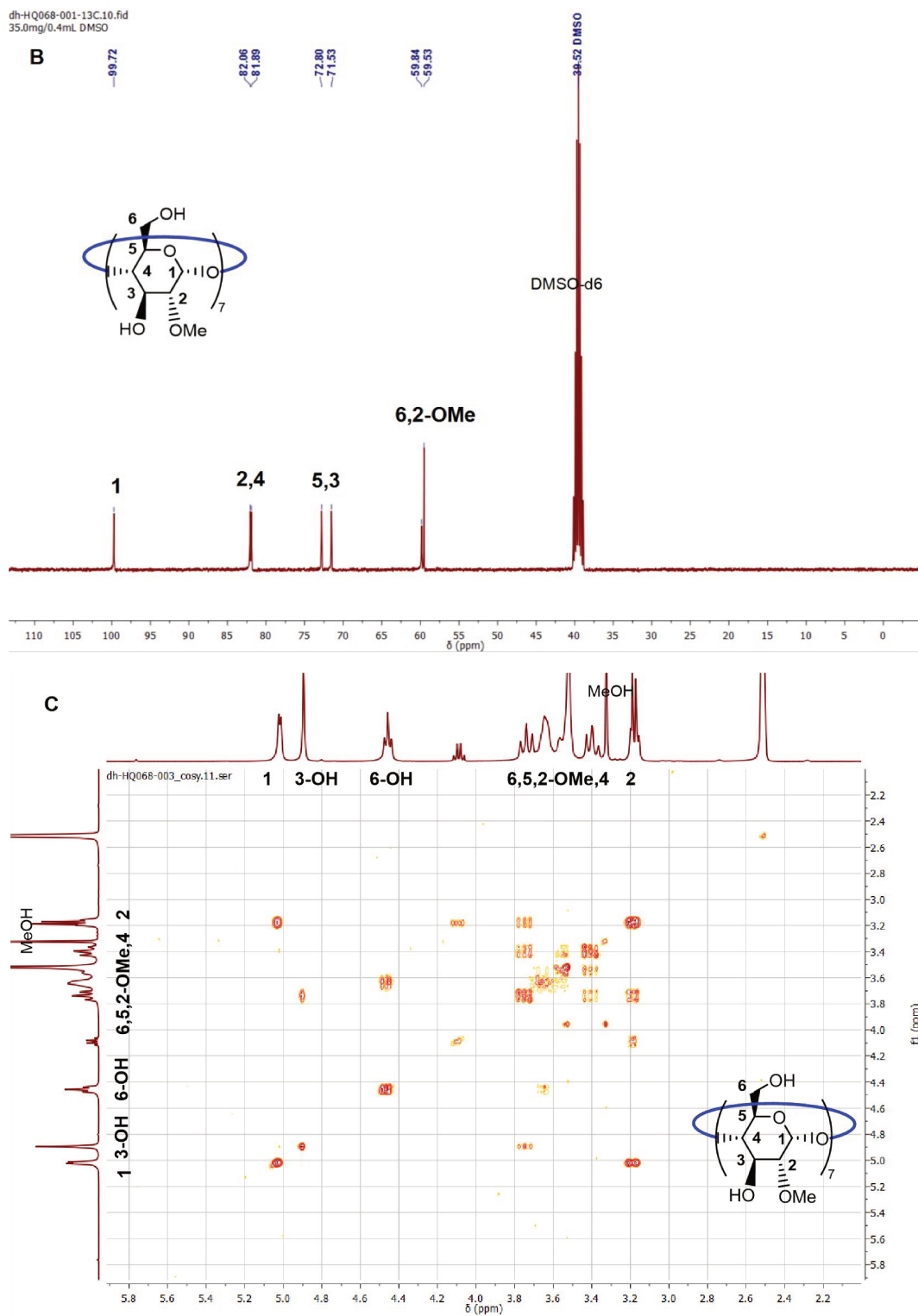


**Figure A3 (continued).** Representative (B)  $^{13}\text{C}$  NMR and (C) COSY spectra of per(2-O-Me)- $\beta$ CD (product **3** in Scheme 1), recorded in MeOD- $d_4$ , at 300 K.

(4) per(2-O-Me-3,6-di-O-Allyl)- $\beta$ CD (product 4 in Scheme 1):

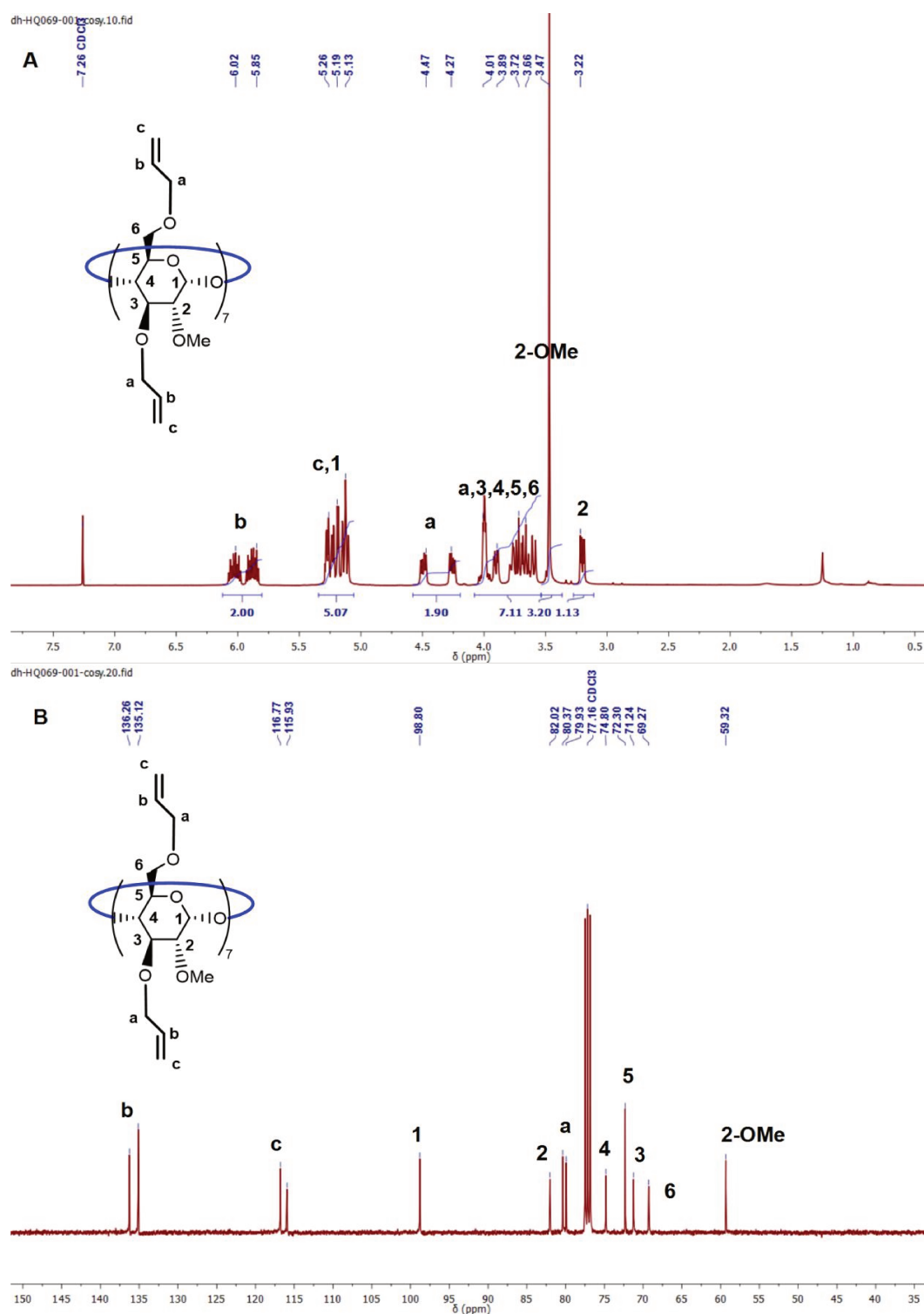


**Figure A4.** Representative (A)  $^1\text{H}$  NMR and (B)  $^{13}\text{C}$  NMR spectra of per(2-O-Me-3,6-di-O-Allyl)- $\beta$ CD (product 4 in Scheme 1), recorded in  $\text{CDCl}_3\text{-d}_1$ , at 300 K.

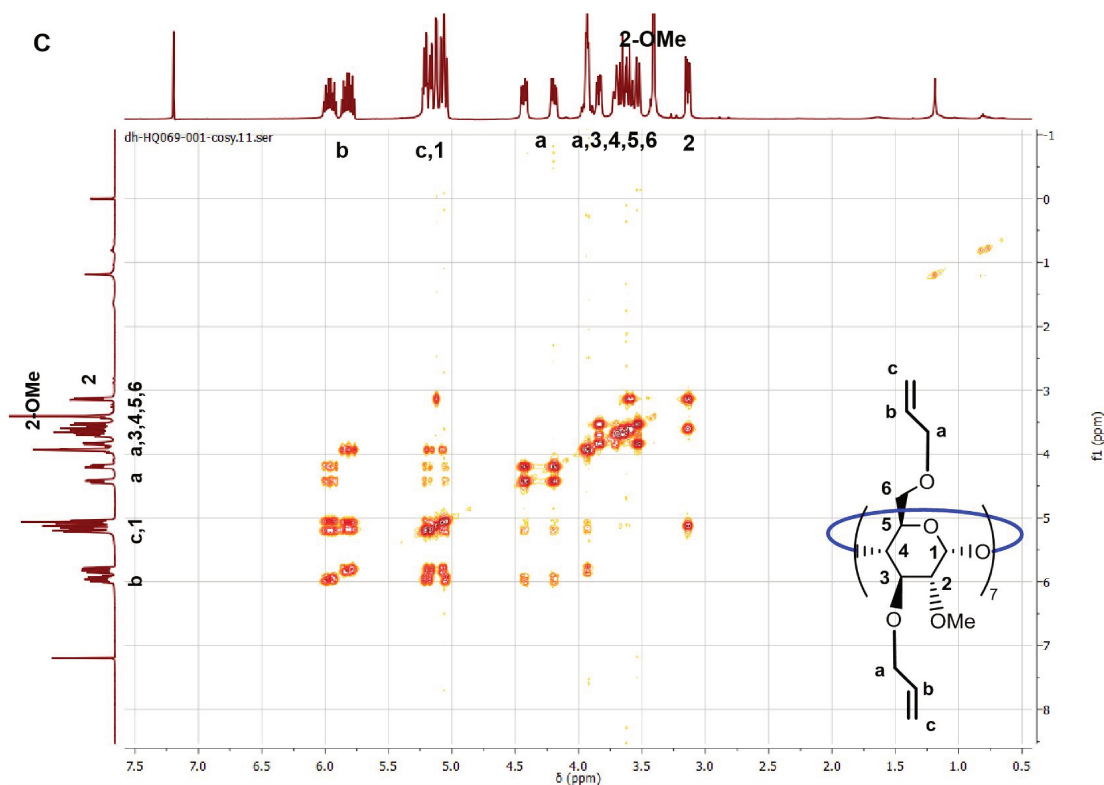


**Figure A4 (continued).** (C) Representative COSY spectra of per(2-O-Me-3,6-di-O-Allyl)- $\beta$ CD (product **4** in Scheme 1), recorded in  $\text{CDCl}_3\text{-d}_1$ , at 300 K.

## 6.2 Estimation of the theoretical formula of star copolymer $\beta\text{CD}-(\text{PBO}_m\text{-PGL}_n)_{14}$

A star copolymer  $\beta\text{CD}-(\text{PBO}_m\text{-PGL}_n)_{14}$  is generally synthesized via three steps, namely, homopolymerization of BO, copolymerization of EEGE, and deprotection to give GL units, in sequence. The reaction mixture is used directly in the next step without purifying the byproducts. In other words, the final product composition is determined by the sequentially obtained intermediates. The synthetic pathway is discussed as followed, step by step.

### Step 1, Homopolymerization of BO

Homopolymerization was conducted with an initial ( $t = 0$ ) feeding (molar) ratio of  $[\text{BO}]_0/[\beta\text{CD}]_0 = M_0/1$  (calculated from feeding masses). At the end ( $t = t_{\text{ho}}$ ), BO conversion is  $p_{\text{BO}}$  (determined by  $^1\text{H}$  NMR). The total equivalent of BO consumed is  $M$ , including  $M_s$  equivalent for star PBO ( $\beta\text{CD}-(\text{PBO}_m)_{14}$ ) and  $M_b$  equivalent for byproduct (HO-PBO-OH, denoted as “Byproduct 1”). Star PBO and Byproduct 1 are well separated by SEC, producing two peaks with the peak areas (RI detector) being  $A_{s,\text{ho}}$  and  $A_{b,\text{ho}}$ , respectively. The subscripts  $s$  and  $b$  respectively denote star-shaped polymer and byproduct, and  $\text{ho}$  means the homopolymerization. The characteristic of

the homopolymerization step is displayed in Table A1 emphasizing on the product compositions of the targeted star polymer and byproduct.

**Table A1.** Homopolymerization of BO with Emphasis on Product Compositions.

	BO		Star PBO <sup>a</sup>		Byproduct 1 <sup>b</sup>		
	<i>Eq.</i> <sub>BO</sub>	<i>Eq.</i> <sub>BO</sub>	<i>Mn</i> <sup>c</sup>	<i>RI Area</i> <sup>d</sup>	<i>Eq.</i> <sub>BO</sub>	<i>Mn</i> <sup>c</sup>	<i>RI Area</i> <sup>d</sup>
$t = 0$	$M_0$	0	0	0	0	0	0
$t = t_{ho}$	$M_0 - M$	$M_s$	$M_s Mr_{BO} + Mr_I$	$A_{s,ho}$	$M_b$	$M_b Mr_{BO}$	$A_{b,ho}$

<sup>a</sup>The formula of star PBO is βCD-(PBO<sub>m</sub>)<sub>14</sub>, with *m* being the number of BO units per arm; <sup>b</sup>The Byproduct 1 is the linear HO-PBO-OH initiated by water; <sup>c</sup>*Mn* is the relative molar mass calculated from the composition.  $Mr_{BO}$  and  $Mr_I$  are the relative molar masses of BO and the initiator; <sup>d</sup>*RI area* is the peak area recorded with an RI detector.

First of all, derived from SEC peak areas, the purity of homopolymerization product ( $f_{ho}$ ), namely the (mass) fraction of the star PBO (βCD-(PBO<sub>m</sub>)<sub>14</sub>), is estimated as

$$f_{ho} \sim \frac{A_{s,ho}}{A_{s,ho} + A_{b,ho}} \quad (A1)$$

by assuming the specific refractive index increments ( $dn/dc$ ) of star PBO and Byproduct 1 are close under the SEC characterization conditions, *i.e.*, in DMF at 60 °C or in THF at 40 °C.

With above assumption, then the formula of the star PBO can be estimated using following relations.

$$M = M_0 \times p_{BO} \quad (A2)$$

$$M = M_s + M_b \quad (A3)$$

$$\frac{A_{s,ho}}{A_{b,ho}} = \frac{Mr_{BO} \times M_s + Mr_I \times 1}{Mr_{BO} \times M_b} \quad (A4)$$

Taking into account above equations, the equivalent of BO in star PBO ( $M_s$ ) can be estimated from the available parameters as:

$$M_s = \frac{Mr_{BO} \times (M_0 \times p_{BO}) \times A_{s,ho} - Mr_I \times 1 \times A_{b,ho}}{Mr_{BO} \times (A_{s,ho} + A_{b,ho})} \quad (A5)$$

and thus, the theoretical value of  $m$  in  $\beta$ CD-(PBO<sub>m</sub>)<sub>14</sub> is

$$m_{\text{theo.}} = \frac{M_s}{14} \quad (\text{A6})$$

## Step 2, Copolymerization of EEGE

Copolymerization is performed with an initial ( $t = 0$ ) feeding (molar) ratio of  $[\text{EEGE}]_0/[\beta\text{CD}]_0 = N_0/1$  (calculated from feeding masses). At the end ( $t = t_{\text{co}}$ ), EEGE conversion is  $p_{\text{EEGE}}$  (determined by  $^1\text{H}$  NMR). The total equivalent of EEGE consumed is  $N$ , including  $N_s$  equivalent for star copolymer ( $\beta\text{CD}-(\text{PBO}_m\text{-PEEGE}_n)_{14}$ ) and  $N_b$  equivalent for byproducts (linear PBO-PEEGE and linear PEEGE, denoted as byproduct 2). Star PBO-PEEGE and byproduct 2 are well separated by SEC producing two peaks with the peak areas being  $A_{s,\text{co}}$  and  $A_{b,\text{co}}$ , respectively. The subscripts  $s$  and  $b$  denote star-shaped product and byproduct, respectively, and  $\text{co}$  means copolymerization. The characteristic of the copolymerization step is displayed in Table A2 with emphasis on the product compositions of the targeted star polymer and byproduct.

**Table A2.** Comopolymerization of EEGE with Emphasis on Product Compositions.

	EEGE		Star PBO-PEEGE <sup>a</sup>			Byproduct 2 <sup>b</sup>			
	<i>Eq.</i> <sub>EEGE</sub>	<i>Eq.</i> <sub>BO</sub>	<i>Eq.</i> <sub>EEGE</sub>	<i>Mn</i> <sup>c</sup>	<i>RI area</i> <sup>d</sup>	<i>Eq.</i> <sub>BO</sub>	<i>Eq.</i> <sub>EEGE</sub>	<i>Mn</i> <sup>c</sup>	<i>RI area</i> <sup>d</sup>
$t = 0$	$N_0$	0	0	0	0	0	0	0	0
$t = t_{\text{co}}$	$N_0 - N$	$M_s$	$N_s$	$M_s M_{\text{rBO}} + N_s M_{\text{rEEGE}} + M_{\text{rI}}$	$A_{s,\text{co}}$	$M_b$	$N_b$	$M_b M_{\text{rBO}} + N_b M_{\text{rEEGE}}$	$A_{b,\text{co}}$

<sup>a</sup>The formula of star PBO-PEEGE is  $\beta\text{CD}-(\text{PBO}_m\text{-PEEGE}_n)_{14}$ , with  $m$  and  $n$  being respectively the numbers of BO and EEGE units per arm; <sup>b</sup>Byproduct 2 is the mixture of linear PBO-PEEGE and PEEGE; <sup>c</sup> $Mn$  is the relative molar mass calculated from the composition.  $M_{\text{rBO}}$ ,  $M_{\text{rEEGE}}$  and  $M_{\text{rI}}$  are the relative molar masses of BO, EEGE and the initiator; <sup>d</sup> $RI$  area is the peak area recorded with an RI detector.

The fraction of the star copolymer  $\beta\text{CD}-(\text{PBO}_m\text{-PEEGE}_n)_{14}$  ( $f_{\text{co}}$ ) is estimated as

$$f_{\text{co}} = \frac{A_{s,\text{co}}}{A_{s,\text{co}} + A_{b,\text{co}}} \quad (\text{A7})$$

by assuming the  $dn/dc$  values of star copolymer and the byproducts (taken as a whole) are close under the SEC characterization conditions, *i.e.*, in DMF at 60 °C or in THF at 40 °C.

With this assumption, the formula of βCD-(PBO<sub>m</sub>-PEEGE<sub>n</sub>)<sub>14</sub> can be estimated using the following relations:

$$N = N_0 \times p_{\text{EEGE}} \quad (\text{A8})$$

$$N = N_s + N_b \quad (\text{A9})$$

$$\frac{A_{s,\text{co}}}{A_{b,\text{co}}} = \frac{Mr_{\text{BO}} \times M_s + Mr_{\text{EEGE}} \times N_s + Mr_1 \times 1}{Mr_{\text{BO}} \times M_b + Mr_{\text{EEGE}} \times N_b} \quad (\text{A10})$$

Based on above relations, the equivalent of EEGE in star PBO-PGL copolymer can be estimated from the available values as:

$$N_s = \frac{Mr_{\text{BO}} \times (M_b \times A_{s,\text{co}} - M_s \times A_{b,\text{co}}) + Mr_{\text{EEGE}} \times (N_0 \times p_{\text{EEGE}}) \times A_{s,\text{co}} - Mr_1 \times 1 \times A_{b,\text{co}}}{Mr_{\text{EEGE}} \times (A_{s,\text{co}} + A_{b,\text{co}})}$$

(A11)

in which,  $M_s$  and  $M_b$  are available from the Equations A2, A3 and A5.

Thus, the theoretical value of  $n$  in βCD-(PBO<sub>m</sub>-PEEGE<sub>n</sub>)<sub>14</sub> is

$$n_{\text{theo.}} = \frac{N_s}{14} \quad (\text{A12})$$

### Step 3, Deprotection to give GL units

The copolymerization product obtained in step 2, consisting of both star-shaped PBO-PEEGE and byproducts, is treated in acidic conditions to get the PGL blocks. It proved that the acidic deprotection conditions are mild and the polyether backbone of the arms as well as the initiator are intact. Therefore, the theoretical values of  $m$  and  $n$  in βCD-(PBO<sub>m</sub>-PGL<sub>n</sub>)<sub>14</sub> are taken same as the ones in βCD-(PBO<sub>m</sub>-PEEGE<sub>n</sub>)<sub>14</sub>.

Moreover, star PBO-PGL ((βCD-(PBO<sub>m</sub>-PGL<sub>n</sub>)<sub>14</sub>) and the byproducts (Byproduct 3) are well separated by SEC producing two peaks with the peak areas respectively being  $A_s$  and  $A_b$ . The subscripts  $s$  and  $b$  denote star-shaped product and byproduct, respectively. The characteristics of the deprotected product were listed in Table A3 emphasizing the product compositions of the targeted star polymer and byproduct.

**Table A3.** Characteristics of Deprotected Product with Emphasis on Product Compositions.

Star PBO-PGL <sup>a</sup>			Byproduct 3 <sup>b</sup>				
<i>Eq.</i> BO	<i>Eq.</i> GL	<i>Mn</i> <sup>c</sup>	RI area <sup>d</sup>	<i>Eq.</i> BO	<i>Eq.</i> GL	<i>Mn</i> <sup>c</sup>	RI area <sup>d</sup>
$M_s$	$N_s$	$M_s M_{r_{BO}} + N_s M_{r_{GL}} + M_{r_I}$	$A_s$	$M_b$	$N_b$	$M_b M_{r_{BO}} + N_b M_{r_{GL}}$	$A_b$

<sup>a</sup>The formula of star PBO-PGL is  $\beta$ CD-(PBO<sub>m</sub>-PGL<sub>n</sub>)<sub>14</sub>, with *m* and *n* being respectively the numbers of BO and GL units per arm; <sup>b</sup>Byproduct 3 is the mixture of linear PBO-PGL and PGL; <sup>c</sup>*Mn* is the relative molar mass calculated from the composition.  $M_{r_{BO}}$ ,  $M_{r_{GL}}$ , and  $M_{r_I}$  are the relative molar masses of BO, GL and the initiator; <sup>d</sup>RI area is the peak area recorded with an RI detector.

The (mass) fraction of  $\beta$ CD-(PBO<sub>m</sub>-PGL<sub>n</sub>)<sub>14</sub> (*f*) is estimated as

$$f = \frac{A_s}{A_s + A_b} \quad (\text{A13})$$

by assuming again the *dn/dc* values of star PBO-PGL and hydroducts (taking as a whole) are close under the SEC characterization conditions, *i.e.*, in DMF at 60 °C or in THF at 40 °C.



**Chapter 4.**  
**Polymersome Membrane Permeability to H<sup>+</sup>**

## Content

<b>1. Introduction.....</b>	<b>183</b>
<b>2. Materials and Methods.....</b>	<b>185</b>
2.1 Materials and instruments.....	185
2.2 Preparation of the HPTS-encapsulated polymersomes (HPTS-pos).....	186
2.3 Encapsulation efficiency (EE) of HPTS.....	187
2.4 Determination of the interior pH value of polymersomes.....	189
2.5 Investigation on the polymersome membrane permeability to H <sup>+</sup> .....	190
<b>3. Results and Discussions.....</b>	<b>191</b>
3.1 Validation of the experimental procedure for the preparation of HPTS-encapsulated polymersomes (HPTS-pos).....	191
3.2 Determination of the encapsulation efficiency (EE) of HPTS in polymersomes.....	193
3.3 Determination of the interior pH value of polymersomes.....	199
3.3 Polymersome membrane permeability to H <sup>+</sup> .....	202
3.3.1 Validation of the investigation protocol.....	202
3.3.2 Determination of the permeability of all the polymersomes to H <sup>+</sup> .....	207
<b>4. Conclusions.....</b>	<b>212</b>
<b>5. References.....</b>	<b>212</b>

## 1. Introduction

As stated in Chapters 2 and 3, both the linear and star amphiphilic block copolymers, composed of hydrophobic PBO and hydrophilic PGL blocks, could self-assemble into different morphologies, including spherical micelles and polymersomes, depicted by the hydrophilic-to-hydrophobic ratio.

Polymersomes are especially attractive for their unique structures and great potentials in biotechnological applications [1–3]. Polymersomes are featured by an aqueous interior enclosed by the hydrophobic membrane, which is further stabilized by the outer hydrophilic corona, and thus they can load both hydrophilic molecules (inside the aqueous interior) and hydrophobic molecules (in the membrane). This feature is very attractive to serve as drug delivery nanosystems [4]. Instead of drugs, enzymes have been loaded, turning polymersomes into nanoreactors [5]. Compared with free enzymes, the enzymes in polymersome compartments are protected from external harmful environments. The strategy of compartmentalization also makes enzymatic reactions more effective profiting from the confinement effect [6]. Additionally, polymersome compartments are usually more stable and robust due to the entanglements of polymer chains producing thicker membrane and can be tailor-made with diversity of characteristics (*e.g.*, stimuli-responsiveness), in comparison to liposome compartments, another type of compartments has been widely studied [7,8]. Therefore, the enzyme-loaded polymersomes, namely, polymersome nanoreactors are promising nanosystems to study the reactions occurring in the organism [9] and to replace the dysfunctional organelles when they are further functionalized as artificial organelles [10].

Obviously, membrane permeability is an important consideration for polymersome nanoreactors. Typically, enzymes are encapsulated in the aqueous interior of polymersomes. Therefore, polymersome membrane is required to be permeable to the substrates to trigger reaction, at the same time, to be able to retain enzymes inside.

Herein the permeability to proton (H<sup>+</sup>) was particularly of interest because H<sup>+</sup> involves in many biochemical reactions and the ability to form and maintain pH gradient is essential for the function of a variety of cellular and organellar membranes, such as the lysosome membrane and the mitochondrial inner membrane [11]. In the cases of biomimetic membranes, the transmembrane pH gradient has been exploited to improve the loading efficiency of ionizable anticancer drugs into both liposomes and polymersomes [12,13]. A pH gradient across polymersome membrane was also constructed to facilitate the hydrolysis of fluorescein diacetate inside the confined polymersome interior (a basic environment) [14].

The membrane permeability to H<sup>+</sup>/OH<sup>-</sup> has been extensively studied in the last decades, with lipid bilayers. However, the reported values varied a lot, with orders-

of-magnitude variability [15]. The mechanism of  $H^+/OH^-$  permeation is also incompletely resolved with several models [16]. Additionally, the studies of polymersome membrane permeability to  $H^+/OH^-$  were much less reported although there are many advantages of polymeric membranes over lipid bilayers as mentioned above.

It is generally thought that polymersome membranes are less permeable than lipid bilayers due to the high-molar-mass constituents of polymersome membranes [17,18]. For instance, the polymersome membrane made of polystyrene (PS) was highly impermeable due to the high glass transition temperature ( $T_g$ ) of PS. The membrane permeability was thus tuned by adding dioxane to the external solution [19]. In another work on the membrane permeability to  $OH^-$  of poly(ethylene glycol)-*block*-polybutadiene (PEG-PB) polymersomes, the results showed that the relatively flexible PB membrane was more permeable than the solid-like PS membrane but less permeable than lipid bilayers [14], demonstrating the chemical nature of the membrane-forming segment greatly influence the membrane permeability. Additionally, the results also indicated that the membrane permeability could be tuned via the variation in the membrane thickness which can be achieved by changing the length of PB segment [14].

Therefore, in this part, we will study the membrane permeability to  $H^+$  of the polymersomes made from linear copolymers (PGL-PBO-PGL) or star copolymers ( $\beta$ CD-(PBO-PGL)<sub>14</sub>), aiming to probe the relation between membrane permeability and membrane thickness in the context of PBO membrane, as well as the effect of the introduction of  $\beta$ CD cavities on the PBO membrane permeability. To this end, the fluorescent probe, 8-hydroxypyrene-1,3,6-trisulfonic acid trisodium salt (HPTS) is used as a pH indicator. HPTS has been widely used to determine both the interior and external pH values of liposomes and polymersomes due to the merits, such as, it has a good solubility in water (300 mg mL<sup>-1</sup>, at 25 °C), and the ratiometric assays by fluorescence spectroscopy offer good accuracy [14,19].

In the present work, HPTS probes were first encapsulated into polymersomes via thin-film rehydration method. The encapsulation efficiency (EE) of HPTS was calculated by fluorospectrometry after the un-encapsulated probes were removed via dialysis. The effects of polymer composition, polymer architecture, and the thickness of polymersome membrane on EE were studied. Subsequently, the resultant fluorescent polymersomes, with HPTS probes being exclusively encapsulated in the interior, were used to study the membrane permeability to  $H^+$  with HPTS as the pH indicator of the interior aqueous solution. In order to figure out the influence of membrane thickness on the membrane permeability, a library of triblock copolymers with varied lengths of PBO block was systematically studied. At the same time,  $\beta$ CD-

cored star copolymers were studied to probe the effect of  $\beta$ CD cavities on membrane permeability.

## 2. Materials and Methods

### 2.1 Materials and instruments

The amphiphilic copolymers for preparation of polymersomes include linear triblock copolymers, PGL<sub>n</sub>-PBO<sub>2m</sub>-PGL<sub>n</sub>, and  $\beta$ CD-cored star block copolymers,  $\beta$ CD-(PBO<sub>m</sub>-PGL<sub>n</sub>)<sub>14</sub>, which were synthesized via ring-opening copolymerization and well characterized as previously detailed in Chapter 2 and Chapter 3, respectively. The main characteristics of the copolymers and the respective polymersomes were listed in Table 1.

**Table 1.** Characteristics of the Amphiphilic Copolymers and the Respective Self-assembled Polymersomes According to the Weight Fraction of PGL Blocks ( $w_{\text{PGL}}$ ).

Entry	Amphiphilic Copolymers <sup>a</sup>			Polymersomes <sup>b</sup>	
	Formula	<i>M</i> <sub>n</sub> (kg mol <sup>-1</sup> )	$w_{\text{PGL}}$	<i>R</i> <sub>H</sub> (nm)	PDI
<b>Linear Copolymers</b>					
HQ033	PGL <sub>12</sub> -PBO <sub>84</sub> -PGL <sub>12</sub>	8.0	0.22	124	0.12
HQ031	PGL <sub>6</sub> -PBO <sub>40</sub> -PGL <sub>6</sub>	3.9	0.23	109	0.10
HQ081B	PGL <sub>21</sub> -PBO <sub>84</sub> -PGL <sub>21</sub>	9.2	0.33	111	0.18
HQ034	PGL <sub>6</sub> -PBO <sub>20</sub> -PGL <sub>6</sub>	2.4	0.35	88	0.21
HQ119B	PGL <sub>18</sub> -PBO <sub>62</sub> -PGL <sub>18</sub>	7.3	0.37	133	0.20
HQ077	PGL <sub>25</sub> -PBO <sub>80</sub> -PGL <sub>25</sub>	9.6	0.39	90	0.08
<b>Star Copolymers</b>					
HQ107	$\beta$ CD-(PBO <sub>22</sub> -PGL <sub>7</sub> ) <sub>14</sub>	31.2	0.23	111	0.10
HQ151	$\beta$ CD-(PBO <sub>13</sub> -PGL <sub>6</sub> ) <sub>14</sub>	21.4	0.28	90	0.10
HQ137	$\beta$ CD-(PBO <sub>7</sub> -PGL <sub>5</sub> ) <sub>14</sub>	13.9	0.35	84	0.16

<sup>a</sup>The formula, molar mass (*M*<sub>n</sub>) and the weight fraction of PGL blocks ( $w_{\text{PGL}}$ ) were reported as the theoretical values. <sup>b</sup>The radius (*R*<sub>H</sub>) and polydispersity index (PDI) of the self-assemblies were measured by DLS. Details of the characterizations and calculations were described in Chapter 2 for the linear copolymers and in Chapter 3 for the star copolymers.

The buffering solutions include phosphate-buffered saline solution (PBS) and a series of phosphate buffering solutions (PB) of varied pH values. PBS was prepared by dissolving 8.00 g of NaCl (VWR), 1.44 g of Na<sub>2</sub>HPO<sub>4</sub> (Sigma–Aldrich), 200 mg of

KCl (Sigma–Aldrich), and 245 mg of  $\text{KH}_2\text{PO}_4$  (Sigma–Aldrich) into 1 L of DI  $\text{H}_2\text{O}$ . The series of PB solutions of varied pH values was prepared by adjusting the pH value of a 25 mM  $\text{NaH}_2\text{PO}_4$  (Sigma–Aldrich) solution with 1 M NaOH (Sigma–Aldrich) solution or 0.5 M  $\text{H}_3\text{PO}_4$  (Sigma–Aldrich) solution to the desired pH values. The chemicals were used as received.

Other chemicals include 8-hydroxypyrene-1,3,6-trisulfonic acid trisodium salt (HPTS, Sigma–Aldrich, 99%) and MeOH (VWR). Both were used as received.

Dynamic light scattering (DLS) data were acquired on a ZetaSizer Nano ZS90 (Malvern) at 20 °C and analyzed with the Zetasizer software. The details of data analyses refer to Chapters 2 and 3. pH values of the solutions were measured using a Mettler Toledo pH meter at room temperature (r.t.). Fluorescence data were recorded on a Cary Eclipse fluorophotometer at r.t. and analyzed using the OriginPro 8 software.

## **2.2 Preparation of the HPTS-encapsulated polymersomes (HPTS-pos)**

The fluorescent polymersomes with HPTS being exclusively encapsulated inside, named HPTS-pos, were prepared by thin-film rehydration method [14,20]. Typically, 10.0 mg of polymer was first dissolved in 4 mL of MeOH. Then, MeOH was removed by rotavapor (5 mbar, 40 °C, 30 min) to get the thin polymer film sited on the inner wall of a glass vial. The film was subsequently rehydrated with 10.0 mL of HPTS solution (0.2 mg  $\text{mL}^{-1}$  in PBS). The mixture was stirred at r.t. allowing the film to detach from the inner wall and to be suspended homogeneously. The rehydrated mixture was repeatedly extruded through a 0.45  $\mu\text{m}$  PTFE syringe filter repeatedly (in one direction), for 10 times typically, so as to remove dusts and/or ill-aggregates and to get the homogeneous suspension of unilamellar polymersomes [21]. The homogeneity of the extruded suspension was checked by DLS with the presence of a unimodal intensity particle size distribution (PSD) curve.

Afterwards, the extruded suspension was dialyzed against PBS with a regenerated cellulose (RC) membrane (MWCO 3.5 kDa, Spectrum Laboratories, Inc.). In a dialysis process, the dialysis reservoir (1 L) was changed several times until the unencapsulated HPTS probes were totally removed, typically 4 times, which was assayed by fluorophotometer as no HPTS signal in the final dialysis reservoir. At the end, the dialysis retention solution, namely the suspension solution of the HPTS-pos, was collected and used for the following investigations.

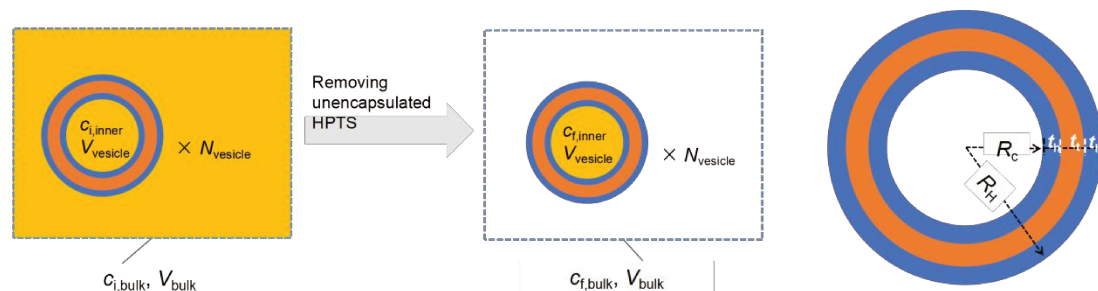
### 2.3 Encapsulation efficiency (EE) of HPTS

Considering that the loss of samples in the preparation of HPTS-pos is negligible and there is no dilution on the solution during dialysis, therefore, the encapsulation efficiency (EE) is defined as the concentration ratio of the HPTS in the finally dialyzed HPTS-pos suspension ( $c_{f,bulk}$ ) to the one in the feeding solution initially used to rehydrate the film ( $c_{i,bulk}$ ), shown as the following equation:

$$EE = \frac{c_{f,bulk}}{c_{i,bulk}} \quad (1)$$

wherein, the subscripts  $i$  and  $f$  denote the *initial* and *final* concentrations, respectively, while *bulk* denotes the total *bulk* solution. To make it clearer, the concentrations are graphically illustrated in Scheme 1.

**Scheme 1.** (Left) Graphic Illustrations of the Initial and Final Concentrations in Bulk Solution ( $c_{bulk}$ ) and Polymersome Interior ( $c_{inner}$ ). (Right) Structural Parameters of a Polymersome.



The value of  $c_{i,bulk}$  is an experimental value as the HPTS concentration of the solution used to hydrate the polymer film, and the value of  $c_{f,bulk}$  could be determined, with the aid of a concentration calibration curve, using the following protocol.

First, a concentration calibration curve was built. Herein, to avoid inner filter effect, the calibration curve was constructed in a concentration range where the fluorescence intensity increased linearly with concentration. Typically, a set of working solutions of varied concentrations varying from 0.25 to 2.5  $\mu\text{g mL}^{-1}$  was first prepared by diluting a stock HPTS solution (1.0  $\text{mg mL}^{-1}$  in PBS). Then 0.3 mL of the working solution mixed with 0.7 mL of H<sub>2</sub>O and 2.0 mL of MeOH. The mixture was applied to the fluorophotometer to record the fluorescence excitation spectrum with the emission wavelength ( $\lambda_{em}$ ) as 509 nm, with both the ex-slit and em slit as 5 nm, at r.t. Each sample was recorded 5 times. The average values of the fluorescence intensity

at 402 nm ( $I_{402}$ ) and the concentrations ( $c$ ) of the recording samples were fitted into a linear relation to give the concentration calibration curve.

Then, the value of  $c_{f,bulk}$  was determined with the aid of the calibration curve: 0.3 mL of the HPTS-pos suspension mixed with 0.7 mL of H<sub>2</sub>O and 2.0 mL of MeOH to disassemble the polymersomes and release the probes. The fluorescence excitation spectrum of the mixture was recorded 5 times under the same conditions as those used to construct the calibration curve. The average value of  $I_{402}$  was substituted into the calibration curve to give the HPTS concentration in the disassembled polymersome solution ( $c_{dis}$ ). Then, the concentration in the HPTS-pos suspension ( $c_{f,bulk}$ ) was determined as  $c_{f,bulk} = 10 \times c_{dis}$ .

To note that  $c_{f,bulk}$  is the HPTS concentration of the total bulk HPTS-pos suspension, while the HPTS concentration in the vesicular interiors ( $c_{f,inner}$ , Scheme 1) was calculated using following equations.

$$c_{f,inner} = \frac{c_{f,bulk} V_{bulk}}{V_{inner}} \quad (2)$$

wherein,  $V_{bulk}$  is the bulk volume of the HPTS-pos suspension.  $V_{inner}$  is the total inner volume enclosed by all the polymersomes, calculated as

$$V_{inner} = N_{vesicles} V_{vesicle} \quad (3)$$

wherein,  $N_{vesicles}$  is the number of polymersomes (Scheme 1), calculated on the basis of the molecular weight of the nanoparticles ( $MW_{NPs}$ ) which is derived from the Debye plot acquired by SLS, as

$$N_{vesicles} = \frac{m_{polymer}}{MW_{NPs}} N_A \quad (4)$$

And,  $V_{vesicle}$  in Equation 3 is the inner volume per polymersome (Scheme 1) estimated using the following equations:

$$V_{vesicle} = \frac{4}{3} \pi R_c^3 \quad (5)$$

$$R_c = R_H - t_t - 2t_h \quad (6)$$

wherein  $R_H$  is the hydrodynamic radius measured by DLS,  $t_t$  and  $t_h$  are respectively the thicknesses of PBO layer and PGL layer determined by SAXS fitting, as illustrated in the right panel of Scheme 1.

Moreover, the percentage of the total inner volume enclosed by the vesicles ( $\%V_{\text{inner}}$ ) was calculated, using the following equation:

$$\%V_{\text{inner}} = \frac{V_{\text{inner}}}{V_{\text{bulk}}} \times 100 \quad (7)$$

$\%V_{\text{inner}}$  was an interesting parameter to check because this value is thought to define the upper limit of the encapsulation efficiency under specific conditions [21].

## 2.4 Determination of the interior pH value of polymersomes

The interior pH value of the polymersomes was determined by fluorospectrometry via the following protocol with the aid of a pH calibration curve.

First, the pH calibration curve was constructed using the following protocol: a set of working solutions was prepared by diluting a stock solution of HPTS (1.0 mg mL<sup>-1</sup> in H<sub>2</sub>O) to a constant concentration (*e.g.*, 1.0 µg mL<sup>-1</sup>) with the PB solutions of varied pH values. The pH values of the working solutions were measured by the electronic pH meter, and then the fluorescence excitation spectra were recorded at r.t. with  $\lambda_{\text{em}}$  as 509 nm, with both the ex-slit and em slit as 2.5 nm. Each spectrum was recorded 5 times. Derived from the spectra, the ratios of the intensity at 455 nm ( $I_{455}$ ) to the one at 402 nm ( $I_{402}$ ), *i.e.*,  $I_{455}/I_{402}$  were calculated. At last, the pH calibration curve was produced by fitting the measured pH values and the intensity ratios of  $I_{455}/I_{402}$  into the Henderson–Hasselbalch relation (Equation 8) [14,19].

$$pH = \frac{A3 - \log\left(\frac{A2 - r}{r - A1}\right)}{A4} \quad (8)$$

wherein,  $r$  is the ratio of  $I_{455}/I_{402}$ . pH is the pH value measured by the electronic pH meter. The constants  $A1$ ,  $A2$ ,  $A3$ , and  $A4$  are the fitting parameters using the OriginPro8 software.

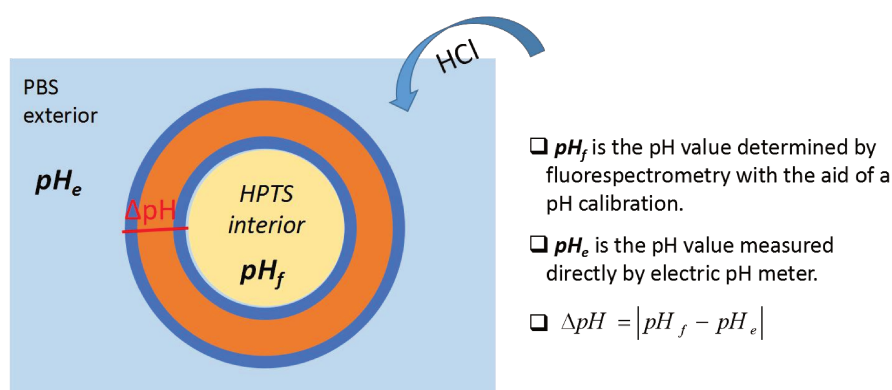
Then, the interior pH value of the polymersomes was determined via the pH calibration curve: the excitation spectrum of the HPTS-pos suspension was recorded 5 times under the same conditions as those in the construction of the pH calibration curve. The average value of  $I_{455}/I_{402}$  was calculated and substituted into the calibration curve, giving the interior pH of the polymersomes, denoted as pH<sub>f</sub>, considering it was determined by fluorospectrometry.

At the meantime, the exterior pH value of the polymersomes was measured by the electronic pH meter of the bulk HPTS-pos suspension, and thus denoted as pH<sub>e</sub>.

## 2.5 Investigation on the polymersome membrane permeability to H<sup>+</sup>

The investigation was conducted following a published method [14] with minor modifications. The principle is to create an initial pH gradient across the polymersome membrane by adding a HCl solution into the bulk HPTS-pos suspension, namely the outside of the polymersomes, as illustrated in Scheme 2. When H<sup>+</sup> permeates the membrane, the interior pH value decreases. The decrease of the interior pH can be observed, when the excitation spectrum of HPTS-pos is recorded continuously by the fluorophotometer.

**Scheme 2.** Scheme of the Investigation on Polymersome Membrane Permeability to H<sup>+</sup>.



Specifically, the initial pH value of the HPTS-pos suspension was measured by pH meter (initial  $pH_e$ ). Then 2.5 mL of the HPTS-pos suspension was charged into a quartz cell ( $1 \text{ cm}^2 \times 4 \text{ cm}$ ). The fluorescence excitation spectrum of the solution was continuously recorded for 10 minutes with a time interval of 0.5 minutes, which gave the initial pH value of the polymersome interiors (initial  $pH_f$ ). Subsequently, 10  $\mu\text{L}$  of HCl (1 M) was dropped into the suspension. At steady state (without stirring), the excitation spectrum of the mixture was immediately recorded, and the recording lasted for 2 hours with an interval of 0.5 minutes. This would produce a curve depicting the change of the interior pH value ( $pH_f$ ) with time. After the recording, the mixture in the cuvette was mixed by pipette sufficiently, and then the spectrum was recorded again for 10 minutes with an interval of 0.5 minutes, which gave the final interior pH value (final  $pH_f$ ). After finishing the spectra recordings, the pH value of the final mixture was measured again by electronic pH meter (final  $pH_e$ ). In this procedure, the interior pH values ( $pH_f$ ) were calculated with the aid of the pH calibration curve.

The control experiment was performed sequentially, using a HPTS solution having the same concentration as the one of the HPTS-pos ( $c_{f,\text{bulk}}$ ) so as to minimize the possible influences of HPTS concentration and experimental temperature on the results.

### 3. Results and Discussions

#### 3.1 Validation of the experimental procedure for the preparation of HPTS-encapsulated polymersomes (HPTS-pos)

HPTS probes were encapsulated in the aqueous interior of the polymersomes by thin-film rehydration method, *i.e.*, the polymer film being rehydrated by a HPTS solution.

First, the possible effects of suspension media and feeding concentration of HPTS ( $c_{i,bulk}$ ) on the particle size and distribution of polymersomes were assayed in the case for example of the polymersomes made from PGL<sub>12</sub>-PBO<sub>84</sub>-PGL<sub>12</sub> (polymer Entry HQ033). A set of polymersomes suspending in DI H<sub>2</sub>O or PBS was prepared by rehydrating the polymer film with the HPTS solutions of various  $c_{i,bulk}$  values. The sizes ( $R_H$ ) and polydispersity indexes (PDI) of the polymersomes (without dialysis) were characterized by DLS, and the values were listed in Table 2.

**Table 2.** DLS Data of the Polymersomes Prepared under Various HPTS Feeding Concentrations<sup>a</sup> in DI water or PBS.

Entry	$c_{i,bulk}^a$ ( $\mu\text{g mL}^{-1}$ )	$R_H^b$ (nm)	PDI <sup>b</sup>
<b>In DI H<sub>2</sub>O</b>			
033-Blank1	0	137	0.11
033-3	10	142	0.13
<b>In PBS</b>			
033-Blank2	0	124	0.12
033-5	2	128	0.10
033-6	160	149	0.12
033-7	1000	127	0.12

<sup>a</sup>The polymersomes were prepared by hydrating the polymer film of PGL<sub>12</sub>-PBO<sub>84</sub>-PGL<sub>12</sub> (Polymer Entry HQ033) with HPTS solution of various concentrations ( $c_{i,bulk}$ ); <sup>b</sup> $R_H$  and PDI were respectively the radius and the polydispersity index of the particles, reported as the average value of 5 measurements by DLS at 20 °C.

One can see that neither the feeding concentration ( $c_{i,bulk}$ ) nor the suspension media (DI H<sub>2</sub>O or PBS) had an influence on the particle size and particle distribution. This is reasonable since HPTS has a very good aqueous solubility and the polymer solutions studied herein were rather dilute. The results were also consistent with other reports [19,22].

Subsequently, the mixture of HPTS probes and polymersomes were dialysed so as to remove the unencapsulated HPTS probes without diluting the sample. First, the dialysis conditions were optimized using the HPTS solutions only. The HPTS solution (10 mL),  $10 \mu\text{g mL}^{-1}$  in  $\text{H}_2\text{O}$  or  $2 \mu\text{g mL}^{-1}$  in PBS, was dialysed against  $\text{H}_2\text{O}$  or PBS (1 L) using a cellulose ester dialysis tubing (CE membrane, MWCO 3.5 kDa) or a regenerated cellulose dialysis membrane (RC membrane, MWCO 3.5 kDa). During dialysis, the dialysis reservoir was changed every 24 hours, for three times, and at last for 72 hours. At the end of each dialysis period (four periods in total), the dialysis reservoir was characterized by fluorophotometer to check the presence of the HPTS probes. The spectra of the four dialysis reservoirs collected in a dialysis process were displayed in Figure 1.

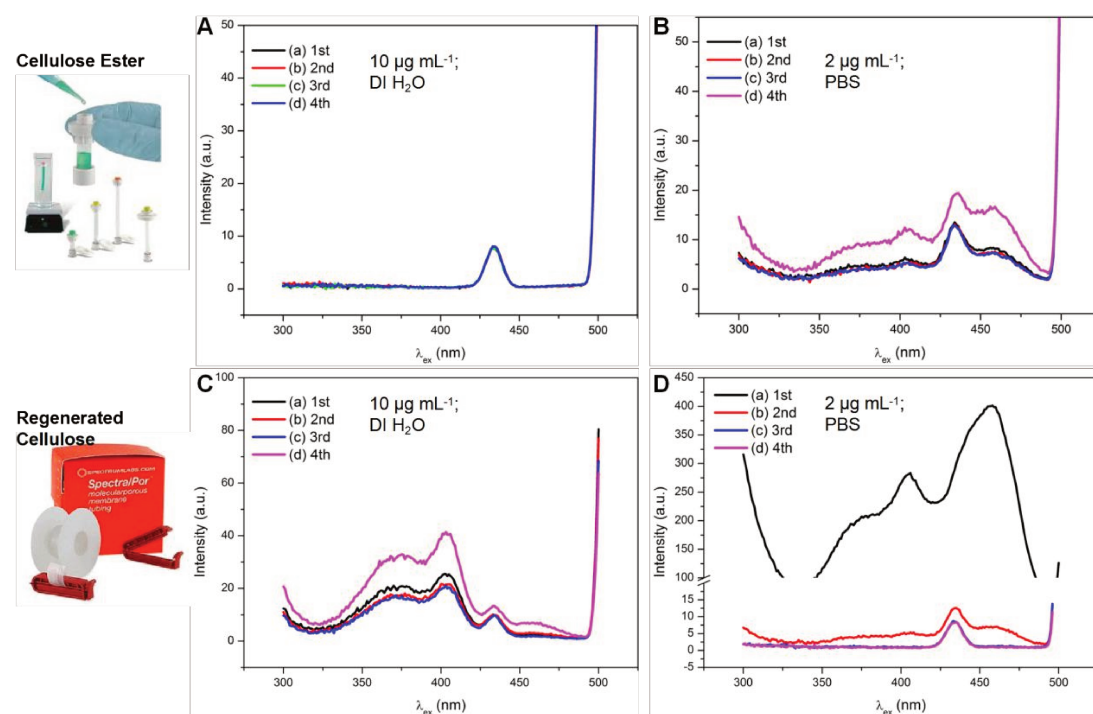


**Figure 1.** Fluorescence excitation spectra of the dialysis reservoirs collected at the end of each dialysis period in a dialysis process performed under different conditions: (A) CE membrane, DI  $\text{H}_2\text{O}$ ; (B) CE membrane, PBS; (C) RC membrane, DI  $\text{H}_2\text{O}$ ; and (D) RC membrane, PBS. Dialysis reservoir was changed every 24 h three times, and at last 72 h. Spectra were recorded at r.t. with  $\lambda_{\text{em}}$  as 509 nm, with ex-slit and em-slit as 10 nm.

As a reminder, the molar mass of HPTS is  $524 \text{ g mol}^{-1}$ , and the molecular weight cut-off (MWCO) of the dialysis membranes used herein both are 3.5 kDa, adequately larger than the molar mass of HPTS. However, it was surprising to find out that using the cellulose ester (CE) membrane, HPTS probes were not removed at all in the DI

H<sub>2</sub>O condition (Figure 1A) and only a few were removed in the PBS condition (Figure 1B). On the contrary, with the regenerated cellulose (RC) membrane, more HPTS probes were removed in DI H<sub>2</sub>O condition (Figure 1C) comparing to CE membrane (Figure 1A), and all the probes were successfully removed in PBS condition (Figure 1D).

These unexpected results were further checked by the retention ratio, which was defined as the ratio of the HPTS concentration of the retention solution inside the dialysis membrane to the HPTS feeding concentration. It was found that, with the CE membrane, the retention ratio was 99% in water condition and 90% in PBS condition, in agreement with the low signals in the dialysis reservoirs respectively shown in Figure 1A and 1B. On the other hand, with the RC membrane, the retention ratio was 0.09% in PBS condition, consistent with the results shown in Figure 1D. But the retention ratio was still 101% in water condition, contrary to the results displayed in Figure 1C. The abnormal value might arise from the operative difficulties: some of the HPTS-pos suspension was left at the heading of the membrane which part did not immerse in the dialysis reservoir and in consequence the HPTS-pos was not actually purified. However, this part was not specially removed and thus was counted in the calculation of the retention ratio. Attention should be paid in the experimental process when the RC dialysis membrane was applied.

In short, the results indicated that among the four conditions, only the one where RC membrane was used in PBS condition allowed to remove efficiently the HPTS probes. The reasons for the three other inefficient dialyses were unclear. It was guessed that, first, regarding the influence of media, the significantly different dialysis efficiency originated from the instinct of HPTS molecules that HPTS can exchange protons with water [23,24], while PBS provided a buffering surrounding to suppress this kind of negative effects [25]; and then, in terms of the influence of dialysis membrane, the different results were ascribed to the hydrophobic CE membrane which might prevent the negatively charged HPTS molecules to go across. This was avoided in the case of the hydrophilic RC membrane.

Even though the interactions involved during the dialysis process were unclear, an effective dialysis protocol (RC membrane, in PBS condition) was found and thus it was adopted to prepare the polymersomes with HPTS encapsulated inside (HPTS-pos) in the following section.

### **3.2 Determination of the encapsulation efficiency (EE) of HPTS in polymersomes**

To prepare the HPTS-pos suspensions without unencapsulated probes, the aforementioned dialysis protocol was adopted, and the dialysis reservoirs were

intensively checked so as to confirm the completion of the dialysis process. For the example of Entry 081B-7, the polymer film of PGL<sub>21</sub>-PBO<sub>84</sub>-PGL<sub>21</sub> (polymer Entry HQ081B) was hydrated with the HPTS solution (0.2 mg mL<sup>-1</sup> in PBS), after extrusions, the suspension was dialyzed against PBS. The dialysis reservoir was changed four times, respectively after 6 h, 18 h, 24 h, 48 h, and at last the dialysis period (the 5<sup>th</sup>) was performed for 48 h. At the end of each dialysis period, the dialysis reservoir was characterized by fluorophotometer to detect the HPTS probes, as shown in Figure 2.

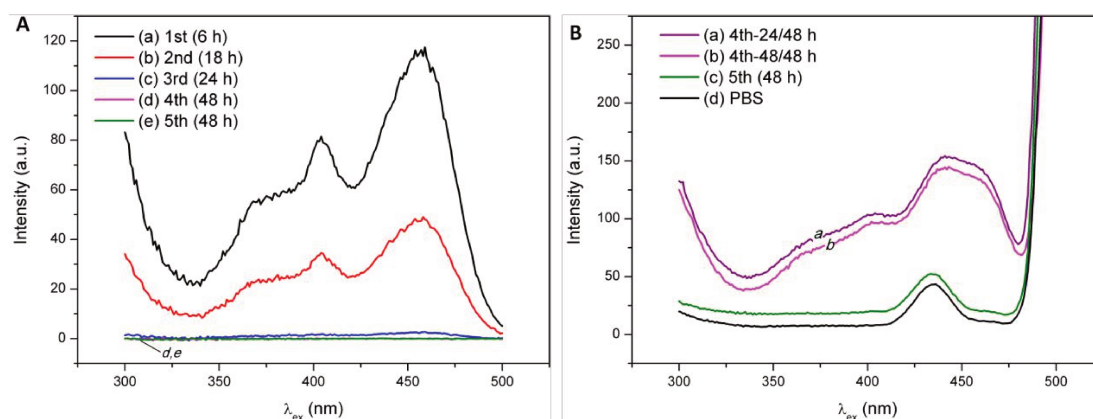


**Figure 2.** (A) Fluorescence excitation spectra of the dialysis reservoirs collected at the end of each dialysis period, recorded with both the ex slit and em slit as 2.5 nm. (B) Fluorescence excitation spectra of the dialysis reservoirs collected (a) at 24 h and (b) 48 h in the 4<sup>th</sup> dialysis period and (c) at the end of the 5<sup>th</sup> dialysis period (48 h), as well as (d) the spectrum of PBS solution, recorded with ex-slit and em-slit as 20 nm. All spectra were recorded at r.t. with  $\lambda_{em}$  as 509 nm.

It can be seen that in the 1<sup>st</sup> and 2<sup>nd</sup> dialysis reservoirs (1 L), the HPTS probes were detected even with the small ex slit and em slit (both 2.5 nm; traces *a* and *b* in Figure 2A), in the contrast, the intensities were very small in the 4<sup>th</sup> and 5<sup>th</sup> dialysis reservoirs (traces *d* and *e* in Figure 2A). The signals of the last two dialysis reservoirs were then carefully checked by using larger ex slit and em slit (both 20 nm; Figure 2B), there were some HPTS probes in the dialysis reservoir collected in the 4<sup>th</sup> dialysis period at 24 h (trace *a* in Figure 2B). But after another 24 hours, the intensity did not increase (trace *b* in Figure 2B), implying the unencapsulated probes had been removed. To verify this, the dialysis reservoir was changed once more, and after 48 hours, no HPTS was detected in this dialysis reservoir (trace *c* in Figure 2B), firmly indicating the unencapsulated HPTS probes were totally removed.

Therefore, the dialysis process was stopped, and the retention solution was collected with cautions. The collected solution, namely the HPTS-pos suspension, was characterized by fluorophotometer to determine the HPTS concentration ( $c_{f,bulk}$ ) with the aid of the calibration curve, as  $1.05 \mu\text{g mL}^{-1}$ . Divided by the feeding concentration ( $c_{i,bulk}$ ),  $200 \mu\text{g mL}^{-1}$ , the encapsulation efficiency (EE, defined in equation 1) was determined as 0.53%.

Additionally, the polymersomes were characterized by DLS before and after dialysis. The results showed that there was no change in either the particle size or the particle distribution, and that the polymersome suspension was not diluted verified by the unchanged mean count rates measured under the same conditions. The results also indicated that the polymersomes were stable in the intensive dialysis procedure.

The validity of the preparation protocol was also assayed by changing the feeding HPTS concentration and with different polymersomes. The results were listed in Table 3.

**Table 3.** Encapsulation Efficiency (EE) of HPTS in the Polymersomes Prepared with Different Feeding Concentrations ( $c_{i,bulk}^a$ ).

Entry	$c_{i,bulk}^a$ ( $\mu\text{g mL}^{-1}$ )	$c_{f,bulk}^a$ ( $\mu\text{g mL}^{-1}$ )	EE <sup>b</sup> (%)
<b>PGL<sub>21</sub>-PBO<sub>84</sub>-PGL<sub>21</sub> (Polymer Entry 081B)</b>			
081B-4	50	0.32	0.64
081B-5	100	0.54	0.54
081B-6	200	1.06	0.53
081-B-7	200	1.05	0.53
<b><math>\beta</math>CD-(PBO<sub>13</sub>-PGL<sub>6</sub>)<sub>14</sub> (Polymer Entry HQ151)</b>			
151-1	1000	4.69	0.47
151-2	250	1.31	0.52

<sup>a</sup> $c_{i,bulk}$  is the HPTS concentration of the solution used to hydrate the polymer film, and  $c_{f,bulk}$  is the HPTS concentration in the dialyzed HPTS-pos solution, determined with the aid of the concentration calibration curve; <sup>b</sup>EE is the encapsulation efficiency, defined as the concentration ratio of  $c_{f,bulk}/c_{i,bulk}$  (Equation 1).

The results showed that, the HPTS concentration in the finally dialyzed HPTS-pos solution ( $c_{f,bulk}$ ) increased with the feeding concentration ( $c_{i,bulk}$ ), while the EE value was almost constant, indicating that the preparation protocol was reproducible.

Following the same preparation protocol, the EE values of HPTS in different polymersomes were calculated, as gathered in Table 4.

**Table 4.** Encapsulation Efficiency (EE) of HPTS in Different Polymersomes According to the EE Value.

Polymersomes <sup>a</sup>			HPTS Encapsulation Results <sup>b</sup>					
Entry	Polymer formula	$w_{\text{PGL}}$	$t_t$ (nm)	$\%V_{\text{inner}}$ (%)	$c_{i,\text{bulk}}$ ( $\mu\text{g mL}^{-1}$ )	$c_{f,\text{bulk}}$ ( $\mu\text{g mL}^{-1}$ )	$c_{f,\text{inner}}$ ( $\mu\text{g mL}^{-1}$ )	EE (%)
034-2	PGL <sub>6</sub> -PBO <sub>20</sub> -PGL <sub>6</sub>	0.35	2.9	0.8	100	0	0	0
137-2	βCD-(PBO <sub>7</sub> -PGL <sub>5</sub> ) <sub>14</sub>	0.35	3.2	2.2	500	0	0	0
033-7	PGL <sub>12</sub> -PBO <sub>84</sub> -PGL <sub>12</sub>	0.22	6.7	3.6	1000	0.74	21	0.074
031-1	PGL <sub>6</sub> -PBO <sub>40</sub> -PGL <sub>6</sub>	0.23	4.3	4.1	1000	0.82	20	0.082
107-1	βCD-(PBO <sub>22</sub> -PGL <sub>7</sub> ) <sub>14</sub>	0.23	5.6	6.3	200	0.19	3	0.095
077-1	PGL <sub>25</sub> -PBO <sub>80</sub> -PGL <sub>25</sub>	0.39	7.3	1.3	200	0.82	60	0.38
119B-2	PGL <sub>18</sub> -PBO <sub>62</sub> -PGL <sub>18</sub>	0.37	6.1	11.5	500	2.34	20	0.47
151-2	βCD-(PBO <sub>13</sub> -PGL <sub>6</sub> ) <sub>14</sub>	0.28	4.4	4.3	250	1.31	31	0.52
081B-7	PGL <sub>21</sub> -PBO <sub>84</sub> -PGL <sub>21</sub>	0.33	6.8	2.2	200	1.05	48	0.53

<sup>a</sup>Polymersomes were prepared by thin-film rehydration method. The formula of the polymersome-forming polymers and the weight fraction of PGL blocks ( $w_{\text{PGL}}$ ) were reported as the theoretical values.  $t_t$  is the thickness of the hydrophobic layer of the polymersomes determined by SAXS fitting.  $\%V_{\text{inner}}$  is the percentage of the total vesicular interior volumes enclosed by polymersomes ( $V_{\text{inner}}$ ) to the volume of the bulk solution where the vesicles suspended ( $V_{\text{total}}$ ), as defined in Equation 7; <sup>b</sup> $c_{i,\text{bulk}}$  is the HPTS concentration of the solution used to hydrate the polymer film.  $c_{f,\text{bulk}}$  is the HPTS concentration in the dialyzed HPTS-pos suspension determined with the aid of the concentration calibration curve.  $c_{f,\text{inner}}$  is the HPTS concentration inside the polymersomes, as defined in Equation 2. EE is the encapsulation efficiency, as defined in Equation 1.

HPTS has been widely used as the pH indicator in liposomes [15,26] and polymersomes [14,19]. However, the encapsulation efficiency has seldom been reported. Despite the lack of comparable research results, the values in Table 4 were interestingly small. First, the inefficient encapsulations (Entry 034-1 and Entry 137-2) were far from expectation. Secondly, it was supposed that, in the equilibrated polymersome suspension, the initial HPTS concentration inside the polymersomes ( $c_{i,\text{inner}}$ ) should be the same as that in the exterior continuous phase ( $c_{i,\text{bulk}}$ ) thanks to the good aqueous solubility of HPTS (Scheme 1). Correspondingly, the encapsulation efficiency (EE) was supposed to be delimited by the vesicular inner volume percentage ( $\%V_{\text{inner}}$ ) [27]. However, the EE values here were far from the  $\%V_{\text{inner}}$  values (Table 4).

Firstly, to explain the unexpected low EE values in this work, the encapsulation protocol was commented by comparing with other works.

The EE values obtained here were much smaller than that reported in Parnell A. J.'s work [20]. In that work, Rhodamine B ( $M_w = 479 \text{ g mol}^{-1}$ ) was encapsulated into the polymersomes made of PBO<sub>36</sub>-PEO<sub>28</sub> via hydrating the polymer film by the aqueous solution of Rhodamine B, the same protocol as the one used here. Later, the unencapsulated probes were removed by chromatography, giving the EE value as 2.0%. As a reminder, dialysis was usually applied to study the *in-vitro* drug-release kinetics after the drug was loaded into the polymersomes [28]. Thus, it was thought that the relatively long and intensive dialysis protocol adopted here attributed to the rather low encapsulation efficiency. Typically, the dialysis was performed for 5 days with 4 changes of the dialysis reservoir.

Additionally, in the aforementioned work [20], the authors also encapsulated Rhodamine B by preloading the probes in the polymer film, before being hydrated with water, followed with the removal of unloaded probes by chromatography. This protocol gave relatively higher encapsulation efficiency (5.4%) than that obtained via hydrating the polymer film with the solution of Rhodamine B (2.0%). Moreover, the authors further investigated the influences of the details in the hydration protocol on the encapsulation efficiency, including the mass of preloaded drug, annealing and pretreatment with water vapor. At last, under optimal conditions, the encapsulation efficiency was further increased to 13.6%. This systematical investigation reminded one that the details in the protocol might influence a lot the final encapsulation efficiency.

Many reports have indicated that the preparation methodology played a great role in the encapsulation efficiency [29,30]. For example, in the thin-film rehydration method [31], the polymer film is hydrated and detaches from the surface of the substrate, after water or aqueous solution of drug permeates into the lamella. Thus, it is easy to understand that the upper limit of encapsulation is the percentage of the total inner volume enclosed by the vesicles, when the film is hydrated by the aqueous solution containing the drugs to be encapsulated, or the upper limit is 50%, when the drug molecules are preloaded into the polymer film [20]. These limits were calculated assuming that the polymersomes are unilamellar, and that there is no special interaction between the drugs with either the hydrophobic or hydrophilic segments of the polymers. As another example, Rhodamine B was inefficiently loaded into the polymersomes of PDEAMA<sub>81</sub>-PEO<sub>45</sub> with a pH-switch methodology, even the unloaded probes were removed by chromatography [29]. The reported inefficiency was ascribed to the special polymersome formation mechanism.

Contrarily, rather high encapsulation efficiency was reported in some special drug-vesicle pairs. One case concerns the encapsulation of doxorubicin hydrochloride (DOX·HCl) into the polymersomes made of  $\beta$ CD-cored star copolymers with three poly(ethylene glycol)-*block*-polylactide arms ( $\beta$ CD-(mPEG-PLA)<sub>3</sub>). DOX·HCl was

loaded into the polymersomes via solvent evaporation method, and the un-loaded drugs were removed by dialysis for 8 hours. The encapsulation efficiency was found as high as 99.99% under optimal conditions. In contrast, in the same conditions, an efficiency of 30.08% was only obtained in the polymersomes made of linear mPEG-PLA (without  $\beta$ CD). The significantly increased encapsulation efficiency was attributed to the host–guest interaction between  $\beta$ CD and DOX [32]. Another case deals with DNA being loaded into the polymersomes made from poly(2-(methacryloyloxy)ethyl-phosphorylcholine)-*block*-poly(2-(diisopropylamino)ethyl methacrylate) (PMPC-PDPA), the favorable interactions between DNA and polymersomes allowed the encapsulation efficiency as high as 55% via a solvent-switch protocol [33].

In brief, the low EE values reported here were supposed to originate from the following reasons: first, there was no favorable interaction between HPTS and PGL-PBO-PGL or  $\beta$ CD-(PBO-PGL)<sub>14</sub> polymersomes; secondly, and more importantly, it was caused from the limitation of the thin-film rehydration method and the intensive purification process adopted here.

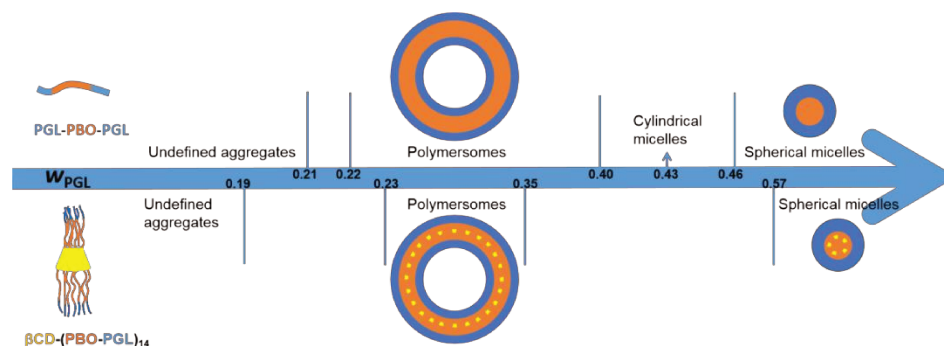
Despite the rather low EE values (Table 4), there were obvious differences between the different polymersomes. As aforementioned, EE was driven by the type of polymersomes rather than the feeding concentration (Table 3). To explain the different results obtained, two important factors, namely the thickness of the hydrophobic layer ( $t_i$ ) and the weight fraction of PGL blocks ( $w_{\text{PGL}}$ ), were discussed.

According to the EE values (Table 4), the polymersomes were divided into three groups. The first group concerns the polymersomes with EE values as zero, the second group those having EE values less than 0.1%, and the third group the polymersomes having relatively larger EE values ranging from 0.38% to 0.53%. To note that in each group, there were both the linear-copolymer-formed polymersomes and the star-copolymer-formed polymersomes, meaning the architectural effect was not evident herein.

In the first group, the inefficient encapsulations were thought to result from the relatively thinner polymersome membranes compared with the others. In the second group, the low encapsulation efficiency was supposed to originate from the imperfect polymersomes, which was defined by  $w_{\text{PGL}}$  of the polymersome-forming copolymers studied here. To explain this more clearly, the phase diagrams of the linear triblock copolymers and the star copolymers were displayed here again (Scheme 3). From the phase diagrams, one can see that when  $w_{\text{PGL}}$  values are as low as 0.22 (Entry 033-7) and 0.23 (Entry 031-1 and Entry 107-1), there might be some undefined aggregates together with the polymersomes and the aggregates would be removed via the extrusions before dialysis, causing the loss of sample. For these two reasons, the actual available encapsulation volume of the polymersomes ( $V_{\text{inner}}$ ) decreased,

resulting in relatively low encapsulation efficiency. In contrast, the polymersomes in the third group produced relatively higher encapsulation efficiency, consistent with the facts that these polymersomes have thicker membrane and are formed by the polymers having proper  $w_{\text{PGL}}$  values in which range pure and defined polymersomes are anticipated.

**Scheme 3.** Self-assembly Morphology Defined by the Weight Fraction of PGL blocks ( $w_{\text{PGL}}$ ).



By the way, one might think that the negatively charged outer PGL corona of the polymersomes would influence the encapsulation efficiency of the negative HPTS molecules via electrostatic interactions and/or hydrogen-bonding interactions, to some extent. However, it cannot make such conclusions based on the available data herein. Similarly, from the available data, the roles of  $\beta$ CD core played in the encapsulation efficiency cannot be concluded either.

### 3.3 Determination of the interior pH value of polymersomes

HPTS is a pH-sensitive fluorescence probe and has been widely used to determine the vesicular interior pH values thanks to its good aqueous solubility as well as the facile and robust methodology [14]. To report pH values via HPTS, a pH calibration curve is required. To this end, the excitation spectra of HPTS solutions at different pH levels varying from pH 3 to 10 were recorded under the same conditions (Figure 3A). Two characteristic peaks centered at 402 nm and 455 nm were observed, being respectively assigned to the protonated and deprotonated forms of HPTS [19]. Therefore, when pH increased (from  $a$  to  $j$ ), the intensity at 402 nm ( $I_{402}$ ) decreased and the intensity at 455 nm ( $I_{455}$ ) increased, especially from pH 6 to 9. Based on these spectra, the calibration curve was constructed by fitting pH values (measured by pH meter) and the intensity ratios of  $I_{455}/I_{402}$  into the Henderson–Hasselbalch relation (Equation 8), as shown in Figure 3B. The experimental data fitted well with the value of  $R^2$  as 0.9997 (the insert of Figure 3B).

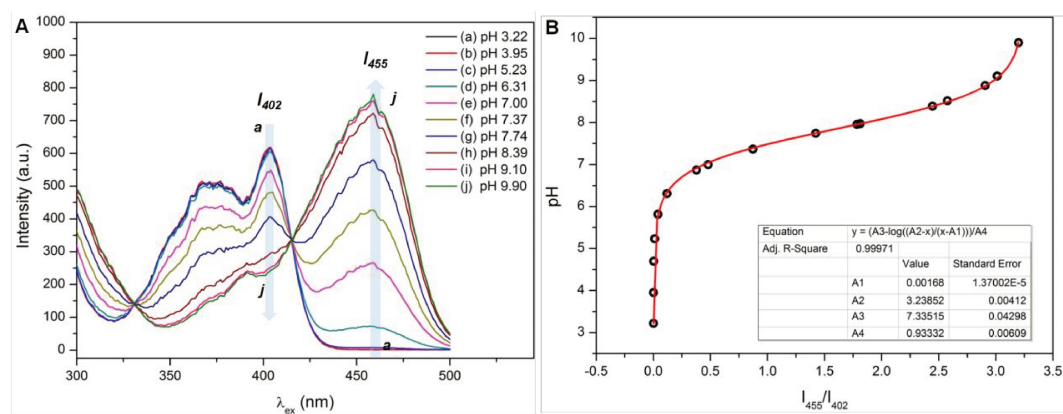


**Figure 3.** (A) Fluorescence excitation spectra of the HPTS solutions ( $10 \mu\text{g mL}^{-1}$ ) at varying pH levels according to the legends. Spectra were recorded at r.t. (July 2020) with  $\lambda_{\text{em}}$  as 509 nm, with ex-slit and em-slit as 2.5 nm. (B) Experimental data (black circles) and the fitting curve into Henderson–Hasselbalch relation (red line). The insert shows the fitting report.

Considering the fluorophotometer was not equipped with a temperature-controlling module, the influence of the temperature was investigated (this limitation has recently been fixed). The plots of  $\text{pH}-I_{455}/I_{402}$  obtained at different times of the year have been recorded at r.t. and were shown in Figure 4. We strongly suspect that room temperature changes during the year.

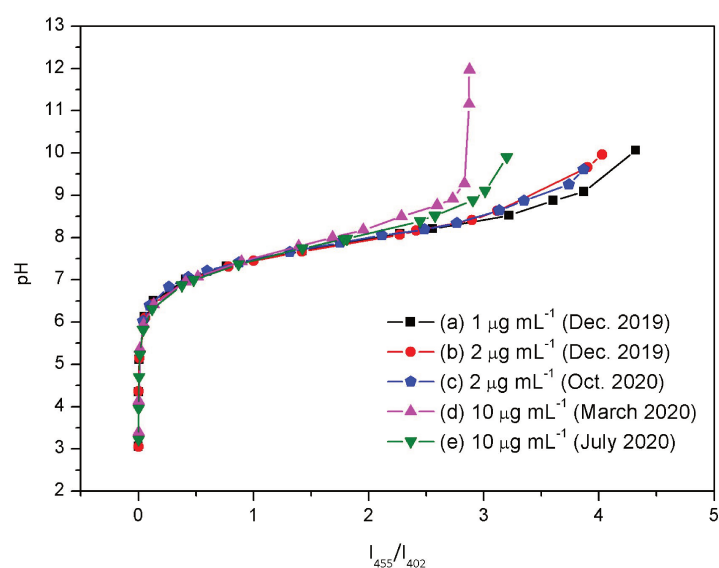


**Figure 4.** Plots of pH versus  $I_{455}/I_{402}$  obtained at different times of the year at r.t., according to the legends. The intensity ratios of  $I_{455}/I_{402}$  were derived from the fluorescence excitation spectra which were recorded at r.t. with  $\lambda_{\text{em}}$  as 509 nm, with ex-slit and em-slit as 2.5 nm.

The results showed that the pH– $I_{455}/I_{402}$  plots varied with HPTS concentration and temperature. The plots at different concentration levels were close to each other when pH was below 8.2, while they were significantly different at higher pH values. On the other hand, comparing the plots constructed at 2  $\mu\text{g mL}^{-1}$  (plots *b* and *c*) with those at 10  $\mu\text{g mL}^{-1}$  (plots *d* and *e*), it seems that temperature affected more the results when HPTS concentration was higher. It is also worth to mention that when pH was below 6.0 or above 9.0, the intensity ratio changed slightly with pH. Conversely, when pH was in the range from 6.0 to 9.0, a small change in pH corresponds to a significant change in  $I_{455}/I_{402}$ , showing this range was the appropriate working pH range under current conditions.

Thus, the plots from pH 6.0 to pH 9.0 were fitted into the Henderson–Hasselbalch relation (Equation 8), and the results were listed in Table 5.

**Table 5.** Fitting Parameters of the pH– $I_{455}/I_{402}$  plots (from pH 6.0 to pH 9.0, in Figure 4) into the Henderson–Hasselbalch Relation (Equation 8).

Conditions		Fitting Parameters					
<b>c</b>	<b>T<sup>a</sup></b>	<b>A1</b>	<b>A2</b>	<b>A3</b>	<b>A4</b>	<b>R<sup>2</sup></b>	<b>A3/A4</b>
	( $\mu\text{g mL}^{-1}$ )						
1	r.t. (Dec. 2019)	$-4 \times 10^{-3}$	4.05	8.0	1.00	0.9996	7.96
2	r.t. (Dec. 2019)	$5 \times 10^{-3}$	3.62	8.1	1.03	0.9997	7.85
2	r.t. (Oct. 2020)	$5 \times 10^{-4}$	3.68	8.2	1.04	0.9997	7.90
10	r.t. (March 2020)	$9 \times 10^{-2}$	3.22	6.0	0.76	0.9994	7.92
10	r.t. (July 2020)	$-2 \times 10^{-2}$	3.29	6.8	0.87	0.9999	7.86
1 mM <sup>b</sup>	20 °C	$-6 \times 10^{-3}$	4.19	7.2	0.92	n.d. <sup>c</sup>	7.83

<sup>a</sup>The fluorescence spectra were recorded at r.t. in different year periods; <sup>b</sup>Published data in the reference [14]; <sup>c</sup>No data reported.

As listed in Table 5, all the fittings had high R<sup>2</sup> values. Although the fitting parameters varied with the conditions (*i.e.*, HPTS concentration and experimental temperature), the ratios of A3/A4 obtained herein were close to each other and consistent with the reported value in the literature [14]. To note, the ratio of A3/A4 is pK<sub>a</sub>-relevant in the context of the Henderson–Hasselbalch relation. Hence, it was concluded that the pH calibration curves obtained herein were reliable in the range of pH 6.0–9.0. Therefore, the vesicular interior pH can be properly determined by fluorescence spectroscopy with the aid of the pH calibration curves.

At the meantime, considering the fluorophotometer was not equipped with temperature-controlling module, the lower concentrations were preferred. Therefore,

the HPTS-pos with  $c_{f,bulk}$  around 1 and 2  $\mu\text{g mL}^{-1}$  (Table 4) were used to investigate the polymersome membrane permeability to  $\text{H}^+$  in the following section, including four linear-copolymer-formed polymersomes (Entries 031-1, 077-1, 081B-7 and 119B-2) and one star-copolymer-formed polymersomes (Entry 151-2).

### 3.3 Polymersome membrane permeability to $\text{H}^+$

#### 3.3.1 Validation of the investigation protocol

As illustrated in Scheme 2, the idea is to add HCl outside of vesicles to produce an initial transmembrane pH gradient (initial  $\Delta\text{pH}$ ). If the membrane is impermeable, then the pH gradient will be maintained. If the membrane is permeable, then the pH gradient will decay gradually. In this period of time,  $\text{H}^+$  permeates into vesicles, inducing the decrease of the vesicular interior pH, which can be continuously determined by fluorescence. Thus, it is important to choose an appropriate time-window so as to detect the change properly. At the same time, the pH value should change from pH 6.0 to pH 9.0 to ensure the pH probes work properly.

First, a HPTS solution (2  $\mu\text{g mL}^{-1}$  in PBS) was used to figure out the appropriate amount of HCl required allowing the pH change in the range of pH 6.0 to pH 9.0. It was found that when 10  $\mu\text{L}$  of HCl (1 M) was added into 2.5 mL of HPTS solution (2  $\mu\text{g mL}^{-1}$  in PBS), the pH changed 0.7 units, ensuring the pH changed in the appropriate working pH range. To note, concentrated HCl solution (1 M) was used in order to change little in the buffering media and to minimize the consequent influences [15]. Then, to find out the proper time-window, preliminary investigations with HPTS-pos and HPTS solution were performed on two set-ups (Scheme 4). One was conducted in a cuvette ( $1\text{ cm}^2 \times 4\text{ cm}$ ) and fluorescence spectra were recorded at steady state (without stirring). The other was performed in a sample vial (8 mL) charged with a stirring bar, and spectra were recorded with the aid of an optic fiber, under stirring.

**Scheme 4.** Two Set-ups Used to Investigate the Permeability to  $\text{H}^+$ : (A) at Steady State, and (B) under Stirring; both at r.t.

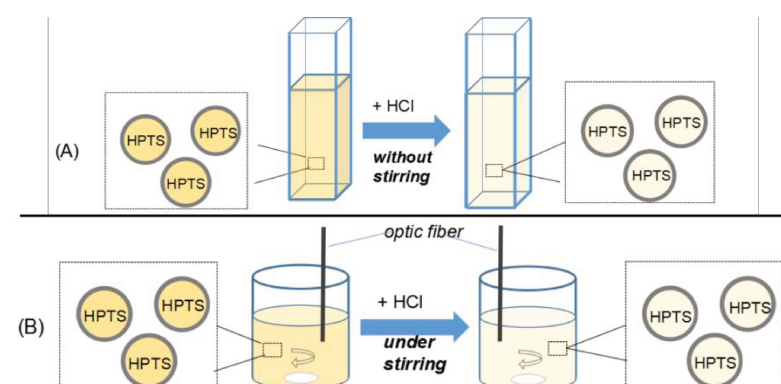
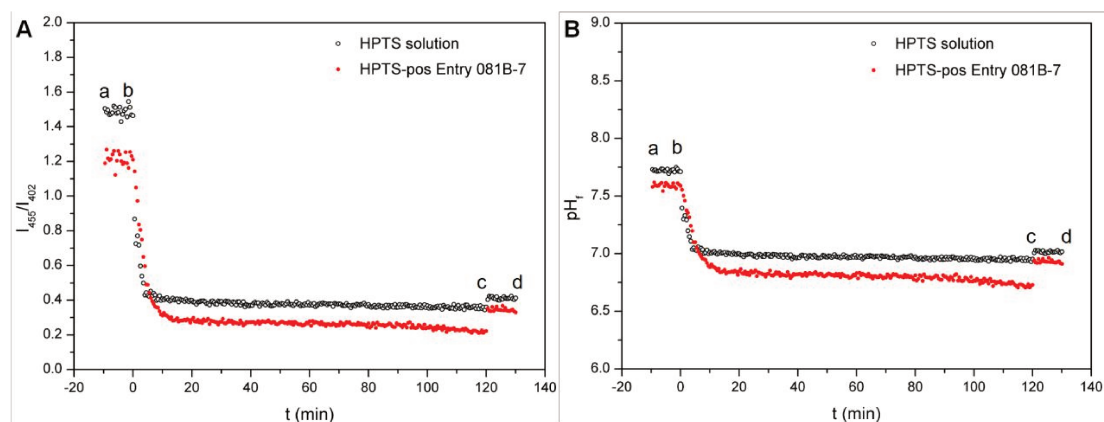


Figure 5 displayed the results obtained at steady state using Set-up A in Scheme 4, for the HPTS-pos Entry 081B-7. In the investigation process, the excitation spectra were continuously recorded with an interval of 0.5 minutes. From these spectra, the change of the intensity ratio of  $I_{455}/I_{402}$  with time ( $t$ ) was obtained, as shown in Figure 5A. The intensity ratios were submitted into the pH calibration curve, producing the plot of  $\text{pH}_f$  changing with  $t$  as depicted in Figure 5B.



**Figure 5.** The changes of (A) the intensity ratio of  $I_{455}/I_{402}$  and (B) the corresponding  $\text{pH}_f$  value with time ( $t$ ), recorded at steady state, for the HPTS-pos Entry 081B-7 (red dots) or the HPTS solution (black circles). Spectra were recorded at r.t. with  $\lambda_{\text{em}}$  as 509 nm and with ex-slit and em-slit as 2.5 nm. The spectra recording of the HPTS solution or the HPTS-pos suspension started at point *a* and ended at point *b* (10 min, with a 0.5-min interval). Then, HCl was dropped into the solution and the spectra were immediately recorded for 120 min (with a 0.5-min interval). At the end, the mixture in the cuvette was mixed sufficiently with pipette. The spectra of the mixture were subsequently recorded again from point *c* to point *d* (10 min, with a 0.5-min interval).

It can be seen that, after the addition of HCl, the intensity ratio decreased immediately (Figure 5A) due to the decrease of  $\text{pH}_f$  (Figure 5B). It can also be noted that even in the HPTS solution (black circles in Figure 5B)  $\text{pH}_f$  decreased gradually before it was constant (about 6 minutes later), this was caused by the mixing process via the free diffusion of the drop of HCl (10  $\mu\text{L}$ ) into the HPTS solution (2.5 mL) at steady state. Similarly, after the addition of HCl (10  $\mu\text{L}$ ) into the HPTS-pos suspension (2.5 mL),  $\text{pH}_f$  decreased gradually until it was constant (about 17 minutes later). The difference of the  $\text{pH}_f$ -decaying time between HPTS solution (in absence of polymersomes) and HPTS-pos suspension was thought to be caused by the polymersome membranes. One can notice that, at the end,  $\text{pH}_f$  increased a little after the solution was mixed sufficiently with the pipette in both cases (from  $\text{pH}_f$  6.95 at  $t = 120$  min to  $\text{pH}_f$  7.01 at point *c* in the HPTS solution, and from  $\text{pH}_f$  6.73 at  $t = 120$

min to  $\text{pH}_f$  6.94 at point *c* in the HPTS-pos solution). This was ascribed to the free diffusion process to some extent.

To eliminate the free diffusion process, the experiments were conducted under stirring state using Set-up B in Scheme 4. The changes in the intensity ratio of  $I_{455}/I_{402}$  and the  $\text{pH}_f$  value were displayed in Figure 6.

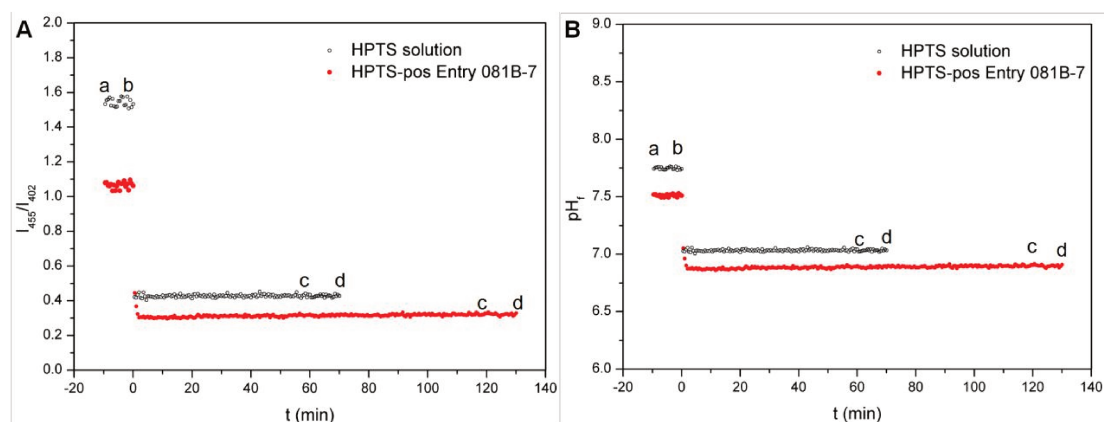


**Figure 6.** The changes of (A) the intensity ratio of  $I_{455}/I_{402}$  and (B) the corresponding  $\text{pH}_f$  value with time ( $t$ ), recorded under stirred state, for the HPTS-pos Entry 081B-7 (red dots) or the HPTS solution (black circles). Spectra were recorded at r.t. under stirring with  $\lambda_{\text{em}}$  as 509 nm, with ex-slit and em-slit as 5 nm. The spectra recording of the HPTS solution or the HPTS-pos suspension started at point *a* and ended at point *b* (10 min, with a 0.5-min interval). Then, HCl was dropped into the solution and the spectra were immediately recorded for 60 min in the case of HPTS solution or 120 min in the case of HPTS-pos suspension (with a 0.5-min interval). At the end, the mixture in the cuvette was mixed sufficiently with pipette. The spectra of the mixture were subsequently recorded again from point *c* to point *d* (10 min, with a 0.5-min interval).

These experiments clearly showed that, under stirring, after the addition of HCl, the intensity ratio decreased immediately and was invariable in both cases of the HPTS solution and HPTS-pos suspension (Figure 6A). Accordingly,  $\text{pH}_f$  decreased immediately and was constant later on (Figure 6B). Also, at the end,  $\text{pH}_f$  did not change after the solution was mixed again by pipette since the mixture was already equilibrated.

To check the reliability of the results, the initial and final pH values were compared, as listed in Table 6. There were two sets of pH values according to the measurement methods, including the  $\text{pH}_f$  values which were determined by fluorospectrometry and the  $\text{pH}_e$  values which were measured by the electronic pH meter. The initial  $\text{pH}_f$  was the average value from point *a* to point *b* (Figure 5B and 6B), and the final  $\text{pH}_f$  was

the average value from point *c* to point *d* (Figure 5B and 6B). Accordingly, the initial pH<sub>e</sub> was the pH value of the HPTS solution or the HPTS-pos suspension (before the addition of HCl) and the final pH<sub>e</sub> was the pH value of the mixture of HCl with the HPTS solution or the HPTS-pos suspension (at the end of fluorescence recordings).

**Table 6.** Initial and Final pH Values Measured in the Investigation of Polymersome Membrane Permeability to H<sup>+</sup> (Entry 081B-7) Performed Under Different Conditions.

	Initial pH <sup>a</sup>			Final pH <sup>b</sup>			pH jump <sup>c</sup>	
	pH <sub>f</sub>	pH <sub>e</sub>	ΔpH	pH <sub>f</sub>	pH <sub>e</sub>	ΔpH	pH <sub>f</sub>	pH <sub>e</sub>
<b>At Steady State<sup>d</sup></b>								
HPTS	7.72	7.50	0.25	7.01	6.78	0.23	-0.71	-0.72
HPTS-pos	7.59	7.45	0.14	6.93	6.78	0.15	-0.66	-0.67
<b>Under Stirring<sup>e</sup></b>								
HPTS	7.75	7.48	0.27	7.03	6.78	0.25	-0.72	-0.70
HPTS-pos	7.51	7.43	0.08	6.90	6.79	0.11	-0.61	-0.64

<sup>a</sup>Initial pH is the pH value of the HPTS solution or HPTS-pos suspension (before the addition of HCl) determined by fluorospectrometry (pH<sub>f</sub>) or measured by electronic pH meter (pH<sub>e</sub>). ΔpH = pH<sub>f</sub> - pH<sub>e</sub>;

<sup>b</sup>Final pH is the pH value of the mixture of HCl with HPTS solution or HPTS-pos suspension (after the fluorescence recordings) determined by fluorospectrometry (pH<sub>f</sub>) or measured by electronic pH meter (pH<sub>e</sub>). ΔpH = pH<sub>f</sub> - pH<sub>e</sub>; <sup>c</sup>pH jump means the pH change induced by the addition of HCl, namely pH jump = Final pH - Initial pH. The negative value corresponds to the decrease of pH; <sup>d</sup>10 μL of HCl (1 M) was added into 2.5 mL of HPTS solution or HPTS-pos suspension at steady state; <sup>e</sup>20 μL of HCl (1 M) was added into 5.0 mL of HPTS solution or HPTS-pos suspension under stirring.

When the HPTS solution was merely considered, it was a little surprising that the pH value measured by pH meter (initial pH<sub>e</sub>) was different from that determined by fluorospectrometry (initial pH<sub>f</sub>), either at steady state or under stirring. The difference was also observed between the final pH<sub>e</sub> and final pH<sub>f</sub> values. However, all the differences (ΔpH values) were identical (taking into account the accuracy of the pH meter), indicating this difference was a kind of systematic errors which might originate from the buffer solutions [25]. Indeed, the buffer solution used in the construction of pH calibration curve were phosphate buffering (PB) solutions, while the buffer used in the permeability investigation was PBS solution. However, when the pH jump was considered, one can see that the pH jump measured by fluorospectrometry (pH<sub>f</sub> jump) was the same as the one measured by electronic pH meter (pH<sub>e</sub> jump), either at steady state or under stirring. These results showed the protocol was reliable, and the values were sensible for further analyses.

The results of the HPTS-pos suspension obtained at steady state were discussed: In the context of HPTS-pos, pH<sub>f</sub> was the vesicular interior pH value, while pH<sub>e</sub> was the

exterior pH value. The initial  $pH_e$  of the HPTS-pos suspension (pH 7.50) was the same as the one of the HPTS suspension (pH 7.45), meaning the exterior pH of the polymersomes was equal to the one of the buffering solution. However, the initial  $pH_f$  of the HPTS-pos suspension (pH 7.59) was smaller than the one of the HPTS solution (pH 7.72), showing the interior pH of the polymersomes was smaller than that of the buffering solution. The smaller initial  $pH_f$  of the HPTS-pos was thought to result from the influence of the polymersome inner layer on the ionization of HPTS molecules [14,23].

In the HPTS-pos suspension, the system was in equilibrium initially with the initial  $\Delta pH$  as 0.14 (caused by systematic errors). At the end, the final  $\Delta pH$  was 0.15, indicating the system reached the equilibrium again with no pH gradient across the membrane. From the point of view of the pH changes, at the end, the exterior pH decreased by 0.67 units ( $pH_e$  jump) and the interior pH decreased by 0.66 units ( $pH_f$  jump), demonstrating that  $H^+$  permeated across the membrane into the polymersomes resulting in the decay of interior pH and at last there was no pH gradient across the polymersome membrane.

Then, we can see that the results of the HPTS-pos suspension obtained under stirred state were the same as those obtained at steady state, and thus, the same conclusion can be made: the polymersome membrane (Entry 081-7) was rather permeable to  $H^+$ .

In short, even though there were some inevitable systematic errors, the protocol and the data were reliable. The results obtained either at steady state or under stirred state firmly indicated that the polymersome membranes composed of PGL<sub>21</sub>-PBO<sub>84</sub>-PGL<sub>21</sub> (Entry 081B-7) were permeable to  $H^+$ . However, under stirring, the permeation was too fast to make any sense on the role played by the polymersome membrane (Figure 6). So the  $pH_f$  curves of the HPTS solution and the HPTS-pos suspension obtained at steady state (Figure 5B) were analyzed and compared.

The  $pH_f$  curves as a function of time ( $t$ ) were fitted using the exponential decay function (Equation 9) [15].

$$pH_f = Ae^{(-t/\tau)} + pH_{f0} \quad (9)$$

in which, the constants  $A$ ,  $\tau$ , and  $pH_{f0}$  are fitting parameters using the OriginPro8 software, with  $\tau$  and  $pH_{f0}$  standing for fluorescence lifetime and initial  $pH_f$  value, respectively. To note that the values of  $\tau$  are determined only for the purpose of qualitative comparison herein. A larger  $\tau$  value represents a slower decaying rate of  $pH_f$  and thus indicates a less permeable membrane for proton transporting, in the current investigation conditions.

The fitting curves of both the HPTS solution (control experiment) and the HPTS-pos suspension were portrayed in Figure 7 (left panel), together with the fitting parameters (right panels).

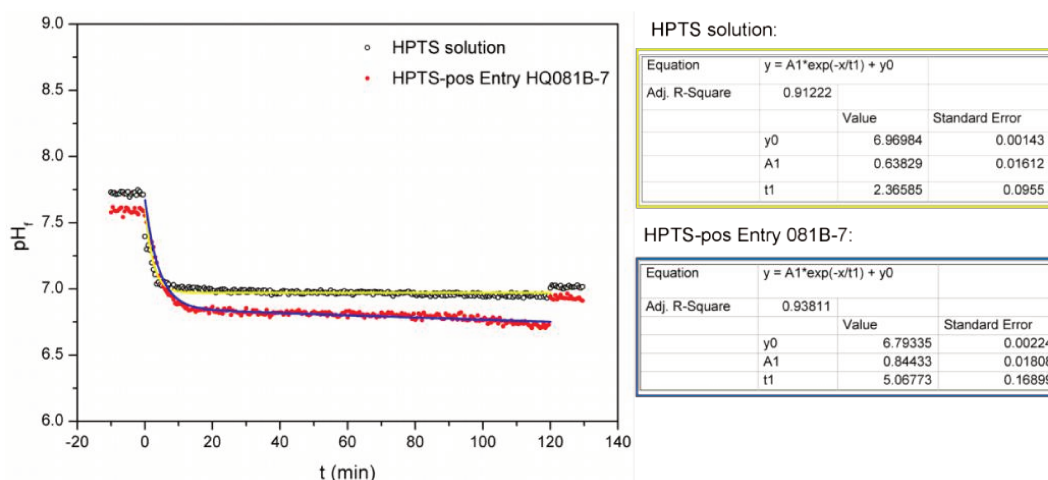


**Figure 7.** (Left) Curves of the decrease of pH<sub>f</sub> induced by the addition of HCl into the HPTS solution (black circles) and the HPTS-pos suspension (red dots) obtained at steady state, and the respective fitting curves (yellow and blue, respectively) using the exponential decay function (Equation 9), and (Right) the respective fitting reports.

It can be seen that the pH<sub>f</sub>–t curves ( $t = 0$  to 120 min) fitted well into the exponential decay function, with the values of R<sup>2</sup> as 0.91 for the HPTS solution and 0.94 for the HPTS-pos (Figure 7). The fitting results gave the decay time in the HPTS solution ( $\tau_{\text{Blank}}$ ) as 2.37 min (top of the right panels in Figure 7), while the decay time in the HPTS-pos suspension ( $\tau_{\text{pos}}$ ) was a little longer as 5.07 min (bottom of the right panels in Figure 7). The time lag ( $\Delta\tau$ ) between these two cases ( $\Delta\tau = \tau_{\text{pos}} - \tau_{\text{Blank}}$ ) was 2.70 min, which was proposed to be ascribed to the contribution of the polymersome membranes under current conditions.

### 3.3.2 Determination of the permeability of all the polymersomes to H<sup>+</sup>

Adopting the same protocol, the investigations on the membrane permeability of the other polymersomes were conducted. The changes of pH<sub>f</sub> in the absence and presence of polymersomes were plotted and compared, as portrayed in Figure 8.

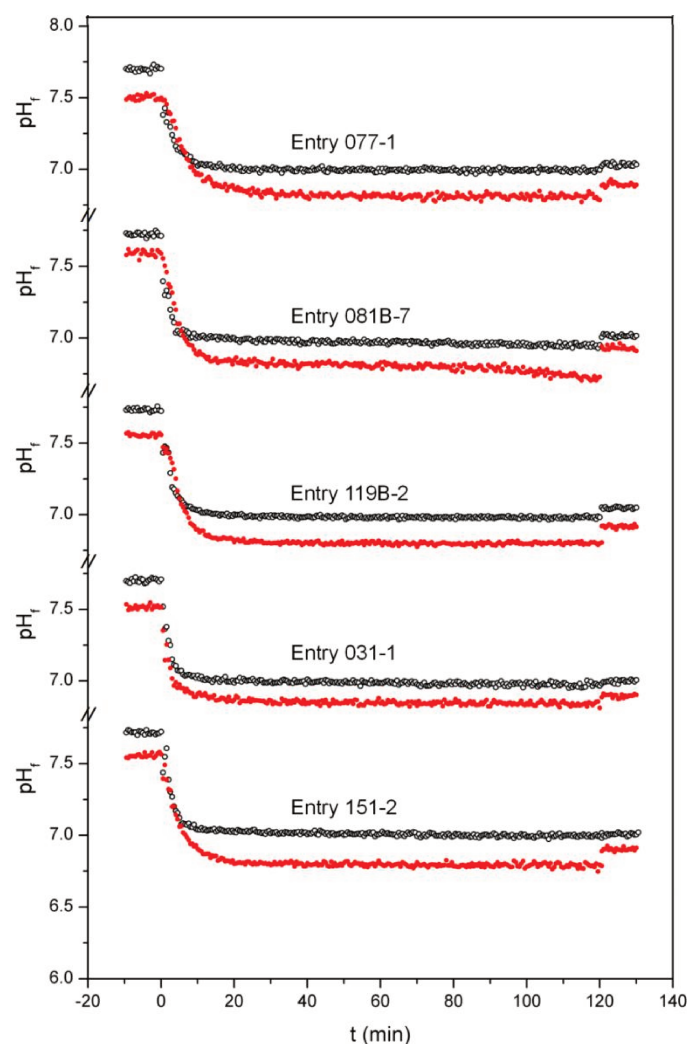


**Figure 8.** Stacked  $\text{pH}_f$ - $t$  curves obtained in the absence (black circles, HPTS solution) and presence (red dots, HPTS-pos suspension) of polymersomes made from different copolymers, according to the legends.

One can see that, the curves were similar in the decaying tendency. In the absence of polymersomes (control experiment, black circles),  $\text{pH}_f$  decayed gradually and stopped decreasing after 10 minutes of the addition of HCl in all cases, while it took more time for  $\text{pH}_f$  to be stable in the presence of polymersomes (red dots). In other words,  $\text{pH}_f$  decayed faster in the HPTS solutions than in the respective HPTS-pos suspensions. To quantitatively compare the decaying behaviors, the curves were all analyzed by fitting into the exponential decay function (Equation 9) to get the decay times ( $\tau_{\text{pos}}$  and  $\tau_{\text{Blank}}$ ) and the corresponding time lag ( $\Delta\tau = \tau_{\text{pos}} - \tau_{\text{Blank}}$ ). The fitting results were gathered in Table 7, together with the initial and final pH values.

**Table 7.** Initial and Final pH Values in the Investigations on the Membrane Permeability to H<sup>+</sup> of Different Polymersomes<sup>a</sup> According to the Thickness of the Hydrophobic Layer ( $t_t$ )<sup>b</sup>.

	pH <sub>f</sub> <sup>c</sup>			pH <sub>e</sub> <sup>d</sup>			ExpDec Fitting <sup>e</sup>		
	Initial	Final	pH jump	Initial	Final	pH jump	$\tau$ (min)	R <sup>2</sup>	$\Delta \tau$ (min)
<b>Entry 077-1</b> ( $t_t = 7.3$ nm, PGL <sub>25</sub> -PBO <sub>80</sub> -PGL <sub>25</sub> )									
Blank	7.70	7.03	-0.67	7.44	6.79	-0.65	3.65	0.9541	
pos	7.51	6.89	-0.62	7.41	6.79	-0.62	6.51	0.9755	2.87
<b>Entry 081B-7</b> ( $t_t = 6.8$ nm, PGL <sub>21</sub> -PBO <sub>84</sub> -PGL <sub>21</sub> )									
Blank	7.72	7.01	-0.71	7.50	6.78	-0.72	2.37	0.9122	
pos	7.59	6.93	-0.66	7.25	6.78	-0.67	5.07	0.9381	2.70
<b>Entry 119B-2</b> ( $t_t = 6.1$ nm, PGL <sub>18</sub> -PBO <sub>62</sub> -PGL <sub>18</sub> )									
Blank	7.73	7.05	-0.68	7.53	6.80	-0.73	3.23	0.9676	
pos	7.55	6.92	-0.63	7.48	6.81	-0.67	5.29	0.9798	2.06
<b>Entry 031-1</b> ( $t_t = 4.3$ nm, PGL <sub>6</sub> -PBO <sub>40</sub> -PGL <sub>6</sub> )									
Blank	7.70	7.00	-0.70	7.44	6.75	-0.69	2.38	0.9535	
pos	7.52	6.89	-0.63	7.41	6.76	-0.65	2.99	0.9244	0.61
<b>Entry 151-2</b> ( $t_t = 4.4$ nm, $\beta$ CD-(PBO <sub>13</sub> -PGL <sub>6</sub> ) <sub>14</sub> )									
Blank	7.71	7.01	-0.70	7.56	6.83	-0.73	3.14	0.9399	
pos	7.56	6.90	-0.66	7.51	6.82	-0.69	5.21	0.9837	2.07

<sup>a</sup>Polymersomes were those having proper HPTS concentrations ( $c_{f,bulk}$ ) listed in Table 5. The control experiment (“Blank”) for each polymersomes (“pos”) was respectively performed to minimize the possible influences of temperature and HPTS concentration; <sup>b</sup>The thickness of the hydrophobic layer of polymersomes ( $t_t$ ) was determined by SAXS; <sup>c</sup>pH<sub>f</sub> values were the values determined by fluorospectrometry. Initial pH<sub>f</sub> is the value of the HPTS solution or HPTS-pos suspension (before the addition of HCl), reported as the average value from point *a* to point *b* illustrated in Figure 5B. Final pH<sub>f</sub> is the value of the mixture of HCl with the HPTS solution or HPTS-pos suspension, reported as the average value from point *c* to point *d* illustrated in Figure 5B. pH<sub>f</sub> jump = Final pH<sub>f</sub> - Initial pH<sub>f</sub>; <sup>d</sup>pH<sub>e</sub> values were the values determined by the electronic pH meter. Initial pH<sub>e</sub> is the value of the HPTS solution or HPTS-pos suspension (before the addition of HCl). Final pH<sub>e</sub> is the value of the mixture of HCl with the HPTS solution or HPTS-pos suspension (after the fluorescence recordings). pH<sub>e</sub> jump = Final pH<sub>e</sub> - Initial pH<sub>e</sub>; <sup>e</sup>ExpDec fitting results were obtained by fitting the pH<sub>f</sub>-*t* curves (Figure 8) into the exponential decay function (Equation 9). The time lag ( $\Delta\tau$ ) is the decay time difference between “pos” and “Blank”, as  $\Delta\tau = \tau_{pos} - \tau_{Blank}$ .

As already thoroughly discussed in the case of Entry 081B-7 (Table 6), the non-zero pH gradient measured here ( $\Delta\text{pH} = \text{pH}_f - \text{pH}_e$ ) was due both to the addition of HCl and the systematic errors. Thus, Table 7 paid more attention to the pH difference between the initial and final pH values, namely the pH jump induced by the addition

of HCl (pH jump = Final pH - Initial pH). It can be seen that, in each control experiment, the pH jump measured by fluorospectroscopy (pH<sub>f</sub> jump) was the same as that measured by electronic pH meter (pH<sub>e</sub>), showing the protocols were valid.

In the context of HPTS-pos suspension, the pH<sub>f</sub> jump was the pH change inside the polymersomes and the pH<sub>e</sub> jump was the pH change outside the polymersomes. The data showed that, in all the polymersomes, the pH<sub>f</sub> jump was equal to the pH<sub>e</sub> jump. Considering that, initially, the vesicular interior pH was equal to the exterior pH because of intensive dialysis process, thus, the equal pH jumps inside (pH<sub>f</sub>) and outside (pH<sub>e</sub>) of the polymersomes demonstrated that the interior and exterior were in equilibrium again at last. In other words, there was no pH gradient across the membrane at the end. Together with the pH<sub>f</sub> decaying curves in Figure 8, it can be concluded that all the polymersome membranes were quite permeable to H<sup>+</sup>.

As shown in Table 7, the decay times ( $\tau$ ) in the HPTS solutions (“Blank”) varied from each other which possibly result from the varied HPTS concentrations and/or experimental temperature. The potential influence of HPTS concentration was minimized by performing the control experiment with the HPTS solution having the same HPTS concentration as that in the HPTS-pos suspension ( $C_{f,bulk}$ , Table 5). It took about 2.5 h for each experiment; the experiment with HPTS-pos suspension and its control experiment were performed sequentially so as to minimize the potential influence of temperature. In this way, the time lag ( $\Delta\tau = \tau_{pos} - \tau_{Blank}$ ) was though mainly dependent on the characteristics of the polymersomes, like the thickness [14,34] and the chemical composition [25] of the membranes.

The relation between the measured  $\Delta\tau$  values and the membrane thicknesses ( $t_l$ ) was discussed with the aid of the commonly-known parameter, that is the membrane permeability ( $P$ ).

According to Fick’s first law, membrane thickness ( $t_l$ ) and membrane permeability ( $P$ ) obey the following relation [14]:

$$P = D^* / t_l \quad (10)$$

with  $D^*$  being the apparent diffusion coefficient of H<sup>+</sup> herein.

On the other hand, the decay time, in fact the decay time difference under current conditions ( $\Delta\tau$ ) is related to  $P$  via the following equation [35]:

$$\Delta\tau = C \cdot R_{outer} / P \quad (11)$$

with  $C$  being a constant (without unit) and  $R_{outer}$  being the exterior radius of the polymersomes as  $R_{outer} = R_H - t_h$  illustrated in Scheme 1.

Substituting Equation 10 into Equation 11, a relationship between  $\Delta\tau$  and  $t_t$  is obtained, in the form of

$$\frac{\Delta\tau}{R_{\text{outer}}} = \frac{C}{D^*} \times t_t \quad (12)$$

For the PGL-PBO-PGL polymersome membranes studied herein, the apparent diffusion coefficient ( $D^*$ ) to H<sup>+</sup> is constant, thus  $\Delta\tau/R_{\text{outer}}$  should be linear to  $t_t$ .

Figure 9 portrayed the plot of  $\Delta\tau/R_{\text{outer}}$  versus  $t_t$  as well as the linear fitting results. It can be seen that there was a good linearity between  $\Delta\tau/R_{\text{outer}}$  and  $t_t$  with R<sup>2</sup> value as 0.91, evidencing the reliability of the  $\Delta\tau$  values.

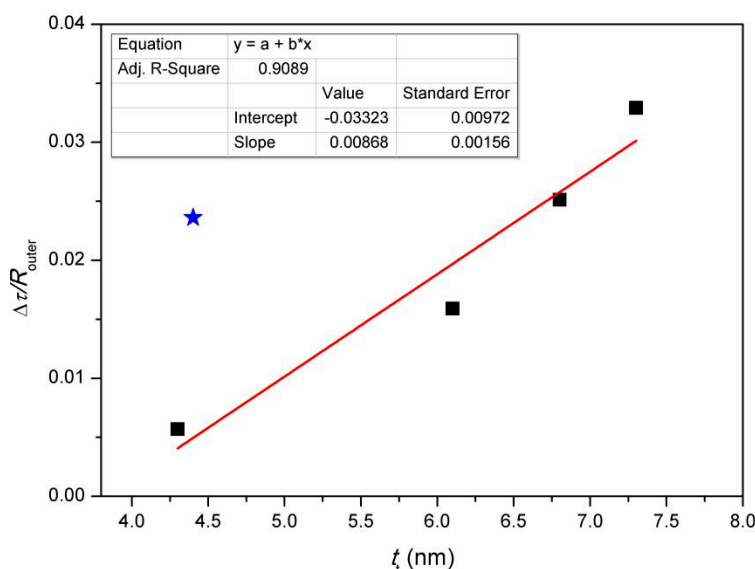


**Figure 9.** Plot of  $\Delta\tau/R_{\text{outer}}$  against  $t_t$  (Equation 12) in the context of the polymersomes made from linear triblock copolymers PGL-PBO-PGL. The blue star is the data of the HPTS-pos of  $\beta\text{CD}-(\text{PBO}_{13}\text{-PGL}_6)_{14}$  (Entry 151-2).

As showed above that the  $R_{\text{outer}}$ -normalized time lag ( $\Delta\tau/R_{\text{outer}}$ ) was proportional to the membrane thickness ( $t_t$ ) in the context of the polymersomes made from linear triblock copolymers. But the data of the star-copolymer-formed polymersomes (Entry 151-2) deviated far from the master curve, as shown in Figure 9 (the blue star). It is worth to mention that the polymersomes made from  $\beta\text{CD}-(\text{PBO}_{13}\text{-PGL}_6)_{14}$  (Entry 151-2) has the similar hydrophobic thickness ( $t_t = 4.4$  nm) to that of the polymersome made of PGL<sub>6</sub>-PBO<sub>20</sub>-PGL<sub>6</sub> (Entry 031-1,  $t_t = 4.3$  nm), however the star-copolymer-formed polymersome membrane had a much larger  $\Delta\tau/R_{\text{outer}}$  value, meaning it had a

much smaller permeability to  $H^+$  (Equation 11). This was supposed to originate from the hydrophobic cavity of the  $\beta$ CD core, which prevented the permeation of  $H^+$  [36].

#### 4. Conclusions

In this part, HPTS was used as the pH indicator of the vesicular interior pH, so as to study the polymersome membrane permeability to  $H^+$ . First of all, the HPTS probes were encapsulated inside the polymersomes by hydrating the polymer film with HPTS solution. The encapsulation efficiency (EE) of HPTS probes was found quite low, might be limited by the preparation methodology and the extensive dialysis process which was applied to remove the unencapsulated probes. Additionally, in current conditions, the EE values were found related with the thickness of the polymersome membrane ( $t_i$ ) and the morphology-decided factor, namely the weight fraction of PGL blocks ( $w_{PGL}$ ) in the cases of both the linear triblock copolymers and the  $\beta$ CD-cored star copolymers. Relatively high EE values were obtained only with the polymers having proper  $w_{PGL}$  and relatively long PBO segments allowing to self-assemble into defined polymersomes with thicker membranes.

The HPTS-pos with varied membrane thicknesses or compositions were studied in the aspect of polymersome membrane permeability to  $H^+$ . With an optimized protocol, the permeability to  $H^+$  was analyzed quantitatively via a modified decay time-permeation method. First, it was found that  $H^+$  permeated all the membranes fast under current conditions. Secondly, the calculation results indicated that for the polymersomes composed of linear triblock copolymers the radius-normalized decay time lag ( $\Delta\tau/R_{outer}$ ) was proportional to the membrane thickness ( $t_i$ ). Thirdly, results also showed that the hydrophobic cavity of the  $\beta$ CD cores embedded in the middle of the membrane prevented the permeation of  $H^+$  to some extent.

#### 5. References

1. Iqbal S, Blenner M, Alexander-Bryant A, et al. Polymersomes for therapeutic delivery of protein and nucleic acid macromolecules: from design to therapeutic applications[J]. *Biomacromolecules*, 2020, 21(4): 1327-1350.
2. Zhu Y, Yang B, Chen S, et al. Polymer vesicles: Mechanism, preparation, application, and responsive behavior[J]. *Progress in Polymer Science*, 2017, 64: 1-22.
3. Zartner L, Muthwill M S, Dinu I A, et al. The rise of bio-inspired polymer compartments responding to pathology-related signals[J]. *Journal of Materials Chemistry B*, 2020, 8(29): 6252-6270.
4. Mu X, Gan S, Wang Y, et al. Stimulus-responsive vesicular polymer nano-integrators for drug and gene delivery[J]. *International journal of nanomedicine*, 2019, 14: 5415.
5. Che H, van Hest J C M. Adaptive polymersome nanoreactors[J]. *ChemNanoMat*, 2019,

- 5(9): 1092-1109.
6. Chen Q, Schönherr H, Vancso G J. Block-Copolymer Vesicles as Nanoreactors for Enzymatic Reactions[J]. *Small*, 2009, 5(12): 1436-1445.
  7. Vance J A, Devaraj N K. Membrane Mimetic Chemistry in Artificial Cells[J]. *Journal of the American Chemical Society*, 2021.
  8. Rideau E, Dimova R, Schwille P, et al. Liposomes and polymersomes: a comparative review towards cell mimicking[J]. *Chemical society reviews*, 2018, 47(23): 8572-8610.
  9. Baumann P, Spulber M, Fischer O, et al. Investigation of Horseradish Peroxidase Kinetics in an “Organelle-Like” Environment[J]. *Small*, 2017, 13(17): 1603943.
  10. Einfalt T, Witzigmann D, Edlinger C, et al. Biomimetic artificial organelles with in vitro and in vivo activity triggered by reduction in microenvironment[J]. *Nature communications*, 2018, 9(1): 1-12.
  11. Nichols J W, Abercrombie R F. A view of hydrogen/hydroxide flux across lipid membranes[J]. *The Journal of membrane biology*, 2010, 237(1): 21-30.
  12. Choucair A, Lim Soo P, Eisenberg A. Active loading and tunable release of doxorubicin from block copolymer vesicles[J]. *Langmuir*, 2005, 21(20): 9308-9313.
  13. Bertrand N, Bouvet C, Moreau P, et al. Transmembrane pH-gradient liposomes to treat cardiovascular drug intoxication[J]. *ACS nano*, 2010, 4(12): 7552-7558.
  14. Paxton W F, Price D, Richardson N J. Hydroxide ion flux and pH-gradient driven ester hydrolysis in polymer vesicle reactors[J]. *Soft Matter*, 2013, 9(47): 11295-11302.
  15. Schroeder T B H, Leriche G, Koyanagi T, et al. Effects of lipid tethering in extremophile-inspired membranes on H<sup>+</sup>/OH<sup>-</sup> flux at room temperature[J]. *Biophysical journal*, 2016, 110(11): 2430-2440.
  16. Hanneschlaeger C, Horner A, Pohl P. Intrinsic membrane permeability to small molecules[J]. *Chemical reviews*, 2019, 119(9): 5922-5953.
  17. LoPresti C, Lomas H, Massignani M, et al. Polymersomes: nature inspired nanometer sized compartments[J]. *Journal of Materials Chemistry*, 2009, 19(22): 3576-3590.
  18. Palivan C G, Goers R, Najer A, et al. Bioinspired polymer vesicles and membranes for biological and medical applications[J]. *Chemical society reviews*, 2016, 45(2): 377-411.
  19. Wu J, Eisenberg A. Proton diffusion across membranes of vesicles of poly(styrene-b-acrylic acid) diblock copolymers[J]. *Journal of the American Chemical Society*, 2006, 128(9): 2880-2884.
  20. Parnell A J, Tzokova N, Topham P D, et al. The efficiency of encapsulation within surface rehydrated polymersomes[J]. *Faraday discussions*, 2009, 143: 29-46.
  21. Hope M J, Bally M B, Webb G, et al. Production of large unilamellar vesicles by a rapid extrusion procedure. Characterization of size distribution, trapped volume and ability to maintain a membrane potential[J]. *Biochimica et Biophysica Acta (BBA)-Biomembranes*, 1985, 812(1): 55-65.
  22. Wehr R, Gaitzsch J, Daubian D, et al. Deepening the insight into poly(butylene oxide)-block-poly(glycidol) synthesis and self-assemblies: micelles, worms and vesicles[J]. *RSC advances*, 2020, 10(38): 22701-22711.
  23. Chakraborty S, Nandi S, Bhattacharyya K, et al. Time Evolution of Local pH Around a Photo-Acid in Water and a Polymer Hydrogel: Time Resolved Fluorescence Spectroscopy of Pyranine[J]. *ChemPhysChem*, 2019, 20(23): 3221-3227.

24. Siwick B J, Bakker H J. On the role of water in intermolecular proton-transfer reactions[J]. *Journal of the American Chemical Society*, 2007, 129(44): 13412-13420.
25. Avnir Y, Barenholz Y. pH determination by pyranine: medium-related artifacts and their correction[J]. *Analytical biochemistry*, 2005, 347(1): 34-41.
26. Paula S, Volkov A G, Van Hoek A N, et al. Permeation of protons, potassium ions, and small polar molecules through phospholipid bilayers as a function of membrane thickness[J]. *Biophysical journal*, 1996, 70(1): 339-348.
27. Xu X, Khan M A, Burgess D J. Predicting hydrophilic drug encapsulation inside unilamellar liposomes[J]. *International journal of pharmaceutics*, 2012, 423(2): 410-418.
28. Liu G Y, Lv L P, Chen C J, et al. Biocompatible and biodegradable polymersomes for pH-triggered drug release[J]. *Soft Matter*, 2011, 7(14): 6629-6636.
29. Adams D J, Adams S, Atkins D, et al. Impact of mechanism of formation on encapsulation in block copolymer vesicles[J]. *Journal of controlled release*, 2008, 128(2): 165-170.
30. Messenger L, Gaitzsch J, Chierico L, et al. Novel aspects of encapsulation and delivery using polymersomes[J]. *Current opinion in pharmacology*, 2014, 18: 104-111.
31. Kamata Y, Parnell A J, Gutfreund P, et al. Hydration and ordering of lamellar block copolymer films under controlled water vapor[J]. *Macromolecules*, 2014, 47(24): 8682-8690.
32. Hu M, Shen Y, Zhang L, et al. Polymersomes via self-assembly of amphiphilic  $\beta$ -cyclodextrin-centered triarm star polymers for enhanced oral bioavailability of water-soluble chemotherapeutics[J]. *Biomacromolecules*, 2016, 17(3): 1026-1039.
33. Lomas H, Du J, Canton I, et al. Efficient Encapsulation of Plasmid DNA in pH-Sensitive PMPC-PDPA Polymersomes: Study of the Effect of PDPA Block Length on Copolymer-DNA Binding Affinity[J]. *Macromolecular bioscience*, 2010, 10(5): 513-530.
34. Battaglia G, Ryan A J, Tomas S. Polymeric vesicle permeability: a facile chemical assay[J]. *Langmuir*, 2006, 22(11): 4910-4913.
35. Hanneschlaeger C, Barta T, Pechova H, et al. The effect of buffers on weak acid uptake by vesicles[J]. *Biomolecules*, 2019, 9(2): 63.
36. Murata K, Mitsuoka K, Hirai T, et al. Structural determinants of water permeation through aquaporin-1[J]. *Nature*, 2000, 407(6804): 599-605.

## **Chapter 5.**

**Polymeric Membrane Permeability to  $K^+$  and  $Cl^-$ :**

**Black lipid membrane-type electric measurements**

## Content

<b>1. Introduction.....</b>	<b>217</b>
<b>2. Materials and Methods.....</b>	<b>217</b>
2.1 Materials.....	217
2.2 BLM-type electric measurements.....	218
<b>3. Results and Discussion.....</b>	<b>220</b>
3.1 Investigation of the ability to form planar polymeric membranes from linear copolymers.....	220
3.2 Attempts to insert synthetic nanopores into planar polymeric membranes.....	223
3.3 Attempts to insert biological nanopores into planar polymeric membranes....	226
3.4 Investigation of the ability to form planar polymeric membranes from star copolymers.....	229
<b>4. Conclusions.....</b>	<b>231</b>
<b>5. References.....</b>	<b>232</b>

## 1. Introduction

The first results of membrane permeability obtained for the  $PGL_n$ - $PBO_{2m}$ - $PGL_n$  polymersomes were related to proton permeability (Chapter 4). While these results are relevant for a mitochondrial exchange with the surrounding cytoplasm modelisation [1,2], other inorganic salts may also be of interest since the well-known balance between  $K^+$  and  $Na^+$  is of fundamental importance to maintain the cell homeostasis [3]. Determination of such cation permeability through an amphiphilic membrane can hardly be achieved by fluorometry, but we observed that black lipid membrane-type electric detection could provide interesting results for membranes obtained from lipids [4–6]. This technique is adapted from Coulter counter experiments and can be extended to the analysis of cell membranes in the case of patch-clamp analysis.

While the study of polymeric vesicles has exploded, few investigations on polymeric membrane permeability using this BLM-type technique has been reported [7,8]. We believe that the change of scale could be an explanation, *i.e.* the vesicles are at the 100 nanometer scale, while the polymeric membranes for electric detection must be formed at a 100 micrometer scale, and be stable at time scale above a few hours. This large-scale difference might have discouraged many researchers from investigation using this technique. However, in the present analysis, we suggest the study of membrane stability of amphiphilic copolymers for electric detection, and we will perform seminal analysis of  $K^+$  and  $Cl^-$  permeation through these polymeric membranes, depending on their physical characteristics.

## 2. Materials and Methods

### 2.1 Materials

The series of linear triblock copolymers,  $PGL_n$ - $PBO_{2m}$ - $PGL_n$ , as well as two selected star copolymers,  $\beta CD$ - $(PBO_m$ - $PGL_n)_{14}$ , used for this black lipid membrane (BLM)-type investigation, were synthesized via ring-opening copolymerization as detailed in Chapter 2 and Chapter 3, respectively. In the meantime, They were also characterized as copolymer on one hand and as self-assembled structure on the other hand. The main characteristics of these copolymers and their self-assembled structures are collected in Table 1.

**Table 1.** Characteristics of Copolymers and the Respective Self-assemblies According to the Weight Fraction of PGL Blocks ( $w_{\text{PGL}}$ ).

Amphiphilic copolymers				DLS analysis		
Entry	Formula	$M_n$ ( $\text{kg mol}^{-1}$ )	$w_{\text{PGL}}$	$R_H$ (nm)	PDI	Morphology
<b>Linear triblock copolymers</b>						
HQ153	PGL <sub>11</sub> -PBO <sub>85</sub> -PGL <sub>11</sub>	7.2	0.20	- <sup>a</sup>		Aggregates
SK1	PGL <sub>8</sub> -PBO <sub>78</sub> -PGL <sub>8</sub>	7.2	0.20			
SK2	PGL <sub>9</sub> -PBO <sub>68</sub> -PGL <sub>9</sub>	6.5	0.22	65	0.18	Mixture of Polymersomes and Aggregates
SK3	PGL <sub>8</sub> -PBO <sub>59</sub> -PGL <sub>8</sub>	5.8	0.25	85	0.10	
SK4	PGL <sub>10</sub> -PBO <sub>49</sub> -PGL <sub>10</sub>	5.1	0.28	89	0.13	Polymersomes
SK5	PGL <sub>8</sub> -PBO <sub>42</sub> -PGL <sub>8</sub>	4.4	0.33	95	0.13	
SK6	PGL <sub>9</sub> -PBO <sub>33</sub> -PGL <sub>9</sub>	3.7	0.38	50	0.26	
HQ034	PGL <sub>6</sub> -PBO <sub>20</sub> -PGL <sub>6</sub>	2.4	0.35	88	0.21	
<b>Star Copolymers</b>						
HQ152	$\beta$ CD-(PBO <sub>30</sub> -PGL <sub>4</sub> ) <sub>14</sub>	35.8	0.11	- <sup>a</sup>		Aggregates
HQ151	$\beta$ CD-(PBO <sub>13</sub> -PGL <sub>6</sub> ) <sub>14</sub>	21.4	0.28	90	0.10	Polymersomes
HQ093	$\beta$ CD-(PBO <sub>8</sub> -PGL <sub>12</sub> ) <sub>14</sub>	22.2	0.57	7.7	0.28	Micelles

<sup>a</sup>No data.

Other chemicals include KCl (VWR), decane (anhydrous, Sigma–Aldrich), CHCl<sub>3</sub> (VWR), methanol (VWR), and melittin from honey bee venom (> 85% HPLC, Sigma–Aldrich). All are used as received.

## 2.2 BLM-type electric measurements

The BLM technique consists in measuring electric currents through an amphiphilic membrane, separating two compartments filled with a concentrated salt solution, by applying a voltage. The intensity is recorded as a function of time and as a function of the applied voltage. The home-made set-up is made up of several elements as shown in Figure 1.

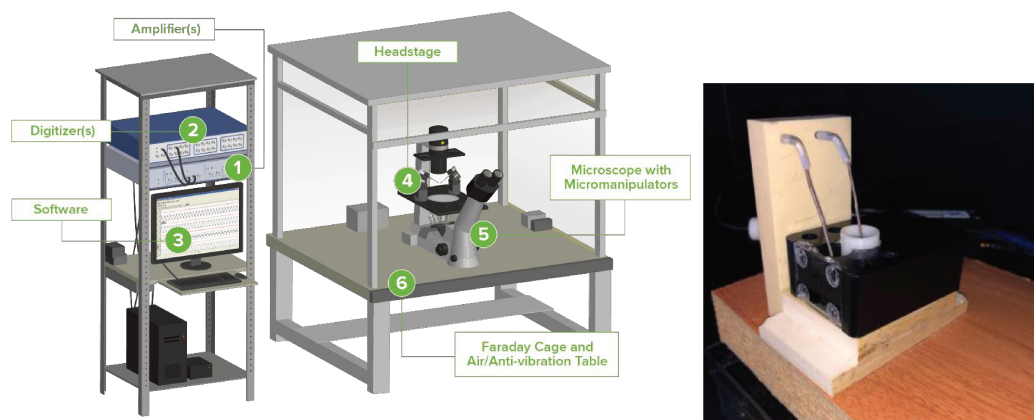


**Figure 1.** (Left) Scheme of the BLM set-up [9], and (Right) picture of a typical home-made BLM base.

The left panel of Figure 1 schematically shows the different elements of the BLM set-up. The central element of the device is the amplifier (BLM Axopatch 200B – 1) which measures the electric current passing through the membrane for an applied voltage. This amplifier is directly connected to a digitizer (2) to convert the collected analogic signals into digital signals. Data are acquired at 100 kHz and filtered at 10 kHz with the Measured Computing Digitizer. The two mentioned elements are connected to a computer where a software (Labview – 3) allows visualizing the results. All the data are analyzed via IGOR Pro software.

The base of the set-up (4) has two chambers where Ag/AgCl electrodes are inserted, allowing the desired voltage to be applied (the right panel of Figure 1). They are usually filled with KCl solution, here 1 M KCl solution. This set-up is protected from electric and environmental noises thanks to a Faraday cage and air/anti-vibration table (6). The microscope (5) helps us to form the bilayers.

It has been reported that lipid bilayers are mostly impermeable to ions, meaning that, when the voltage is applied on each side of the membrane, the current is equal to zero: the  $K^+$  and  $Cl^-$  ions cannot pass through the membrane, preventing any intensity detection. When the membrane is porous (permeable) or when a channel is inserted in the lipid bilayers, ion diffusion is allowed. We observe in Figure 2 current jumps corresponding to the ion fluxes at the opening and the closing of a pore that is inserted from time to time in a lipid bilayer [4–6].

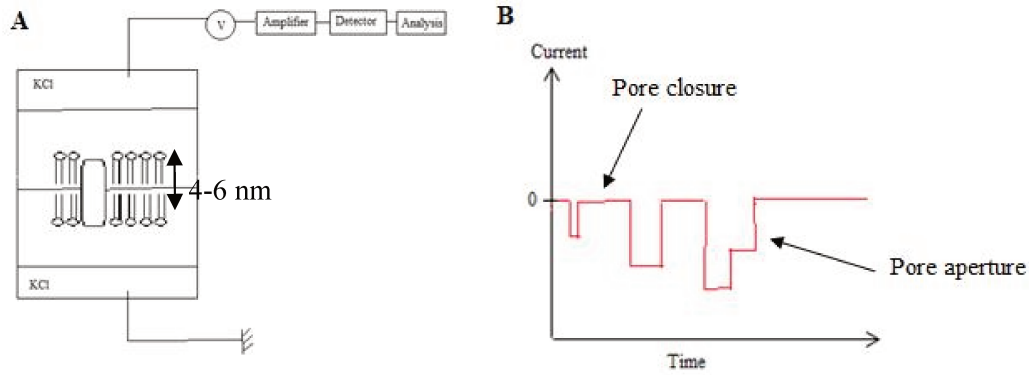


**Figure 2.** (A) Schematic representation of BLM set-up and (B) a typical record of intensity versus time obtained when a channel is incorporated and expelled from the membrane.

Experimentally, it is possible to measure a capacitance, which allows to characterize the membrane. Indeed, the capacitance ( $C$ ) is directly linked to the thickness of the membrane ( $e$ ) with the Equation 1:

$$C = \epsilon_0 \epsilon \frac{S}{e} \quad (1)$$

in which,  $S$  is the area of the bilayer which is delimited by the aperture of  $150 \mu\text{m}$  of diameter. So,  $S = \pi R^2$  with  $R$  being the radius of the aperture.  $S = 1.77 \times 10^{-8} \text{ m}^2$ ;  $\epsilon_0$  is the electrical permittivity of vacuum ( $\epsilon_0 = 8.8542 \times 10^{-12} \text{ F m}^{-1}$ ); and  $\epsilon$  is the dielectric constant of the bilayer ( $\sim 2$  of lipid bilayers).

### 3. Results and Discussion

#### 3.1 Investigation of the ability to form planar polymeric membranes from linear copolymers

To the best of our knowledge, few teams attempted to set a polymeric membrane on a  $150\text{-}\mu\text{m}$  large window and studied its stability as a function of time [7,8]. Furthermore, we observed that an antifouling property of PGL block is observed in water at DP above 10 [10]. One of our goals is to further study insertion of nanopores into polymeric membrane, thus we chose to perform the following studies with copolymers with a DP around 10 for PGL blocks.

In the present study, the usual lipid bilayer is replaced by a polymeric membrane that we attempt to form. To prepare a lipid bilayer, the lipid is dissolved in decane at a concentration of  $10 \text{ mg mL}^{-1}$ ,  $0.4 \mu\text{L}$  are deposited on the surface of the  $150\text{-}\mu\text{m}$  wide window and are left 40 minutes, before preparing the membrane. Then, the lipid

solution is used to paint the window until the formation of a stable lipid bilayer that fully separates both compartments of the set-up.

In the case of the polymeric membranes, we adapted and optimized the protocol from the work of Nardin et al. [11]: 5 mg of triblock copolymer was dissolved in a solvent mixture of 200  $\mu\text{L}$  of  $\text{CHCl}_3$ , 200  $\mu\text{L}$  of decane and 100  $\mu\text{L}$  of methanol. 1  $\mu\text{L}$  of this solution was deposited/painted on the surface of the 150- $\mu\text{m}$  window and left for 1 hour. After this time, the ‘painting’ operation was repeated. We call this step the formation of a pre-layer. After one hour of ‘drying’, the polymeric membrane was attempted to be formed, as mentioned in the case of lipid bilayers. To define the success of a membrane formation, we measured the recorded intensity plotted as a function of time, when a voltage was applied at both sides of the membrane. If a capacitance could be measured and if the recorded intensity was low, the separation of the two compartments was obtained and the formation of insulating membranes was demonstrated.

The Table 2 gathers the number of attempts performed from various copolymers and the number of membranes we managed to obtain.

**Table 2.** BLM Results for the Formation of Polymeric Membranes from Linear Copolymers.

Copolymer		BLM results	
Entry	Formula	Number of attempts	Number of insulating membranes obtained
HQ153	PGL <sub>11</sub> -PBO <sub>85</sub> -PGL <sub>11</sub>	5	3
SK3	PGL <sub>8</sub> -PBO <sub>59</sub> -PGL <sub>8</sub>	3	3
SK4	PGL <sub>10</sub> -PBO <sub>49</sub> -PGL <sub>10</sub>	4	2
SK5	PGL <sub>8</sub> -PBO <sub>42</sub> -PGL <sub>8</sub>	14	7
SK6	PGL <sub>9</sub> -PBO <sub>33</sub> -PGL <sub>9</sub>	8	3
HQ034	PGL <sub>6</sub> -PBO <sub>20</sub> -PGL <sub>6</sub>	8	3

The first information given by this table is that we managed to paint a large flat membrane using all the synthesized copolymers, whatever the assemblies they are providing (polymersomes, aggregates). It is necessary to note that the solvents used for BLM experiments are not the same as the one used for the study of the morphology and the phase diagram strongly depends on the solvent used. However, all the copolymers tested formed an insulating membrane, with different statistics of success, but still with a quite good percentage of success of the order of what is found

for lipids. It is noteworthy that the experimental capacitances obtained were similar to the ones obtained with lipid membranes, given an indication of the thickness of the membrane. Indeed, if we look at the literature [12], the dielectric constants of polymeric polymers are in the range of 2 to 4, we can then consider that the thickness of the polymeric membrane is around 4 to 8 nm, in agreement with the values obtained by SAXS analyses.

Figures 3 and 4 show the recorded intensity versus time (trace) obtained for two triblock copolymers (PGL<sub>8</sub>-PBO<sub>42</sub>-PGL<sub>8</sub> and PGL<sub>11</sub>-PBO<sub>85</sub>-PGL<sub>11</sub>) set in the 150- $\mu$ m window. These traces were representative of the traces obtained for all the tested copolymers.

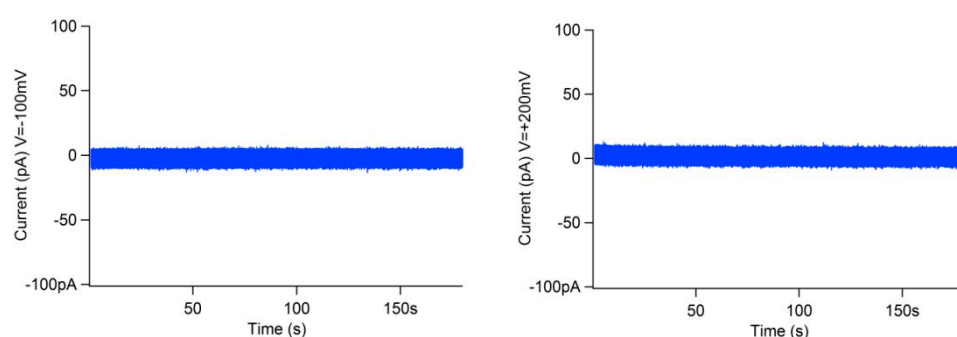


**Figure 3.** Current measurement as a function of time (zoom of 3 minutes of experiment run during 30 min per conditions) for PGL<sub>8</sub>-PBO<sub>42</sub>-PGL<sub>8</sub> with an applied voltage of -100 mV (left) and +200 mV (right).

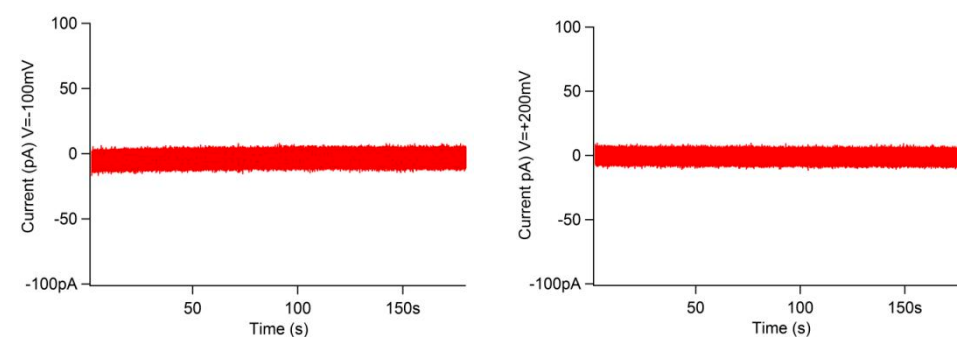


**Figure 4.** Current measurement as a function of time (zoom of 3 minutes of experiment run during 30 min per conditions) for PGL<sub>11</sub>-PBO<sub>85</sub>-PGL<sub>11</sub> with an applied voltage of -100 mV (left) and +200 mV (right).

The intensity versus time is constant up to thirty minutes at a value close to 0 pA for voltage up to +/-200 mV. The low diffusion of K<sup>+</sup> and Cl<sup>-</sup>, *i.e.* low intensity, remains constant all over the record period, suggesting that these membranes are very stable

much more than lipid membranes that tend to collapse at voltage higher than +/-100 mV.

From these results, one cannot strictly discriminate a non-permeable membrane from a semi-permeable membrane if no event characterizes the intensity (for example the insertion of a nanopore). However, the intensity versus time for all the tested copolymers is a constant value, typical for impermeable membrane. Indeed, semi-permeable membrane tends to give intensity that diverges from a constant value, different from the one can measure with this copolymer library. Furthermore, one can observe that changing a negative voltage to a positive voltage does not change the recorded intensity, a result that strongly supports the fact that the membranes are impermeable to KCl and that this 0-intensity value is issued from an intensity drift.

It was unexpected that, whatever the morphologies (polymersomes, aggregates), polymeric membranes were obtained. It is important to notice that the polymeric membranes were painted on a hole of 150  $\mu\text{m}$  of diameter, whereas the assemblies in solution had a size of 100–200 nm of diameter.

### 3.2 Attempts to insert synthetic nanopores into planar polymeric membranes

After the demonstration of polymeric membrane formation on the 150- $\mu\text{m}$  window, the insertion of  $\beta\text{CD}$ -based star synthetic nanopores in those polymeric membranes was attempted. To favour the nanopore insertion, a similar composition and chemical nature of the copolymer forming the membrane and that of the arms forming the nanopores was set. Then,  $\beta\text{CD}-(\text{PBO}_{30}\text{-PGL}_4)_{14}$  and  $\beta\text{CD}-(\text{PBO}_8\text{-PGL}_{12})_{14}$  were synthesized to fit at best with the copolymer membranes. It must be recalled that those star copolymers have been shown to insert in lipid bilayers [4].

Once the polymeric membrane formed, the star copolymer was gradually added, in both chambers of the BLM base (right panel of Figure 1), with the concentration of the stock star polymer solution being 5 mg mL<sup>-1</sup> in THF. The star polymers were placed in the presence of all the membranes discussed previously, and the current intensity versus time was then recorded for 30 minutes, after a voltage being applied. Variation of the recorded intensity versus time would demonstrate the interaction and the insertion of star copolymers in the polymeric membrane. The results are reported in Table 3.

**Table 3.** Attempts of Insertion of Star Copolymers in Polymeric Membranes

Copolymer membrane	Synthetic nanopores	Variation of the intensity <sup>a</sup>
PGL <sub>11</sub> -PBO <sub>85</sub> -PGL <sub>11</sub>	$\beta$ CD-(PBO <sub>30</sub> -PGL <sub>4</sub> ) <sub>14</sub>	2/2
	$\beta$ CD-(PBO <sub>8</sub> -PGL <sub>12</sub> ) <sub>14</sub>	0/1
PGL <sub>8</sub> -PBO <sub>59</sub> -PGL <sub>8</sub>	$\beta$ CD-(PBO <sub>30</sub> -PGL <sub>4</sub> ) <sub>14</sub>	0/1
	$\beta$ CD-(PBO <sub>8</sub> -PGL <sub>12</sub> ) <sub>14</sub>	0/1
PGL <sub>10</sub> -PBO <sub>49</sub> -PGL <sub>10</sub>	$\beta$ CD-(PBO <sub>8</sub> -PGL <sub>12</sub> ) <sub>14</sub>	0/2
PGL <sub>8</sub> -PBO <sub>42</sub> -PGL <sub>8</sub>	$\beta$ CD-(PBO <sub>8</sub> -PGL <sub>12</sub> ) <sub>14</sub>	0/3
PGL <sub>6</sub> -PBO <sub>20</sub> -PGL <sub>6</sub>	$\beta$ CD-(PBO <sub>8</sub> -PGL <sub>12</sub> ) <sub>14</sub>	0/1

<sup>a</sup>Results given on number of variation / number of attempts

Table 3 reports that no current variation induced by the star copolymers was recorded for all the copolymer membranes, except for the PGL<sub>11</sub>-PBO<sub>85</sub>-PGL<sub>11</sub> membrane associated to the  $\beta$ CD-(PBO<sub>30</sub>-PGL<sub>4</sub>)<sub>14</sub>, for which the intensity versus time is reported on Figure 5.

**A - Without  $\beta$ CD-(PBO<sub>30</sub>-PGL<sub>4</sub>)<sub>14</sub>**

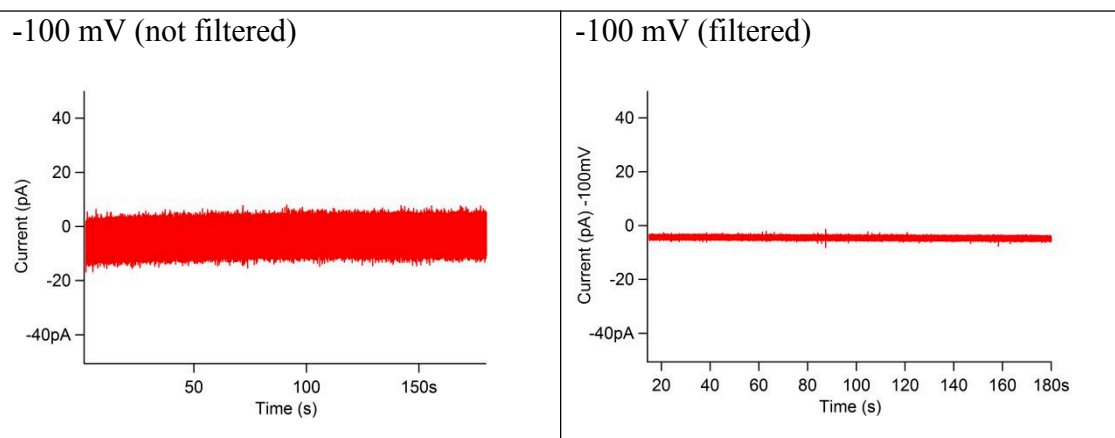
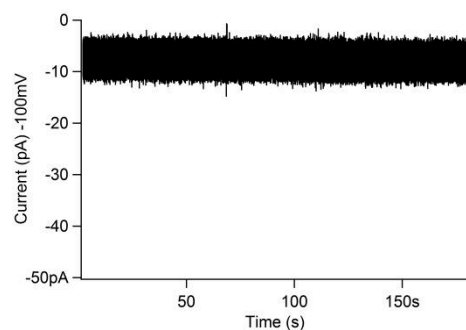


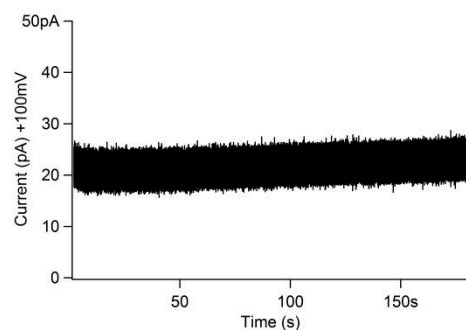
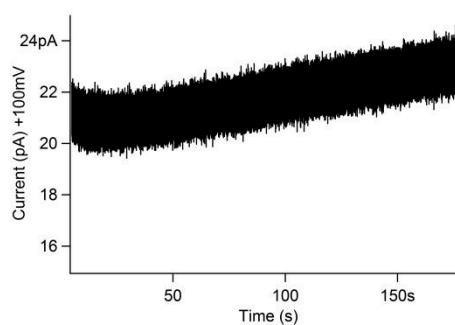
**Figure 5.** (A) Current measurement as a function of time for PGL<sub>11</sub>-PBO<sub>85</sub>-PGL<sub>11</sub> with an applied voltage of -100 mV without  $\beta$ CD-(PBO<sub>30</sub>-PGL<sub>4</sub>)<sub>14</sub>.

**B - With  $\beta$ CD-(PBO<sub>30</sub>-PGL<sub>4</sub>)<sub>14</sub>**

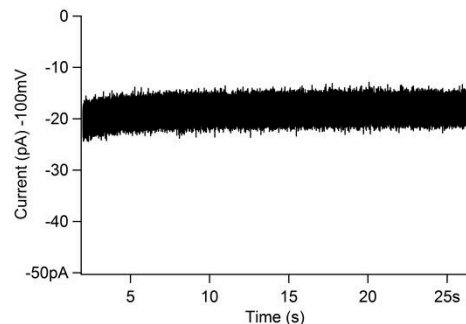
-100 mV after 15 minutes (not filtered)



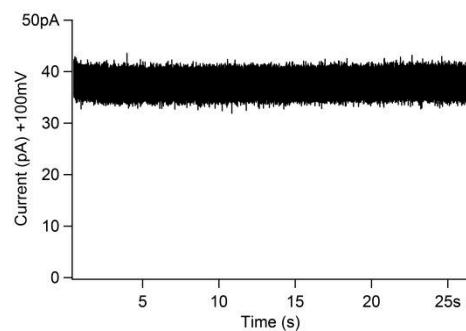
+100 mV after 30 minutes (not filtered)

+100 mV after 30 minutes (filtered)  
**trace C**

-100 mV (not filtered)



+100 mV after 1 hour (not filtered)



+100 mV after 1 hour (filtered)

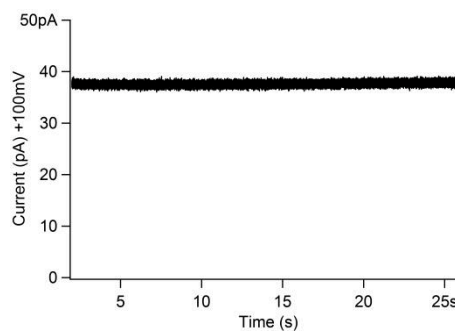


**Figure 5 (continued).** (B) Current measurement as a function of time for PGL<sub>11</sub>-PBO<sub>85</sub>-PGL<sub>11</sub> with  $\beta$ CD-(PBO<sub>30</sub>-PGL<sub>4</sub>)<sub>14</sub> 50  $\mu$ g mL<sup>-1</sup> at -100 mV and +100 mV, at different times after the addition of  $\beta$ CD-(PBO<sub>30</sub>-PGL<sub>4</sub>)<sub>14</sub>. Trace C emphasizes the zoomed and filtered signals.

Figure 5A presents the electrical trace obtained at -100mV, with PGL<sub>11</sub>-PBO<sub>85</sub>-PGL<sub>11</sub> polymeric membrane, without the addition of  $\beta$ CD-(PBO<sub>30</sub>-PGL<sub>4</sub>)<sub>14</sub>. A constant intensity value is recorded as a function of time, and a value close to zero is obtained. The membrane is then considered as impermeable. When  $\beta$ CD-(PBO<sub>30</sub>-PGL<sub>4</sub>)<sub>14</sub> is added in both compartments surrounding the copolymer membrane (Figure 5B), after 30 minutes, the current has changed from 0 pA to -20 pA, when applying a voltage of -100 mV, and from 0 pA to 20 pA, when applying a voltage of +100 mV, showing a permeabilization, namely, a porosity of the membrane attributed to the star copolymer. However, we do not observe current jumps as in Figure 2B, but a steady shift of the current with time (the trace C of Figure 5B).

According to the SAXS analyses discussed in the chapters 2 and 3, the hydrophobic thickness of the assembly formed from PGL<sub>11</sub>-PBO<sub>85</sub>-PGL<sub>11</sub> was found around 7 nm, similar as the one of the  $\beta$ CD-(PBO<sub>30</sub>-PGL<sub>4</sub>)<sub>14</sub>, whereas the characteristic hydrophobic dimension of  $\beta$ CD-(PBO<sub>8</sub>-PGL<sub>12</sub>)<sub>14</sub> was 3 nm. It was then expected that the variation of the intensity for the case PGL<sub>11</sub>-PBO<sub>85</sub>-PGL<sub>11</sub>/ $\beta$ CD-(PBO<sub>30</sub>-PGL<sub>4</sub>)<sub>14</sub> was observed, considering the thickness, namely the hydrophobic length.

### 3.3 Attempts to insert biological nanopores into planar polymeric membranes

A work published in September 2021 by Meier et coll. [13] showed the possibility to insert membrane protein OmpF in Giant Unilamellar Vesicles obtained from assemblies of PBO-PGL diblock copolymers. In parallel to this work and considering the difficulty to insert synthetic nanopores in the polymeric membranes, it was therefore decided to investigate the insertion of melittin in the polymeric membranes. It has to be noted that the modes of action of melittin on the lipid bilayers are various and that there is no consensus concerning the interactions existing between melittin and lipid bilayers, varying from hemolytic activity, to voltage-gated channel formation and melittin-induced bilayer micellization and fusion [14–17]. Still, it is accepted that the poration of a lipidic membrane by melittin is addressed by melittin aggregates of various size, conducting to ill-defined intensity signal.

Herein, melittin was dissolved in DMSO at a concentration of 1 mg mL<sup>-1</sup> and was added gradually, in both chambers of the BLM base, after the formation of polymeric membranes, for three copolymers: PGL<sub>11</sub>-PBO<sub>85</sub>-PGL<sub>11</sub>, PGL<sub>10</sub>-PBO<sub>49</sub>-PGL<sub>10</sub> and PGL<sub>9</sub>-PBO<sub>33</sub>-PGL<sub>9</sub>. The membrane thicknesses issued from these copolymers ranged between 4 and 8 nm.

No change of the intensity versus time was recorded when melittin was placed in the vicinity of PGL<sub>11</sub>-PBO<sub>85</sub>-PGL<sub>11</sub> and PGL<sub>10</sub>-PBO<sub>49</sub>-PGL<sub>10</sub> membrane, suggesting that no melittin insertion in the copolymer membrane occurred for this range of

membrane thickness, with a PBO hydrophobic layer. However, the data with the triblock PGL<sub>9</sub>-PBO<sub>33</sub>-PGL<sub>9</sub> membrane and melittin are shown in Figure 6.

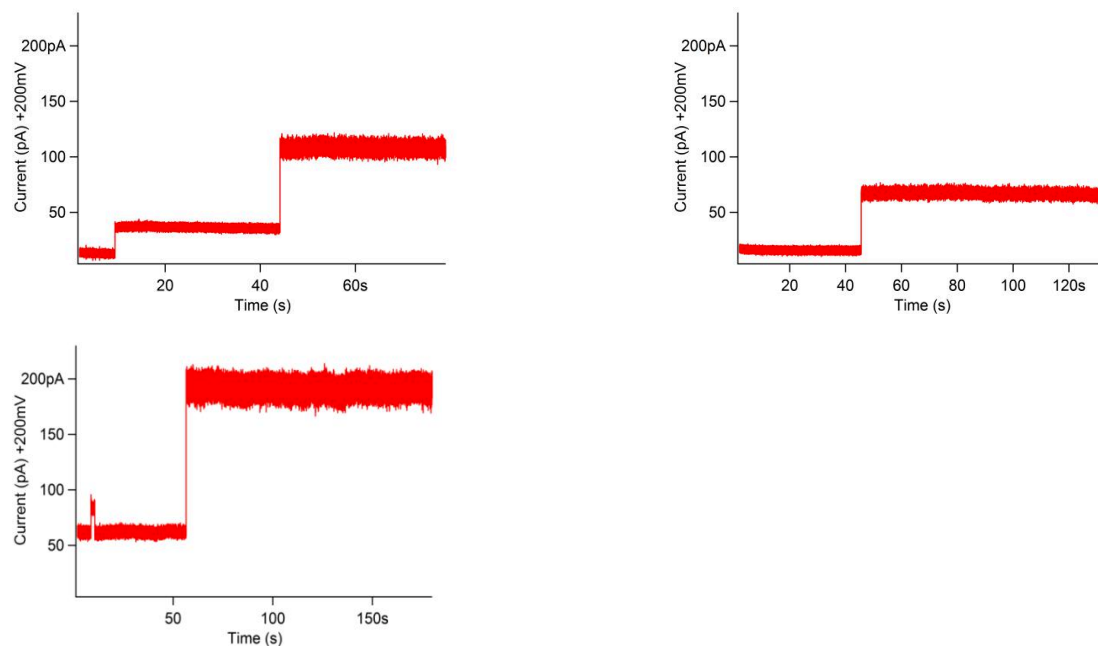


**Figure 6.** Current measurement as a function of time for PGL<sub>9</sub>-PBO<sub>33</sub>-PGL<sub>9</sub> (Capacitance = 29 pF) with an applied voltage of +200 mV, in the presence of melittin ( $30 \mu\text{g mL}^{-1}$ ).

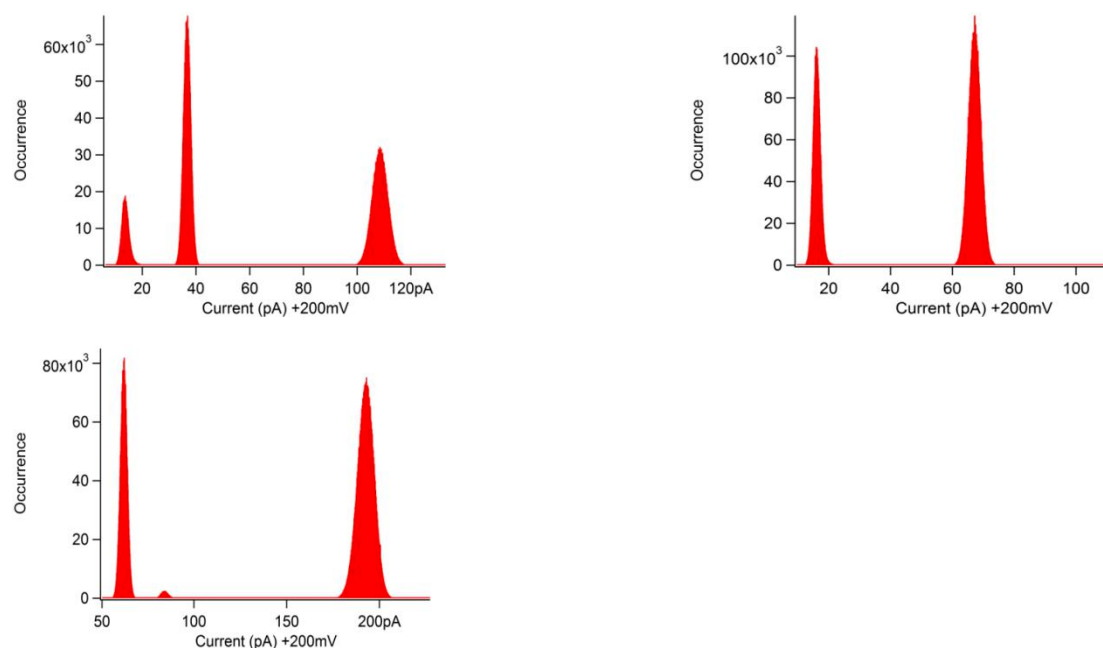


**Figure 7.** Occurrence as a function of current for PGL<sub>9</sub>-PBO<sub>33</sub>-PGL<sub>9</sub> (Capacitance = 29 pF) with an applied voltage of +200 mV (analysis of the traces in Figure 6), in the presence of melittin ( $30 \mu\text{g mL}^{-1}$ )

In Figure 6, the presence of current jumps and breaks such as the schematic representation in Figure 2 allows us to conclude on the insertion of melittin at  $30 \mu\text{g mL}^{-1}$ . Figure 7 shows the occurrence as a function of the current. The occurrence corresponds to the number of points with the same current value. This implies that for a population with the same current, a peak will be represented on the plot given the occurrence versus the current.

We can estimate, on the Figure 7, for an applied voltage of +200 mV, different populations at about 14 pA, 37 pA, 60 pA, 67 pA, 84 pA, 108 pA and 192 pA. When nanopores are inserted in lipid membranes, it is possible to estimate the unitary current induced by the insertion of the melittin, by plotting the current versus the number of pores (Figure 8).

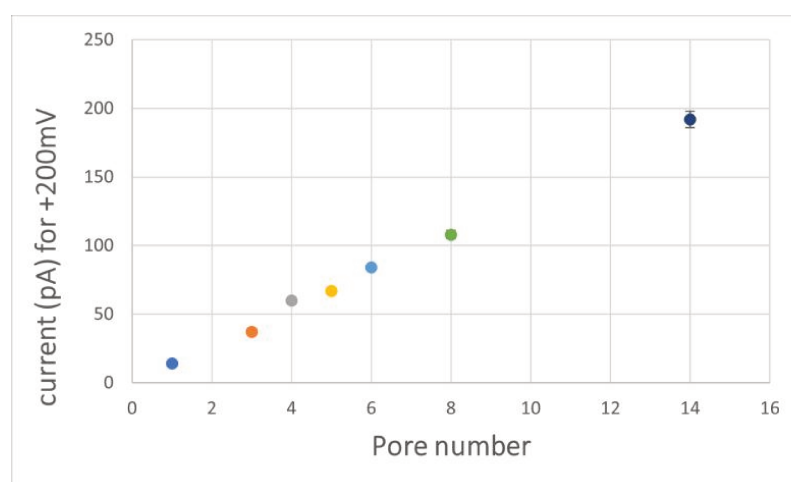


**Figure 8.** Current induced by the insertion of melittin ( $30 \mu\text{g mL}^{-1}$ ) v.s. the number of pores (applied voltage of +200 mV).

It seems possible that the first jump (14 pA) corresponds to the insertion of one pore constituted by melittin, the other values corresponding to multiple insertions of the melittin.

The experiment was then repeated to confirm/infirm the insertion of nanopores in the polymeric membrane. Figure 9 shows the results obtained.

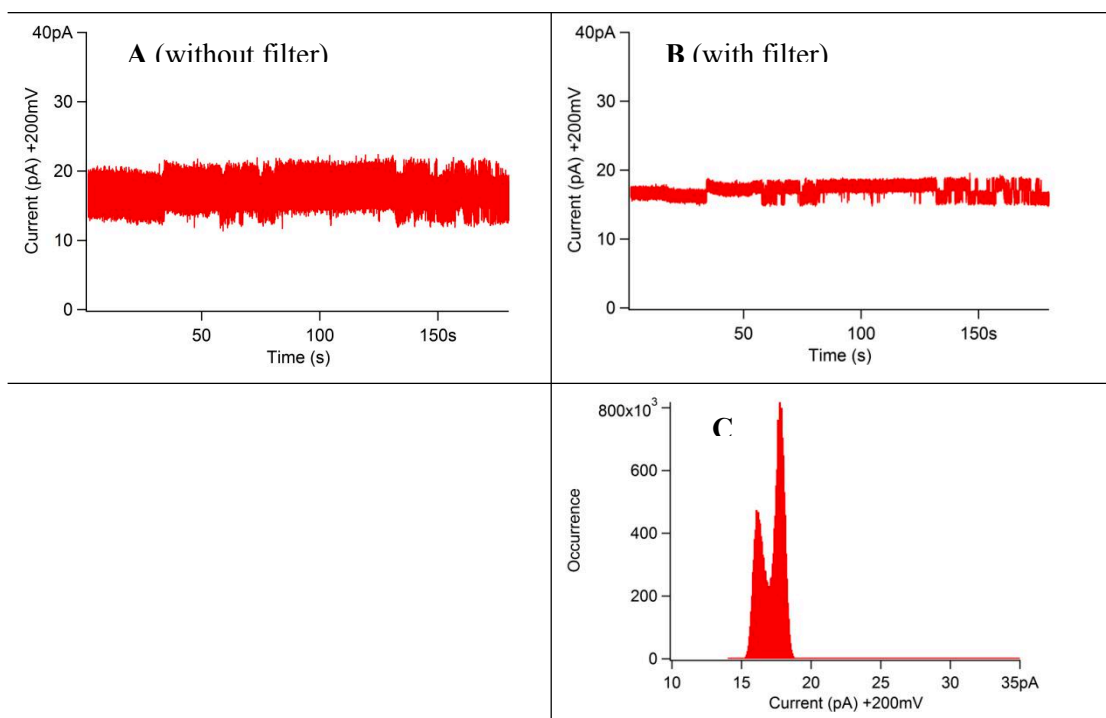


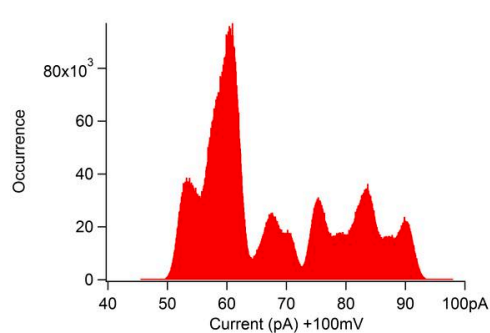
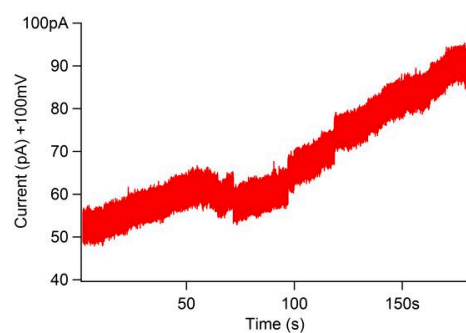
**Figure 9.** (A, B) Current measurement as a function of time (zoom of 3 minutes of an experiments run during 30 min per conditions) and (C) corresponding occurrence for PGL<sub>9</sub>-PBO<sub>33</sub>-PGL<sub>9</sub> (Capacitance = 26 pF) with an applied voltage of +200 mV, in the presence of melittin (15  $\mu\text{g mL}^{-1}$ ). A without filter, and B with filter.

In Figure 9, the presence of current jumps and breaks is demonstrated, allowing to conclude on the insertion of melittin at 15  $\mu\text{g mL}^{-1}$ . The current jumps are less intense than the ones observed in the first experiments (Figure 6). It is necessary to emphasize the fact that the capacitance of the membrane was lower, meaning that the polymeric membrane thickness is higher, and that the concentration of melittin was lower, that could explain these lower values of currents. We still need to repeat the experiments to have statistics on our results.

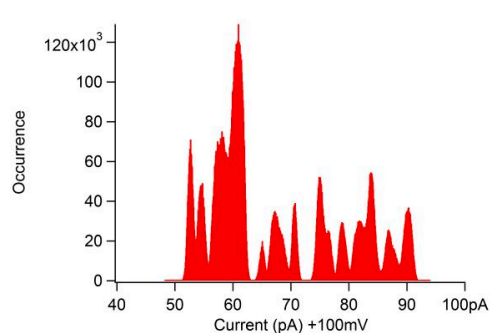
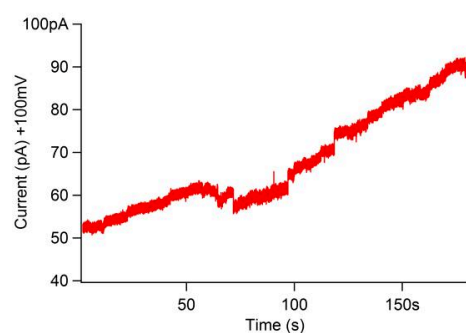
### 3.4 Investigation of the ability to form planar polymeric membranes from star copolymers

In a last attempt, we wanted to investigate the ability of  $\beta\text{CD}-(\text{PBO}_{13}\text{-PGL}_6)_{14}$  star copolymer to form planar polymeric membrane and to study the permeability to KCl. 5 mg of the star copolymer was dissolved in a solvent mixture of 250  $\mu\text{L}$  of decane, 50  $\mu\text{L}$  of  $\text{CHCl}_3$  and 50  $\mu\text{L}$  of methanol. 1  $\mu\text{L}$  of this solution is deposited/painted on the surface of the white cell and left for 1 hour. After this time, the ‘painting’ operation is repeated. After one hour of ‘drying’ (pre-layer), a polymeric membrane is attempted to be formed. Figure 10 presents the results obtained.

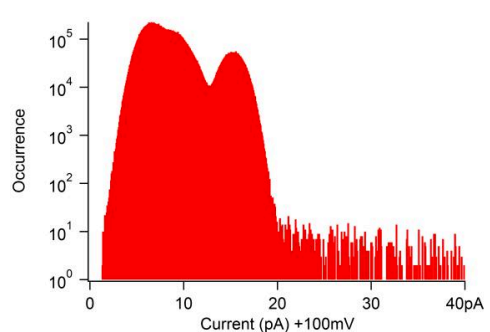
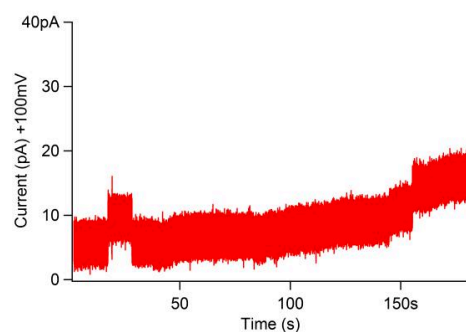
**First attempt: Trace A (without filter)**



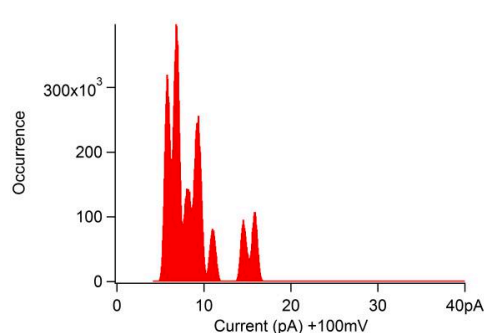
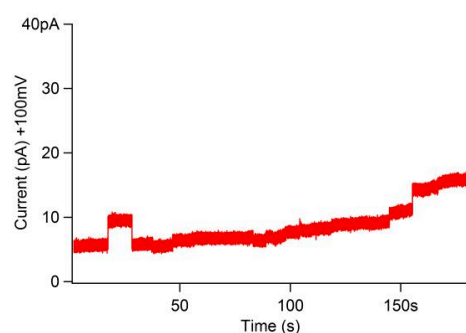
**Trace B : trace A with filter**



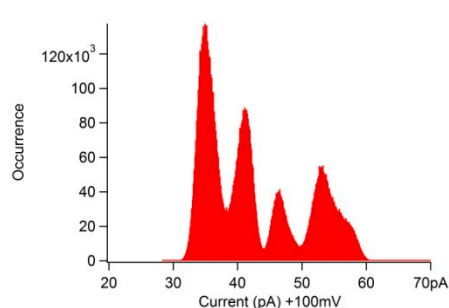
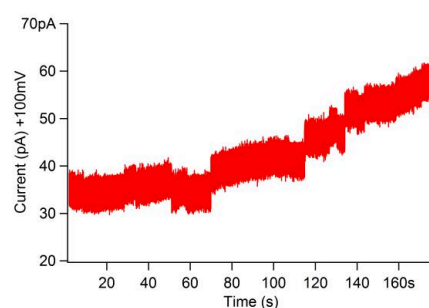
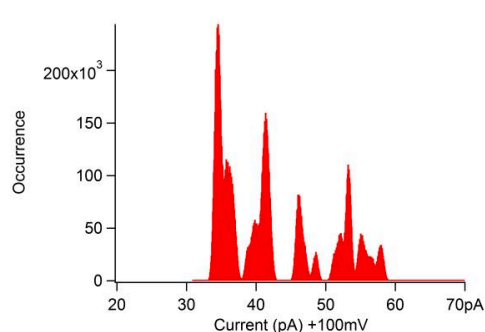
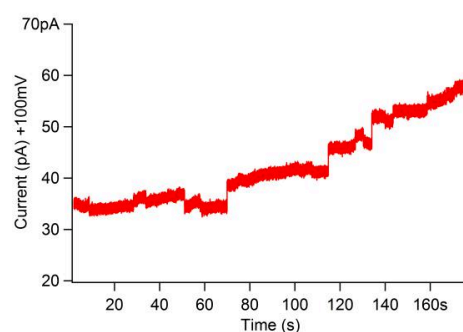
**Second attempt: Trace C (without filter)**



**Trace D : trace C with filter**



**Figure 10.** (Left panels) Current measurements as a function of time (zoom of 3 minutes, experiments during 30 min per conditions) and (Right panels) corresponding occurrence, for  $\beta$ CD-(PBO<sub>13</sub>-PGL<sub>6</sub>)<sub>14</sub> with an applied voltage of +100 mV.

**Third attempt:** Trace E (without filter)**Trace F :** trace E with filter

**Figure 10 (continued).** (Left panels) Current measurements as a function of time (zoom of 3 minutes, experiments during 30 min per conditions) and (Right panels) corresponding occurrence, for  $\beta$ CD-(PBO<sub>13</sub>-PGL<sub>6</sub>)<sub>14</sub> with an applied voltage of +100 mV.

Those results seem to demonstrate that the membranes obtained from  $\beta$ CD-(PBO<sub>13</sub>-PGL<sub>6</sub>)<sub>14</sub> let the K<sup>+</sup>Cl<sup>-</sup> ions pass through the membranes, in contrary to the membranes obtained from the linear copolymers. This porosity could be induced by the presence of the cavity of the beta-cyclodextrin. Indeed, if we look at the literature, the unitary currents of the star copolymers inserted in the lipid bilayers are in the same range than the ones obtained in these experiments [4–6]. However, we are a bit confused on the fact that the porosity/permeabilization increases versus time. We thought that this porosity would be indeed dependent on the number of nanopores present, but stable versus time, or at least would increase and decrease in case of dynamics of the membrane.

#### 4. Conclusions

The BLM method demonstrated that it was possible to obtain polymeric membranes regardless of the length of the hydrophobic part and the morphology in solution. This phenomenon has not been explained yet, but research is under way. The ability of  $\beta$ CD-based amphiphilic star copolymers to insert in the polymeric membranes has

not been proved yet but the insertion effect of the star copolymer was demonstrated. Finally, the insertion of biological nanopores (melittin) permits to constitute nanopores in the polymeric membrane of the triblock PGL<sub>9</sub>-PBO<sub>33</sub>-PGL<sub>9</sub>.

We have to keep in mind that these results are considered as preliminary results and that it is necessary to repeat the experiment to confirm all the results.

## 5. References

1. Brookes P S, Rolfe D F S, Brand M D. The proton permeability of liposomes made from mitochondrial inner membrane phospholipids: comparison with isolated mitochondria[J]. *The Journal of membrane biology*, 1997, 155(2): 167-174.
2. Yu Y, Jiang X, Gong S, et al. The proton permeability of self-assembled polymersomes and their neuroprotection by enhancing a neuroprotective peptide across the blood–brain barrier after modification with lactoferrin[J]. *Nanoscale*, 2014, 6(6): 3250-3258.
3. Clausen M J V, Poulsen H. Sodium/potassium homeostasis in the cell[M]//*Metallomics and the Cell*. Springer, Dordrecht, 2013: 41-67.
4. Faye I, Huin C, Illy N, et al.  $\beta$ -Cyclodextrin-Based Star Amphiphilic Copolymers: Synthesis, Characterization, and Evaluation as Artificial Channels[J]. *Macromolecular Chemistry and Physics*, 2019, 220(2): 1800308.
5. El Ghouli Y, Renia R, Faye I, et al. Biomimetic artificial ion channels based on beta-cyclodextrin[J]. *Chemical Communications*, 2013, 49(99): 11647-11649.
6. Eskandani Z, Le Gall T, Montier T, et al. Polynucleotide transport through lipid membrane in the presence of starburst cyclodextrin-based poly(ethylene glycol)s[J]. *The European Physical Journal E*, 2018, 41(11): 1-7.
7. Wong D, Jeon T J, Schmidt J. Single molecule measurements of channel proteins incorporated into biomimetic polymer membranes[J]. *Nanotechnology*, 2006, 17(15): 3710.
8. Martin M, Dubbs T, Fried J R. Planar Bilayer Measurements of Alamethicin and Gramicidin Reconstituted in Biomimetic Block Copolymers[J]. *Langmuir*, 2017, 33(5): 1171-1179.
9. <https://www.moleculardevices.com/technology/electrophysiology> (28/02/2021)
10. Du H, de Oliveira F A, Albuquerque L J C, et al. Polyglycidol-Stabilized Nanoparticles as a Promising Alternative to Nanoparticle PEGylation: Polymer Synthesis and Protein Fouling Considerations[J]. *Langmuir*, 2020, 36(5): 1266-1278.
11. Nardin C, Hirt T, Leukel J, et al. Polymerized ABA triblock copolymer vesicles[J]. *Langmuir*, 2000, 16(3): 1035-1041.
12. <https://polymerdatabase.com/polymer%20physics/Epsilon%20Table.html>
13. Wehr R, Dos Santos E C, Muthwill M S, et al. Fully amorphous atactic and isotactic block copolymers and their self-assembly into nano- and microscopic vesicles[J]. *Polymer chemistry*, 2021.
14. Dempsey C E. The actions of melittin on membranes[J]. *Biochimica et Biophysica Acta (BBA)-Reviews on Biomembranes*, 1990, 1031(2): 143-161.

15. Hanke W, Methfessel C, Wilmsen H U, et al. Melittin and a chemically modified trichotoxin form alamethicin-type multi-state pores[J]. *Biochimica et Biophysica Acta (BBA)-Biomembranes*, 1983, 727(1): 108-114.
16. Irudayam S J, Berkowitz M L. Binding and reorientation of melittin in a POPC bilayer: computer simulations[J]. *Biochimica et Biophysica Acta (BBA)-Biomembranes*, 2012, 1818(12): 2975-2981.
17. Lundquist A, Wessman P, Rennie A R, et al. Melittin–Lipid interaction: A comparative study using liposomes, micelles and bilayerdisks[J]. *Biochimica et Biophysica Acta (BBA)-Biomembranes*, 2008, 1778(10): 2210-2216.



## **General Conclusion and Perspectives**

This PhD project aimed to construct a versatile platform for nanotechnological applications, such as to serve for nanoreactor constructs. This platform was designed as a PGL-based polymersomal compartment with  $\beta$ CD-based artificial nanochannel scaffolds being inserted in the membrane. To achieve the targeted architecture, each component was first synthesized and well characterized in terms of polymer structures and amphiphilicity. Subsequently, the two components were combined and the resultant system was characterized.

First, well defined polymersomes made of linear amphiphilic block copolymers, either PBO-PGL or PGL-PBO-PGL, have been produced, possessing long-term storage stability (at least one month at 4 °C) and antifouling capacity versus various systemic proteins (BSA, IgG and lysozyme, at pH 7.4). Well-defined  $\beta$ CD-cored star amphiphilic copolymers,  $\beta$ CD-(PBO-PGL)<sub>14</sub>, have also been synthesized with tailor-made length of each block, low polydispersity and high purity. The self-assembly behaviors of the amphiphilic linear and star copolymers synthesized herein were similar, giving positive indication that they were chemically and dimensionally compatible.

Then, the permeability of the polymeric membrane made of linear or star copolymers to small ions were investigated. In the 3D format, *i.e.*, in the context of polymersomes, it was found that the membrane permeability of PGL-PBO-PGL polymersomes to H<sup>+</sup> decreased with increasing membrane thickness, consistent with the general rules. It was also interestingly found that the membrane of  $\beta$ CD-(PBO-PGL)<sub>14</sub> polymersome, which contained  $\beta$ CD moieties in the hydrophobic membrane, was less permeable than its linear counterpart of comparable thickness. This result was attributed to the hydrophobic nature of  $\beta$ CD cavity, considering PBO chains were a little more stretched in  $\beta$ CD-(PBO-PGL)<sub>14</sub> polymersomes than the case of PGL-PBO-PGL polymersomes.

In the planar format, the PGL-PBO-PGL membranes were impermeable to K<sup>+</sup> and Cl<sup>-</sup>, similar to lipid bilayers, but with a stability under a high voltage which is an important characteristic. The  $\beta$ CD-(PBO-PGL)<sub>14</sub> membrane seemed to be permeable, with the observation of unitary currents similar than the ones obtained when the star copolymers were inserted in lipid bilayers. However, unexpected phenomena were observed and need to be explained.

At the end, with the aid of BLM technique, the possibility to insert natural and synthetic nanopores into the polymeric membranes was studied. The preliminary results indicated that mellitin, known as natural nanopore, could be inserted into the PGL-PBO-PGL planar membrane and the resultant pores were observed in two different assays. The BLM technique also allowed the determination of the formation of ill-defined nanopores, information that has never been addressed yet in the case of polymeric membrane. However, in the case of  $\beta$ CD-(PBO-PGL)<sub>14</sub> star copolymer,

synthesized as artificial nanochannel, the ability to insert in planar polymeric membrane has not yet been proved, even if the insertion of star copolymers seemed to be possible.

In conclusion, our current work has proved the targeted versatile platform, a  $\beta$ CD-based nanochannel-equipped polymersome reachable, by the successful preparation of the tailor-made linear and star amphiphilic copolymers as well as the positive preliminary BLM characterization results. Indeed, the polymeric membranes made of linear copolymers are stable and robust, and the  $\beta$ CD-based star copolymers interact with the planar polymeric membrane.

We anticipate the targeted fully synthetic platform is promising for nanotechnological applications due to its tunable physicochemical properties, good stability and antifouling capacity. Therefore, this research topic deserves deeper and further explorations in the following aspects, to name but a few:

One is to probe the size-selective permeability of the polymersome membranes made of linear copolymers or  $\beta$ CD-based star copolymers. In the current work, the results concerning the permeability to  $H^+$  demonstrated the difference between the polymersomes made of linear copolymers and those made of star copolymers originating from  $\beta$ CD cavities. These results encourage us to take advantage of the specific properties of  $\beta$ CD cavities, in terms of size-selective permeability [1]. It is expected that, in the presence of  $\beta$ CD cavities, the membrane is more permeable to the low-molar-mass neutral molecules (*e.g.* glucose) than that without  $\beta$ CD cavities. Another challenge would be to also go deeper in the ion-selective permeability.

Furthermore, it is possible to construct polymersome compartments with tunable permeability, by adjusting the molar ratio of  $\beta$ CD moieties in the membrane. Co-assembly of polymer blend has been demonstrated as a feasible and facile strategy to tune the morphology of assembled nanostructures and the membrane permeability of the resultant polymersomes [2–4]. This idea was recently adopted to build mellitin-inserted polymersomes [5]. As emphasized in many research works, in the co-assembly method, both the chemical and dimensional compatibility between the different components is crucial to construct stable structures. In this project, the linear and star copolymers are similarly designed in terms of chemical composition and each can be tailor-made in terms of the lengths of blocks. Therefore, it is foreseen that the co-assembled polymersomes with tunable membrane permeability are achievable.

These permeable polymersomes can be further developed into nanoreactors by encapsulating enzymes (*e.g.*, CalB, GOx) inside the aqueous lumen and performing enzymatic reactions [6].

In parallel with the three-dimensional investigations, it would be interesting to deepen the study of the insertion of  $\beta$ CD-based star copolymers into planar polymeric

membranes by BLM method. It was reported that membrane curvature plays a critical role in the functional insertion of natural nanopores into both lipid bilayers and polymeric membranes [5]. Additionally, BLM method is favorable to study the interactions and insertions at molecular level [7,8], while the common three-dimensional studies usually provide statistically average results. Having those two points of view is really valuable to understand the mechanism involved in the insertion or the permeability.

In the current work, the planar polymeric membranes made of linear block copolymers have been proved inherently stable and insulating. The preliminary results also showed that the unitary current induced by the  $\beta$ CD cavities in the planar membrane made of  $\beta$ CD-based star copolymers. Additionally, the interactions between  $\beta$ CD-based star copolymers and polymeric membrane is also observed, although the typical current jumps resulting from the translocation of ions through the nanopores are not yet detected. The positive point is that the synthetic nanochannel scaffolds (*i.e.*,  $\beta$ CD-based star copolymers) and the polymeric membranes (*i.e.*, linear copolymers) are designed to be chemically compatible, therefore, the nanochannels are expected to be functionally inserted into the polymeric membranes, when the dimensions match.

As a reminder, the length of the polymer chains on  $\beta$ CD core should also be optimized considering the risk of blockage of the  $\beta$ CD cavity by the polymer chains [9]. It was recently reported that it was difficult to insert mellitin into the pre-formed planar polymeric membrane which was less dynamic/fluid [5]. Hence, a “co-painting” method is also suggested herein. The concept of “co-painting” is similar to that of the aforementioned co-assembly strategy, consisting in constructing polymeric membrane and inserting nanochannels simultaneously, by “painting” the solution of the mixture of linear and star copolymers on the 150- $\mu$ m window to form “pre-layer”, and sequentially adding the mixture solution into the chamber so as to form the polymeric membrane and insert nanochannels simultaneously.

Another possibility would be to change the chemical composition of the linear copolymers and star copolymers, to induce a change in the dynamics of the chains and possibly a change of permeability.

We hope our investigation on the  $\beta$ CD-based nanochannel-inserted polymeric membranes could add a brick to the wall of biomimetism of eukaryotic cell.

## References

1. Himmelein S, Sporenberg N, Schönhoff M, et al. Size-selective permeation of water-soluble polymers through the bilayer membrane of cyclodextrin vesicles investigated by PFG-NMR[J]. Langmuir, 2014, 30(14): 3988-3995.

2. Wright D B, Patterson J P, Gianneschi N C, et al. Blending block copolymer micelles in solution; obstacles of blending[J]. *Polymer chemistry*, 2016, 7(8): 1577-1583.
3. Steinschulte A A, Gelissen A P H, Jung A, et al. Facile screening of various micellar morphologies by blending miktoarm stars and diblock copolymers[J]. *ACS Macro Letters*, 2017, 6(7): 711-715.
4. Bueno C Z, Apolinario A C, Duro-Castano A, et al. L-Asparaginase Encapsulation into Asymmetric Permeable Polymersomes[J]. *ACS Macro Letters*, 2020, 9(10): 1471-1477.
5. Belluati A, Mikhalevich V, Yorulmaz Avsar S, et al. How do the properties of amphiphilic polymer membranes influence the functional insertion of peptide pores?[J]. *Biomacromolecules*, 2019, 21(2): 701-715.
6. Peters R J R W, Louzao I, van Hest J C M. From polymeric nanoreactors to artificial organelles[J]. *Chemical Science*, 2012, 3(2): 335-342.
7. El Ghoul Y, Renia R, Faye I, et al. Biomimetic artificial ion channels based on beta-cyclodextrin[J]. *Chemical Communications*, 2013, 49(99): 11647-11649.
8. Faye I, Huin C, Illy N, et al.  $\beta$ -Cyclodextrin-Based Star Amphiphilic Copolymers: Synthesis, Characterization, and Evaluation as Artificial Channels[J]. *Macromolecular Chemistry and Physics*, 2019, 220(2): 1800308.
9. Eskandani Z, Le Gall T, Montier T, et al. Polynucleotide transport through lipid membrane in the presence of starburst cyclodextrin-based poly (ethylene glycol) s[J]. *The European Physical Journal E*, 2018, 41(11): 1-7.



**[Nanopores artificiels à base de beta-cyclodextrine insérés dans une membrane polymère]**

**Résumé :**

Ce projet de thèse visait à construire une plateforme polyvalente en nanotechnologie, conçue comme un compartiment de type polymère, équipé de nanocanaux artificiels à base de beta-cyclodextrine ( $\beta$ CD). Des polymersomes bien définis ont été produits via l'auto-assemblage de copolymères à blocs amphiphiles linéaires, polyglycidol-*b*-poly(oxyde de butylène)-*b*-polyglycidol (PGL-PBO-PGL), possédant une stabilité à long terme et une capacité antisalissure. Des copolymères amphiphiles en étoile, à cœur  $\beta$ CD, bien définis,  $\beta$ CD-(PBO-PGL)<sub>14</sub>, ont également été synthétisés avec une longueur sur mesure de chaque bloc, une faible dispersité et une pureté élevée. Les comportements d'auto-assemblage des copolymères étoiles amphiphiles étaient similaires à ceux de leurs homologues linéaires. En outre, la perméabilité de la membrane polymère, constituée de copolymères linéaires ou en étoile, aux ions ( $H^+$ ,  $K^+$ ,  $Cl^-$ ) a été étudiée par spectroscopie de fluorescence et par mesures de type BLM : il a été montré des comportements différents pour les copolymères linéaires et en étoile. Il semble que les copolymères étoiles  $\beta$ CD-(PBO-PGL)<sub>14</sub> pourraient s'insérer dans la membrane plane PGL-PBO-PGL, mais des investigations supplémentaires doivent être effectuées.

Mots clés : [copolymères amphiphiles, auto-assemblage, polymersomes, nanopores artificiels]

**[*beta*-Cyclodextrin-based Artificial Nanochannel Scaffolds Inserted in Polymeric Membrane]**

**Abstract :**

This PhD project aimed to construct a versatile platform for nanotechnological applications, which was designed as a polyglycidol (PGL)-based polymersomal compartment equipped with beta-cyclodextrin ( $\beta$ CD)-based artificial nanochannels. Well-defined polymersomes have been produced via self-assembling of linear amphiphilic block copolymers, polyglycidol-*block*-poly(butylene oxide)-*block*-polyglycidol (PGL-PBO-PGL), possessing long-term storage stability and antifouling capacity. Well-defined  $\beta$ CD-cored star amphiphilic copolymers,  $\beta$ CD-(PBO-PGL)<sub>14</sub>, have also been synthesized with tailor-made length of each block, low polydispersity and high purity. The self-assembly behaviors of the amphiphilic star copolymers were similar to those of their linear counterparts. Additionally, the permeability of the polymeric membrane made of linear or star copolymers to small ions ( $H^+$ ,  $K^+$ ,  $Cl^-$ ) were investigated by fluorescence spectroscopy and BLM-type measurements: different behaviors for linear and star copolymers have been shown. It seems that  $\beta$ CD-(PBO-PGL)<sub>14</sub> star copolymers could insert into the planar PGL-PBO-PGL membrane, but further investigations have to be performed.

Keywords: [amphiphilic copolymers, self-assembly, polymersomes, artificial nanochannels]